IMPROVING PRE-SALT RESERVOIRS SEISMIC IMAGES WHEN CONSIDERING THE STRATIFIED EVAPORITES INSERTION IN THE INITIAL MODEL FOR THE VELOCITY UPDATING PROCESSES PRIOR TO THE SEISMIC MIGRATION

Alexandre Rodrigo Maul[1,2], Marco Antonio Cetale Santos[2], Cleverson Guizan Silva[2],
Leonardo Márcio Teixeira da Silva[1,2], María de Los Ángeles González Farias[3], Josué Sá da Fonseca[1],
Roberto de Melo Dias[1], João Batista Teixeira Boechat[1], Filipe Augusto de Souto Borges[1],
Lívia Falcão Fernandes[1], Thiago Martins Yamamoto[1,2] and Rodrigo Leandro Bastos Pontes[1,2]

ABSTRACT. Structurally complex areas, such as the pre-salt section in the offshore Santos Basin, SE Brazil, are challenging to represent geologically using seismic images. One of the main causes of the observed imaging problems is the evaporitic section and its considerations about velocities used for seismic migration purposes. Some authors consider set to this section an almost constant value (close to 4,500 m/s) which approximately represents the halite velocity, the most abundant mineral in this salt formation. Others, over these models, apply the tomographic inversion or FWI schemes giving to the velocity model the mathematical support to build confident seismic images. We believe in the importance of building starting velocity models reflecting the existing geological features prior to applying the tomographic/FWI updating. In this sense, we propose the insertion of the so-called stratifications within the evaporitic section using an adaptation of the model-based seismic inversion technique. Following this new velocity model including the stratification, we suggest tomographic iterations update or FWI, to add to the geological constrains of the model the needed mathematical convergence. Finally, in this work, we performed the seismic migration with and without inserting these geological features in the initial velocity model and compared the results.

Keywords: evaporitic section, stratifications, velocity model, seismic migration, seismic image.

RESUMO. Em áreas estruturalmente complexas, como na seção pré-sal da Bacia *offshore* de Santos, região SE do Brasil, é um desafio representar a geologia utilizando imagens sísmicas. Uma das principais causas dos problemas observados está nas considerações sobre a seção evaporítica e suas velocidades com propósito de migração sísmica. Alguns autores consideram esta seção como tendo velocidades geralmente constantes (próximas de 4.500 m/s), o que representa aproximadamente o comportamento da halita, o mineral mais abundante nesta seção. Outros, sobre este modelo, aplicam a atualização por inversão tomográfica ou FWI para dar ao modelo de velocidades o suporte matemático necessário para construir imagens sísmicas confiáveis. Nós acreditamos na importância de construir modelos iniciais de velocidades que reflitam as características geológicas existentes antes de aplicar esta atualização tomográfica/FWI mencionada. Neste sentido, propomos a inserção das denominadas estratificações dentro da seção evaporítica, utilizando uma adaptação da técnica de inversão sísmica *model-based*. Seguindo este novo modelo incluindo as estratificações, sugerimos a atualização por iterações tomográficas ou FWI, para adicionar ao controle geológico do modelo a convergência matemática necessária. Finalmente, neste trabalho, nós realizamos a migração com e sem a inserção destas características geológicas no modelo inicial de velocidades e comparamos os resultados.

Palavras-chave: seção evaporítica, estratificações, modelo de velocidade, migração sísmica, imagem sísmica.

[1]Petrobras - Reservoir Geophysics, Avenida Henrique Valadares, 28 / 6º andar, 20031-030, Rio de Janeiro, RJ, Brazil – E-mails: alexandre.maul@petrobras.com.br, lmtsilva@petrobras.com.br, josuefonseca@petrobras.com.br, roberto.dias@petrobras.com.br, jboechat@petrobras.com.br, filipeborges@petrobras.com.br, liviafalcao@petrobras.com.br, thiagomyamamoto@petrobras.com.br, rpontes@petrobras.com.br

[2]Universidade Federal Fluminense – UFF, Geology and Geophysics, Av. Milton Tavares de Souza, s/nº - Gragoatá, 24210-340, Niterói, RJ, Brazil – E-mails: marcocetale@id.uff.br, cguizan@id.uff.br

[3]Emerson Automation Solutions, Av. Rio Branco, 138, sala 1702, 20040-002, Rio de Janeiro, RJ, Brazil – E-mail: maria.g.gonzalez@emerson.com

INTRODUCTION

Drilling in the Brazilian offshore pre-salt reservoirs, in the Santos Basin, always requires crossing an evaporitic section that ranges from dozens of meters to a few kilometers of salt thickness. Besides, the presence of different types of evaporitic minerals, with diverse mechanical behaviors, imposes the creation of structural complex scenarios. Therefore, understanding and properly characterizing the rocks inside this section are essential for diverse activities as safety during the well drilling operations, geomechanical hazard evaluations, and geological velocity modeling for seismic processing, among many others processes.

Ji et al. (2011) defend the idea that homogenous velocity for the evaporitic section affects the images quality under the salt section. They cite the weakness and discontinuity in seismic reflection, diffractions-like events and misinterpretation as the main problems when choosing those homogeneous compressional velocity models over more heterogeneous ones. They propose the insertion of heterogeneities inside the evaporitic section, to better represent the compressional velocity variations.

Huang et al. (2010), evaluating seismic images in the Santos Basin, consider that good images for the pre-salt reservoir do not ensure a reliable depth position for the base of salt, which is the reference for the top of pre-salt reservoir. They associate this phenomenon with the usage of simple velocity models in the evaporitic section. These models disregard the velocity inhomogeneity as they are noticed by the stratifications inside the evaporitic section. They also confirm the necessity to adopt a complete "salt model" to correctly position the reservoir structures.

Jones & Davison (2014) mention many difficulties for the seismic imaging around or inside the salt bodies and use a dataset of the Santos Basin as the main example to emphasize those difficulties. They cite the inaccuracies in the compressional velocity assumptions or representations for the evaporitic section velocity model as the probable cause of this issue. They also observe some features such as interbedded layers (stratifications), overlying layers (a superior anhydrite and/or the Albian rafts presence) and salt flanks (encompassed within the HSD – Hidden Stratified Domain as proposed by Maul et al., 2018b).

Jackson et al. (2015) emphasize the presence of "enigmatic structures" within the evaporitic section in the Santos Basin. In Mohriak et al. (2008), we found the first statement of the term "enigmatic reflectors" which we believe have same meaning of the "enigmatic structures" as mentioned by Jackson et al. (2015).

These features probably are the part of the seismic response of interbedded layers as mentioned by Jones & Davison (2014).

Since 2015, several results related to the evaporitic stratification modeling intending to enhance the pre-salt projects have been presented (Maul et al., 2015; Jardim et al., 2015; Meneguim et al., 2015). Maul et al. (2018b) summarize and state these features as the evaporitic stratifications caused by the mineral variation.

During the methodology development, several applications have taken advantage of using this strategy of modeling evaporitic stratifications. The more promising applications are related to uncertainties (Maul et al., 2015; Jardim et al., 2015), geomechanics (Toríbio et al., 2017; Teixeira et al., 2018), Kirchhoff migration and Reverse Time Migration – RTM (Gobatto et al., 2016; Fonseca et al., 2018; Maul et al., 2018a) and the initial model for Least-Square Migration (Dias et al., 2019).

In seismic migration tasks, until the early 2000's, the evaporitic section in the Santos Basin was usually considered as almost constant (compressional velocity around 4,500 m/s), with some tomography approach in order to update the compressional velocity, observing the gather alignment behaviors. Falcão (2017) proves that a reasonable depth migration in complex areas such as the pre-salt reservoirs in the Santos Basin depends on the accuracy of the geological velocity models.

Although the tomographic inversion supports the entire migration process, it is not a perfect solution for the velocity models updating (Guo & Fagin, 2002). These authors emphasize the necessity of incorporating a reasonable geological knowledge into velocity modeling workflow. Potentially, the FWI (Full-Waveform Inversion) methodology can generate high-resolution velocity models (Vigh & Starr, 2008), which are currently appropriate for the RTM (Reverse Time Migration) technique. However, according to Vigh et al. (2009), one of the main challenges for the FWI techniques is to produce (or to reproduce) a good initial velocity model to generate the seismic images with geological confidence regarding the subsurface geology.

Currently, the state-of-the-art regarding processing techniques are FWI for velocity model building (Ben-Hadj-Ali et al., 2008; Barnes & Charara, 2009; Operto et al., 2013; Vigh et al., 2014) and Least-Square Migration (LSM) for imaging as per discussed in Nemeth et al. (1999); Hu et al. (2001); Dias et al. (2017); Wang et al. (2017); Dias et al. (2018). These techniques are becoming the standard for the pre-salt projects in the Santos Basin, offshore Brazil.

Even though laboratory measurements indicate that the anisotropy in core evaporite samples is negligible (Yan et al., 2016), the multilayered rock sequences impose extrinsic anisotropy behavior when the seismic wavelength is significantly larger than the thickness of any individual layers (Backus, 1962).

Raymer et al. (1999, 2000) state that the salt extrinsic anisotropy could be over than 7% in the preferred direction of evaporation. Landrø et al. (2011) analyze salt-mine outcrops and infer a moderate degree of anisotropy in the order of 5% difference between horizontal and vertical velocities. Several authors consider that anisotropy for any geological layer is mandatory in order to generate more realistic seismic images (Cogan et al., 2011; Zdraveva et al., 2011; Cooke et al., 2012).

The importance of the anisotropy for the seismic imaging process is undoubtable. However, this aspect is not within the scope of this work and further discussions about this matter are not presenting in our results.

METHODOLOGY

The first part of the methodology applied in this project follows the workflow presented in González et al. (2016), see Figure 1. This method allows the insertion of the salt stratifications or the layered sequence using seismic acoustic inversion (as presented by Meneguim et al., 2015), or any other seismic attribute if the inversion output is not available. The 1D analysis is performed with well logs and cutting supporting all stages. The first 3D approach is an initial model with geological constraints, where the stratifications are represented by combining velocities and seismic attributes. Then, a model-based inversion can be done for a better characterization of the rocks in the evaporitic section. Finally, a seismic facies classification, using impedance response in a Bayesian probabilistic approach, is performed to improve the modeling and to include uncertainty analysis to work with several scenarios. This gives to the evaporitic section the needed heterogeneity, especially to generate the initial compressional velocity model for the tomographic/FWI updating process, which precedes the migration as postulated by Fonseca et al. (2018), see Figure 2. The workflow requires previous stratigraphic interpretation, rock-physics analysis, model-based seismic inversion building and conversion from acoustic impedance to compressional velocity. It provides the initial velocity model to velocity updating (Tomography/FWI). After those velocity updating processes, and the gather alignment evaluation, another seismic migration is performed, generating a new and enhanced seismic image.
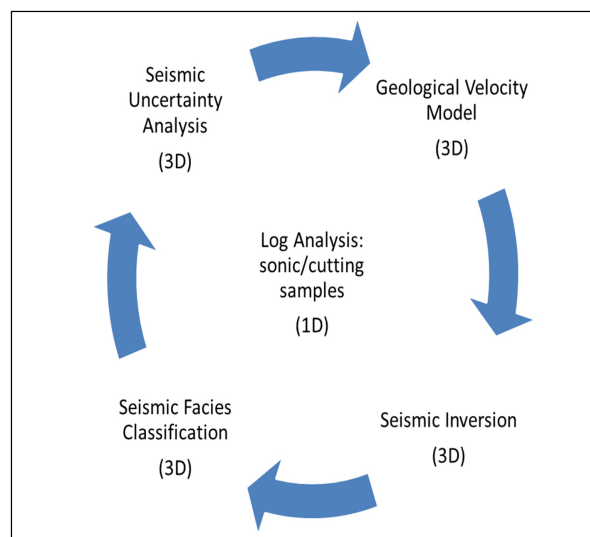
Figure 1 – Proposed workflow to generate a more realistic geological seismic velocity model (adapted from González et al., 2016).
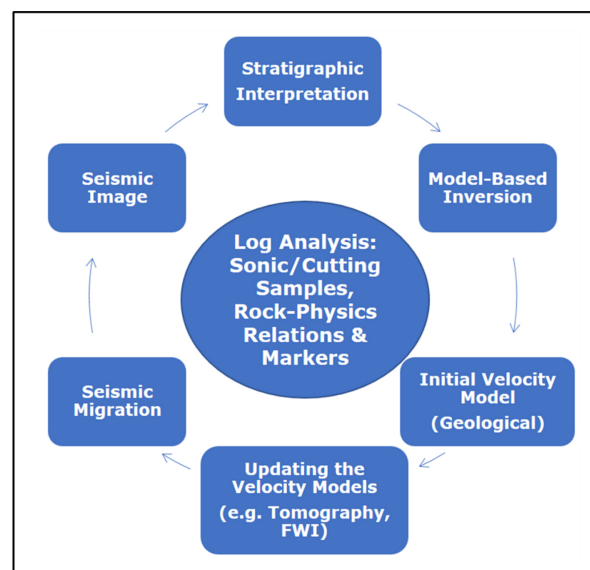
Figure 2 – Proposed workflow for the seismic image updating (adapted from Fonseca et al., 2018).

To verify the efficiency of the methodology, we performed the tomographic inversion process and analyzed the gather alignment panels over two models. The first model is the standard one, which considers an almost constant compressional velocity model for the evaporitic section; the second is the stratified one, generated by an acoustic seismic inversion, as tested and presented in Gobatto et al. (2016); Fonseca et al. (2017); Fonseca et al. (2018); Maul et al. (2018a).
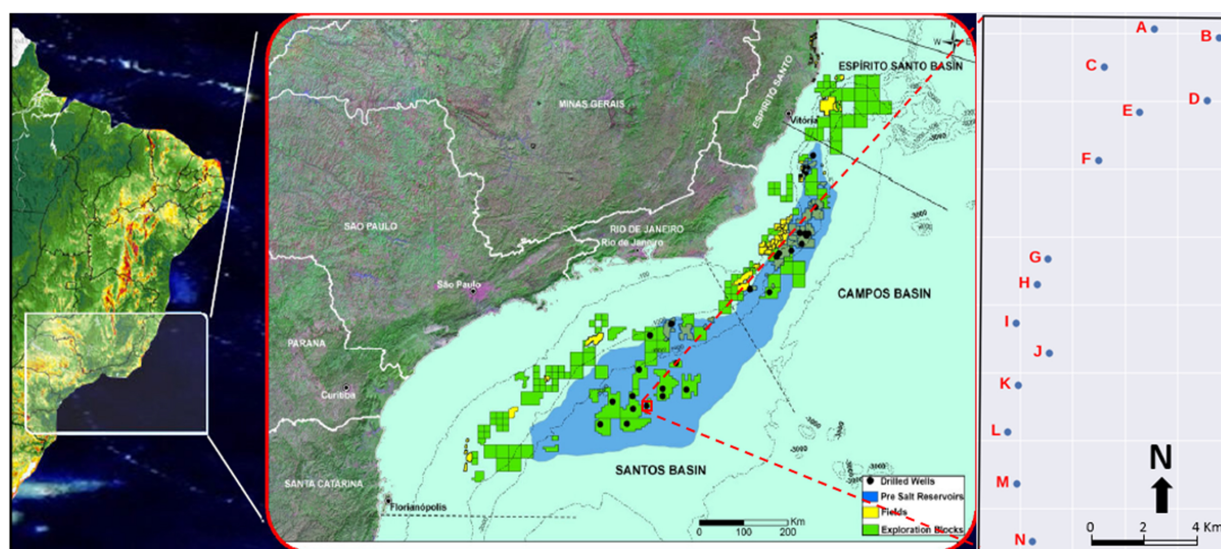
Figure 3 – Location of study area (regional) and details of the available data. Dark blue shading is the area with hydrocarbon occurrences in the pre-salt province in the Santos and Campos Basins, covering an area of approximately 350,000 km². Water column ranges from 2,000 to 3,000 m.

STUDY AREA AND AVAILABLE DATA

The study area is located in the pre-salt province in the Santos and Campos Basins. The specific tested dataset for this work is inserted into the project area that the first author has the formal authorization from the Agência Nacional do Petróleo, Gás Natural e Biocombustíveis (ANP) to develop his doctorate research. This area is a piece of the pre-salt Santos Basin province (Fig. 3) and contains a pre-stack depth migrated (PSDM) covering an area of approximately 200 km² and 14 wells with a broad suite of logs. In this study, the wells were labeled with capital letters from A to N, and the official names can be found in Table 1. Maul et al. (2018a & 2018c) demonstrate, using 182 wells of different 9 projects/fields in the Santos Basin, that the evaporitic section of these studied fields has many features in common, such as mineral percentages of occurrence, mineral percentages x thickness relation and velocity ranges per mineral groups.

RESULTS, ANALYSIS AND DISCUSSIONS

The type variation of minerals, occurrence frequency and velocity are important considerations addressed when analyzing heterogeneities inside the evaporitic section. Figure 4 shows some wells drilled in the Santos Basin emphasizing the multilayered evaporite sequence. In this sense, Maul et al. (2018c) summarized the study of these 182 wells (Table 2), reflecting the average occurrence for each field, based on the following grouping: Low Velocity Salt (LVS); Halite and High Velocity Salt (HVS). The low velocity salt group (LVS) is mainly

composed by carnallite, tachyhydrite, sylvite and other mobile salts; and the high velocity salt group (HVS) is basically composed by anhydrite and gypsum.

Table 1 – Correspondence between the well designations used in this study and the official names from ANP.

This Study	ANP
A	3-BRSA-788-SPS
B	9-BRSA-1037-SPS
C	8-SPH-23-SPS
D	8-SPH-13-SPS
E	7-SPH-14D-SPS
F	7-SPH-8-SPS
G	7-SPH-4D-SPS
H	9-BRSA-928-SPS
I	7-SPH-5-SPS
J	9-BRSA-1043-SPS
K	1-BRSA-594-SPS
L	7-SPH-1-SPS
M	7-SPH-2D-SPS
N	3-BRSA-923A-SPS

Figure 5 illustrates how the compressional velocity varies among the minerals. In this study, we considered the average value per mineral plus the variation (+/-) taking two standard deviations as the reference.
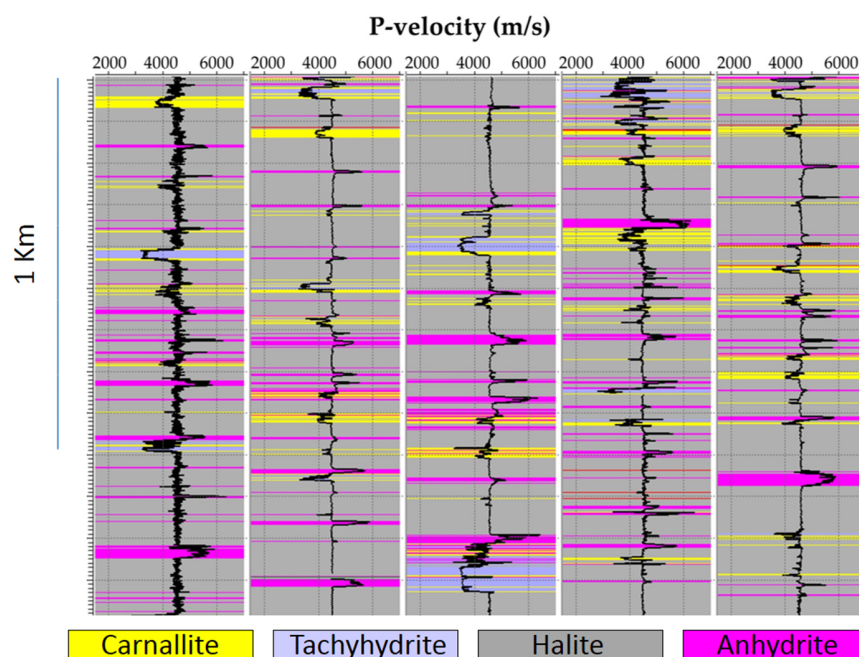
Figure 4 – Identified stratifications inside the evaporitic section, considering a small piece of wells (5) from the 182 previously mentioned. Adapted from Maul et al. (2018a).

**Table 2** – Salt proportions and interval velocities (m/s) for nine fields inside the Santos Basin.

Field	# Wells	% LVS	LVS ACV	% Halite	Halite ACV	% HVS	HVS ACV	WCV
1	20	8	4,018.56	83	4,480.88	8	5,210.27	4,462.56
2	29	9	4,218.47	82	4,563.69	9	4,975.84	4,567.53
3	17	12	4,054.42	77	4,498.25	12	4,989.92	4,505.66
4	3	13	3,971.00	71	4,507.09	16	4,927.59	4,505.04
5	5	3	4,167.00	84	4,538.00	13	5,123.33	4,576.00
6	7	3	4,264.19	80	4,509.87	17	5,061.36	4,596.05
7	72	8	4,122.33	81	4,526.47	11	5,105.84	4,560.03
8	25	4	4,182.53	88	4,533.59	8	5,003.35	4,547.16
9	4	6	4,055.63	81	4,486.58	13	5,077.49	4,535.67
TNW	182							
AVG		7	4,117.13	81	4,516.05	12	5,052.78	4,539.52

LVS: Low Velocity Salt; HVS: High Velocity Salt; ACV: Average Compressional Velocity; WCV: Weighted Compressional Velocity; TNW: Total Number of Wells; AVG: Average; Compressional Velocity (m/s). Modified from Maul et al. (2018c).

In Figure 6, Fonseca et al. (2018), using 2 among the 182 available wells, illustrate how the mineral occurrence can be quantified per well, considering the mineral grouping proposed by Maul et al. (2018b), following the methodology described in Amaral et al. (2015), which intends to fill the well-log gaps using the interpreted drill cutting samples. In the mentioned study, the authors calculated the average compressional velocity for each well location, weighting by each mineral grouping proportion.
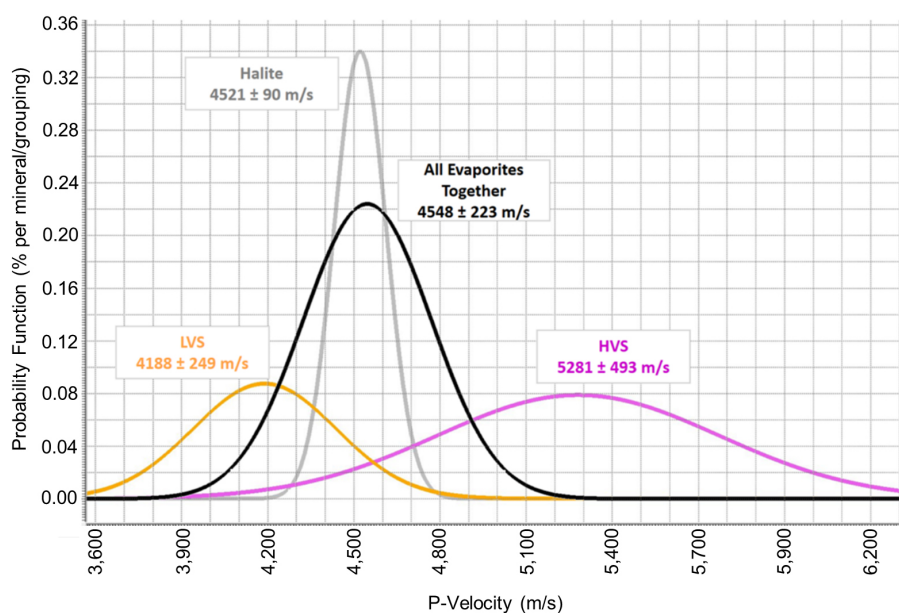
Figure 5 – Mineral compressional velocity variation obtained from the logs considering a sample of 10 wells, among the 182 ones summarized in Table 2. Adapted from Maul et al. (2018a).
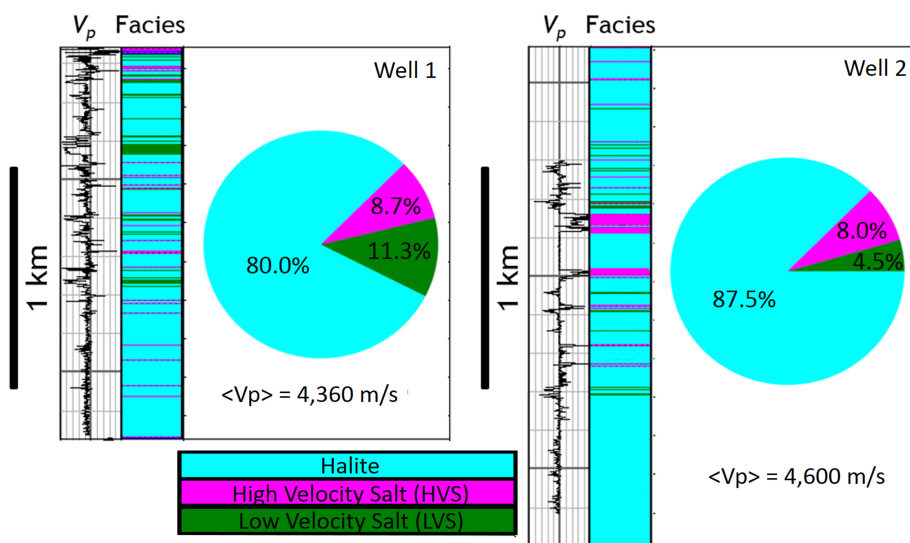
Figure 6 – Example of the mineral occurrence (grouping) of 2 wells from the 182 wells analyzed for the development of the methodology. Adapted from Fonseca et al. (2018).

Analyzing Figure 6, it is reasonable to infer that the mineral content would be influencing the average compressional velocity at any well location. At well 1, the LVS proportion is higher than the HVS one. This difference affects the average compressional velocity in this well, decreasing its value. On the opposite way, analyzing well 2, the HVS content is higher than the LVS, increasing the average velocity compressional velocity. However, in both cases, the seismic velocity used for the legacy migration at those locations is close to 4,500 m/s, representing only the halite compressional velocity.

Figure 7 depicts the compressional velocity for the evaporitic section considering the stratification insertion by combining rock-physics and seismic inversion. We also compare it with the tomographic compressional velocity provided by
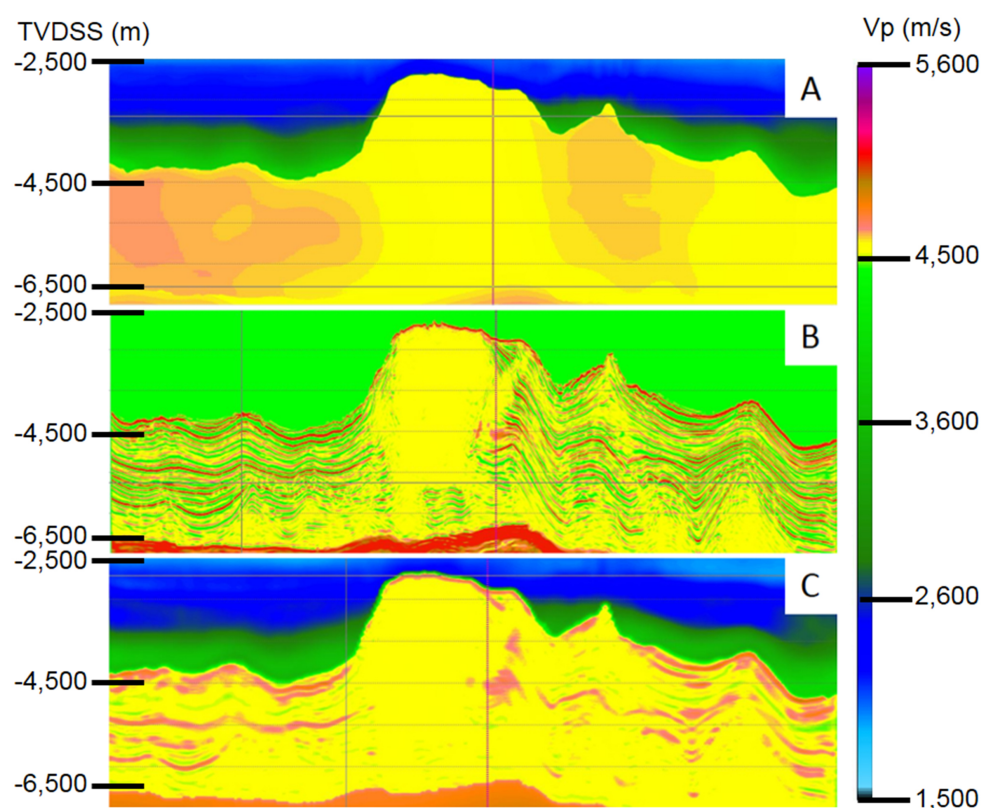
Figure 7 – Salt heterogeneity representation: A: Compressional velocity obtained from the inversion tomography. This model corrects the almost constant velocity model using gather alignment as criteria; B: Compressional velocity obtained from the acoustic inversion results (model-based approach) applying a polynomial transformation to the impedance guided by the well logs. It illustrates the existing stratification controlled by amplitude response and well information; C: Smoothed compressional velocity model obtained from the inversion results. In this case, after applying a polynomial transformation guided by the well logs, we smoothed the model vertically. Adapted from Maul et al. (2018a).

the seismic processing. It is important to notice that, in order to use the stratified model to migrate the data, a vertical smoothing is necessary (Fig. 7C). The importance of considering the model-based inversion approach to better establish the stratification is well exemplified and documented in several works (Meneguim et al., 2015; Teixeira et al., 2017; Toríbio et al., 2017; Barros et al., 2017, Fonseca et al., 2018; Teixeira et al., 2018; Maul et al., 2019a, 2019b; Teixeira & Lupinacci, 2019).

As mentioned in Figure 7, the acoustic inversion output (Acoustic Impedance - Ip) must be converted to compressional velocity (Vp) to be used in the migration process. In this case, we consider the polynomial fit illustrated in Figure 8. It is important to mention that the curve-fitting choice is a source of uncertainties for the entire study. Thus, considerations about uncertainties are important in the development of similar studies. To emphasize this uncertainty estimation and the alternatives in controlling it,

Teixeira & Lupinacci (2019) suggest the confidence level for the estimation as one possibility. In this case the authors regards the 95% of the best-fitting curve and propose that inside this confidence level any alternative fit are defensible. However, the physical implications in the choice of different equations need to be carefully analyzed and constrained by well logs, essentially because they can lead to incorrect depth positioning.

In Figure 9 we present two maps of the average compressional velocity for the evaporitic section. Figure 9A illustrates the average compressional velocity map for the evaporitic section considering the original tomographic velocity model (the standard approach). In that case, the methodology applied a "flooded salt model" (initially almost constant – 4,500 m/s), followed by tomography – three iterations were necessary to achieve a good gather alignment. In the second map (Fig. 9B), we built the compressional velocity model for the evaporitic section
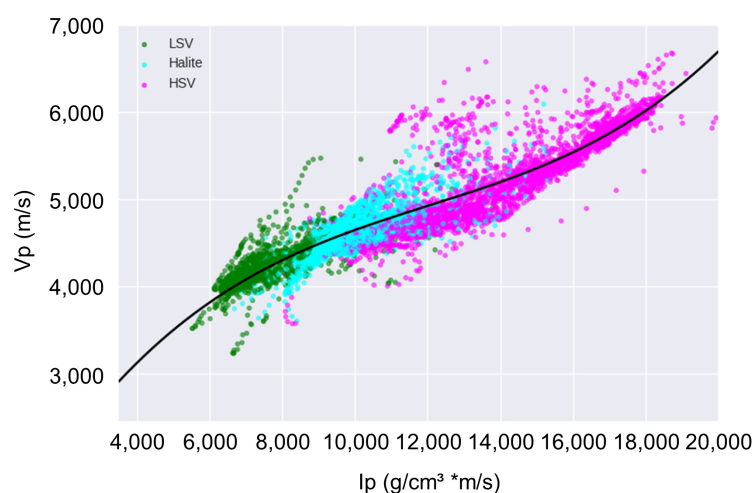
Figure 8 – Transformation from Acoustic Impedance (Ip) to Compressional Velocity (Vp). Well-log cross-plot (Vp versus Ip). Colors are mineral groups (Green – LVS; Light Blue – Halite and Purple – HVS). Black line is the polynomial fit considered in Maul et al., 2019b.
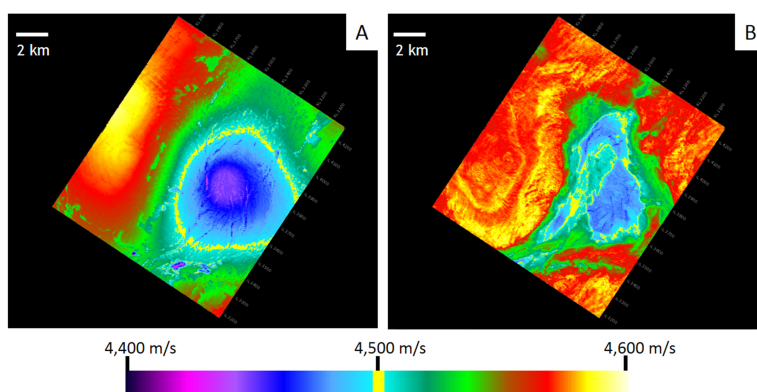
Figure 9 – Average compressional velocity (Vp) map for the evaporitic section. A: Considering the almost constant Vp (4,500 m/s) as the initial model, plus the three tomographic inversion updates for the evaporitic section; B: Considering the stratified velocity model as the initial model, plus the one tomographic inversion update for the evaporitic section. Adapted from Maul et al. (2018a).

using the combination of rock-physics analysis and model-based acoustic inversion. Remarkably, only one tomographic iteration was necessary to achieve a similar level of gather alignment.

The stratification insertion imposes to the evaporitic compressional velocity model the heterogeneities observed in the seismic response (the reflections inside the evaporitic section), and sampled during the well drilling process. Therefore, the average compressional velocity map must reflect it, which we can observe only on Figure 9B. Figure 9A does not present these heterogeneities, since it considers a smooth compressional velocity model for the evaporitic section.

Figure 10 presents a seismic section and an example of gather alignment. The main difference when adopting the stratified model is the reduction in the number of iterations necessary during the tomographic inversion. The "cost" reduction due to the application of this procedure also ensures a good image quality.

We can see through the analysis of Figures 11, 12 and 13 that, besides the gain related to the reduction of computational cost, the image quality has also improved, with better images focusing, structural representation, and vertical positioning. In these images, the only difference is the velocity model used
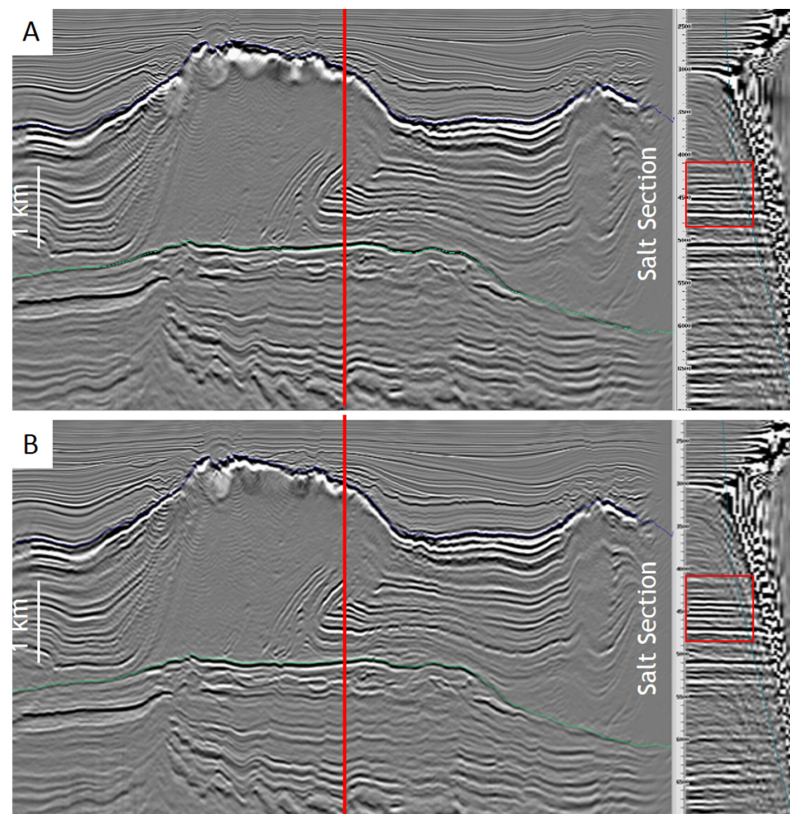
Figure 10 – Migrated seismic section and a piece of a seismic gather panel illustrating the obtained alignment considering (the vertical red lines in the left part of figures "A" and "B" represent the position where the gathers were analyzed and the boxes in the right part represent the details of the gather alignment in both cases): A: The starting compressional velocity model, almost constant, after the three tomographic inversion iterations to align the analyzed gathers; B: The starting compressional velocity model delivered by the stratification insertion, after the single tomographic inversion iteration to align the analyzed gathers. Observe the same level of gather alignment in both examples, which implies a reduction of computational cost when considering the stratified model. Adapted from Maul et al. (2018a).

for migration. Another point to be considered is the fact that due to computational limitations, the Kirchhoff algorithm was the choice for the seismic migration, although we are aware of better algorithms to be applied in this dataset, like Reverse Time Migration (RTM) and Least Square Migration (LSM). In other words, we believe that the image quality could be even more enhanced when considering more appropriate algorithms.

CONCLUSIONS

We believe that the way to improve seismic images in structurally complex areas such as the pre-salt reservoirs in the Santos Basin is to choose wisely the correct migration algorithm and to construct more realistic compressional velocity model containing reliable geology features.

The combination of rock-physics and model-based acoustic inversion approach gives to the evaporitic section an important contribution in terms of geology by inserting the existing multilayered stratifications.

The representation of geological features decreases the computational effort as it reduces the numbers of iterations in order to obtain good gather alignments prior to the final migration process (Maul et al., 2018a).

Besides the decrease in computational effort, the most important result when applying this combined approach (to perform the velocity update over the stratified model plus a good migration algorithm) is a more confident seismic image,
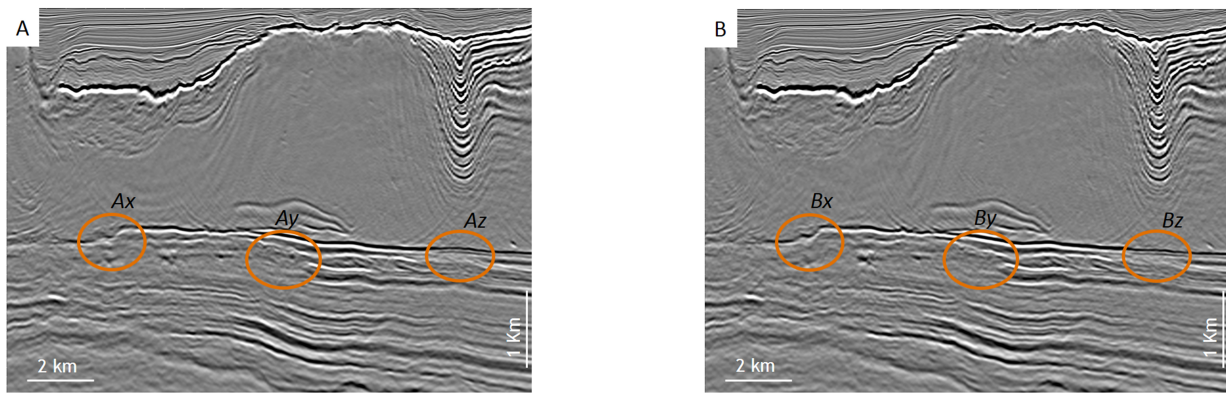
Figure 11 – Migrated seismic sections using both models: A: The starting compressional velocity model, almost constant, after the three tomographic inversion iterations to align the analyzed gathers; B: The starting compressional velocity model delivered by the stratification insertion, after the one tomographic inversion iteration to align the analyzed gathers. Observe the better imaging when using the model with the stratification insertion: better continuity of the reflector Bx over Ax and By over Ay, and the more coherent positioning in Bz than Az (notice the evaporitic behavior above the analyzed point). Adapted from Maul et al. (2018a).
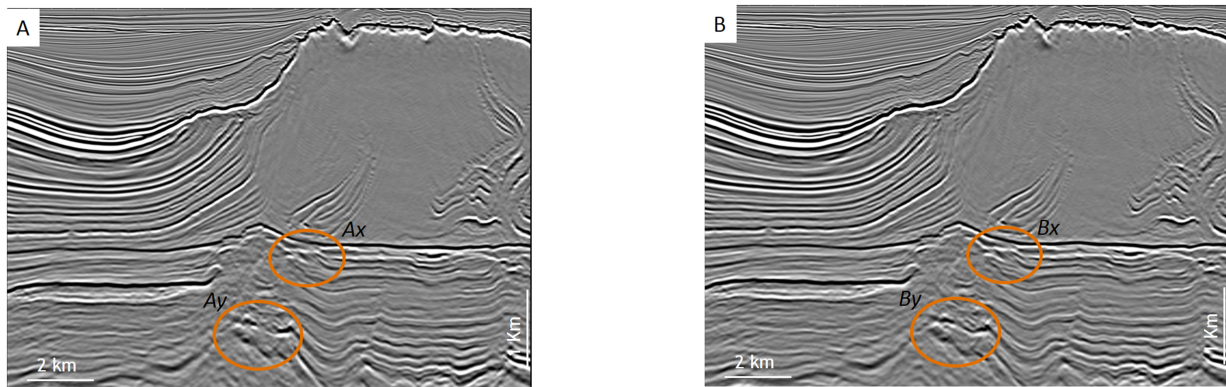
Figure 12 – Migrated seismic sections using both models: A: The starting compressional velocity model, almost constant, after the three tomographic inversion iterations to align the analyzed gathers; B: The starting compressional velocity model delivered by the stratification insertion, af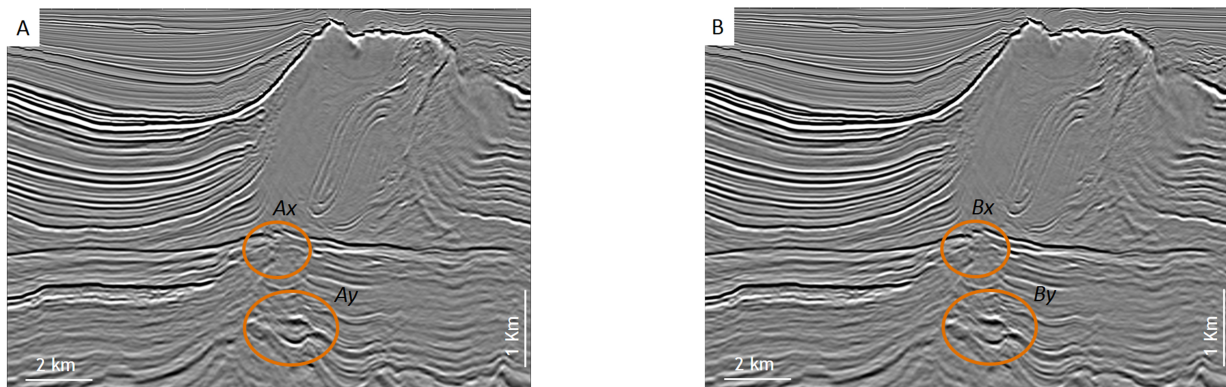ter the one tomographic inversion iteration to align the analyzed gathers. Observe the better focusing of the image when using the model with the stratification insertion: positions Bx over Ax, and better imaging building (continuity in geology) in By than Ay. Adapted from Maul et al. (2018a).

Figure 13 – Migrated seismic sections using both models: A: The starting compressional velocity model, almost constant, after the three tomographic inversion iterations to align the analyzed gathers; B: The starting compressional velocity model delivered by the stratification insertion, after the one tomographic inversion iteration to align the analyzed gathers. Observe the better imaging (the fault sharping) when using the model with the stratification insertion: positions Bx over Ax, and better event focusing when comparing By over Ay. Adapted from Maul et al. (2018a).

which covers several aspects: better representation of structures, geological event continuity, depth predictions and signal quality, allowing a better rock property distribution based on the seismic quantitative interpretation.

We still believe that the anisotropy of the evaporitic section could also consider the stratified model to guide the distribution of the three-dimension anisotropic parameters.

The methodology was tested in several seismic processing projects. Moreover, we also tested those models for new seismic design studies such as illumination studies (Maul et al., 2015), uncertainty analysis regarding both depth and lateral positioning and accuracy in reservoir property distribution (Meneguim et al., 2015; Paes et al., 2019), security in well drilling (Teixeira et al., 2015), geomechanical flow simulation (Teixeira et al., 2018).

Therefore, despite the seismic ambiguity and seismic resolution, we believe that it is an approach to consider in all projects for the pre-salt section in any basin around the world.

It is also important to take care about other relevant aspects in terms of compressional velocity model building not only for the evaporitic section as described in this paper. The authors are also researching and applying similar methodologies, looking for the incorporation of other important geologic features such as the Albian rafts in the Santos and Campos Basins, Brazilian offshore, structural complexity related to folds and faults, among others.

ACKNOWLEDGMENTS

REFERENCES

AMARAL PJ, MAUL A, FALCÃO L, GONZÁLEZ M & GONZÁLEZ G. 2015. Estudo Estatístico da Velocidade dos Sais na Camada Evaporítica na Bacia de Santos. In: 14th International Congress of the Brazilian Geophysical Society. Rio de Janeiro, RJ, Brazil: SBGf. doi: 10.1190/sbgf2015-131.

BACKUS GE. 1962. Long-wave elastic anisotropy produced by horizontal layering. Journal of Geophysical Research, 67: 4427-444427-4440. doi: 10.1029/jz067i011p04427.

BARNES C & CHARARA M. 2009. The Domain of Applicability of Acoustic Full-Waveform Inversion for Marine Seismic Data. Geophysics, 74(6): WCC91–WCC103. doi: 10.1190/1.3250269.

BARROS P, FONSECA J, TEIXEIRA L, MAUL A, YAMAMOTO T, MENEGUIM T, QUEIROZ LE, TORÍBIO T, MARTINI A, GOBATTO F & GONZÁLEZ M. 2017. Salt Heterogeneities Characterization in Pre-Salt Santos Basin Fields. In: Offshore Technology Conference. Rio de Janeiro, RJ, Brazil: OTC. doi: 10.4043/28147-MS.

BEN-HADJ-ALI H, OPERTO S & VIRIEUX J. 2008. Velocity Model Building by 3D Frequency-Domain, Full-Waveform Inversion of Wide-Aperture Seismic Data. Geophysics, 73(5): VE101-VE117. doi: 10.1190/1.2957948

COGAN M, ZDRAVEVA O, KAIRZHANOVA T & SCHOEMANN M. 2011. A Wide Azimuth TTI Model Building and Imaging Case Study from the Central Gulf of Mexico. In: 81st Annual Meeting. San Antonio, TX, USA. SEG – Society of Exploration Geophysicist. doi: 10.1190/1.3628053.

COOKE A, LE DIAGON F, DE MARCO R, AMAZONAS D, BUNTING T, MOLDOVEANU N, KLUG S & MATTOS E. 2012. Full-Azimuth Towed-Streamer Seismic: An Exploration Tool for Pre-Salt Hydrocarbon Exploration Offshore Brazil. In: 82nd Annual Meeting. Expanded Abstracts. San Antonio, TX, USA. SEG - Society of Exploration Geophysicist. doi: 10.1190/segam2012-1076.1.

DIAS BP, BULCÃO A, SOARES FILHO DM, SANTOS LA, DIAS RM, LOUREIRO FP & DUARTE FS. 2017. Least-Squares Migration in the Image Domain with Sparsity Constraints: An Approach for Super-Resolution in Depth Imaging. In: 15th International Congress of the Brazilian Geophysical Society. Expanded Abstracts. Rio de Janeiro, RJ, Brazil: SBGf. doi: 10.1190/sbgf2017-236.

DIAS BP, GUERRA C, BULCÃO A & DIAS RM. 2018. Exploring Inversion Strategies in Image Domain Least Squares Migration. In: First EAGE/SBGf Workshop on Least Squares Migration. Rio de Janeiro, RJ. Brazil. LMSTU01. doi: 10.3997/2214-4609.201803060.

DIAS R, FONSECA J, BULCÃO A, DIAS B, TEIXEIRA LM, MAUL A & BORGES F. 2019. Salt Stratification and Least Square Migration to Improve Pre-Salt Images: Santos Basin, Brazilian Offshore Example. In: 2nd EAGE/PESGB Workshop on Velocities. London, United Kingdom. doi: 10.3997/2214-4609.201900051.

FALCÃO LF. 2017. O Sal Estratificado e sua Importância na Modelagem de Velocidades para Fins de Migração Sísmica. Master Dissertation. Universidade Federal Fluminense, UFF. Dinâmica Oceânica e Costeira. Niterói, RJ, Brazil. 91 pp.

FONSECA J, GOBATTO F, BOECHAT J, MAUL A, YAMAMOTO T, BORN E, TEIXEIRA L & GONZÁLEZ M. 2017. Dealing with Evaporitic Salts Section in Santos Basin during Geological Seismic Velocity Construction. In: 15th International Congress of the Brazilian

Geophysical Society. Expanded Abstracts. Rio de Janeiro, RJ, Brazil: SBGf. doi: 10.1190/sbgf2017-350.

FONSECA J, TEIXEIRA L, MAUL A, BARROS P, BOECHAT J & GONZÁLEZ M. 2018. Modelling Geological Layers into new Velocity Models for Seismic Migration Process: A Brazilian Pre-Salt Case. In: First EAGE/PESGB Workshop on Velocities. London, United Kingdom. doi: 10.3997/2214-4609.201800010.

GOBATTO F, MAUL A, TEIXEIRA L, GONZÁLEZ G, FALCÃO L, GONZÁLEZ M & BOECHAT JT. 2016. Refining Velocity Model within the Salt Section in Santos Basin: An Innovative Workflow to Include the Existing Stratification and its Considerations. In: 87th Annual Meeting. Dallas, TX, USA. SEG – Society of Exploration Geophysicist. doi: 10.1190/segam2016-13685489.1.

GONZÁLEZ M, GOBATTO F, MAUL A, FALCÃO L, GONZÁLEZ G, OLIVEIRA L, MENEGUIM T & AMARAL P. 2016. Proposed Workflow to Incorporate Stratification within Salt Section using Velocity and Seismic Attributes. In: Third EAGE/SBGf Workshop on Quantitative Seismic Interpretation of Lacustrine Carbonates. Expanded Abstracts. Rio de Janeiro, RJ, Brazil. EAGE/SBGf. doi: 10.3997/22144609.201600050.

GUO N & FAGIN S. 2002. Becoming Effective Velocity-Model Builders and Depth Imagers, Part 2 – The Basics of Velocity-Model Building, Examples and Discussions. The Leading Edge, 21(12): 1210–1216.

HU J, SCHUSTER GT & VALASEK PA. 2001. Poststack Migration Deconvolution. Geophysics, 66(3): 939-952. doi: 10.1190/1.1444984.

HUANG Y, LIN D, BAI B, ROBY S & RICARDEZ C. 2010. Challenges in Pre-Salt Depth Imaging of the Deepwater Santos Basin, Brazil. The Leading Edge, 29(7): 820–825. doi: 10.1190/1.3462785.

JACKSON CA-L, JACKSON MPA, HUDEC MR & RODRIGUEZ CR. 2015. Enigmatic Structures within Salt Walls of Santos Basin – Part 1: Geometry and Kinematics from 3D Seismic Reflection and Well Data. Journal of Structural Geology, 75: 135-162. doi: 10.1016/j.jsg.2015.01.010.

JARDIM F, MAUL A, FALCÃO L & GONZÁLEZ G. 2015. Estimating Amplitude Uncertainties through Illumination Studies for a Pre-Salt Reservoir. In: 14th International Congress of the Brazilian Geophysical Society. Expanded Abstracts. Rio de Janeiro, RJ, Brazil: SBGf. doi: 10.1190/sbgf2015-160.

JI S, HUANG T, FU K & LI Z. 2011. Dirty Salt Velocity Inversion: The Road to a Clearer Subsalt Image. Geophysics, 76(5): WB169-WB174. doi: 10.1190/GEO2010-0392.1.

JONES IF & DAVISON I. 2014. Seismic Imaging in and around Salt Bodies. Interpretation, 2(4): SL1–SL20. doi: 10.1190/INT-2014-0033.1.

LANDRØ M, PUIGDEFABREGAS C & ARNTSEN B. 2011. Anisotropy in the Salt Outcrop at Cardona, Catalonia – Implications for Seismic Imaging. First Break, 29: 41-45. doi: 10.3997/1365-2397.2011022.

MAUL A, JARDIM F, FALCÃO L & GONZÁLEZ G. 2015. Observing Amplitude Uncertainties for a Pre-Salt Reservoir using Illumination Study (Hit-Maps). In: 77th EAGE Conference & Exhibition. Madrid, Spain. doi: 10.3997/2214-4609.201412921.

MAUL A, FONSECA J, TEIXEIRA L, BARROS P, BOECHAT JB, NUNES JP, YAMAMOTO T, GONZÁLEZ M & GONZÁLEZ G. 2018a. Modeling Intra-Salt Layers when Building Velocity Models for Depth Migration. Examples of the Santos Basins, Brazilian Offshore. In: 88th Annual Meeting. Anaheim, CA, USA. SEG - Society of Exploration Geophysicist. doi: 10.1190/segam2018-2996209.1.

MAUL AR, SANTOS MAC & SILVA CG. 2018b. Few Considerations, Warnings and Benefits for the E&P Industry when Incorporating Stratifications inside Salt Sections. Brazilian Journal of Geophysics, 36(4): 461-477. doi: 10.22564/rbgf.v36i4.1981.

MAUL AR, SANTOS MAC & SILVA CG. 2018c. Evaporitic Section Characterization and its Impact over the Pre-Salt Reservoirs, Examples in Santos Basin, Offshore. In: Rio Oil & Gas Exposition and Conference. Rio de Janeiro, RJ, Brazil: IBP.

MAUL AR, SANTOS MAC, SILVA CG, FONSECA JS, GONZÁLEZ MLAF, TEIXEIRA LMS, YAMAMOTO TM, BORGES FAS & PONTES RLB. 2019a. Geological Characterization of Evaporitic Sections and its Impacts on Seismic Images: Santos Basin, Offshore Brazil. Brazilian Journal of Geophysics, 37(1): 55-68. doi: 10.22564/rbgf.v37i1.1989.

MAUL AR, SANTOS MAC, SILVA CG, GONZÁLEZ MLAF, FONSECA JS, BORGES FAS & ABREU CEBS. 2019b. Evaporitic Velocity Modeling Uncertainties and Variabilities: Implication for Pre-Salt Projects in the Santos Basin, Brazil. Brazilian Journal of Geophysics, 37(2): 175-186. doi: 10.22564/rbgf.v37i2.2003.

MENEGUIM T, MENDES SC, MAUL A, FALCÃO L, GONZÁLEZ M & GONZÁLEZ G. 2015. Combining Seismic Facies Analysis and Well Information to Guide new Interval Velocity Models for a Pre-Salt Study, Santos Basin, Brazil. In: 14th International Congress of the Brazilian Geophysical Society. Rio de Janeiro, RJ, Brazil: SBGf. doi: 10.1190/sbgf2015-271.

MOHRIAK W, NEMCOK M & ENCISO G. 2008. South Atlantic Divergent Margin Evolution: Rift-Border Uplift and Salt Tectonics in the Basins of SE Brazil. Geological Society, London, UK. Special Publications, 294(1): 365-398.

NEMETH T, WU C & SCHUSTER GT. 1999. Least-Squares Migration of Incomplete Reflection Data. Geophysics, 64: 208–221. doi: 10.1190/1.1444517.

OPERTO S, GHOLAMI Y, PRIEUX V, RIBODETTI A, BROSSIER R, METIVIER L & VIRIEUX J. 2013. A Guided Tour of Multiparameter Full-Waveform Inversion with Multicomponent Data: From Theory to Practice. The Leading Edge, 32: 1040–1054. doi: 10.1190/tle32091040.1.

PAES M, PEREIRA CE, PINTO V, MAUL A, GONZÁLEZ M, MENEGUIM T, GONZÁLEZ G, MEYER R & FURLAND L. 2019. Brazilian Pre-Salt Gross-Rock Volume Uncertainties: Integration between Velocity Model and Seismic Resolution. In: 81st EAGE 2019. Conference and Exhibition. London, UK. doi: 10.3997/2214-4609.201901460.

RAYMER DG, KENDALL JM, BEAUDOIN MC, MUELLER MC & KENDALL RR. 1999. Measuring the Anisotropy of Salt in the Mahogany Oil Field, Gulf of Mexico. In: AAPG International Conference and Exhibition. Birmingham, England. p. 100-103.

RAYMER DG, TOMASSI A & KENDALL JM. 2000. Predicting the Seismic Implications of Salt Anisotropy using Numerical Simulations of Halite Deformation. Geophysics, 65: 1272-1280. doi: 10.1190/1.1444818.

TEIXEIRA L, GOBATTO F, MAUL A, CRUZ N, GONÇALVES C & LAQUINI J. 2017. Rock Physics and Seismic Inversion to Identify Stratification within Salt Section Supporting Velocity, Facies Modeling and Geomechanical Analysis. In: 15th International Congress of the Brazilian Geophysical Society. Expanded Abstracts. Rio de Janeiro, RJ, Brazil: SBGf. doi: 10.1190/sbgf2017-002.

TEIXEIRA L, NUNES JP, FONSECA J, MAUL A, BARROS P & BORGES F. 2018. Seismic-Based Salt Characterization for Geomechanical Modelling of a Pre-Salt Reservoir. In: 80th EAGE Conference & Exhibition. Copenhagen, Denmark. doi: 10.3997/2214-4609.20180131.

TEIXEIRA L & LUPINACCI W. 2019. Elastic Properties of Salt in the Santos Basin: Relations and Spatial Predictions. Journal of Petroleum Science and Engineering, 180: 215-230. doi: 10.1016/j.petrol.2019.05.024.

TORÍBIO T, QUEIROZ LE, TEIXEIRA L, YAMAMOTO T, MENEGUIM T, LEONARDI O, CORTEZ M, RELVAS MT., MOLITERNO AM, TARTARINI A, FONSECA J & MAUL A. 2017. Characterizing Evaporitic Section and Geomechanical Properties using Seismic Inversion, a Case Study for Santos Basin. In: 15th International Congress of the Brazilian Geophysical Society. Expanded Abstracts. Rio de Janeiro, RJ, Brazil: SBGf. doi: 10.1190/sbgf2017-226.

VIGH D, JIAO K, WATTS D & SUN D. 2014. Elastic Full-Waveform Inversion Application using Multicomponent Measurements of Seismic Data Collection. Geophysics, 79(2): R63–R77. doi: 10.1190/geo2013-0055.1.

VIGH D & STARR EW. 2008. 3D Prestack Plane-wave, Full-waveform Inversion. Geophysics, 73(5): VE135-VE144. doi: 10.1190/1.2952623.

VIGH D, STARR EW & DINGWALL K. 2009. 3D Prestack Full Waveform Inversion. In: Offshore Technology Conference. Houston, TX, USA (OTC 19897). doi: 10.4043/OTC-19897-MS.

WANG P, HUANG H & WANG M. 2017. Improved Subsalt Images with Least-Squares Reserve Time Migration. Interpretation, 5(3): SN25-SN32. doi: 10.1190/INT-2016-0203.1.

YAN F, HUA H, YAO Q & CHEN XL. 2016. Seismic Velocities of Halite Salt: Anisotropy, Heterogeneity, Dispersion, Temperature, and Pressure Effects. Geophysics, 81(4): D293–D301. doi: 10/1190/geo2015-0476.1.

ZDRAVEVA O, WOODWARD M, NICHOLS D & OSYPOV K. 2011. Building Anisotropic Models for Depth Imaging: comparing different approaches. In: 12th International Congress of the Brazilian Geophysical Society. Society of Exploration Geophysicists and Brazilian Geophysical Society, Expanded Abstracts. Rio de Janeiro, Brazil. doi: 10.4043/22827-MS.

Revista Brasileira de Geofísica

RBGf

Brazilian Journal of Geophysics

GEOPHYSICS APPLIED TO THE MAPPING OF NATURAL CAVES HOSTED
IN IRON ORE IN CARAJÁS (PA), BRAZIL

Maria Filipa Perez da Gama[1], Marco Antonio Braga[1], Marcelo Roberto Barbosa[2], Rafael Guimarães de Paula[2],
Daniele Freitas Gonçalves[2] and Iuri Viana Brandi[2]

ABSTRACT. The Brazilian environmental licensing for mining activities requires technical-scientific studies to demonstrate that natural caves will be protected from the impact of the mining operations. This study presents the results of near-surface geophysical methods applied to geostructural mapping of the rock mass in which the caves are hosted. The ferruginous karstic terrains are challenging to the geophysical interpretation due to the caves' modest dimensions and the large variations in the host rock physical properties. Electrical Resistivity and GPR (Ground Penetrating Radar) geophysical surveys, were performed overlaying a natural cave located in the surroundings of the N4EN iron mine, in the Carajás Province, northern Brazil. The resistivity data were useful to discriminate different lithotypes and the presence of humidity, while the GPR data revealed details of the fracturing of the rock mass. The results indicated that the presence of humidity and fractures in the rock mass may constitute zones of greater fragility of the cave walls and ceiling.

Keywords: speleology, GPR, electrical resistivity, near-surface geophysics.

RESUMO. O licenciamento ambiental brasileiro para atividades de mineração requer que estudos técnico-científicos demonstrem que as cavernas serão protegidas do impacto das operações de mineração. Este artigo apresenta os resultados de métodos geofísicos rasos aplicados ao mapeamento geoestrutural do maciço rochoso em que as cavernas estão hospedadas. Os terrenos cársticos ferruginosos são desafiadores para a interpretação geofísica, devido às modestas dimensões das cavernas e às grandes variações nas propriedades físicas da rocha hospedeira. Levantamentos geofísicos de Resistividade Elétrica e GPR (Radar de Penetração no Solo) foram realizados sobre uma caverna localizada no entorno da mina de ferro N4EN, na Província de Carajás, região Norte do Brasil. Os dados de resistividade foram úteis para discriminar diferentes litotipos e a presença de umidade, enquanto os dados de GPR revelaram detalhes do fraturamento do maciço rochoso. Os resultados indicaram que a presença de umidade e fraturas no maciço rochoso podem constituir zonas de maior fragilidade nas paredes e teto da caverna.

Palavras-chave: espeleologia, GPR, resistividade elétrica, geofísica rasa.

[1]Universidade Federal do Rio de Janeiro – UFRJ, IGeo - CPGA, Rio de Janeiro, RJ, Brazil – E-mails: filipa@geologia.ufrj.br; marcobraga@geologia.ufrj.br
[2]VALE, Nova Lima, MG, Brazil – E-mails: marcelo.roberto.barbosa@vale.com; rafael.guimaraes@vale.com; daniele.freitas.goncalves@vale.com; iuri.brandi@vale.com

INTRODUCTION

Mining operations face the challenge of extracting the ore without causing negative impacts to the environment, which includes, in many cases, underground natural caves. The Brazilian Constitution of 1988 considered underground natural caves as public property. Current Brazilian legislation requires scientific studies to demonstrate that mining operations will not cause any physical impact to caves that have historical, scenic, artistic, archaeological, paleontological, ecological and/or scientific value. Until these studies are completed and approved, a protection distance of 250 meters should be maintained, causing blockage of reserves and losses to the mineral industry. Some caves can be suppressed provided all legal requirements are met.

Often a combination of more than one geophysical method is used in geophysical surveys to investigate underground caves (natural or man-made). Chalikakis et al. (2011) analyzed the literature on geophysics applied to karst regions and compiled an indicative table of the most appropriate methods for each type of problem, emphasizing that often the combination of more than one method is necessary. Day-Lewis et al. (2017) discussed the applicability of various geophysical methods to environmental problems in fractured rocks, highlighting the electrical resistivity as the most appropriate method for identification and monitoring of fractured zones, and GPR (Ground Penetrating Radar) as appropriate for mapping fractured zones, since the electrical properties of the rock masses are mostly controlled by the presence of fractures and the connectivity between them. Many authors have published studies on near-surface geophysical methods applied to the investigation of underground caves (e.g. Driad-Lebeau et al., 2008, in old salt and marl mines in France; Cardarelli et al., 2010, in old underground pozzolana mines in Italy; Putiška et al., 2014, in carbonatic karst in Slovakia; Ferreira et al., 2017, in quartzite caves in Brazil). The combined geophysical methods allowed the authors to create geological models of the subsurface, with different success rates in cave detection or collapse prediction for each geological context and geophysical method.

In Brazil, mainly after 2008, with the increasing of the cave protection laws, there was a great expansion of the scientific literature about caves in ferriferous terrains (e.g. Ruchkys et al., 2015; Carmo & Kamino, 2015; Jacobi et al., 2015). In spite of the growing interest on this speleological subject, there are still few studies on the application of near-surface geophysics (e.g. Barbosa et al., 2016) although these techniques can be used to map and characterize the rock mass in which the caves are hosted without causing them any damage.

The major challenges of applying near-surface geophysical methods to iron ore caves are the great heterogeneity of the environment in which they occur, their small size and, especially in the Carajás region, the extremely humid climate. The variable response that these caves present in the sections of electrical resistivity is expected, because depending on the degree of humidity in the walls of the cavities the geophysical signature can be inverted, with the cavity presenting a conductive response instead of the high resistivity corresponding to the air (Putiška et al., 2012). The main challenges to the GPR method application using high frequencies, which allow better resolution to map the small variations of properties in subsurface, is the very small penetration of the signal, due to the presence of a humid clayey layer just below the lateritic crust. For the lower GPR frequencies, which can penetrate deeper than the higher frequencies, the great complexity and heterogeneity of the subsurface is a challenge, as well as the rugged relief of the edges of the plateaus where the caves are inserted. This study aims mainly to evaluate the effectiveness of the application of the electrical resistivity and GPR (Ground Penetrating Radar) geophysical methods in the subsurface investigation and monitoring of the physical integrity of the natural cavities in iron formations. It is also intended to determine how the geophysical data obtained by these methods can contribute to the improvement of the geological and structural knowledge of the cave environment.

GEOLOGICAL CONTEXT

The Carajás Mineral Province is located in the southeastern portion of the Amazonian Craton, in the state of Pará, Brazil. It is located in the Central Amazon Province, and it is limited to the north by the Amazonas Basin and to the east by the Araguaia Belt. Tolbert et al. (1971) published the first results of the geological mapping of the region of Carajás after the discovery of the iron ore deposits in 1967, classifying the rocks in: gneisses granites and amphibolites of Precambrian age; quartzites, phyllites and schists, interleaved with the iron formation; banded iron formation (jaspilite) consisting of quartz and iron oxides with lamination of variable thicknesses; sandstones and conglomerates, and mafic rocks. These authors were also the first to describe the existence of large caves below the lateritic crust, known as "canga", in this region. DOCEGEO (1988) grouped the greenstone belts of Archean age in the Andorinhas Supergroup, older than 2.85 Gy, composed of the

region's oldest rocks, overlapped by the Itacaiúnas Supergroup, constituted by lithologically distinct volcano sedimentary rocks, including the Carajás iron formations. The iron ore deposits are hosted in the rocks of the Carajás Formation composed of banded iron formations, represented by jaspilites, and are classified in three districts (North, South and East Ranges), where several discontinuous bodies of high-grade ore occur (Pereira, 2017). The rocks of the Carajás Formation are superimposed by mafic rocks of the Parauapebas Formation. The N4 mine is hosted in rocks of the Grão-Pará Group, aged 2.76 Gy (Machado et al., 1991). For many authors (e.g. Lobato et al., 2005; Rosière et al., 2006), the province presents a stratigraphic problem, as it was affected by the effects of regional folds, transcurrent faults, contact metamorphism and metasomatism around granitic intrusions, as well as hydrothermal alteration related to the various mineralization events. All these factors heterogeneously affected the volcano-sedimentary sequences, resulting in abrupt contacts between similar lithologies, but with different degrees of hydrothermal alteration, thermal metamorphism and deformation intensity. In the Serra Norte domain, the iron formations are predominantly jaspilite, with compositions varying between 17 and 43% Fe and 35-61% SiO_2, and present sedimentary and hydrothermal structures.

The bodies of iron formations are lenticular, discontinuous and include large and rich deposits of iron (65% Fe) which are closely associated with deformed iron formations, although significant amounts of iron oxides are associated with other rocks, including the mafic rocks that are intercalated with the iron formations. The deposits of Serra Norte developed in the zones of greater permeability along the Carajás fold axis (Rosière et al., 2006). Zuchetti (2007), through geochemical studies of metabasalts and detailed studies of fluid inclusions, achieved a better understanding of the hydrothermal alteration in relation to the geotectonic environment of the Grão Pará Group, and inferences about the mineralizing hydrothermal fluid and the processes associated with ore deposition. The author observed that the metabasalts have calcium-alkaline magmatic affinity, continental arc geochemical characteristics and subduction zone signature. Evidence of crustal contamination was observed and suggests that the Grão Pará Group volcanic rocks may have spilled over attenuated continental crust in a back-arc environment. The magmatic hydrothermal fluid had high salinity and alkaline composition, and was rich in U, LREE and Th. In the early hydrothermal stage, the fluid had fO_2 in equilibrium with magnetite, suggesting relatively oxidizing conditions. In the late-hydrothermal stage, the fluid was relatively acidic, causing

the alkali to leach from mafic rocks. There may also have been extraction of Fe_{2+} from the host rock. The presence of sulfides in the hydrothermal veins shows that the fluid has evolved to relatively reducing conditions. Despite evidence of relatively fluid-reducing conditions, hematite is the dominant oxide in the late hydrothermal stage. Hematite precipitation in this case can be explained by the relatively acidic conditions of the hydrothermal fluid and/or the mixture of magmatic and meteoric fluids. Figueiredo e Silva et al. (2008) suggested that the Carajás high-grade iron ore deposits could have been formed by hydrothermal alteration associated with fluids derived from magmatic intrusions mixed with meteoric waters, with later supergene enrichment, based upon the following observations: (i) iron orebodies vary in composition according to geometry that does not follow the weathering profiles; (ii) contacts between ores and wall rocks as well as jaspilite and mafic rocks are not always concordant; (iii) the high porosity of the soft ores may be the result of hydrothermal alteration; (iv) the characteristics of the ore of different deposits vary as function of structural variations, indicating that post-sedimentary structures directly influenced the mineralogical and chemical ore composition; and (v) discordant stratigraphic contact between the jaspilitic sequence and iron mineralization.

SPELEOGENESIS

The genesis of the caves in iron ore seems to be the result of the interaction of several processes, not yet fully clarified, since there is no consensus among the researchers. Combination of chemical dissolution processes, iron reduction by bacteria, formation of lateritic crusts and differential erosion are involved, and have interacted over time giving rise to the various types of ferruginous caves. According to Piló et al. (2015), a large number of caves were recorded in the mineralized jaspilite where there are broad coverings of crusts of iron breccias, known as canga, which function as a support element for the tops of the dissected plateau, regionally represented by the Serra dos Carajás. A large number of caves were also recorded in the contact zone between the lateritic crusts and the iron formation, as well as exclusively within the crusts. Shuster et al. (2012) estimated the erosion rate in the Carajás canga plateaus at about 1 m/My, and that these surfaces were exposed to cosmic radiation for a long period (>20 My). The low erosion rate of the lateritic crusts suggests that once formed, the crusts serve as a shield for the more friable rocks below it, corroborating the geomorphological observations in the region, while Monteiro et al. (2018) calculated even lower erosion

rates (0.08 and 0.09 m/My) in canga samples from plateaus N1 and S11D. These authors analyzed weathering profiles of Carajás, having identified goethite precipitation throughout the Cenozoic. The paleosurface that was carved by receding cliffs and formed the present plateaus of Carajás may have been much more extensive in the geological past. Exposure ages of at least 7 My, according to the authors, suggest that plateaus were eroded very slowly during the Cenozoic. Many caves are located at the interface between the lateritic crusts and other lithologies, possibly because the hard crusts support or form the roof of the cave. According to Piló & Auler (2009), the positioning of the caves can be divided into three groups: caves positioned on the edges of lagoons on top of plateaus, caves located at the edges of drainage and headwaters and caves embedded in the sloping edges of the plateaus, including occurrences in the low, medium and high strands. According to the authors, the caves developed inside the canga crust, within the iron formation, or in the contact between them as well as in the ferricrete. The genesis of caves in iron ore seems to have begun with the same processes of silica dissolution that enriched the Carajás iron formations. The dissolution of dolomite, quartz and hematite, leads to the formation of a zone of altered iron ore of high porosity that may reach 50% of the rock volume.

According to Auler et al. (2014), the dissolution initially creates voids at great depths, hundreds of meters from the surface. Maurity & Kotschoubey (1995), in a detailed study on caves in the Serra Norte, described the genesis of the laterite caves as a three-stage process: 1) percolation of aqueous solutions along fissures and fractures, and development of a void reticulate system - Fe and Al mobilization; 2) Fe and Al oxyhydroxides filling fissures and fractures at the crust-saprolite interface by Fe and Al oxyhydroxides generating box-work structures; and 3) development of a low-density zone through dissolution and lateral eluviation of the clayey matrix. The partial collapse of this zone leads to cavity formation. More specifically over the iron formations, according to the same authors, the cavernous level is due to the degradation of most of the crust's hematitic fragments, previously transformed into friable goethitic products. This low-density zone evolves due to its resistance to the physical and chemical action of groundwater. Where the crusts remain stable, the gradual destruction of the low-density skeletal structures by water lead to the development of underground halls and galleries. In the caves, the collapse of ceiling blocks was certainly an important auxiliary phenomenon, which led to the development of cavities close to the surface and

the notable increase in the height of both halls and galleries. These authors have identified three main types of lateritic coverings: iron-aluminous laterite, hematite breccia and lateritic conglomerate. The iron-aluminous laterite originates from mafic rocks, and consists of a large saprolite horizon composed mainly of kaolinite and goethite, where centimetric cavities were observed capped by a crust up to 5 m thick. The hematite breccia is limited to the zones of occurrence of the desilicified iron formations, and corresponds to thick deposits composed of densely packed hematite fragments, in a clay-ferruginous matrix composed predominantly of goethite. The matrix has also a large porosity and is locally cavernous. The lateritic conglomerate, described by the same authors, may cover both the saprolite of the metavolcanics and the desilicified iron formations, and is characterized by accumulations of rounded pebbles of laterite and angular fragments and plaques of iron ore. The matrix has a clayey consistency and locally presents pseudo-oolitic texture. Gonçalves et al. (2016) studied lateritic profiles in the N4 mine, including the mine bench next to the cave N4E-0026, object of this study, and were able to distinguish three main horizons: lateritic crust, transition horizon and saprolite:

a) *Lateritic crust*: hardened horizon consisting of detrital material of reddish-brown color, composed of sub-angular to angular clasts of centimetric to metric dimensions, cemented by aluminum and iron oxyhydroxides. Locally presents massive texture, and also porous and pisolitic portions. The ratio of clasts/cement varies greatly, as does the thickness of the horizon. The clasts are composed of ore fragments, mainly hematite with relicts of banded texture and/or weathered volcanic mafic rocks, as well as fragments of lateritic crust. It presents brecciated, locally conglomerate appearance;

b) *Transition horizon*: horizon of irregular thickness sometimes presenting features related to the upper lateritic crust or features related to the saprolite below, with fragile textural characteristics. Detrital material from the lateritic crust and saprolite rock fragments coexist in this horizon which often exhibits porous or cavernous textures;

c) *Saprolite*: It comprises reddish clays with whitish or yellowish spots, sometimes kaolinic, originating from alteration of volcanic rocks or jaspilites. This horizon has irregular thickness and commonly contains internally preserved rock boulders.
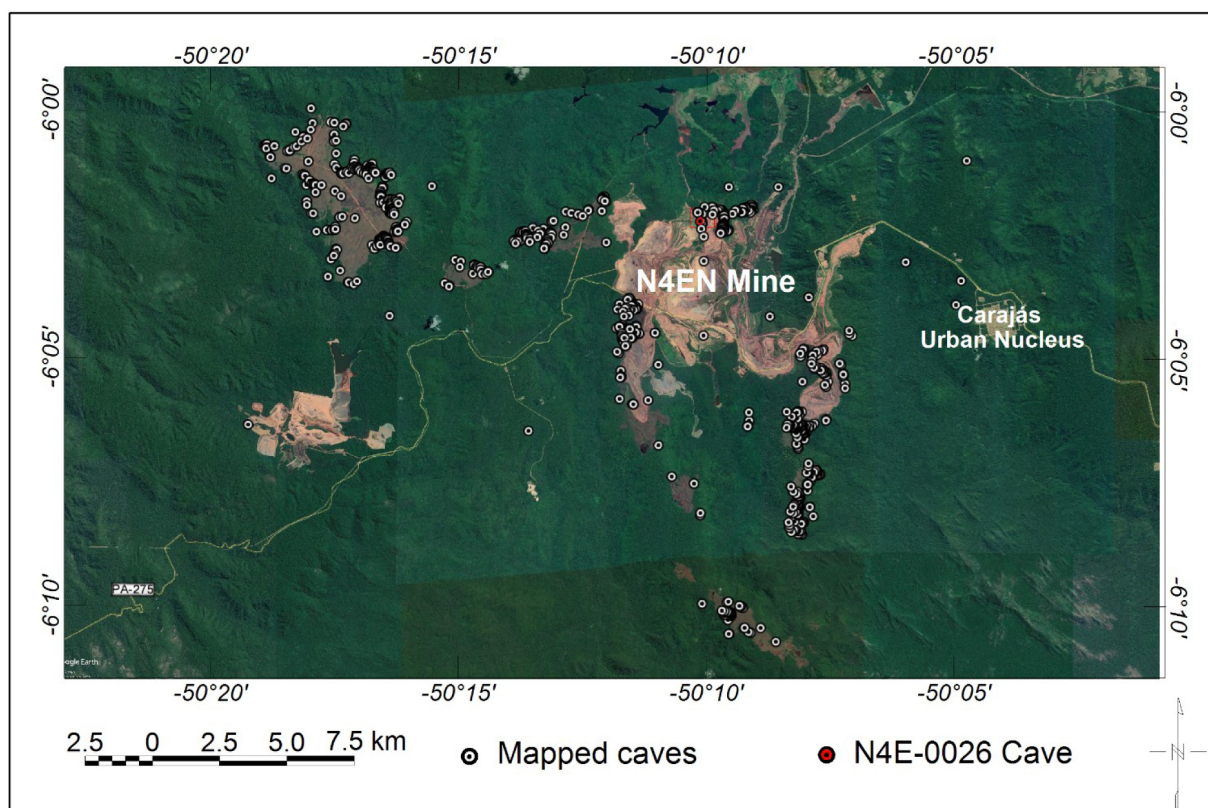
Figure 1 – Location of the Serra Norte caves showing the vast majority of them bordering the plateaus. The N4E-0026 cave is located in the area highlighted in red (Image: Google Earth (Dec/2016), Caves location: MMA, 2018).

LOCATION AREA

This research presents the results of a combined electrical resistivity/GPR survey over a cavity located within the grounds of the N4EN iron mine, in Carajás, northern Brazil. This cave, N4E-0026, was located under the edge of one of the canga plateaus that cover the iron ore in this mine, as illustrated in Figure 1.

According to Coelho et al. (2013), the N4E-0026 cavity developed in the interface between altered jaspilite and detrital canga. The detrital canga covered the iron ore, with thicknesses that varied from a few meters up to 20 meters. This type of canga is formed by blocks of hematite cemented by hydrated iron oxides and usually has a higher Fe content of and lower alumina content than other types of canga. The detrital canga could be observed inside the cave abruptly set over the altered banded iron formation, and contributed with sediments to the cave floor (Fig. 2). The iron formation presented several subvertical fractures and relief joints.

The roof of the cave accompanied the slope of the plateau, at varying depths between 8 and 12 meters. The maximum level difference within the cave was 15 meters.

A geostructural map of the cave was elaborated by direct mapping inside the accessible parts of the cave (Fig. 3).

METHODS

Electromagnetic and electrical geophysical surveys were applied on the plateau exactly in the area over the N4E-0026 cave, in four lines oriented N45°W and spaced 10 m. The line orientation was chosen so that the sections crossed the cave perpendicular to its longest dimension from the largest entrance (entrance 2). GPR (Ground Penetrating Radar) was used with frequencies of 80 MHz and 250 MHz, and Electrical Resistivity, arranged in dipole-dipole array.

The geophysical survey consisted of approximately 710 m of electrical resistivity sections, distributed along four 155 m long lines and one 90 m control line, and 680 m of GPR lines, consisting of four 85 m lines using each equipment and antennas,
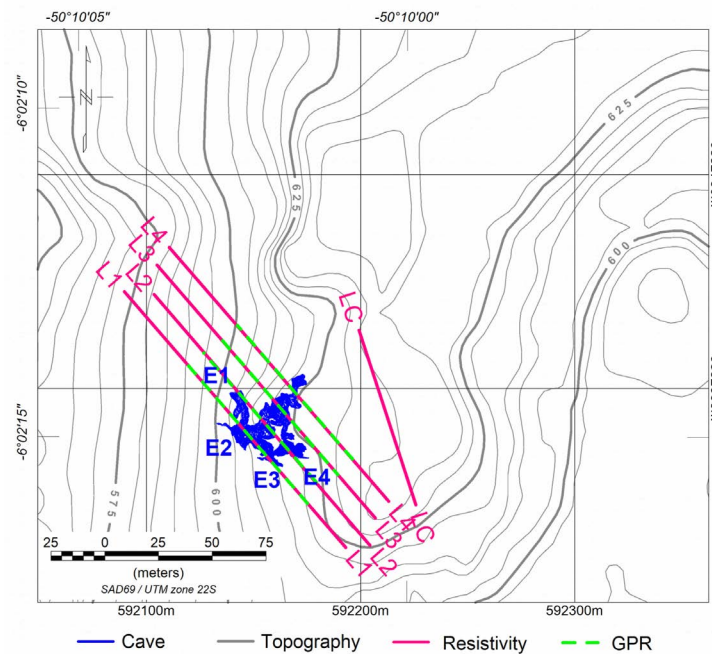
Figure 2 – Cave N4E-0026 entrance 4, where several naturally fallen blocks can be observed (photo taken in Jan/2018).
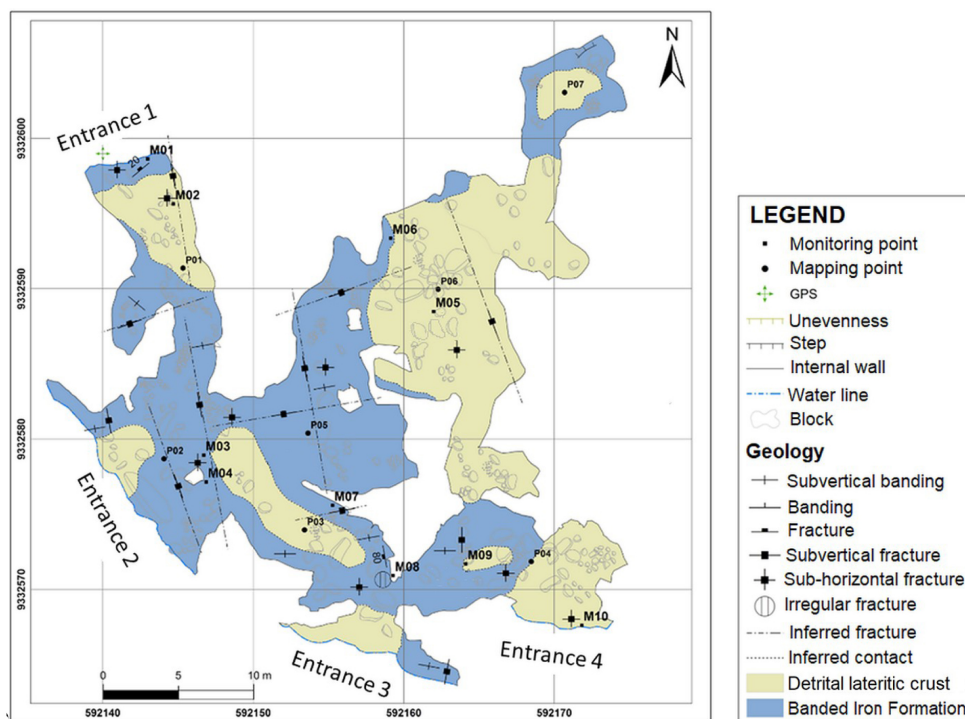
Figure 3 – Geostructural map of the N4E-0026 cave with its four known entrances (Source: Vale).

Figure 4 – Location of the geophysical sections near the N4EN mine pit (E1, E2, E3, and E4: cave entrances).

Table 1 – Electrical resistivity equipment and acquisition parameters.

Equipment	ABEM SAS4000
Number of channels for simultaneous measurements	4
Maximum number of electrodes	64
Electrode Spacing	1.4 m (control line) / 2.8 m (other lines)
Array	Dipole-Dipole
Levels of investigation	28
Maximum current	1000 mA
Minimum current	20 mA
Stacks	4
Error limit	2%

as shown in Figure 4. The control line was acquired close to the nearest mine bench, which was later mapped in detail to constrain the interpretation of the geophysical data. Due to the location of the lines over the plateau edge, it was not possible to obtain continuous measurements along the GPR lines. A 3D model of the cave created using a Leica Laser Scanner model C10, provided by Vale, was transformed into a voxel of 0.1 × 0.1 m which was sliced at the geophysical lines so that the location of the

intersection of the geophysical sections with the cave could be displayed on the images. The location of the geophysical sections with respect of the 3D model of the cave are shown in Figure 5.

The electrode array used in the electrical survey was dipole-dipole, chosen after tests performed prior to the commencement of the survey, over section L1. The parameters used in the data acquisition are summarized in Table 1. The processing and inversion software used was RES2DINV from
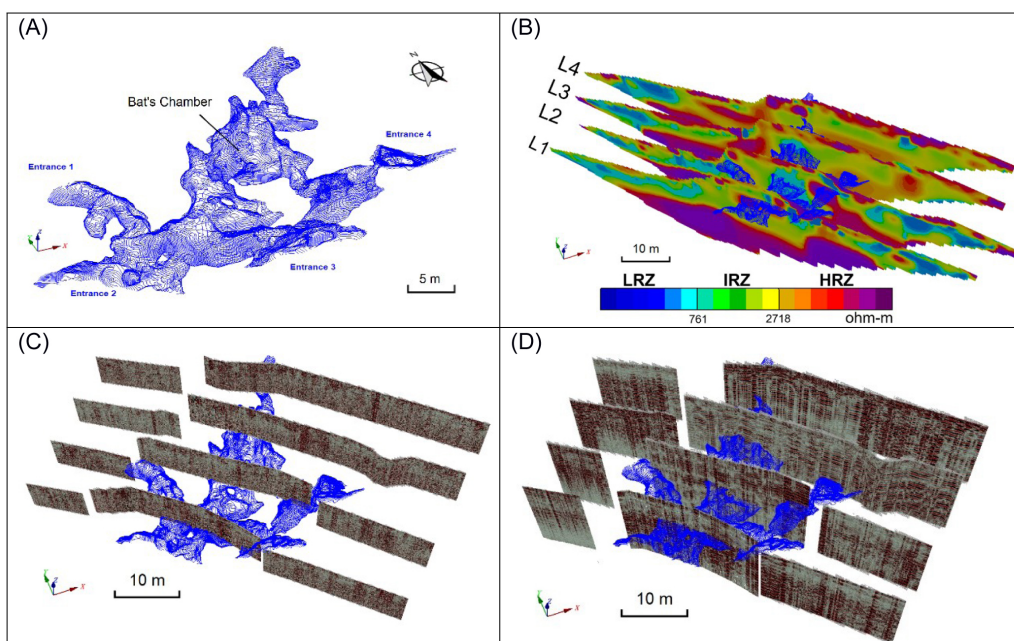
Figure 5 – 3D images of (A) the N4E-0026 cave; (B) electrical resistivity; (C) 250 MHz GPR; and (D) 80 MHz GPR sections, illustrating the depth penetration of each method; cave contour in blue.

Geotomo Software Inc. The field campaign was executed from July to September 2016, during the dry season in Carajás.

Table 2 lists the equipment and parameters selected for the GPR acquisition. The electromagnetic wave propagation velocity obtained in the initial tests performed over a reflector of previously known depth was 0.07 m/ns. The GPR acquisition lines were repeated over the same location using each equipment and parameters. The computer program used for the processing and time to depth inversion was REFLEXW, developed by Sandmeier Inc.

Table 2 – GPR equipment and acquisition parameters.

Equipment	Pulse Ekko Pro	GSSI
Frequency	250 MHz	80 MHz
Antenna	Shielded	Not shielded
Trace interval	5 cm	10 cm
Number of samples	500	512
Time window	200 ns	500 ns
Vertical sampling	0.4 ns	1 ns
Stacks	16	16
Antennas separation	0.4 m	1 m

RESULTS

Electrical Resistivity

Three main resistivity domains were observed in the four electrical resistivity sections, as well as in the control section: LRZ (Low Resistivity Zone), with values below 761 ohm-m; IRZ (Intermediate Resistivity Zone), with values between 761 and 2,718 ohm-m and HRZ (High Resistivity Zone), corresponding to values above 2,718 ohm-m.

The control resistivity section, located over a nearby mine bench, was compared to the conventional lithogeomechanical mapping of the bench, in order to serve as guidance to the interpretation of the four other profiles over the cave. Figure 6 displays the mine bench mapping and the geophysical section highlighting how the different resistivity domains correlate to the mapped lithotypes. The lithotypes on the top surface, denominated "crusts", correspond to the higher resistivity values (HRZ). The Lateritic Iron Formation (LIF) lithotype, although in the high resistivity range, presents more homogeneous and lower values. The Aluminium-Iron Lateritic (AIL) lithotype corresponds to intermediate resistivity values (IRZ), likely due to its higher clay contents, calling attention one nucleus of low resistivity values (LRZ) observed immediately below the Aluminium-Iron Lateritic Crust (AILC) probably due to the presence of water/humidity

below the contact. Table 3 displays the correspondence between the lithotypes mapped on the mine bench and the horizons described by Gonçalves et al. (2016).

In Figure 7 (resistivity Line 1), it is possible to observe three different levels easily identified by their electrical signatures. From top to bottom, occur the crusts lithotypes, up to about five meters thick showing domain of high resistivity values (HRZ), all occurring in a discontinuous and irregular way. Immediately below, the second level, is a thick layer of intermediate resistivity (IRZ), up to 20 m thick, and corresponds to the most clayey zone of the lateritic profile, and is shown to be discontinuous near the cave section where high resistivity (HRZ) and low resistivity (LRZ) anomalies can be observed.

The resistive anomalies around the cave sections can be explained by the fact that the air is dry near entrance 2, the largest entrance (about 12 m wide by 3 m high) and entrance 3 (11 x 3 m), or by the presence of more resistive lithotypes near these entrances. The conductive zone (LRZ) observed between the two entrances is interpreted as a more humid zone, where there is percolation of rainwater, therefore requiring close monitoring.

The high resistivity zone (>12,515 ohm-meter = HRZ) in the lower part of the section corresponds to the iron ore (saprolite), which in the N4EN mine is composed of friable hematite, known for its high resistivity that can be explained by its air-filled pores.

Resistivity section 2 (Fig. 8) presents similar overall characteristics as section 1, showing also the three well defined horizons: the upper crusts, with high resistivity and small thickness (4 to 5 m), the intermediate zone (IRZ) and the high resistivity base (saprolite), which is believed to correspond to the iron ore. Resistive anomalies can be observed close to the cave entrance, though in the central portion of the section, where the section intersects a cave hall, there are no resistive anomalies, possibly because of the small size of the hall and also because it lies in the deeper and more humid part of the cave.

Section 3 (Fig. 9) intersects the cave well inside the massif, crossing the largest chamber, more than 20 meters away from the nearest entrance. In this place the cave section is about 14 meters wide, and up to 4 meters high, thinning towards the sides. The

Table 3 – Weathering horizons and mine bench lithotypes.

Weathering horizon	Lithotype	Initials
Lateritic crust	Detrital Lateritic Crust	DLC
	Ferruginous Lateritic Crust	FLC
	Aluminium-Iron Lateritic Crust	AILC
Transition horizon	Lateritic Iron Formation	LIF
	Aluminium-Iron Laterite	AIL
Saprolite	Not present on the bench	N/A
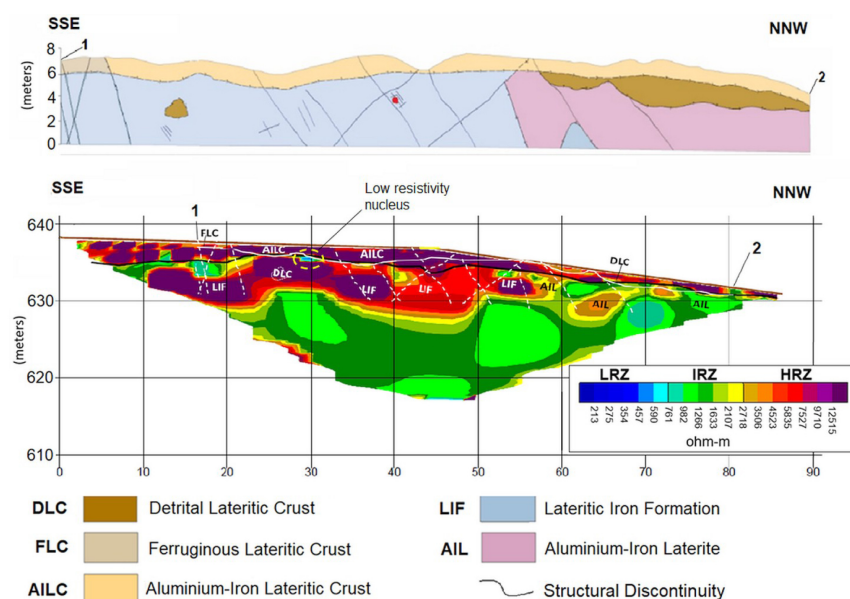
Figure 6 – Lithogeomechanical mapping of the nearby mine bench correlated to the control section resistivity image (LRZ = Low Resistivity Zone, IRZ = Intermediate Resistivity Zone, HRZ = High Resistivity Zone).

crust cap over the cave is 5 meters thick, with resistivity values above 3,506 ohm-meter (HRZ). This part of the cave is located in a very homogeneous intermediate resistivity zone (IRZ) that accompanies the declivity of the plateau above it.

Section 4 (Figure 10) crosses the cave at more than 30 meters distance from the nearest entrance. In this section it is possible to observe a greater thickness of the canga crust, up to 8 meters, and the thinning of the intermediate resistivity zone where the cave is hosted, with higher resistivity values, still within the range of intermediate values (IRZ), between 2,107 and 2,718 ohm-meter.

Ground Penetrating Radar (GPR) – 250 MHz

The GPR sections using the higher frequency antenna (250 MHz) presented high resolution through the first 6 meters from the ground surface and, as expected, presented a shallow depth of penetration, due to the higher frequency and the more conductive material (Jol, 2009). Figure 11 shows detailed images of the GPR sections above and near the cave ceilings sections. Well-defined reflectors can be seen at the top of the GPR images, below which, possibly due to the more conductive clayey material where the caves have developed, the GPR signal is attenuated. Above the cave, the intense fracturing of the rock can be observed, as well as the alternation of contrasted and attenuated reflectors, which can be interpreted as variations in the interface between the crusts and the intermediate zone, also observed in the electrical resistivity sections. The fractures mapped directly by the geologists from inside the cave have been extended in the cave sections, and it is noteworthy that some of them have direct correspondence with the verticalized features that can be observed in the GPR images.

High frequency GPR section 1 (Fig. 11A) has reached the roof of the cave, but as the GPR signal was attenuated below around 6 meters deep, the cave location can't be visualized in the geophysical image. Section 2, again, barely attained the tops of some of the cavity chambers, always in the attenuated zone. Intense fracturing can be observed. Sections 3 and 4 were run above the deeper part of the cave and didn't reach the cave ceiling (Figs. 11C and 11D), though they present the same intense fracturing close to the surface and attenuation beginning at a depth of approximately 6 m.

Ground Penetrating Radar (GPR) – 80 MHz

The GPR sections acquired with the low frequency antenna (80 MHz) showed quite heterogeneous responses, as the penetration was sufficient to cross the cave in depth. GPR section 1 presented fairly contrasting and sinuous reflectors around the cave entrance 2 (Fig. 12A), the largest free span. In the other sections the feature is not so clear. GPR section 2 (Fig. 12B) still presented observable contrasted reflectors above the cave span.

GPR section 3 is less contrasted than the others, and the cave section cannot be distinguished from the host rock (Fig. 12C). In this section the crusts at the surface are more attenuated than in the others. GPR section 4 also presents very contrasted reflectors though the cave position cannot be discerned from the host rock, possibly because of the cave's smaller dimensions where this section crossed the cave.

As regards the structural features, the vertical sequences of reflectors, apparent on all low frequency GPR images, extending from the surface to the base of the images can be attributed to contrasts in the electrical properties of the materials, such as the ferruginous crusts and the cavernous texture observed on the nearby mine bench.

The subvertical fractures observed in the interior of the cave, seem to have expression in the sections, observed as interruptions in the reflectors, although there are many more features of this type in the sections than fractures mapped from inside the cave. A difference in thickness and contrast of the reflectors near the surface can be observed in the four sections corresponding to the limit of the hardened crust and the more weathered material of the intermediate zone between the hardened crusts and the iron ore, were the cave was hosted.

DISCUSSION AND CONCLUSIONS

As preconized by Putiška et al. (2012), the resistivity sections were inconclusive to locate the position of the cavity. It is possible that the humidity on the cave walls has created a thin layer of conductive material that masks the effect of the high resistivity of the air inside the cave. Figure 13 shows a model of the electrical response of a cavity filled with air surrounded by a thin layer of conductive material. The fractured hardened crust cap on the surface and resistive rock underneath the cave are also represented in the model. The high resistivity zones near the cave entrances observed on two of the four resistivity sections that crossed the cave can be explained by the fact that the air is dryer near the entrances, but a difference in lithology cannot be discarded.

The resistivity sections were effective to map possible geotechnical fragility zones, where there is contrast between intermediate and low resistivity, as well as changes in the orientation of the boundaries between the conductive/resistive
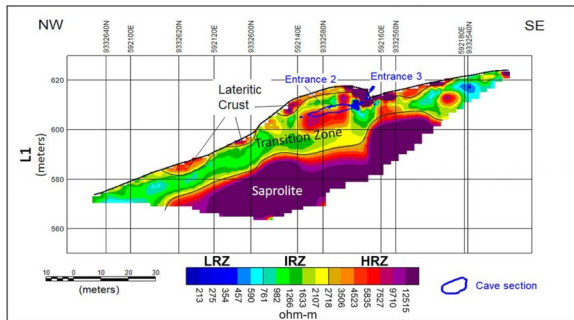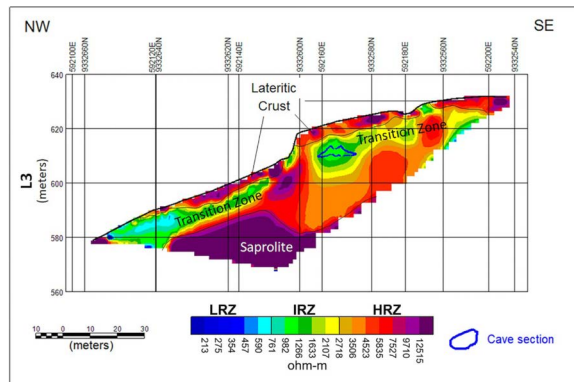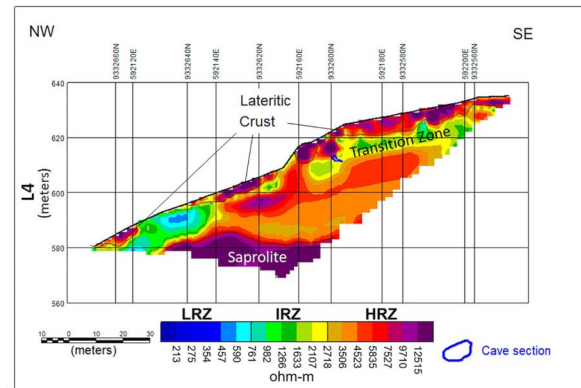
Figure 7 – Resistivity section 1: the three resistivity zones can be clearly distinguished. The largest entrance of the cave was intersected by this section.
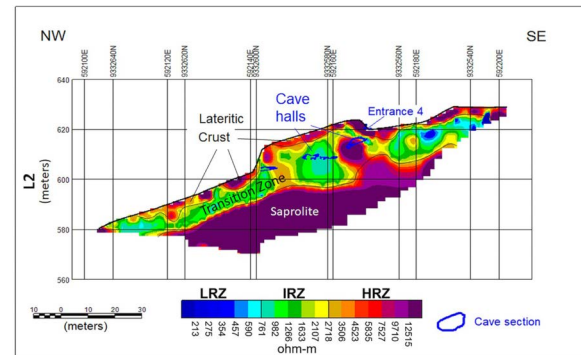

Figure 8 – Resistivity section 2: this section intersects the cave deeper inside the rock massif. Resistive anomalies can still be observed near the cave entrance.


Figure 9 – Resistivity section 3: this section intersects the cave at 20 m from the nearest entrance. The three resistivity zones can still be clearly distinguished.


Figure 10 – Resistivity section 4: this section intersects the cave deeper inside the cavity, where its diameter is only 2 m. The three resistivity zones are still discernible, though the IRZ is thinner than in the other sections.
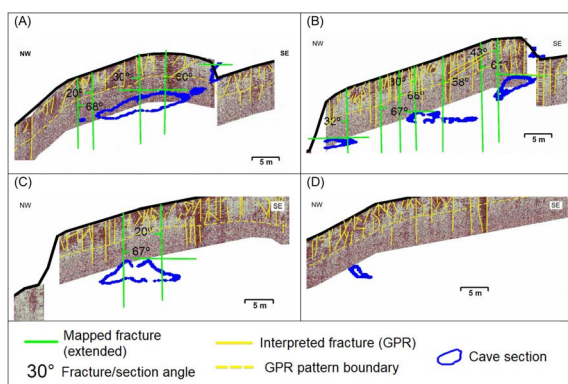
Figure 11 – Details of the high frequency (250 MHz) GPR sections. A) GPR section 1: the cave ceiling is located in the attenuated part of the profile; B) GPR section 2: it crossed a very fractured zone, clearly seen in the fractures extrapolated from the mapping inside the cave and on the image; C) and D) GPR sections 3 and 4: where the cave wasn't intersected by the sections, the heterogenicity and intense fracturing of the crust lithotypes is visible.
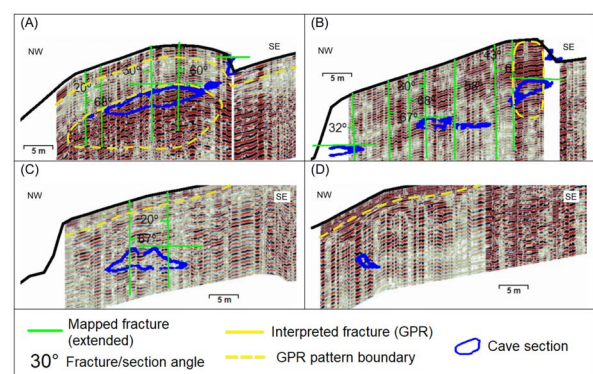
Figure 12 – Details of the low frequency (80 MHz) GPR sections. A) GPR section 1; B) GPR section 2; C) GPR section 3; and D) GPR section 4; high and low contrast regions, as well as discontinuities in the reflectors can be observed.
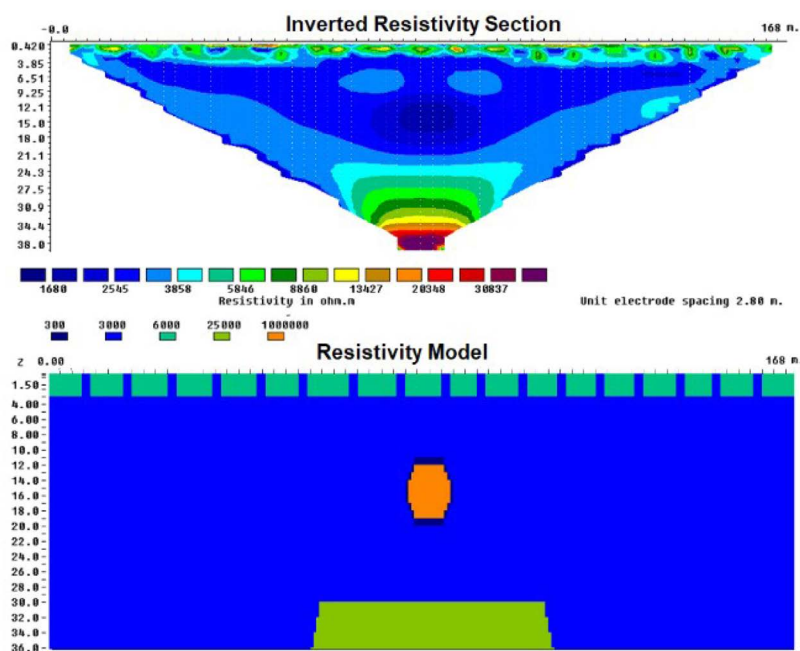
Figure 13 – Synthetic model of an air-filled cavity surrounded by a very conductive thin layer, hosted in moderately conductive material. The resistive material underneath the cave and the fractured canga cap are also represented. The calculated anomaly corresponding to the cavity in the inverted section is negative, and can hardly be distinguished from the host rock.

zones, that can be interpreted as zones of water percolation, and therefore, greater geotechnical fragility.

The higher frequency (250 MHz) GPR data were effective in mapping the fracturing or individual blocks in the duricrust cap, but were easily attenuated by the more conductive layer immediately below it, at about 6 m depth, and weren't able to reach the cavity roofs. The lithology observed on the nearby mine bench mapping (AIL) is rich in clays, that are known to attenuate the GPR signal. It can be observed in the GPR sections that the most resistive layer observed in the surface part of electric sections and interpreted as hardened crusts lithologies has a good correspondence with the most contrasting GPR reflectors near the ground. The lower frequency (80 MHz) GPR data had a good depth of penetration and mapped well the larger fractures mapped from inside the cave, and revealed others that weren't accessible to direct observation. On the other hand, as expected, the low frequency GPR sections presented a lower resolution and many artifacts due to the rugged terrain and reflections from the escarpments, as well as the very heterogeneous and fractured canga cap.

ACKNOWLEDGMENTS

REFERENCES

AULER, A, PILÓ, L, PARKER, C, SENKO, J, SASOWSKY, I & BARTON, H. 2014. Hypogene cave patterns in iron ore caves: Convergence of forms or processes? In: KLIMCHOUK A, SASOWSKY ID, MYLROIE J, ENGEL SA & ENGEL AS (Eds.). 2014. Hypogene Cave Morphologies. San Salvador Island, Bahamas. Karst Waters Institute Special Publication, 18: 15-19.

BARBOSA, MR, PAULA, RF, BRANDI, I, SEBASTIÃO, CS, MATOS, J, BRAGA, MA & CLAUVER, C. 2016. Aplicação do Método Ground Penetrating Radar (GPR) no Mapeamento Geoestrutural de Cavidades Naturais Subterrâneas em Terrenos Ferríferos–Estudo de Caso da Mina N4E, Carajás. In: Simpósio Brasileiro de Mecânica das Rochas – SBMR 2016, Belo Horizonte, MG, Brazil. 9 pp.

CARDARELLI, E, CERCATO, M, CERRETO, A & DI FILIPPO, G. 2010. Electrical resistivity and seismic refraction tomography to detect buried cavities. Geophysical Prospecting, 58(4): 685-695.

CARMO, F & KAMINO, L. 2015. Geossistemas Ferruginosos do Brasil: áreas prioritárias para conservação da diversidade geológica e biológica, patrimônio cultural e serviços ambientais. Belo Horizonte, MG, Brazil, 3i Editora. 553 pp.

CHALIKAKIS, K, PLAGNES, V, GUERIN, R, VALOIS R & BOSCH, FP. 2011. Contribution of geophysical methods to karst-system exploration: an overview. Hydrogeology Journal, 19(6): 1169-1180.

COELHO, A, AULER, A, PILÓ, LB & FRANCO, FP. 2013. Estudo de Impacto Ambiental de Serra Norte – Espeleologia - EIA GLOBAL - Serra Norte (N4/N5). Belo Horizonte, MG, Brazil. 300 pp. Available on: <http://licenciamento.ibama.gov.br/Mineracao/VALE_Ferro~Carajás~Norte/Espeleologia/>. Access on: Feb. 2, 2018.

DAY-LEWIS, FD, SLATER, LD, ROBINSON, J, JOHNSON, CD, TERRY, N & WERKEMA, D. 2017. An overview of geophysical technologies appropriate for characterization and monitoring at fractured-rock sites. Journal of Environmental Management, 204: 709-720.

DOCEGEO. Equipe-Distrito Amazônia. 1988. Revisão litoestratigráfica da Província Mineral de Carajás. Província Mineral de Carajás – Litoestratigrafia e Principais depósitos minerais. In: 35º Congresso Brasileiro de Geologia. Annex to Belém, PA, Brazil. p. 11-56.

DRIAD-LEBEAU, L, PIWAKOWSKI, B, STYLES, P, BOURGEOIS, B & CONTRUCCI, I. 2008. Geophysical detection of underground cavities. In: Symposium Post-Mining. Vandoeuvre-lès-Nancy, 2008. 17 pp.

FERREIRA, AA, LOPES, P, SALOMÃO, MS, MANE, MA, GERALDES, MC & CINTRA, H. 2017. Caracterização de cavidades naturais no Parque Estadual do Ibitipoca (Minas Gerais) por meio da pesquisa geológico-geofísica. Espeleo-Tema, 28(1): 49-59.

FIGUEIREDO E SILVA, RC, LOBATO, LM, ROSIÈRE, CA, HAGEMANN, S, ZUCCHETTI, M, BAARS FJ, MORAIS R & ANDRADE, I. 2008. A hydrothermal origin for the Jaspilite-hosted, giant Serra Norte iron ore deposits in the Carajás mineral province, Pará State, Brazil. In: HAGEMANN S, ROSIÈRE C, GUTZMER J, & BEUKES N (Eds.). Banded Iron Formation-Related High-Grade Iron Ore. Littleton, Colorado, USA. Society of Economic Geologists, 15: 255-290.

GONÇALVES, DF, DE PAULA, RG, BARBOSA, MR, TELES, C, MAURITY, CW & MACAMBIRA, JB. 2016. Lateritic terrains and the evolution of pseudokarstic features - case study in the iron ore mine N4E, Carajás region – Pará, Brazil. In: 24th World Mining Congress. Rio de Janeiro, Brazil. p. 227-236.

JACOBI, CM, CARMO, FF, & CAMPOS, IC. 2015. Iron geosystems: priority areas for conservation in Brazil. In: TIBBETT M (Ed.). Mining in Ecologically Sensitive Landscapes. Leiden. CRC Press, p. 55-77.

JOL, HM (Ed.). 2009. Ground penetrating radar theory and applications. Elsevier Science, Amsterdam. 544 pp.

LOBATO, LM, ROSIÈRE, CA, SILVA, RCF, ZUCCHETTI, M, BAARS, FJ, SEOANE, JCS, RIOS, FJ, PIMENTEL, M, MENDES, GE & MONTEIRO, AM. 2005. A mineralização hidrotermal de ferro da Província Mineral de Carajás - Controle estrutural e contexto na evolução metalogenética da província. In: ADIMB/DNPM. Caracterização de depósitos minerais em distritos mineiros da Amazônia. DNPM-CT/MINERAL-ADIMB, Brasília, Brazil. 21-92.

MACHADO, N, LINDENMAYER, Z, KROGH, T.E. & LINDENMAYER, D. 1991. U-Pb geochronology of Archean magmatism and basement reactivation in the Carajás area, Amazon shield, Brazil. Precambrian Research, 49: 329-354.

MAURITY, CW, & KOTSCHOUBEY, B. 1995. Evolução recente da cobertura de alteração no Platô N1-Serra dos Carajás-PA. Degradação, pseudocarstificação, espeleotemas. Boletim do Museu Paraense Emílio Goeldi, Série Ciências da Terra, 7: 331-362.

MONTEIRO, HS, VASCONCELOS, PMP, FARLEY, KA, & LOPES, CAM. 2018. Age and evolution of diachronous erosion surfaces in the Amazon: Combining (U-Th)/He and cosmogenic ^{3}He records. Geochimica et Cosmochimica Acta, 229: 162-183.

MMA. Ministério do Meio Ambiente. 2018. Cadastro Nacional de Informações Espeleológicas. ICMBIO. Brasília, Brazil: Centro Nacional de Pesquisa e Conservação de Cavernas – CECAV. Database downloaded on: Jan. 24, 2018.

PEREIRA, HS. 2017. Integração de dados geológicos, geoquímicos, espectrorradiométricos e de propriedades físicas de rocha: o estudo de caso do Corpo N5S, Província Mineral de Carajás. Master Dissertation in Geology. Instituto de Geociências, Universidade de Brasília, DF, Brazil. 150 pp.

PILÓ, LB & AULER, A. 2009. Geoespeleologia das cavernas em rochas ferríferas da região de Carajás, PA. In: Congresso Brasileiro de Espeleologia. 30, Montes Claros, MG, Brazil, Sociedade Brasileira de Espeleologia. p. 181-186.

PILÓ, LB, COELHO, A & REINO, JCR. 2015. Geoespeleologia em rochas ferríferas. In: CARMO, F & KAMINO, L (Eds.). Geossistemas Ferruginosos do Brasil: áreas prioritárias para conservação da diversidade geológica e biológica, patrimônio cultural e serviços ambientais. Belo Horizonte, MG, Brazil, 3i Editora. p. 125-148.

PUTIŠKA, R, NIKOLAJ, M, DOSTÁL, I & KUŠNIRÁK, D. 2012. Determination of cavities using electrical resistivity tomography. Contributions to Geophysics and Geodesy, 42(2): 201-211.

PUTIŠKA, R, KUSNIRAK, D, DOSTAL, I, LACNY, A, MOJZES, A, HOK, J, PASTEKA, R, KRAJNAK, M & BOSANSKY, M. 2014. Integrated geophysical and geological investigations of karst structures in Komberek, Slovakia. Journal of Cave & Karst Studies, 76(3): 155-163.

ROSIÈRE, CA, BAARS, FJ, SEOANE, JCS, LOBATO, LM, SILVA, LL, DE SOUZA, SRC, & MENDES, GE. 2006. Structure and iron mineralization of the Carajás Province. Applied Earth Science, 115(4): 126-133.

RUCHKYS, UA, TRAVASSOS, LEP, RASTEIRO, MA, & FARIA, LE. 2015. Patrimônio espeleológico em rochas ferruginosas: propostas para sua conservação no Quadrilátero Ferrífero, Minas Gerais. Campinas, SP, Brazil. Sociedade Brasileira de Espeleologia. 352 pp.

SHUSTER, DL, FARLEY, KA, VASCONCELOS, PM, BALCO, G, MONTEIRO, HS, WALTENBERG, K, & STONE, JO. 2012. Cosmogenic [3]He in hematite and goethite from Brazilian "canga" duricrust demonstrates the extreme stability of these surfaces. Earth and Planetary Science Letters, 329: 41-50.

TOLBERT, GE, TREMAINE, JW, MELCHER, GC & GOMES, CB. 1971. The recently discovered Serra dos Carajás iron deposits, northern Brazil. Economic Geology, 66(7): 985-994.

ZUCCHETTI, M. 2007. Rochas máficas do grupo Grão Pará e sua relação com a mineralização de ferro dos depósitos N4 e N5, Carajás, PA. Doctoral Dissertation in Economic and Applied Geology, Universidade Federal de Minas Gerais, Belo Horizonte, Brazil. 165 pp.

Revista Brasileira de Geofísica
RBGf
Brazilian Journal of Geophysics

CHARACTERIZING A TROPICAL SOIL VIA SEISMIC IN SITU TESTS

Breno Padovezi Rocha[1,2] and Heraldo Luiz Giacheti[2]

ABSTRACT. The shear wave velocity (V_s) is an important geotechnical parameter to be used in dynamic problems (e.g. earthquakes and vibration problems) as well as in static deformation analysis such as excavations and foundation engineering design. There are several in situ seismic tests to determine V_s such as the crosshole and the downhole techniques, as well as hybrid tests (e.g. seismic dilatometer – SDMT). This paper presents crosshole, downhole and SDMT tests carried out in a typical tropical soil profile from Brazil. Advantages and limitations regarding the test procedures and interpretation are briefly presented and differences observed among V_s determined by these techniques are discussed. Shear wave velocities (V_s) estimated from the crosshole, downhole and SDMT tests ranging from 194 to 370 m/s. The shear wave velocity suggests that the experimental site could be divided into two strata, which are in agreement with soil profile description. The maximum shear modulus (G_0) calculated from the V_s by theory of elasticity can be used to show the investigated tropical soil is a typical unusual geomaterial. This article also emphasizes that the SDMT is a useful test for site investigation since it allows a great means for profiling geostratigraphy and soil engineering properties during routine site investigation as well as for statics and dynamics problems.

Keywords: shear wave velocity, maximum shear modulus, crosshole, downhole, SDMT.

RESUMO. A velocidade de onda cisalhante (V_s) é um parâmetro geotécnico empregado em análises dinâmicas (terremotos e problemas de vibração), bem como em análises estáticas (escavações e projeto de fundações). Existem vários ensaios sísmicos de campo para a determinação de V_s, entre eles as técnicas *crosshole* e *downhole*, e os ensaios híbridos (por exemplo, dilatômetro sísmico – SDMT). Este artigo apresenta os ensaios *crosshole*, *downhole* e SDMT realizados em um perfil típico de solo tropical do Brasil, as vantagens e limitações dos procedimentos de ensaio e de interpretação são brevemente apresentadas, e as diferenças observadas entre os valores de V_s determinados pelas diferentes técnicas são discutidas. Os perfis de V_s determinados pelas técnicas variaram de 194 a 370 m/s. A velocidade da onda cisalhante sugere que o campo experimental investigado pode ser dividido em dois horizontes, os quais estão de acordo com a descrição do perfil do solo estudado. O módulo de cisalhamento máximo (G_0), calculado a partir de V_s pela teoria da elasticidade, pode ser utilizado para demonstrar o comportamento não convencional do solo investigado. Este artigo também enfatiza que o SDMT é um ensaio geotécnico útil para a investigação geotécnica do subsolo, uma vez que permite a definição do perfil estratigráfico e a estimativa de parâmetros estáticos e dinâmicos de um projeto.

Palavras-chave: velocidade de onda cisalhante, módulo de cisalhamento máximo, *crosshole*, *downhole*, SDMT.

[1]Universidade de São Paulo, Departamento de Geotecnia, Avenida Trabalhador São-Carlense, 400, Pq Arnold Schimidt, 13566-590, São Carlos, SP, Brazil – E-mail: brenop@sc.usp.br

[2]Universidade Estadual Paulista, Departamento de Engenharia Civil e Ambiental, Avenida Eng. Luiz Edmundo C. Coube, 14-01, Vargem Limpa, 17033-360, Bauru, SP, Brazil – E-mail: h.giacheti@unesp.br

INTRODUCTION

The shear wave velocity (V_s) profile is of important use in geotechnical engineering. During an earthquake, the ground motion of the site is significantly affected by the local site condition, and the average V_s is the key variable for site characterization in geotechnical earthquake engineering (Sully & Campanella, 1995; UBC, 1997; Bang & Kim, 2007). The V_s values can be used for a static deformation analysis such as slope stability and the settlement and an evaluation for ground improvements (Burland et al., 1977; Kim & Park, 1999; Ashford & Sitar, 2002). Recently, maximum shear modulus (G_0) calculated from V_s profiles has also been used to investigate non-textbook materials (Robertson, 2016; Marchetti & Monaco, 2018). For these reasons, the demand for a site investigation for V_s and G_0 profiling is increasing rapidly in the field of geotechnical engineering.

Several field seismic tests such as the crosshole, downhole, multi-channel analysis of surface waves (MASW) as well as hybrid tests (e.g. seismic cone and seismic dilatometer) are generally used for an evaluation of the V_s profile (Hunter et al., 2002; Stokoe et al., 2004). Each test has its own advantages and limitations and the results may not be coincident in many cases due to scale problems and the difference among the tests. Therefore, it is important to select an adequate field testing technique that considers the site conditions and the importance of the projects for obtaining a reliable V_s profile (Bang & Kim, 2007).

A large portion of Brazil's territory is covered with tropical soils, however, the geotechnical literature about dynamic parameters of these soils is very limited since dynamic tests are not currently carried out in Brazil. The term tropical soil includes both lateritic and saprolitic soils. Saprolitic soils are residual and retain the macro fabric of the parent rock. Lateritic soils can be either residual or transported and are distinguished by the occurrence of the laterization process, which is an enriching of a soil with iron and aluminum and their associated oxides, caused by weathering in regions which are hot, acidic, and at least seasonally humid (Nogami & Villibor, 1981). Following laterization, high concentration of oxides and hydroxides of iron and aluminum bonds support a highly porous structure. The contribution of this microstructure (cementation) to the soil stiffness depends on the strain level the soil will experience. These characteristics increase the preconsolidation stress and cohesion intercept (Vaughan et al., 1988) and the most

existing empirical correlation should be employed with caution (Robertson, 2016).

This paper presents crosshole, downhole, and seismic dilatometer (SDMT) tests carried out in a tropical soil site located at the Universidade de São Paulo, in São Carlos, Brazil. Advantages and limitations regarding the test procedures and interpretation are briefly discussed, and the differences observed between V_s and G_0 profiles determined by these techniques are also discussed. This paper also discusses the use of the G_0/E_D and G_0/M_{DMT} ratio as a useful index for site characterization of tropical soils.

IN SITU SEISMIC TESTS

Crosshole tests

The crosshole seismic test is one of the most effective techniques for the in situ determination of V_s. The main objective of this technique is determining the compression (P) and/or shear (S) propagation velocities along depth, being regulated by ASTM (2007).

The test consists of generating seismic waves in a borehole and registering their arrivals in one or more adjacent boreholes. The spacing between the source borehole and the first receiver borehole has to be around 1.5 to 3.0 m and the distance between subsequent receiver boreholes has to be 3.0 to 6.0 m apart. Spacing between the source borehole and the receiver borehole have to be 1.5 to 5.0 m for two boreholes (ASTM, 2007). The source and the seismic receivers (geophones or accelerometers) are positioned at the same depth, and the V_s is typically determined every meter depth interval. Figure 1 shows a sketch of the crosshole seismic test.

The interpretation of crosshole test data for determining V_s basically consists of identifying the first-arrival time of S-wave from the seismograms. S-waves are characterized by an increase in the amplitude of the signal as well as by the fact that it polarizes: inverting the direction of the blow, all phases corresponding to the shear waves appear inverted. In addition to the increase in the amplitude and its polarization, the S-wave can also be identified when the signal frequency decreases.

Special attention should be given in opening and preparing the source and the receiver boreholes. The procedure suggested by ASTM (2007), consists of coating them with metallic or PVC (polyvinyl chloride) pipes and grouting the borehole by a small diameter grout tube insert to the bottom of the borehole, by means of using a cement mix.
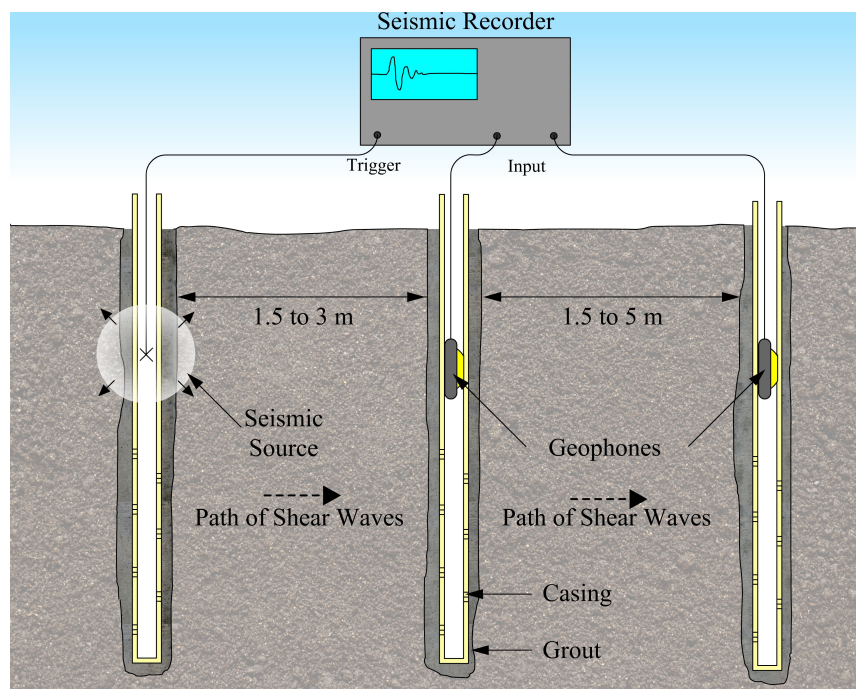
Figure 1 – Sketch of the crosshole seismic test (adapted from ASTM, 2007).

Downhole tests

The downhole seismic test (ASTM, 2008) is carried out using a single borehole. This test is performed inserting a seismic probe in a prepared borehole or into the soil mass and, in this case, there is no need for preparing the borehole. Figure 2 shows a sketch of the downhole seismic test.

The test consists in determining the arrival time of seismic waves generated on the ground surface and travelling down to an array of vertically installed seismic sensors positioned at different depths. The interpretation of the test data considers that the travel path between the source and the receiver follows a linear trajectory. In heterogeneous materials, this path is not a straight line and Snell's law of refraction can to be used.

The determination of shear wave propagation velocity can be done by three different methods: first arrival, cross-over and cross-correlation. According to Campanella & Stewart (1992), the cross-correlation method surpasses the others because it is less affected by signal distortions, leading to more consistent and reliable results.
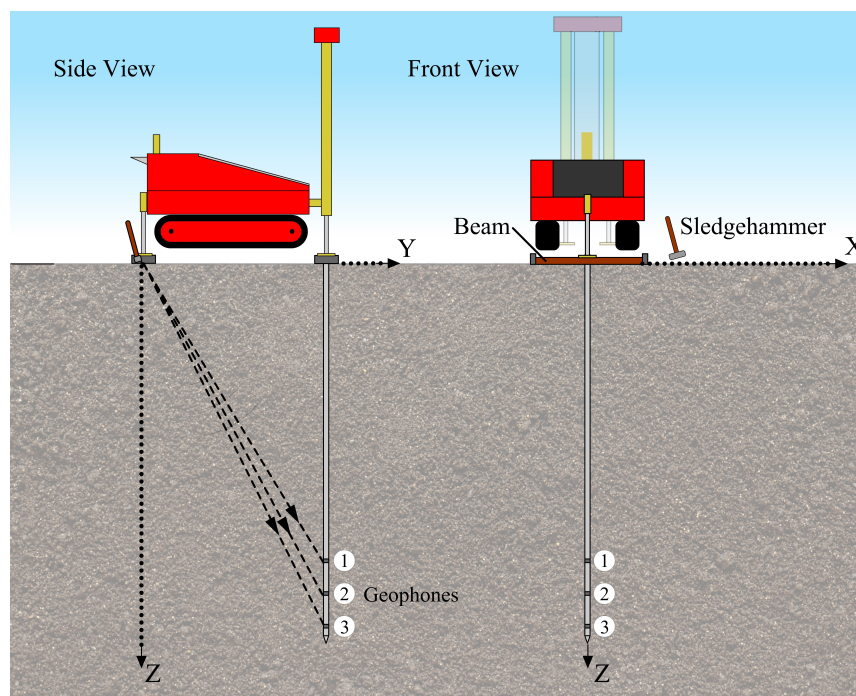
Seismic Dilatometer Test (SDMT)

The dilatometer test (DMT) consists of a stainless-steel blade with a thin flat circular expandable membrane on one site. Gas pressure is applied through the control unit, inflating the

membrane every 0.2 m depth intervals. The intermediate DMT parameters (Material Index - I_D, Horizontal Stress Index - K_D and Dilatometer Modulus - E_D) are calculated from p_0 (corrected first reading) and p_1 (corrected second reading) and are used to soil classification and estimative of geotechnical parameters (Marchetti 1980; Marchetti et al., 2001).

The seismic dilatometer (SDMT) is the combination of the standard DMT equipment with a seismic module for measuring the shear wave velocity V_s (Hepton, 1988; Martin & Mayne, 1997, 1998; Mayne et al., 1999; Marchetti et al., 2008). The test is conceptually equivalent to the seismic cone (SCPT). The seismic module is a cylindrical element placed above the DMT blade, equipped with two receivers, spaced 0.5 m apart (Fig. 3a). V_s is calculated (Fig. 3b) by the ratio between the difference in distance from the source and the two receivers ($S_2 - S_1$) and the delay of the arrival of the impulse from the first to the second receiver (Δt). Figure 3c shows the seismic dilatometer equipment.

The signal is amplified and digitized at depth. The true interval test configuration with two receivers avoids possible inaccuracy in the determination of the "zero time" at the hammer impact, sometimes observed in the pseudo-interval one-receiver configuration (Marchetti et al., 2008). In addition to V_s and G_0 profiles determination, SDMT allows estimating the G-γ decay curves and assessing the presence of microstructure (e.g.

Figure 2 – Side and front view of the downhole test with three geophones seismic probe (adapted from Karl et al., 2006).
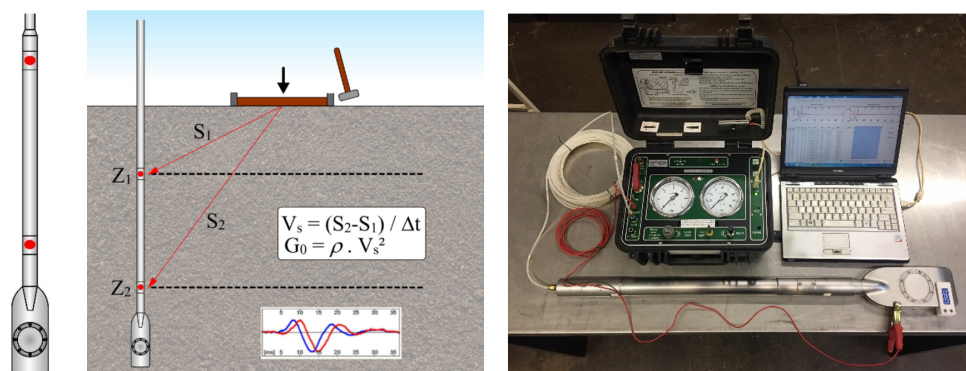
Figure 3 – Seismic Dilatometer (SDMT): (a) DMT blade with seismic module; (b) Schematic representation of the SDMT; (c) Seismic dilatometer equipment (adapted from Marchetti et al., 2008).

bonding and cementation) (Ashford & Sitar, 2002; Marchetti & Monaco, 2018).

MAXIMUM SHEAR MODULUS (G_0), G_0/E_D AND G_0/M_{DMT} RATIO

G_0 is the stiffening parameter that refers to the initial undisturbed state of the soil and allows assessing the stress-strain-strength response of soils for static, cyclic and dynamic loads, both for drained and undrained conditions (Wang et al., 2018). It is largest at very low strains and decreases with increasing shear strain.

It has been found that the initial maximum shear modulus is constant for strains less than 10^{-4}% (Sully & Campanella, 1995) although this may vary with plasticity index (PI) (Vucetic & Dobry, 1991). It can be calculated from shear wave velocity (V_s) by in situ or laboratory tests by the Equation 1 (Woods, 1978):

$$G_o = \rho . (V_s)^2 \qquad (1)$$

where ρ = γ/g total mass density, γ = soil unit weight, and g = gravitational constant.
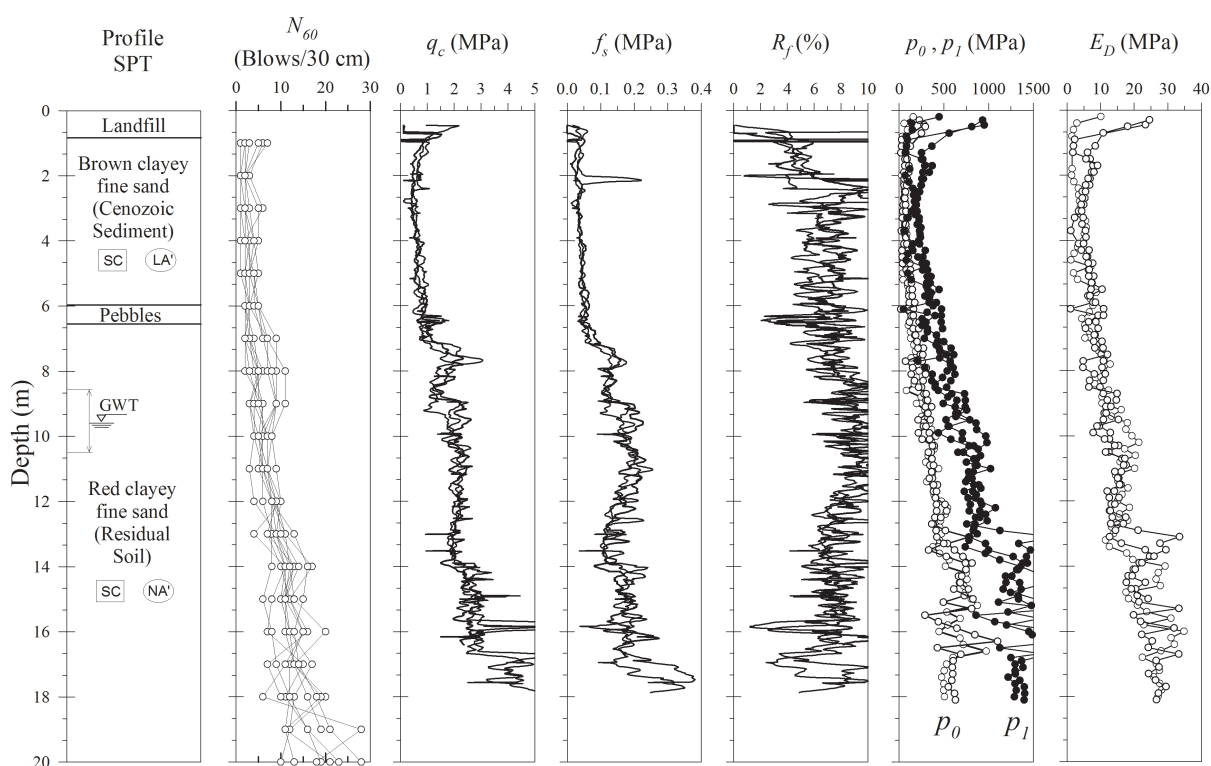
Figure 4 – Synthesis of in situ tests for the study area (adapted from Giacheti et al., 2006a and Rocha, 2018).

Microstructure (e.g. bonding and cementation) improves the mechanical behavior of the soil, however, quantify this effect is not easy (Baligh & Scott, 1975; Robertson, 2016). Penetration probes insertion may partly destroy the microstructure. In general, it can be expected that the DMT insertion may produce pronounced destructive effects in cemented soils (Baligh & Scott, 1975; Marchetti & Panone, 1981; Marchetti & Monaco, 2018).

If SDMT is carried out, G_0 can be calculated from V_s (Eq. 1) and additional information on microstructure can be obtained using the method illustrated by Cruz et al. (2012). These authors have demonstrated the possibility of combining E_D and M_{DMT} (constrained modulus obtained from SDMT) values with G_0 to assess the presence of microstructure as well as to identify the presence of unusual soils. The microstructure affects the behavior of tropical soils and G_0/E_D and G_0/M_{DMT} values of these soils are considerably higher than those observed in sedimentary soils. If soils have significant microstructure the methods and approaches to interpreted in situ tests may not always apply and site or geologic specific modifications may be required (Robertson, 2016; Berisavljevic & Berisavljevic, 2019; Marchetti & Monaco, 2019).

MATERIALS AND METHODS

Study area

The seismic tests were carried out in the experimental test site at the Universidade de São Paulo in São Carlos, Brazil. The soil profile is an example of typical tropical soil (ISSMFE, 1985). This profile is composed of a sandstone residual soil layer covered by a surficial unsaturated lateritic clayey sand layer (colluvial soil). A thick layer (0.2 to 0.5 m) of pebbles separates the surficial layer from the residual soil. The groundwater level varies seasonally between 9 and 12 m below the ground surface. According to the Unified Soil Classification System (ASTM, 2011), both horizons can be classified as clayey sand (SC).

Several site characterization programs including standard penetration (SPT), cone penetration (CPT) and flat dilatometer (DMT) tests were carried out at this site. Sample pits were also excavated to retrieve undisturbed and disturbed soil blocks. Soil samples from these blocks were tested in laboratory for soil characterization and determination of mechanical properties and parameters. Figure 5 presents results of SPT, CPT and DMT tests. N-values from SPT tests and dilatometer modulus (E_D) increase almost linearly with depth. The cone tip resistance (q_c)
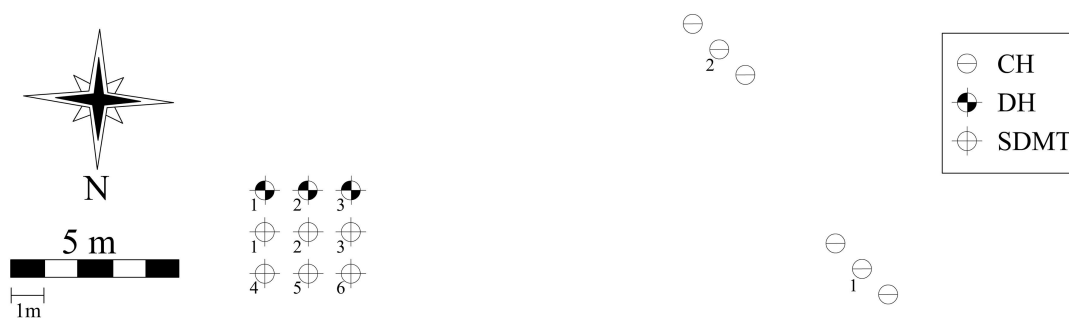
Figure 5 – Test locations of the crosshole (CH), downhole (DH) and SDMT carried out at the investigated site.

and the sleeve friction (*fs*) tends to increase with depth leading to a friction ratio ($Rf = fs/q_c * 100$) between 4 and 8%. The interpretation of MCT classification test (Nogami & Villibor, 1981) data separated lateritic (LA') from non-lateritic (NA') soil behavior almost at the same depth (6 m).

Seismic tests

Two crosshole seismic tests (CH 1 and CH 2) were carried out in the site. Three boreholes spaced 3 m apart were installed for each test. The boreholes were drilled with a 150 mm diameter. The two receiver boreholes were cased with PVC pipes 75 mm diameter and the source borehole with PVC pipes 85 mm diameter. A grout mix that closely matches the formation density was used. The data were taken at every 1.0 m interval for the test CH 1 and at every 0.5 m interval for the test CH 2. The test procedure consisted of generating reverse polarity shear waves, first by impacting one end of a hammer source, and then by impacting the other end. Volts versus time traces, corresponding to each impact, were registered on an oscilloscope and recorded in a laptop computer for subsequent processing and analysis. Source and geophones are maintained at the same elevation for each measurement. Both crosshole tests were performed up to around 9 m depth due to limitation in the opening and preparing the boreholes below the groundwater level with the available equipment.

Three downhole tests were carried out using a seismic probe with three geophone compartments, spaced 0.5 m apart. This probe allows three records every test depth. The geophones are characterized by natural frequency of 28 Hz, sensitivity of 35.4 V/(m/s) and spurious frequency of 400 Hz. The geophones were oriented in a uniaxial configuration, thus the axis of vibration was maintained parallel to the direction of the horizontal impacts of the hammer. This configuration allows the maximum response of the geophones (Campanella & Howie, 2005). A steel bar placed on

the ground surface was used as seismic source. It was positioned 0.3 m away from the borehole opening. The data were interpreted using the cross-correlation method and the true interval. The downhole tests were carried out up to 18 m depth.

Six SDMT (SDMT 1 to 6) were also carried out up to 20 m depth. The seismic source is the same used in the downhole test. It was oriented with its long axis parallel to the axis of the receivers, so that they can offer the highest sensitivity to the generated shear wave. The time delay from SDMT seismograms was determined using the cross-correlation algorithm. Figure 5 shows the location of the seismic tests.

TEST DATA AND DISCUSSION

Seismic tests

Figures 6, 7, and 8 show the seismograms acquired by crosshole, downhole and SDMT tests, respectively. Figure 6 presents the traces at 2 m depth, during the crosshole test CH 1. The arrival time of S-wave was select using the reverse polarity. Figure 7 shows some traces obtained at 10 m depth, during the downhole test DH 1. It demonstrates that all three different geophones provided excellent quality recorders. It is noteworthy that, in general, it is possible to get recordings of similar quality for all the three geophones. Figure 8 shows the seismograms obtained by SDMT 1 at the 3.5, 4.5, and 5.5 m depth at the investigated site. It is a good practice to plot the seismograms side-by-side as recorded and re-phased according to the calculated delay.

Figure 9 shows the V_s profiles measured by the different techniques. There is reasonable agreement among the V_s profiles determined by the different techniques (Fig. 10). The shear wave velocities obtained by three techniques ranged from 194 to 370 m/s, with an average velocity of 295 m/s with a 21 m/s average standard deviation. The V_s values measured from crosshole are little higher than those of downhole and SDMT. This behavior
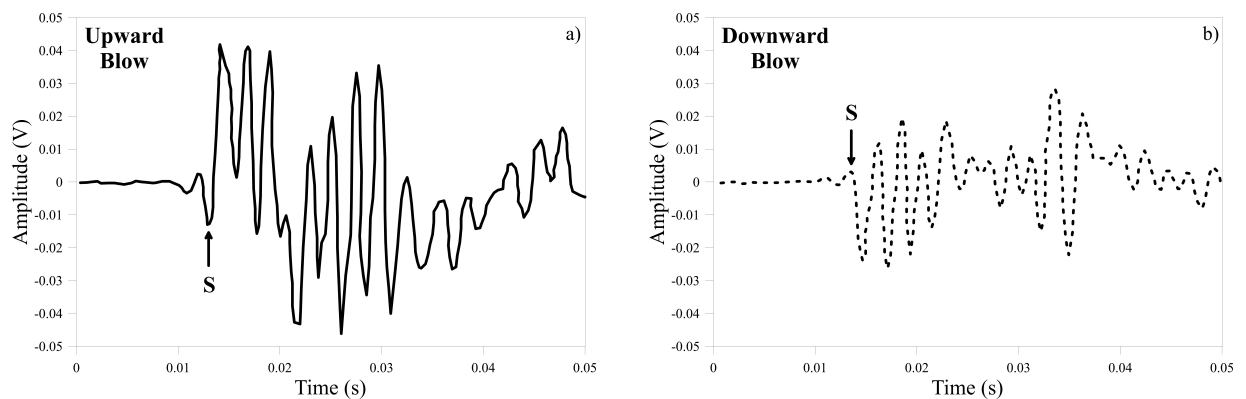
Figure 6 – Typical crosshole arrival traces (CH 2 at 2 m depth); a) Upward blow, b) Downward blow.
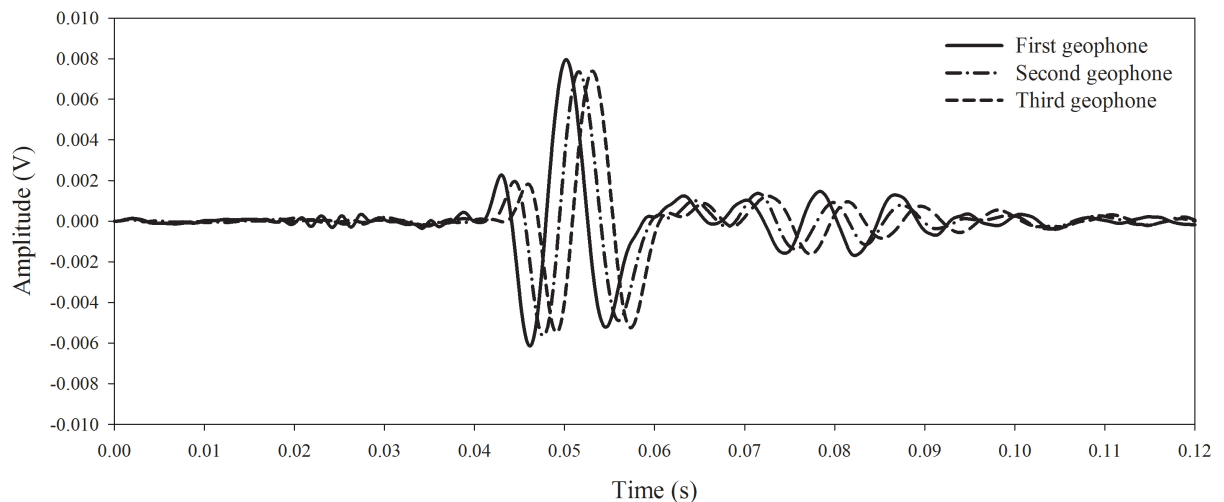

Figure 7 – Typical downhole shear wave arrival traces (DH 1 at 10 m depth).

can be attributed to the difference in the directions of propagation and polarization of shear waves induced by crosshole, downhole and SDMT (Butcher & Powell, 1996; Fioravante et al., 1998; Viana da Fonseca et al., 2005). Cost-wise, the SDMT is clearly the choice for budgetary reasons. Furthermore, the SDMT provides additional readings including: corrected first reading (p_0), corrected second reading (p_1), and time derived from DMT decay dilatometer test (T_{flex}) with depth. The collection of multiple measurements is beneficial towards a comprehensive site characterization program at any given site (Marchetti, 1980; Marchetti et al., 2001; Marchetti & Monaco, 2018). However, the SDMT blade insertion in hard soils can be difficult precluding this test type.

Shear wave velocity are influenced by confining pressure and are expected to increase with the depth. The variation of V_s

with the total vertical stress (σ_v) can be modeled using a power law expression presented in Equation 2, similar to the equation used by Hardin & Drnevich (1972a, 1972b) and Valle-Molina & Stokoe (2012).

$$V_s = A_s \left(\frac{\sigma_v}{P_a} \right)^{n_s} \qquad (2)$$

In this expression, As is the shear wave velocity for 100 kPa of vertical stress, n_s is a dimensionless exponent of vertical pressure normalized by atmospheric pressure (P_a = 100 kPa).

Figure 11 shows the measured V_s and the fitting curves considering Equation 2. The soil unit weight was equal to 14 kN/m^3 up to 8 m depth and to 16 kN/m^3 from then on. From best fitting analysis As is 288 m/s and n_s is 0.15. S-wave velocity increased with the vertical stress with fitted n_s value of the same
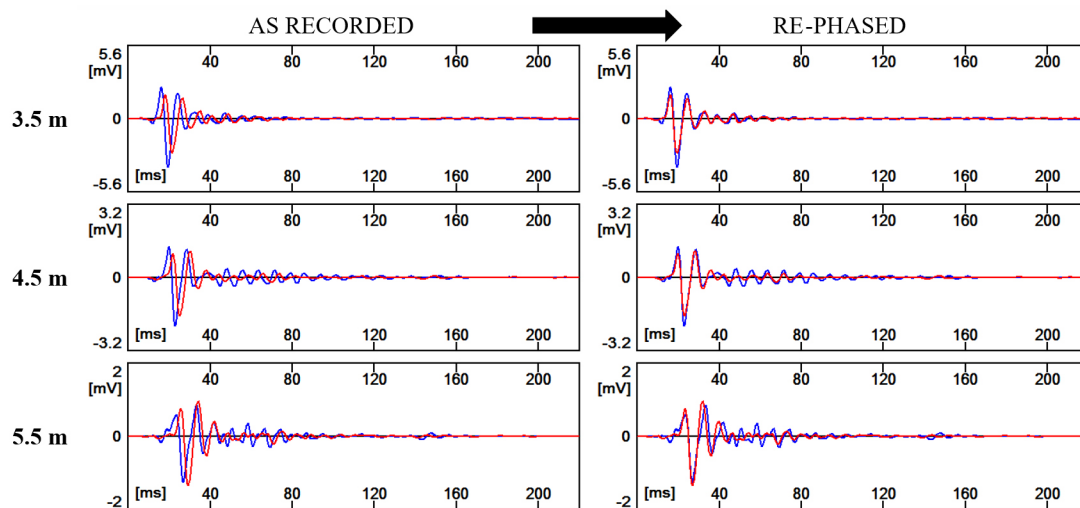
Figure 8 – Example of seismograms obtained by SDMT 1 at the 3.5, 4.5, and 5.5 m depth.
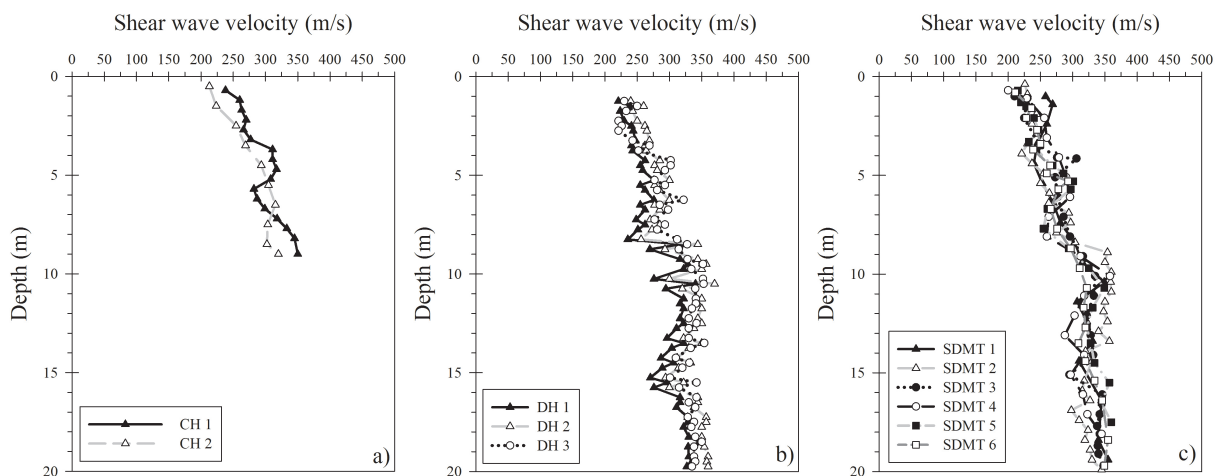

Figure 9 – Comparison among V_s measured by a) crosshole, b) downhole and c) SDMT test for study area.

magnitude of those measured by Valle-Molina & Stokoe (2012) in sands.

The scatter in the crosshole, downhole and SDMT data (Figs. 9 and 10) combined with field observations, suggests that the study area can be divided into two layers, instead of considering it as a uniform media. In fact, it is possible to notice an upper stratum that reaches 8 meters depth. In the upper stratum V_s ranged from 194 to 305 m/s, with an average velocity of 259 m/s. In the lower stratum (between 8 and 18 m depth) V_s ranged from 250 to 370 m/s, with an average velocity of 325 m/s. Table 1 presents the statistics for these data. The mean values of V_s increase from the upper to the lower stratum, which was expected, considering the increase in confining stress and the denser and

stiffer state of the soil. The larger dispersion in upper stratum can be explained to be a consequence of the unsaturated condition (Cho & Santamarina, 2001; Gui & Yu, 2008; Nyunt et al., 2011; Dong & Lu, 2016) as well as the inherent variability (Gidigasu, 1976; ISSMFE, 1985; Giacheti et al., 2006b; Gutierrez et al., 2009) typical in lateritic tropical soils.

The G_0, G_0/E_D and G_0/M_{DMT} ratio

The G_0 was calculated by Equation 1. Soil unit weight (γ) was determined from undisturbed soil samples collected in sample pits excavated at the site (ABNT, 2016). The G_0 range between 75 to 233 MPa, with an average of 151 MPa with a 19 MPa average standard deviation.
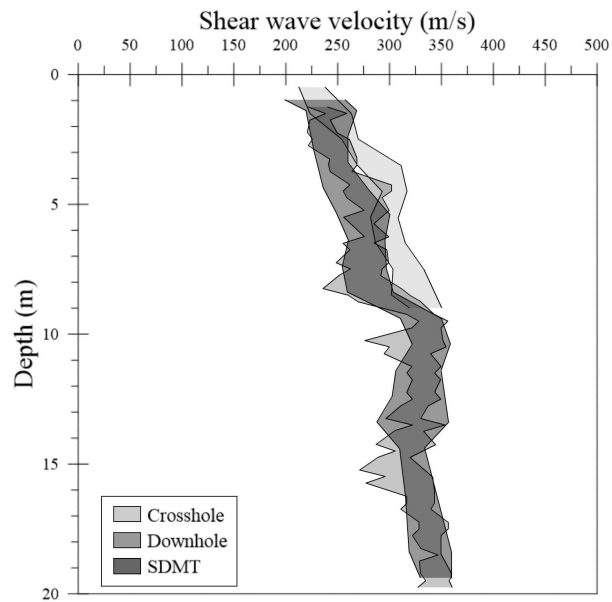
Figure 10 – Shear wave velocity measured in the crosshole, downhole and SDMT tests in the study area.

$$Vs = 288 \text{ m/s} * (\sigma_v/P_a)^{0.15}$$
$$R^2 = 0.66$$
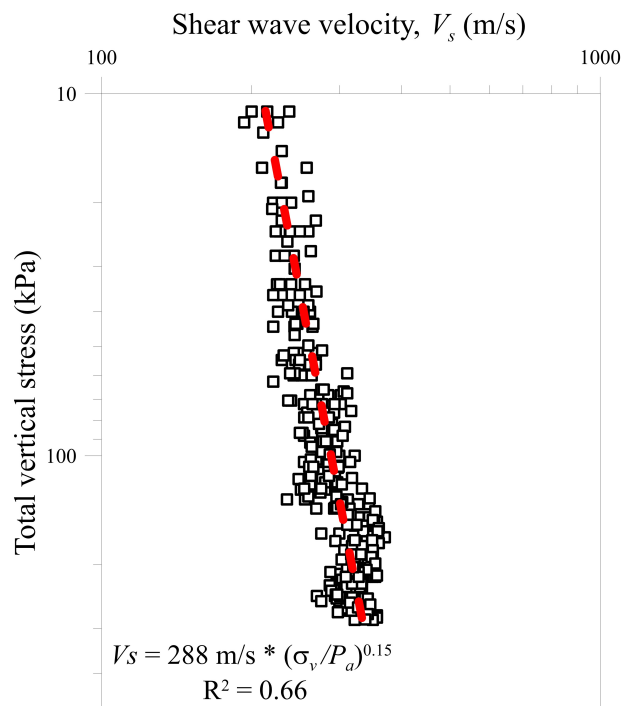
Figure 11 – Variation of shear wave velocity with total vertical stress for the study area.

Table 1 – Statistic of the crosshole, downhole and SDMT tests results.

	Stratum	Observations	Minimum (m/s)	Maximum (m/s)	Average (m/s)	Standard deviation (m/s)	Coefficient of variation
V_S	Upper	152	194	305	259	52	0.200
	Lower	145	250	370	325	40	0.123
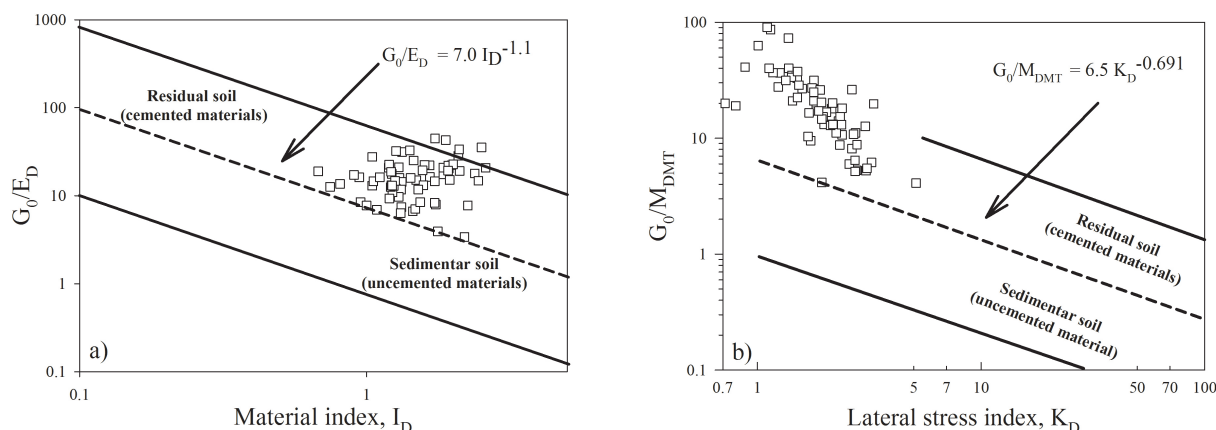
Figure 12 – SDMT data plotted on G_0/E_D vs I_D chart (a) and G_0/M_{DMT} vs K_D chart (b) (adapted from Cruz et al., 2012).

Figures 12a and 12b show the G_0/E_D vs I_D and G_0/M_{DMT} vs K_D charts, respectively, suggested based on the findings from Cruz et al. (2012). I_D, K_D, E_D and M_{DMT} were calculated according to Marchetti (1980) and Marchetti et al. (2001).

In both charts the plotted SDMT data from six tests are above the equation line which separates the sedimentary to the residual soil. It indicates that the bonded structure of studied tropical soils produces G_0/E_D as well as G_0/M_{DMT} that are systematically higher than those measured in sedimentary soils. In soil where there is significant microstructure like the tropical soils the classification of soil type and geotechnical properties estimative becomes less reliable and some judgment is required (Marchetti & Monaco, 2018; Robertson, 2016).

CONCLUSION

The crosshole, downhole and seismic dilatometer (SDMT) tests allow the determination of V_s, and corresponding calculation of G_0 for geotechnical engineering applications mainly in soil dynamic analysis.

V_s and G_0 profiles determined by crosshole, downhole and SDMT show good agreement at the study area. Consequently, any techniques (crosshole, downhole and SDMT) can be used to determined shear wave velocity in this site. The shear wave velocity profile suggests the presence of two strata in the study area, which are in agreement with soil profile description.

Both charts from Cruz et al. (2012) indicate the presence of cemented structures in the site. The bonded structure of tropical sandy soils produces G_0/E_D as well as G_0/M_{DMT} which are systematically higher than those measured in sedimentary soils. If the soil has a significant microstructure the classification charts and most existing empirical correlations may not always be applied and site or geologic specific modifications are required.

The crosshole is the most reliable method to determine in situ V_s profile. However, this technique is less used due to its high cost. The seismic dilatometer (SDMT) is particularly well-suited, efficient and economical tool for routine site characterization. The test data allows a direct quantification of soil properties such as shear strength, deformability and permeability and the G_0 profile is determined directly for soil dynamic analyses.

ACKNOWLEDGMENTS

REFERENCES

ABNT. 2016. NBR 9604. Well opening and soil profile inspection trench, with removal of disturbed and undisturbed soil samples — Procedure. Rio de Janeiro, Brazil: Associação Brasileira de Normas Técnicas - ABNT, 9 pp. [in Portuguese].

ASHFORD SA & SITAR N. 2002. Simplified method for evaluating seismic stability of steep slopes. J Geotech Geoenviron Eng, 128(2): 119–128. doi: 10.1061/(ASCE)1090-0241(2002)128:2(119).

ASTM. 2007. Standard, D4428-07. Standard test methods for Crosshole seismic testing. West Conshohocken, PA, USA: ASTM International. 2007. 11 pp.

ASTM. 2008. Standard, D7400-08. Standard test methods for Downhole seismic testing. West Conshohocken, PA, USA: ASTM International. 2008. 11 pp.

ASTM. 2011. D2487-11. Standard practice for classification of soils for engineering purposes (Unified Soil Classification System). West Conshohocken, PA, USA: ASTM International. 2011, 12 pp.

BALIGH MM & SCOTT RF. 1975. Quasi Static Deep Penetration in Clays. ASCE J Geotech Eng, 101(GT11): 1119-1133.

BANG ES & KIM DS. 2007. Evaluation of shear wave velocity profile using SPT based uphole method. Soil Dyn Earthq Eng, 27(8): 741-758. doi: 10.1016/j.soildyn.2006.12.004.

BERISAVLJEVIC D & BERISAVLJEVIC Z. 2019. Determination of the presence of microstructure in a soil using a seismic dilatometer. Bulletin of Engineering Geology and the Environment, 78(3): 1709-1725. doi: 10.1007/s10064-018-1234-5.

BURLAND JB, LONGWORTH TI & MOORE JFA. 1977. Study of ground and progressive failure caused by a deep excavation in Oxford Clay. Géotechnique, 27(4): 557–591.

BUTCHER AP & POWELL JJM. 1996. Practical considerations for field geophysical techniques used to assess ground stiffness. In: Advances in Site Investigation Practice. Thomas Telford, London, p. 701-714.

CAMPANELLA RG & HOWIE JA. 2005. Guidelines for the use, interpretation and application of seismic piezocone test data. Geotechnical Research Group Department of Civil Engineering. University of British Columbia, Vancouver. 305 pp.

CAMPANELLA RG & STEWART WP. 1992. Seismic cone analysis using digital signal processing for dynamic site characterization. Can Geotech J, 29(3): 477–486. doi: 10.1139/t92-052.

CHO GC & SANTAMARINA JC. 2001. Unsaturated Particulate Materials — Particle-Level Studies. J Geotech Geoenviron Eng,127(1): 84-96. doi: 10.1061/(ASCE)1090-0241(2001)127:1(84).

CRUZ N, RODRIGUES C & FONSECA AV. 2012. Detecting the presence of cementation structures in soils, based in DMT interpreted charts. In: 4th International Conference on Site Characterization (ISC4). Porto de Galinhas, Brazil. v.1. p. 1723-1728.

DONG Y & LU N. 2016. Dependencies of Shear Wave Velocity and Shear Modulus of Soil on Saturation. J Eng Mech, 142(11): 04016083. doi: 10.1061/(ASCE)EM.1943-7889.0001147.

FIORAVANTE V, JAMIOOLKOWSKI M, LO PRESTI DCF, MANFREDINI G & PEDRONI S. 1998. Assessment of the coefficient of Earth pressure at rest from shear wave velocity measurements. Géotechnique. 48(5): 657-666.

GIACHETI HL, DE MIO G & PEIXOTO ASP. 2006a. Cross-hole and seismic CPT tests in a tropical soil site. In: DE GROOT DJ, DEJONG JT, FROST D & BAISE LG (Eds.). Proceedings of GeoCongress 2006: Geotechnical Engineering in the Information Technology Age. American Society of Civil Engineers (ASCE). Atlanta, Georgia. doi: 10.1061/40803(187)92.

GIACHETI HL, DE MIO G, DOURADO JC & MALAGUTTI W. 2006b. Comparing down-hole and cross-hole seismic tests results on the Unesp Bauru research site. In: 13th Brazilian Congress of Soil Mechanics and Geotechnical Engineering. Curitiba, Brazil. v. 2, p. 669-674. [in Portuguese].

GIDIGASU MD. 1976. Laterite Soil Engineering: Pedogenesis and Engineering Principles. Developments in Geotechnical Engineering, Elsevier, N.Y., 554 pp.

GUI M-W & YU C-M. 2008. Rate of strength increase of unsaturated lateritic soil. Can Geotech J, 45(9): 1335-1343. doi: 10.1139/T08-065.

GUTIERREZ NHM, NÓBREGA MT & VILAR OM. 2009. Influence of the microstructure in the collapse of a residual clayey tropical soil. Bull Eng Geol Environ, 68(1): 107-116. doi: 10.1007/s10064-008-0180-z.

HARDIN BO & DRNEVICH VP. 1972a. Shear modulus and damping in soils: measurement and parameter effects. J Soil Mech Found Eng Div, 98(SM6): 603–624.

HARDIN BO & DRNEVICH VP. 1972b. Shear modulus and damping in soils: design equations and curves. J Soil Mech Found Eng Div, 98(SM7): 667–692.

HEPTON P. 1988. Shear wave velocity measurements during penetration testing. In: Penetration Testing in the UK. Birmingham. ICE, 275-278.

HUNTER JA, BENJUMEA B, HARRIS JB, MILLER RD, PULLAN SE, BURNS RA & GOOD RL. 2002. Surface and downhole shear wave seismic methods for thick soil site investigations. Soil Dyn Earthq Eng, 22(9-12): 931-941. doi: 10.1016/S0267-7261(02)00117-3.

ISSMFE. 1985. Committee on Tropical Soils of ISSMFE. 1985. Peculiarities of geotechnical behavior of tropical lateritic and saprolitic soils: progress report (1982-1985). São Paulo, SP, Brazil. Ed. Edile.

KARL L, HAEGEMAN W & DEGRANDE G. 2006. Determination of the material damping ratio and the shear wave velocity with seismic cone Penetration test. Soil Dyn Earthq Eng, 26(12): 1111-1026. doi: 10.1016/j.soildyn.2006.03.001.

KIM DS & PARK HC. 1999. Evaluation of ground densification using SASW method and resonant column tests. Can Geotech J, 36(2): 291–299. doi: 10.1139/t98-103.

MARCHETTI S. 1980. In Situ Tests by Flat Dilatometer. ASCE J Geotech Eng, 106(GT3): 299-321.

MARCHETTI S & MONACO P. 2018. Recent Improvements in the Use, Interpretation, and Applications of DMT and SDMT in Practice. ASTM, Geotech Testing J, 41(5): 837-850. doi: 10.1520/GTJ20170386.

MARCHETTI S & PANONE C. 1981. Distortions Induced in Sands by Probes of Different Shapes. Rivista Italiana di Geotechnica, 15(1): 50-54. [in Italian].

MARCHETTI S, MONACO P, TOTANI G & CALABRESE M. 2001. The Flat Dilatometer Test (DMT) in Soil Investigations. TC16 Report. In: IN SITU 2001, International Conference on In situ Measurement of Soil Properties. Indonesia, 41 pp.

MARCHETTI S, MONACO P, TOTANI G & MARCHETTI D. 2008. In Situ Tests by Seismic Dilatometer (SDMT). In: Symposium Honoring Dr. John H. Schmertmann for His Contributions to Civil Engineering at Research to Practice in Geotechnical Engineering Congress. New Orleans, Louisiana, United States. p. 292-311.

MARTIN GK & MAYNE PW. 1997. Seismic Flat Dilatometer Tests in Connecticut Valley Varved Clay. ASTM Geotech Testing J, 20(3): 357-361.

MARTIN GK & MAYNE PW. 1998. Seismic flat dilatometer in Piedmont residual soils. In: 1st International Conference on Site Characterization ISC'98. Atlanta, vol. 2, p. 837-843.

MAYNE PW, SCHNEIDER JA & MARTIN GK. 1999. Small- and large-strain soil properties from seismic flat dilatometer tests. In: 2nd International Symposium on Pre-Failure Deformation Characteristics of Geomaterials. Turin, Italy. v.1, p. 419-427.

NOGAMI JS & VILLIBOR DF. 1981. A new soil classification for highway purposes. In: Symposium on Tropical Soils in Engineering. Rio de Janeiro, Brazil: COPPE/UFRJ-ABMS. v. 1, p. 30-41. [in Portuguese].

NYUNT TT, LEONG EC & RAHARDJO H. 2011. Strength and Small-Strain Stiffness Characteristics of Unsaturated Sand. Geotech Test J, 34(5): 551-561. doi: 10.1520/GTJ103589.

ROBERTSON PK. 2016. Cone Penetration Test (CPT)-Based Soil Behaviour Type (SBT) Classification System – An Update. Can Geotech J, 53(12): 1910–1927. doi: 10.1139/cgj-2016-0044.

ROCHA BP. 2018. Caracterização Geotécnica de Solos Tropicais Não Saturados por meio de Ensaios de campo. Ph.D. Thesis – Programa de Pós-graduação em Geotecnia. Departamento de Geotecnia, Universidade de São Paulo, Brazil. 2018. 240 pp.

STOKOE KH, JOH SH & WOODS RD. 2004. Some contributions of in situ geophysical measurements to solving geotechnical engineering problems. In: 2nd International Conference on Site Characterization. Porto, Portugal, p. 97-132.

SULLY JP & CAMPANELLA RG. 1995. Evaluation of in-situ anisotropy from crosshole and a downhole shear wave velocity measurements. Géotechnique, 45(2): 267-282. doi: 10.1680/geot.1995.45.2.267.

UBC. 1997. Uniform Building Code (International Building Code), International Code Council. International Conference of Building Officials. 1997.

VALLE-MOLINA C & STOKOE II KH. 2012. Seismic measurements in sand specimens with varying degrees of saturation using piezoelectric transducers. Can Geotech J, 49(6): 671–685. doi: 10.1139/t2012-033.

VAUGHAN PR, MACCARINI M & MOKHTAR SM. 1988. Indexing the engineering properties of residual soil. Quarterly Journal of Engineering Geology, 21(1): 69- 84.

VIANA DA FONSECA A, CARVALHO J & FERREIRA C. 2005. The use of shear wave velocities determined in Down-Hole (V_s^{yh}) and Cross-Hole (V_s^{hv}) tests for the evaluation of K_0 in soils. ABMS, Brazil. Solos e Rochas, 28(3): 271-281.

VUCETIC M & DOBRY R. 1991. Effect of Soil Plasticity on Cyclic Response. ASCE J Geotech Eng, 117: 89-107.

WANG Z, ZHANG N, CAI G, LI Q & WANG J. 2018. Field Investigation of Maximum Dynamic Shear Modulus of Clay Deposit using Seismic Piezocone. Int J Civ Eng, 17(6): 699-708. doi: 10.1007/s40999-018-0306-z.

WOODS RD. 1978. Measurement of dynamic soil properties – State of the Art. In: ASCE Speciality Conference on Earthquake Engineering and Soil Dynamics. Pasadena, California. v.1, p. 91–178.

GEOPHYSICAL METHODS FOR BR TAILINGS DAM RESEARCH AND MONITORING IN THE MINERAL COMPLEX OF TAPIRA – MINAS GERAIS, BRAZIL

Demetrius Cunha Gonçalves da Rocha[1], Marco Antonio da Silva Braga[1] and Camilla Tavares Rodrigues[2]

ABSTRACT. The use of geophysical methods in the BR dam at Tapira mining complex in Minas Gerais state, Brazil, had as main objective to develop a research geophysical methodology complementary to the existing conventional monitoring system. Electrical resistivity and GPR (ground penetrating radar) methods were used. Ten geophysical sections were acquired parallel to the main axis of the BR dam. The water table level delineated by geophysics was later compared to five type-sections data, which comprised the readings of 9 water level indicators (INA). The electrical resistivity results delineated the level of the water table and showed the moisture areas in the BR dam. Low resistivity zones (LRZ) were correlated with regions saturated or with a high moisture content with resistivity responses below 250 ohm-m. The GPR responses, saturated zones presented strong attenuation in the reflectors, being this effect smaller with the decrease in the water content. In some sections it was possible to correlate, patterns of reflectors to different resistive zones. Geophysics results showed great efficiency in the BR dam investigation and monitoring, through the generation of continuous indirect indicator data. Which after processing resulted in a complete 2D and 3D view of the interior of the studied dam.

Keywords: electrical resistivity, geotechnics, applied geophysics.

RESUMO. A utilização de métodos geofísicos na barragem BR do complexo de mineração de Tapira no estado de Minas Gerais, Brasil, teve como principal objetivo desenvolver uma metodologia geofísica investigativa complementar ao monitoramento hoje existente. Foram utilizados os métodos geofísicos de eletrorresistividade e GPR (ground penetrating radar). Durante a aquisição de dados foram levantadas 10 linhas paralelas ao eixo principal do barramento. O nível freático delineado pela geofísica foi posteriormente comparado com o nível freático de 5 seções-tipo mapeado pelas leituras de 9 indicadores de nível d'água (INA). Os resultados da eletrorresistividade delinearam de forma precisa o nível freático, diferenciando áreas secas das úmidas ao longo do barramento. Zonas de baixa resistividade (ZBR), foram correlacionadas com regiões do maciço possivelmente saturadas ou com alto teor de umidade (< 250 ohm-m). Em resposta ao GPR, zonas saturadas apresentaram forte atenuação nos refletores, sendo esta atenuação menor com a diminuição no teor de água. Em algumas seções foram correlacionados padrões dos refletores a diferentes zonas resistivas. A geofísica mostrou ter uma grande eficácia na investigação e no monitoramento dessas estruturas, através da geração de indicadores indiretos contínuos, que após processamento resultaram em um imageamento completo em 2D e 3D do interior da barragem estudada.

Palavras-chave: resistividade elétrica, geotecnia, geofísica aplicada.

[1]Universidade Federal do Rio de Janeiro, Centro de Pesquisa em Geofísica Aplicada (CPGA) Av. Athos da Silveira Ramos, 274, sala G-058, Cidade Universitária, Ilha do Fundão, 21941-916, Rio de Janeiro, RJ, Brazil – E-mails: demetrius@geologia.ufrj.br, marcobraga@geologia.ufrj.br
[2]Tetra Tech, Rio de Janeiro, RJ, Brazil – E-mail: milla_tavares1@hotmail.com

INTRODUCTION

Due to the increase of serious accidents with failure of tailings dams in Brazil, it is expected that the search for the development of new alternatives of investigation and monitoring technologies will contribute to predict geotechnical issues. The rupture of a dam is usually catastrophic, with life, social and financial losses and often generate an incalculable environmental impact, with consequences that can last for a long time.

In some countries, the use of near surface geophysical methods has already been largely used for the investigation and monitoring of different dam types. Nwokebuihe et al. (2016), for example, applied near surface methods in an earthfill dam located in Warren County in the state of Missouri - USA. The induced polarization (IP), self-potential (SP) and electrical resistivity methods were used to investigate a downstream leakage and internal seepage pathways and observe the central drainage pipe position verifying the appropriate operation with the initial design. All results were satisfactory for the research objective. In the earth dam located in Zaria, northwest of Nigeria, the use of electrical resistivity was chosen to investigate possible seepage in the low-velocity seismic waves areas located at the abutments. From these results, it was possible to identify three well defined layers in these regions and to identify low resistivity zones, which were interpreted as being less consolidated or fractured zones, suggesting moisture areas and possible presence of internal seepages (Chinedu & Ogah, 2013).

In Brazil, there are some published research papers on the use of geophysical investigation in these structures, with excellent results. For example, the use of the electrical resistivity method in the concrete dam UHE Governador José Richa, in the Paraná state, showed showed great efficiency for identifying moisture regions near the previously mapped cracks in the concrete structure, complementing the data of SP (self-potential) in the preferential seepage pathways identify along this structure (Zorzi & Rigoti, 2011). The use of electrical resistivity in the Earth dam located in Cordeirópolis, in the São Paulo state, also showed excellent results for the identification of moisture areas and the preferential seepage pathways through the dam (Camarero & Moreira, 2017).

Most tailings dams accidents occur due to a slow anomalous seepage process through discontinuities inside the center of the dam or at the ends of the abutments. This flow will initiate a progressive erosive process with the occurrence of internal cavities and piping process which may cause a considerable structural alteration to the dam and lead to its total rupture (Abdel et al., 2004).

Another known mechanism that can generate the rupture of a tailings dam is static liquefaction. Inefficient drainage may raise the level of the water table, increasing the pore pressure and significantly reducing the effective stresses of the dam. This increase in internal pressure will result in loss of contact between the solid particles, leading the tailings to a total state of fluidity (Ishihara, 1977).

Geophysical methods are non-invasive and have a great potential of detecting internal erosion and anomalous seepages at in early stage before the safety and integrity of the dam is at stake (Abdel et al., 2004). Electrical resistivity and ground penetrating radar (GPR) were the methods used at the geophysical campaign in the BR dam. After acquisition and processing, subsurface images were generated. Once calibrated, based on direct investigations data, the geophysical data allowed a complete internal spatial evaluation through 2D sections generated along the structure. Subsequently, a complete 3D view was built with electrical resistivity data, where it was possible to separate regions with high moisture content classified as LRZ (low resistivity zone) from dry regions denominated as HRZ (high resistivity zone) and IRZ (intermediary resistivity zone) with low moisture content. Geophysics has also been able to identify bedrock using information from drill holes previously made at the BR dam.

In response to the GPR, saturated zones presented strong attenuation in the reflectors. Therefore, a decrease in the water content represents a low attenuation of the reflectors. Besides, it was possible to correlate patterns of reflectors to different resistive zones in some sections.

BR dam description

The BR dam reservoir, owned by Mosaic Fertilizantes, is located at the Tapira Mining Complex, considered to be the largest phosphate mine in Latin America. Its crest center is located at the coordinates: 308,045E / 7,805,260N, (UTM zone 23S, WGS-84 datum), at 400 km west of the Minas Gerais state, Brazil. Currently it bilks to 98,000,000 m³, and it has a total project capacity of 190,000,000 m³. The dam is 570 m long and its maximum height is 61 m, reached 1200 m quota after the latest heightening (Fig. 1). All heightenings were done by the centre line method, using magnetite in the downstream zone, with mechanical scattering and compaction. The tailings launched upstream from the crest of

BR dam, formed a beach with more than 100 m of length (Mosaic Fertilizantes, 2016) (Fig. 2).

Inspection and monitoring of BR dam are done through direct measurements instruments, called ausculation methods. However, due to the local nature of their measurements, these traditional instruments do not have the capacity to continuously investigate of the interior the structure, and can easily fail to show a weakness areas or regions of unexpected water saturation, being volumetrically un representative of the total mass of the dam.

BR dam foundation

The geology of the region of the Tapira Mining Complex is characterized by Canastra Group rock, represented by phyllites, with intercalations of quartzites and quartz-phyllites. The foundation of the abutments was constituted of clayey colluvium, superimposed to a residual soil of grayish silt-quartzite with presence of mica, whose resistance was considered adequate for the dam structure support. The central region of the massif was characterized by the presence of clayey alluvium of low consistency, that was removed reaching the horizon of residual soil of the silt quartzite (Mosaic Fertilizantes, 2016).

Composition of BR dam

According to 35 drill holes logs, it was possible to observe the presence of four (4) main types of materials in the central BR dam region (Fig. 3), from the base to the top, as follow:

- Residual Soil (SR): Residual horizon of silvery gray to greenish quartzite with presence of mica;

- Colluvium (CO): Clay of reddish-brown color, sometimes with gravel presence, of consistency ranging from soft to rigid in the most upstream sectors;

- Magnetite Tailings (MT): Fine sand to medium magnetite of dark color, from little to medium compact;

- Flotation Tailings (FT): Medium-compact, gray-colored sand-silt flotation tailings.

Ausculation instruments

Currently the monitoring at the BR dam are doing by the conventional instruments installed in the structure. This monitoring is constituted of 1 piezometer, 11 water level indicators (INA), 3 drains indicators of flow, 14 slope drains (in the right and left abutments), 11 superficial marks, 1 ruler in the reservoir, 1 pluviometer and 1 evaporimeter.

Five representative type-sections (B, C, D, E, F), transversal to the BR dam were used as a basic and reference for the interpretation. The sections were distributed as follows: C, D, E in the central region of the dam, F in the right abutment and B in the left abutment. The sections were arranged so that they represented well the main structures of the dam (starting dike, blanket drain and foundations) and crossed most of the INA (Fig. 4). The water level measurements used in the interpretative process correspond to the readings closest to the period of acquisition of the geophysical data (11/13/2017). Table 1 shows the location and respective levels of the readings.

METHODOLOGY EMPLOYED

In this paper, the integration of the two geophysical methods employed was proposed. Both methods provided results through different physical parameters in order to construct a set of data necessary to complement the existing direct ausculation methods.

Data acquisition

According to the objective of this paper, ten (10) parallel and longitudinal geophysical survey lines were made on the main axis of the BR dam (Fig. 5), among which two lines (L01 and L02) were acquired in the tailings beach region, seven lines (L03 to L09) located in the zone of the magnetite massif and abutments and one (L10) complementary line on the left abutment. In total, 4594 m of electrical resistivity sections and 4321 m of ground penetrating radar (GPR) were collected (Tab. 2). The spacing between these lines was variable, 15 m in the region of the massif, executed on the berms, and 25 m in the region of the beach. The ground penetrating radar (GPR) data were collected along the same lines as the electrical resistivity sections, however, some lines did not extend to the abutments due to the topographic difficulty. The L10 section was also collected parallel to the main axis of the BR dam but displaced to the left abutment and with partial overlap to section L07, in this region.

Electrical resistivity

The equipment used in this acquisition was the R8 resistivimeter manufactured by AGI with a 64 channels configuration and 3.0 meters spacing between electrodes, maximum current of 2A and cycle of 2s, reached 49.0 meters depth of investigation.

During the field work, a total of 4594 m of electrical resistivity section were acquired, with the electrodes arranged is Dipole-Dipole array. This arrangement was chosen because it

Figure 1 – Overview of the BR dam.

Contact between the flotation tailings and the magnetite sand.

Beach Material – Flotation tailings, fine sandy.

Dam Body Material – Magnetite sand.

Figure 2 – Main constituents of the BR dam.

generated better signal-to-noise ratio during the initial tests, as well as a satisfactory depth of investigation with a good lateral resolution.

As in practice, most of the geological scenarios cannot be considered as homogeneous, the measured amount of ΔV (potential difference) represents a weighted average of all true resistivities in a subsurface material volume. For the Dipole-Dipole arrangement the apparent resistivity (ρ_a) can be expressed by the equation shown in Figure 6. The Dipole-Dipole array commonly used for deitailed work with the dipole spacing parameter (n) (Dentith & Mudge, 2014).

In this arrangement, several receiving dipoles (MN) arranged along the line can be used simultaneously. Each dipole MN corresponds to a level of investigation Z, as illustrate in the Figure 7.

The theoretical depth at each investigated level is taken as $Z = X_{MN}(n+1)/2$ in meters (Dentith & Mudge, 2014).

The depth of penetration of the electric current in the soil is directly correlated to the length of the electrical resistivity section used, and the resolution will decrease with increasing survey depth and different conductive properties of the studied substrate. The Figure 8 illustrates electrical acquisition on the beach region.

Ground Penetrating Radar (GPR)

Initially several tests were performed, with variations of antenna frequencies, in order to determine the best methodology for the acquisition. Tests were performed on lines L01 and L03 (Fig. 9) with an antenna varying the center frequency of 100, 40 and 80 MHz, all in static mode, using the SIR3000 equipment manufactured by GSSI. The 100 MHz antenna achieved a better

Representative section of the left abutment (LA)

Representative section of the right abutment (RA)

Quartzite residual horizon   Colluvium

Magnetite   Flotation Rejection

Representative section of the central region of the BR dam
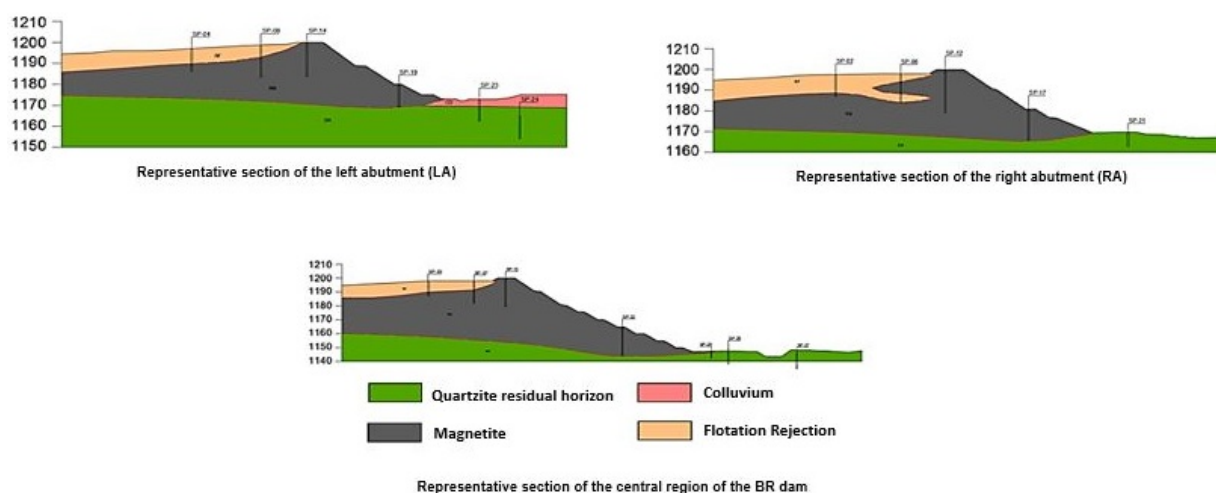
Figure 3 – Main constituents of the BR dam, according to 35 drilling holes.

Table 1 – Location and descriptive aspects of the INA (water level indicators) installed in the BR dam.

Instruments identification	Coordinates		Elevation of the instruments (m)		Length (m)
	North	East	Top	Water level (13/11/17)	
INA 1	7,805,177.755	308,011.379	1,201.238	Dry	36.49
INA 2	7,805,269.943	308,051.092	1,201.162	Dry	41.22
INA 3	7,805,288.220	308,019.059	1,180.280	1,150.32	32.43
INA 4	7,805,293.979	307,995.503	1,170.020	1,149.50	26.92
INA 5	7,805,345.732	308,082.883	1,201.681	1,158.75	43.76
INA 6	7,805,352.500	308,048.448	1,181.680	1,150.36	36.22
INA 7	7,805,367.834	308,026.489	1,170.680	1,149.41	27.37
INA 8	7,805,434.944	308,120.412	1,201.913	Dry	39.76
INA 9	7,805,074.869	307,972.062	1,201.042	1,182.07	20.96

signal-to-noise ratio, thus it was utilized for all GPR surveys. The sampling frequency used was 1000 MHz with 512 samples and intervals of 0.2 meters between traces and dynamic acquisition mode. A 4321 m GPR survey was carried out, parallel to the principal axis of the structure, comprising lines L01 to L10.

During the scanning, the control unit produces and regulates the energy pulses of the radar, which is amplified and transmitted to the subsurface by the antenna. The frequency of the antenna is inversely proportional to the depth reached, which makes the antenna selection the most important step in the survey planning (Desai et al., 2016).

GEOPHYSICAL RESULTS

Electrical resistivity

After processing of the data measured in the field, it was possible to identify zones of high resistivity (HRZ), whose values are above 1,116 ohm-m. Low resistivity zones (LRZ), whose values are below 250 ohm-m and intermediate resistivity zones (IRZ), where the values are between approximately 250 and 1,116 ohm-m (Fig. 10).

In general, in all electrical resistivity sections, the low resistivity zones (LRZ) were delimited to values below 250
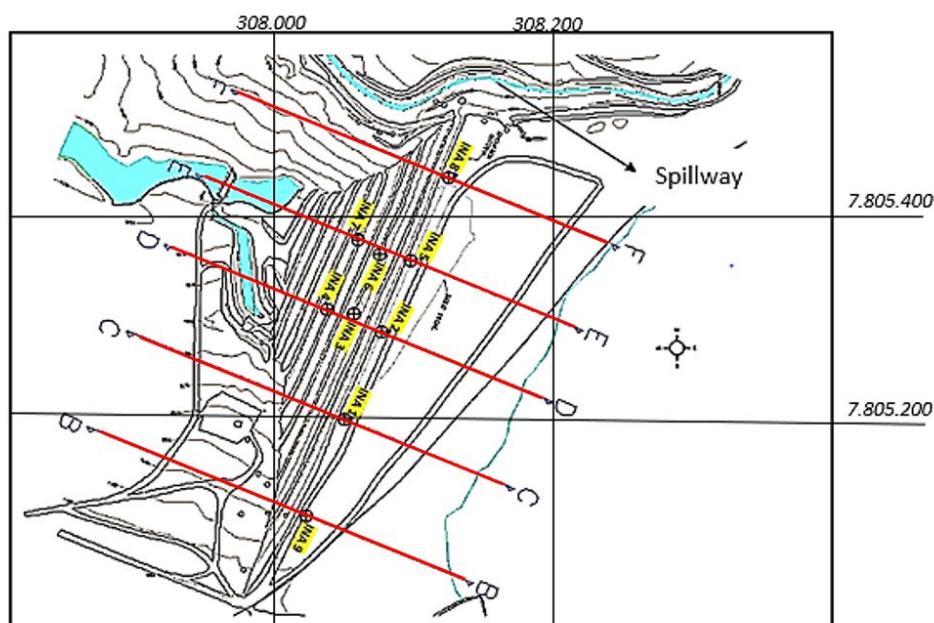
Figure 4 – The five type-sections of the BR dam. The sections positioned so that they crossed as many dam structures and INA (water level indicators) as possible.

Table 2 – Length, in meters, of the geophysical acquisition lines executed at the BR dam.

Lines ID	Electrical Resistivity length (m)	GPR length (m)
L01	585.00	585.00
L02	583.00	583.00
L03	691.00	578.00
L04	479.00	479.00
L05	475.00	475.00
L06	447.00	409.00
L07	516.00	394.00
L08	365.00	365.00
L09	265.00	265.00
L10	188.00	188.00
Total	4594.00	4321.00

ohm-m, can be correlated with regions possibly saturated, or even with a certain moisture content.

For a better understanding of the results, three distinct zones of the BR dam are described separately: central region (massif), left abutment and right abutment.

Central Region

This region is covered by the sections L03 to L09, which showed some common patterns in the responses of resistivity values. After analyzing these sections, it was possible to delimit a surficial
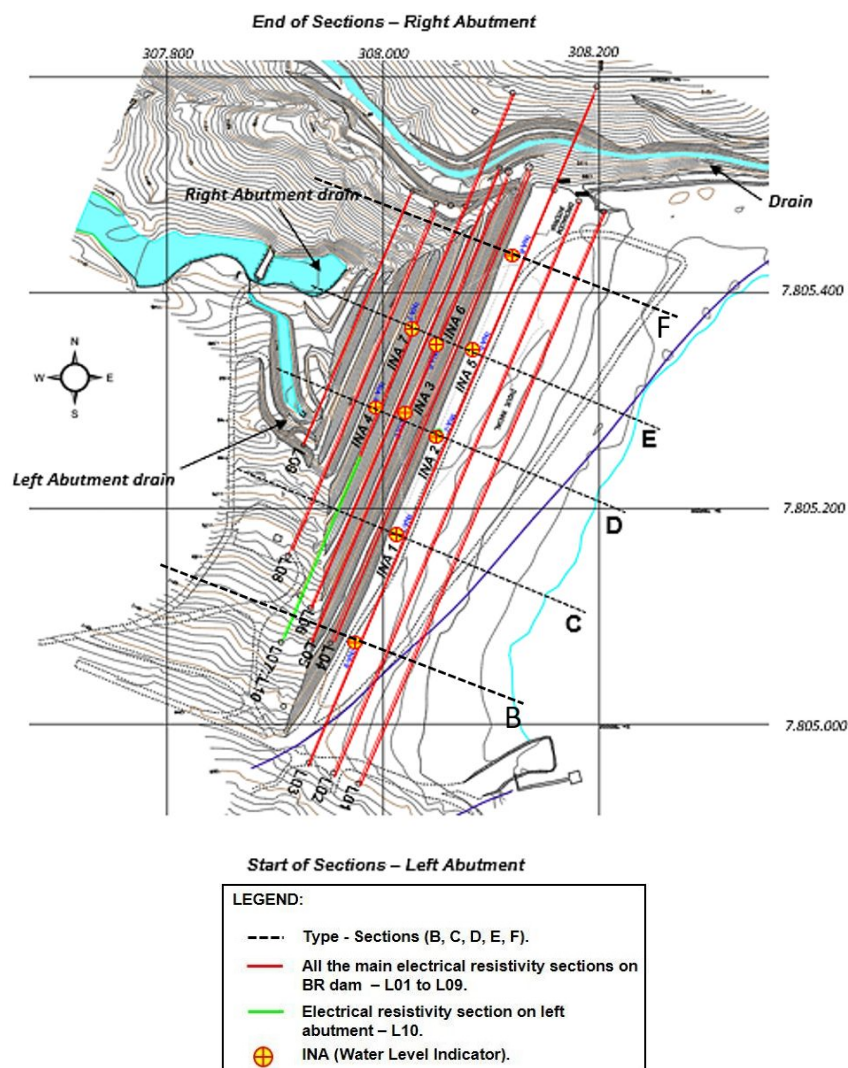
Figure 5 – The ten geophysical acquisition sections surveyed along the BR dam.
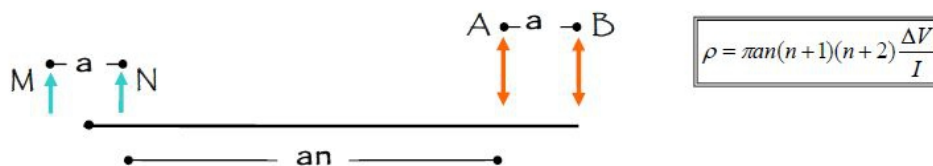
Figure 6 – Formula to calculate the apparent resistivity using the Dipole-Dipole method.

region approximately 3 m thick with intermediate resistivity (IRZ) values (250 to 773 ohm-m). It can be suggested that this horizon is composed of a more sand layer of magnetite where the voids were filled by air and, in smaller amount, by water. This zone is more susceptible to weather effects (precipitation and evaporation).

Below this layer, there is a second zone approximately 6.0 to 7.0 m thick, well delimited, in continuous to moderately continuous form with high resistivity (HRZ) values of 1195 to 3430 ohm-m. Considering that heightening were always made with the same material composed of magnetite, and that according to the data of the SP-09 drill hole, that showed that there
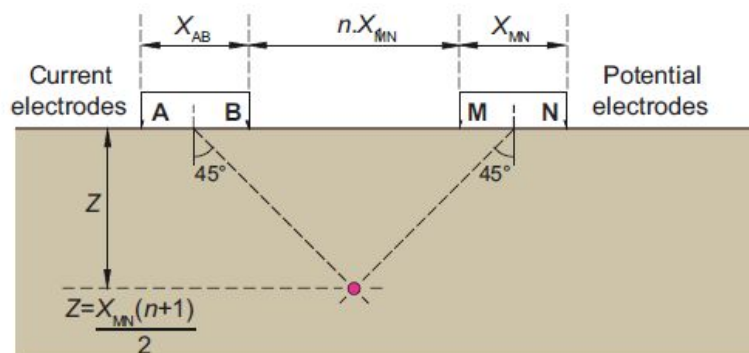
Figure 7 – Electrode configuration in the Dipole-Dipole array arrangement (DDP) (Dentith & Mudge, 2014).
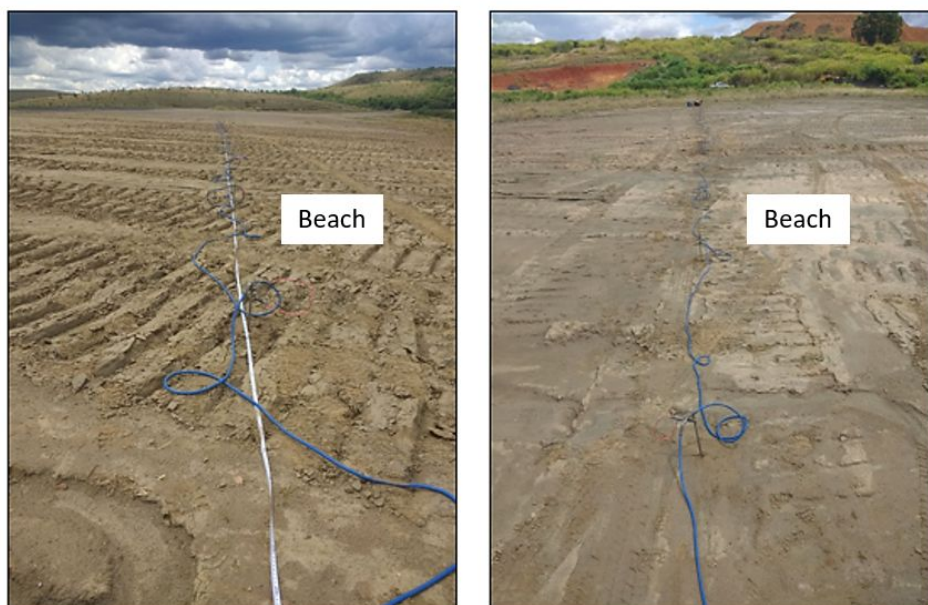
Figure 8 – Electrical survey on the beach region, line L01.

Figure 9 – Acquisition of GPR data at the crest of the BR dam, line L03.
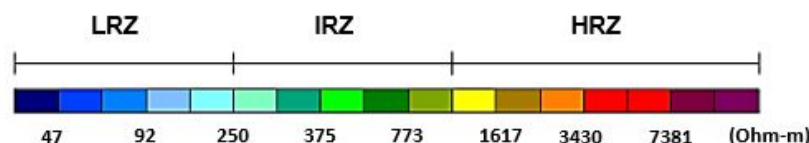
Figure 10 – Scale used for the results of electrical resistivity in ohm-m.

were no changes in this composition, we can interpret that this increase in resistivity values may be related to granulometric differences or different degrees of compaction. Its reflecting directly on the decrease or increase of porosity and permeability and consequently on storage capacity or percolation of water. Lower, there is a transition zone with intermediate (IRZ) of 375 to 1195 ohm-m resistivity values that may be related to a small increase in moisture in the pores, due to its proximity to the zone of low resistivity. Underneath this zone, there is a low resistivity zone (LRZ), marked with values below 250 ohm-m, being associated with high moisture contents (Fig. 11). The top of this anomaly (LRZ) was interpreted as being equivalent to the top of the water table (W.T) and later compared to the INA data and plotted for comparative effect in the type-sections previously used for geotechnical monitoring.

By the positioning of the water table level on L05 in the D type-section, it was possible to observe that the blanket drain was below the top of the conductive anomaly (LRZ). The top of the blanket drain was located at 35 m depth and the top of the water table identified by the electrical resistivity data in this section was 29 m deep, so this draining structure at the time of the geophysical survey showed to be positioned 6 meters below the top of the ZLR. Therefore, this drain structure was drowned in relation to the level of the water table identified by geophysics (Fig. 11).

Analyzing the downstream sections, it was observed an increase in LRZ thickness and a decrease in IRZ and HRZ. The LRZ top elevations become shallower when compared to the upstream sections (Fig. 12).

POSITIONING OF THE WATER TABLE

With the aim of investigating and comparing the direct data provided by the auscultation instruments, it is sought to delimit the level of the water table in the central region of the massif by identifying the of top the anomaly of low resistivity zones (LRZ) on the type-sections (C, D, E) (Fig. 13).

It is important to note that the readings of the water level indicators (INA) present in the type-sections for the central region

of the massif (Section C - INA 1; Section D - INA 2, INA 3 and INA 4; and Section E - INA 5, INA 6 and INA 7), are very close to the data obtained from the electrical resistivity responses on the same site. This fact is corroborated by the correlation of the conductive anomalies top with the water level readings measured by the INA, which are approximately coincident (Fig. 13).

Left Abutment (LA)

The response of the electrical resistivity method in this region are characterized by the presence of a deep gradation of horizons with intermediate to high values (IRZ to HRZ) of resistivity to low values (LRZ) lower. These values of IRZ and HRZ located in the basal part of the left abutment can be interpreted as the residual quartzite soil horizon (2523 to 7381 ohm-m). The low resistivity values (LRZ) underneath to the intermediate to high values may be related to the possible zones of accumulation of water or of sufficient moisture content to generate such conductive anomalies. Other hypothesis may be related to the presence of clayey materials identified in the SP-09 drill hole performed near the L02 section in its initial meters, where the presence of silt was observed at conductive levels (Fig. 14).

It can be observed that the conductive anomaly that appears in a localized form in the left abutment does not seem to have continuity with the central part of the massif, where the position of the water table was defined through the mapping of the LRZ top and confirmed by the geotechnical instruments, through the readings of the INA. Thus, it was not possible to delineate the water table because of the non-continuity of the conductive anomaly to the central part of the massif.

Right Abutment (RA)

In the regions of the geophysical sections near the F type-section, an arrangement of intermediate resistivity zones (IRZ) overlapping with HRZ of greater thickness is noted. The LRZ occur in a punctual way with no continuity to the central region of the
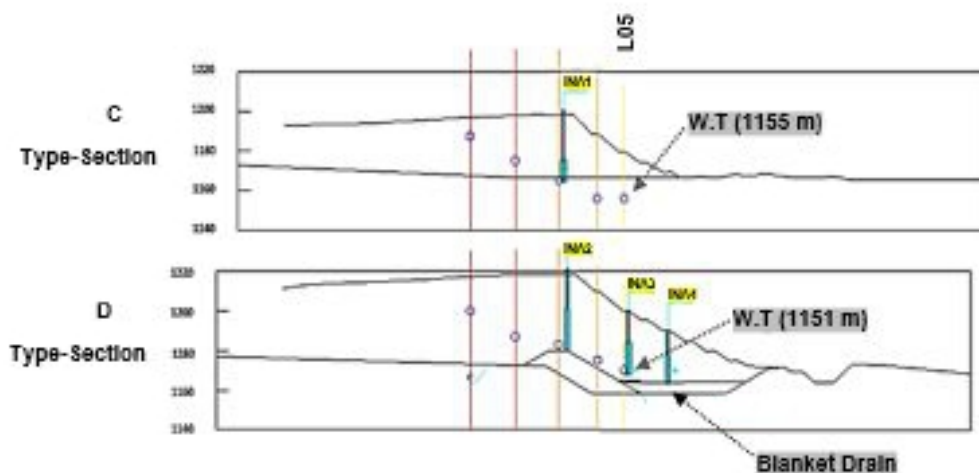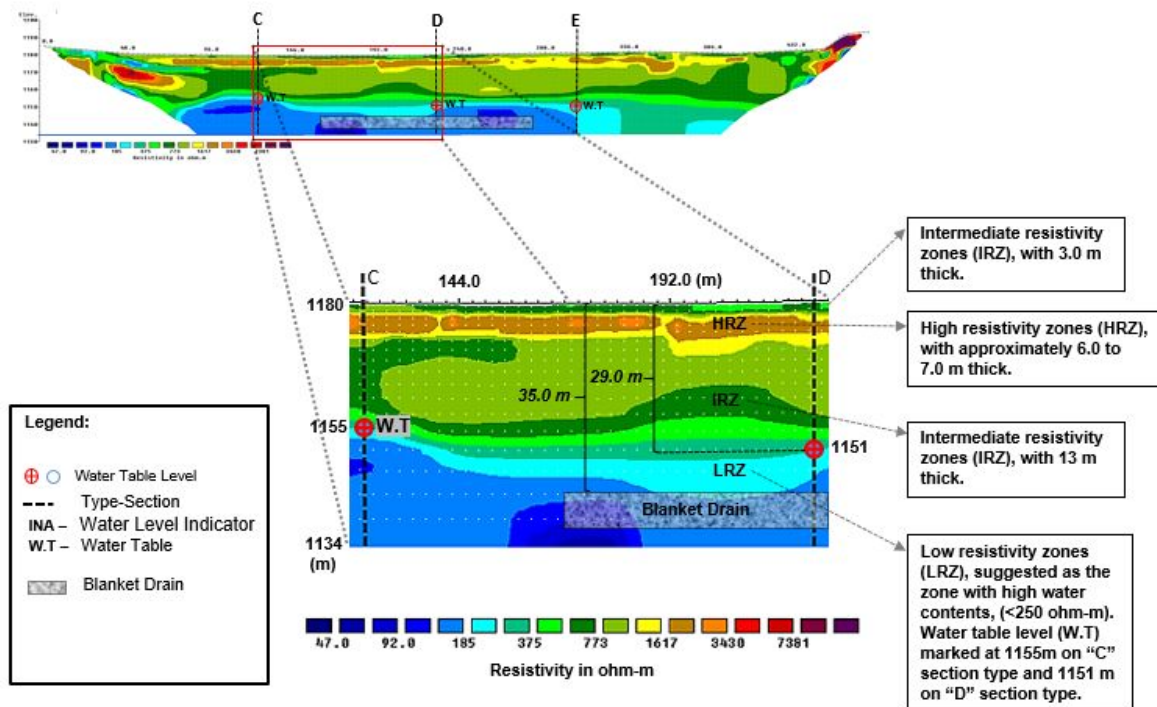
Figure 11 – The L05 section, used as being representative of the central part of the massif, showing the different resistive zones delimited through the results obtained from the electrical resistivity survey. The blanket drain appears to be drowned in 6 m depth in the central part of the massif in relation to the water level elevation in the D type-section. The top of the water table was marked as the top of the zone of low resistivity (< 250 ohm-m).
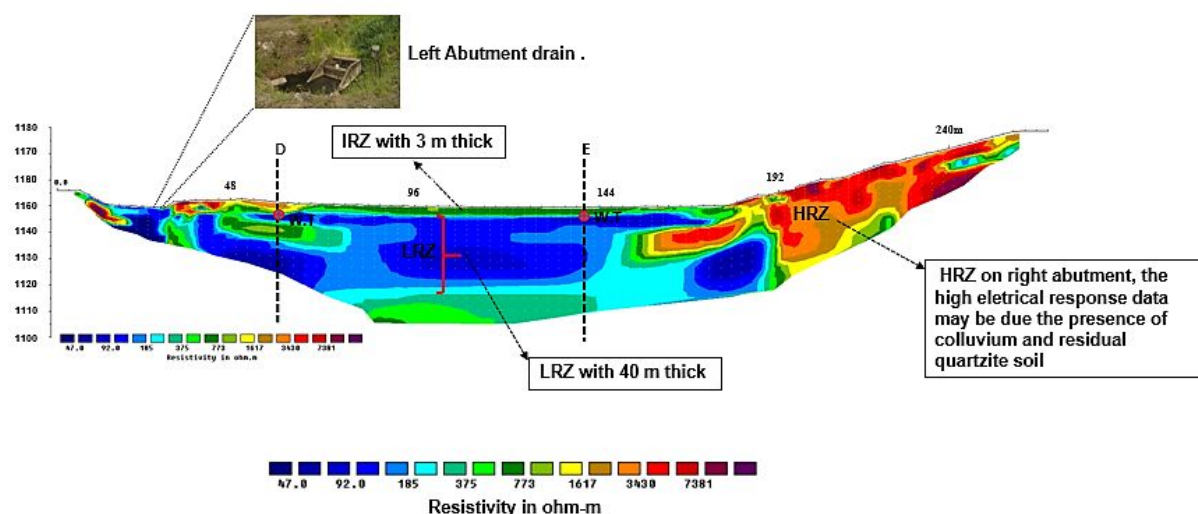
Figure 12 – The L09 section, further downstream, showing the increase of the conductivity anomaly thickness and the shallower dimension of the water table evidenced by the LRZ (<250 ohm-m). The water table levels plotted in sections C and D are 1148 m and 1145 m, respectively. It can be evidenced the increase of the LRZ in subsurface and the reduction of the overlapped IRZ.

massif. Below the LRZ, we again found regions of resistivity with intermediate (IRZ) to high (HRZ) values (Fig. 15).

The occurrence of horizons with high resistivity values suggests the possible presence of foundation materials composed of residual quartzite soil. Such association can be confirmed by drill hole data, which showed the presence of this material in the high resistivity regions (HRZ). Below the spillway region there is a very expressive conductive anomaly possibly resulting from an infiltration into this structure.

GROUND PENETRATING RADAR (GPR)

The GPR interpretation sought to track the patterns and terminations of the reflectors. As well as to map features that could indicate the beginning of internal erosive processes in the BR dam. The GPR geophysical sections reached up to 24 m depth and due to topographical difficulties, it was not possible in some profiles to extend the investigation to the abutments. In the first 2 lines (L01 and L02), a truncation pattern was observed between the reflectors near the abutment's regions (Fig. 16), suggesting a heterogeneity in the arrangement of the flotation tailings released from the crest to upstream. The L03 section, at the crest of the dam until the L09 section, suggested a decrease in the truncation pattern with an increase of the parallelism between the reflectors can be observed.

In these downstream sections a well-marked surface layer, approximately 3.0 m thick, was observed, with a pattern of continuous reflectors, which are generally not very attenuated and

with low amplitude. In addition to this layer, there is a second well-marked layer of approximately 6.0 to 7.0 m thick with a pattern of reflectors of strong contrasts and with larger amplitudes and undulating to wavy ones. Already close to the abutments the reflectors behave in parallel ways and with low amplitudes. An increase in the attenuation of the reflectors with punctual higher contrast passages was observed lower. This third layer may already be suffering from an increase intra-pores moisture due to the direct influence of the region mapped by the electrical resistivity data as the top of the water table of the BR dam.

The L05 section (Fig. 17) was used to exemplify the correlations obtained from GPR and electrical resistivity data. Taking into account that the BR dam massif is composed only of magnetite sand. The different patterns of reflectors that correlate with different distinct electrical zones can be interpreted as:

- Different compaction phases of the embankment;

- Different granulometry of materials of the same composition (magnetite);

- Areas with different moisture content.

CONCLUSION

Applied geophysics contributed significantly to the geotechnical knowledges of the dam, effectively complementing the pre-existing conventional instruments used for the monitoring of the BR dam. Geophysics generated continuous 2D and 3D
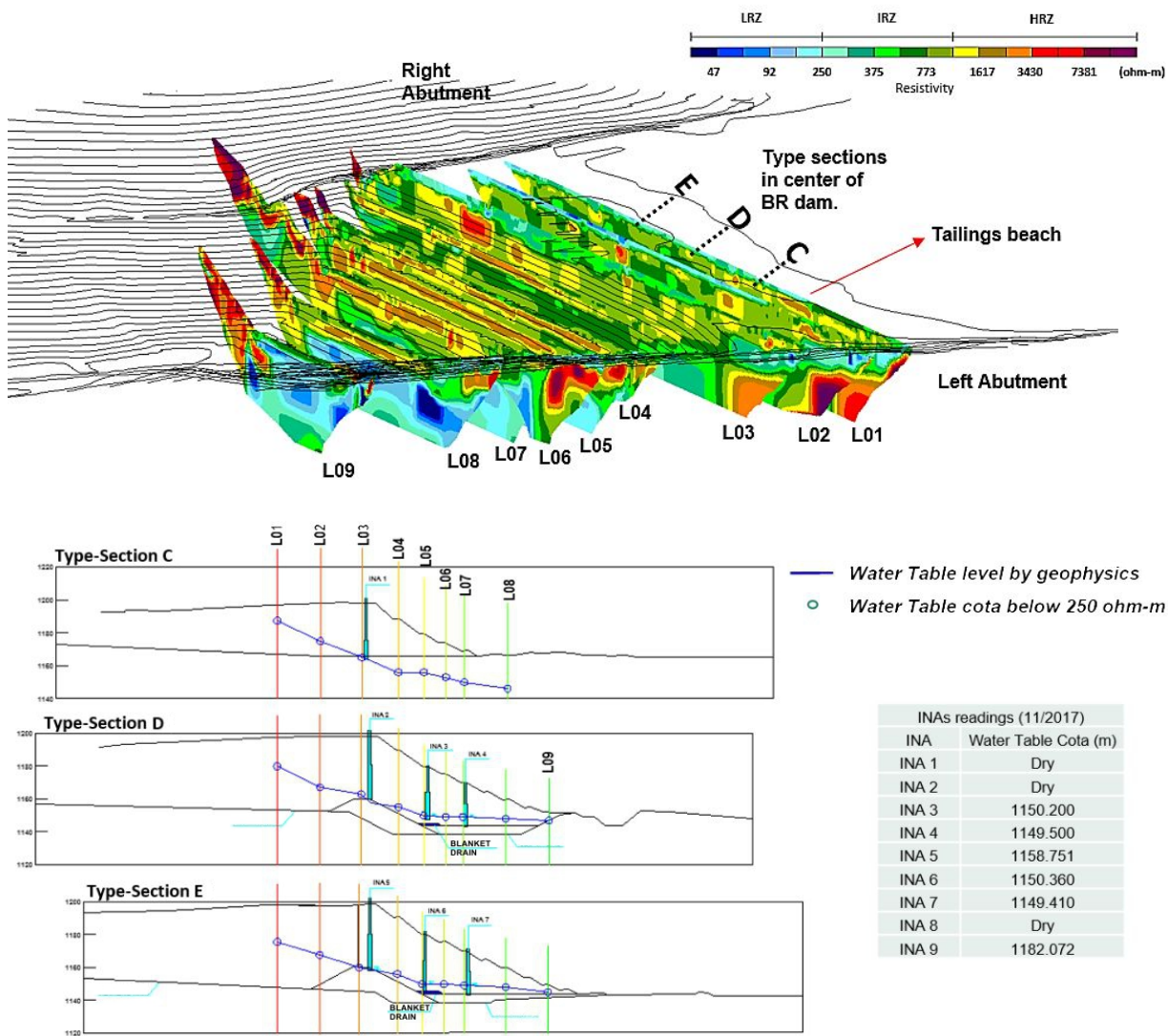
Figure 13 – Electrical survey in 3D (L01 to L09) showing that the position of the water table in the type-sections (C, D and E), inferred by the geophysics in the central region of the BR dam, approximates the position suggested by reading the indicators of the water level (INA).

images of the interior of the dam, where it made a complete imaging along the massif and abutments. Electrical resistivity results showed a good ability to delineate the water table level, internal hydraulic dynamics, local saturations, seepages and was able to identify the main discontinuities of the materials used during the heightening stages. In general, the electrical resistivity method proved to be the one that best identifies dry zones (HRZ) of saturated zones (LRZ) or with some moisture content (IRZ). The resistivity sections showed that the conductive anomalies of the central part of the massif and the abutments do not have

continuity. Thus, it is suggested that there is no evidence on the contribution of flow from the abutments to the central region of the BR dam.

Through the GPR results, it was possible to map different horizons in the BR dam to investigate the appearance of potential internal voids and the different heightening stages. Based on the reflector responses, GPR was able to identify different levels of compaction and the type of materials used. The GPR reflector patterns showed strong attenuation in the moisture zones mapped by electrical resistivity.
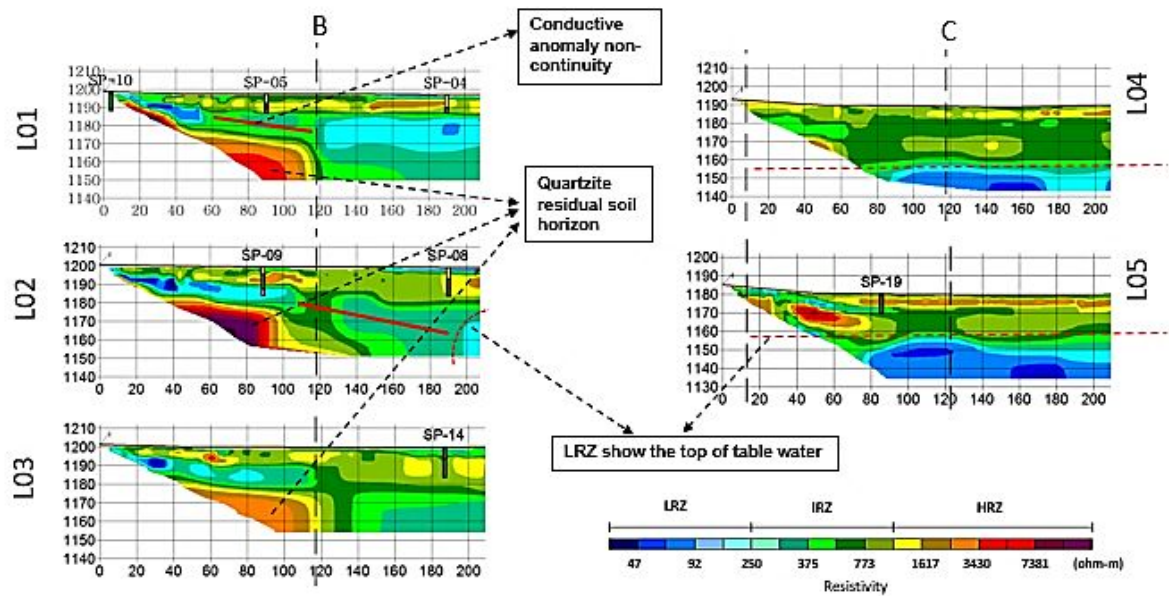
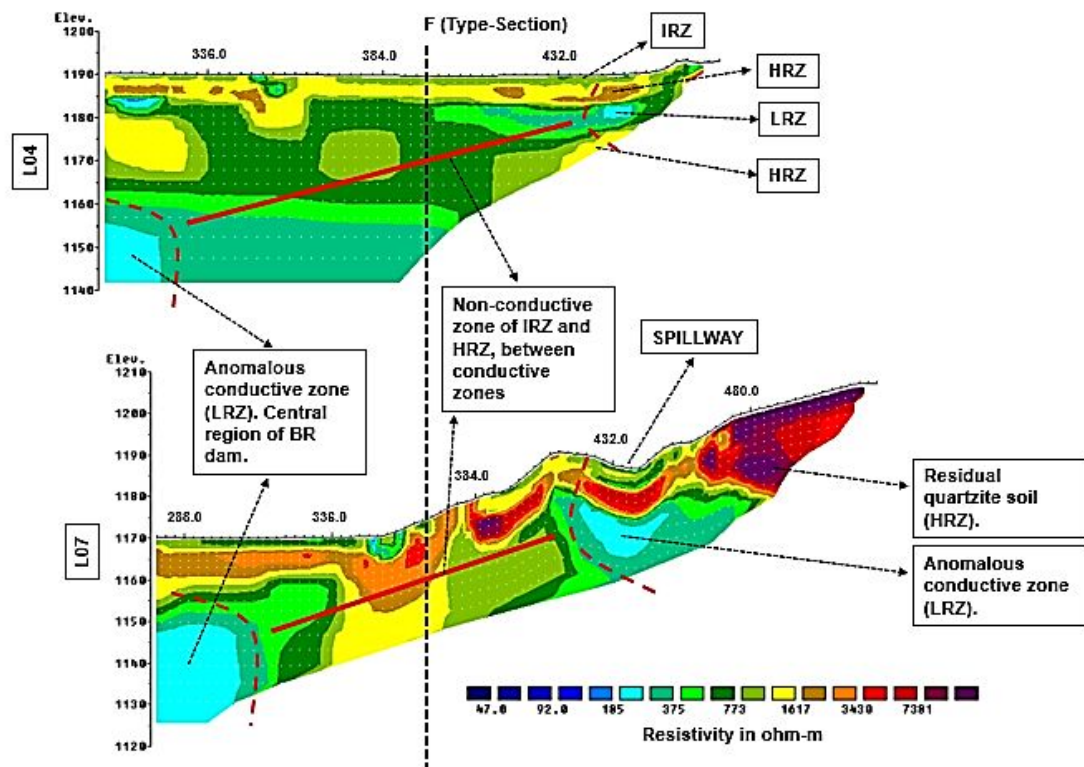**Figure 14** – L01 to L05 sections showing the different zones of resistivity in the left abutment.

Figure 15 – L04 and L07 sections showing the different zones of resistivity in the right abutment.
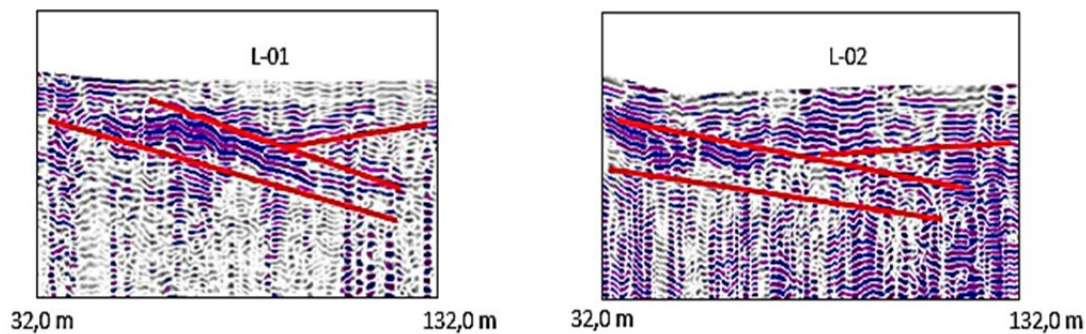
Figure 16 – L01 and L02 sections showing the truncation pattern of the reflectors near the left abutment (LA).
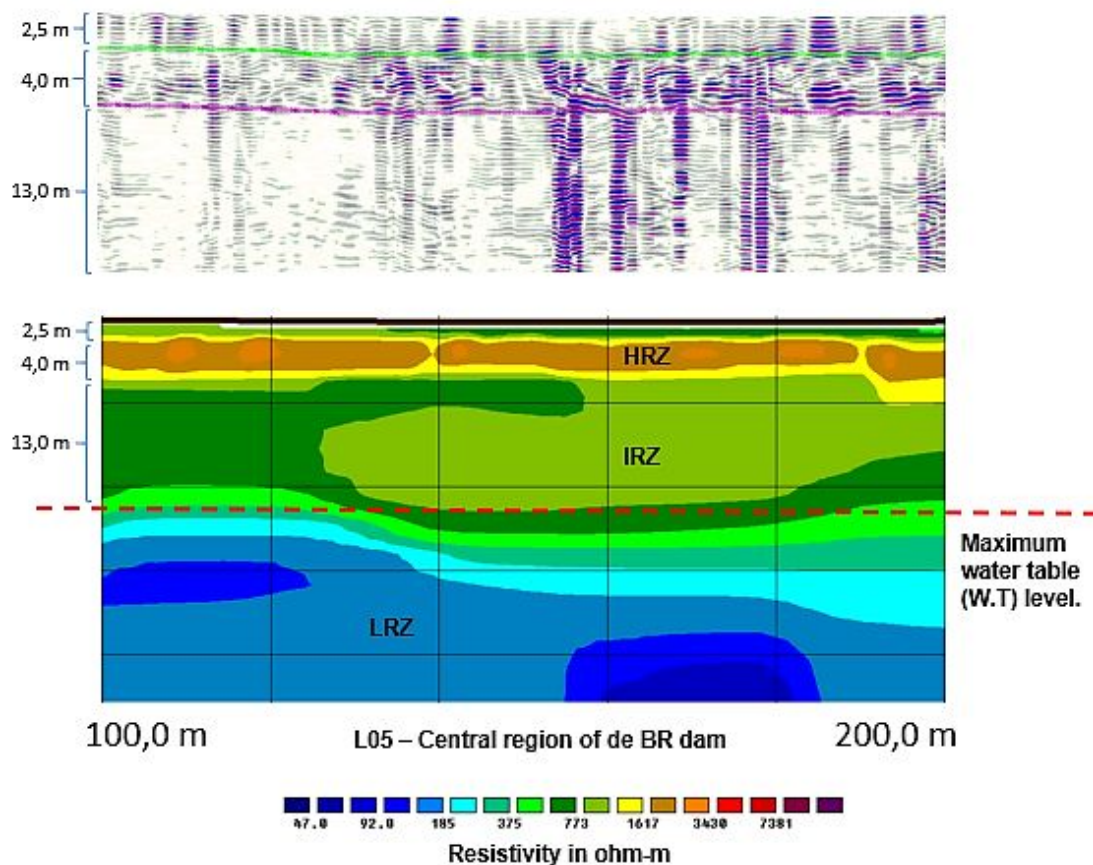

Figure 17 – Excerpt from L05 section showing the correlation between different resistivity zones and reflector patterns.

Finally, it is important to emphasize that the integration of the two geophysical methods is more effective, contributing to the reliability of the acquired results, through the consistency observed between them. Thus, the delimitation of the two groups of reflector patterns described above overlaps satisfactorily with the more superficial levels of the electrical resistivity sections, demonstrating the importance of applying different methods to meet the objective of the present study.

Due to the high risk of accidents involving tailings dams, which could generate enormous social, economic and environmental losses, it is necessary to develop a correct and effective investigation and monitoring method to improve the

safety of the physical and operational integrity of dams in general. This paper shows the efficiency of near surface geophysics as an indispensable complementary tool to conventional geotechnical instruments in the investigation and systematic monitoring of dams.

REFERENCES

ABDEL AAL GZ, ISMAIL AM, ANDERSON NL & ATEKWANA EA. 2003. Geophysical Investigation of Seepage from an Earth Fill Dam, Washington County, MO. In: 3rd International Conference on Infrastructure. Orlando, Florida, USA. 8 pp.

CAMARERO PL & MOREIRA CA. 2017. Geophysical investigation of earth dam using the electrical tomography resistivity technique. *REM - International Engineering Journal*, 70(1): 47-52.

CHINEDU AD & OGAH AJ. 2013. Electrical resistivity imaging of suspected seepage channels in an earthen dam in Zaria, north-western Nigeria. Open Journal of Applied Sciences, 3: 145-154.

DENTITH M & MUDGE ST. 2014. Geophysics for the Mineral Exploration Geoscientist. Cambridge University Press, New York, (5): 438 pp.

DESAI L, JADHA G, SHINDE V & PATIL S. 2016. Ground Penetrating Radar (GPR). Imperial Journal of Interdisciplinary Researcher (IJIR), 13(5): 1508-1511.

ISHIHARA K. 1977. Simple method of analysis for liquefaction of sand deposits during earthquakes. Soils and Foundations, 17(3): 1-17.

MOSAIC FERTILIZANTES. 2016. VAFZ.AL-LT-FTP-103-01. Auditoria técnica de segurança da barragem BR. Relatório de inspeção de segurança regular. Relatório de auditoria técnica de segurança, Complexo de Mineração de Tapira, Brazil. p. 5-8.

NWOKEBUIHE SC, ALOTAIBI AM, ELKRRY A, TORGASHOV EV & ANDERSON NL. 2016. Dam seepage investigation of an earthfill dam in warren County Missouri using geophysical methods. Missouri University of Science and Technology Rolla, Missouri. AIMS Geosciences, 3(1): 1-13.

ZORZI RR & RIGOTI A. 2011. Aplicação de métodos geoelétricos para monitoramento da barragem de concreto da UHE Gov. José Richa. Boletim Paranaense de Geociências, 65: 1-11.

Revista Brasileira de Geofísica

RBGf

Brazilian Journal of Geophysics

COMPARISON OF L2- AND L1-NORM TO PERFORM THE INVERSION OF TRAVEL-TIME CURVES USING NONHYPERBOLIC MULTIPARAMETRIC APPROXIMATIONS WITH UNIMODAL AND MULTIMODAL BEHAVIOR

Nelson Ricardo Coelho Flores Zuniga[1], Fernando Brenha Ribeiro[1] and Viatcheslav Ivanovich Priimenko[2]

ABSTRACT. Many nonhyperbolic multiparametric travel-time approximations were developed in the last decades. As the seismic inversion became more popular, there were studies concerning the objective function of this kind of equations. Many of these approximations have a unimodal behavior where there is only the global minimum region while others have a multimodal statistical distribution with the global minimum region and one or more local minimum regions. However, two approximations showed both unimodal and multimodal behaviors to vary depending on the model. As the variation of the model generates only subtle distortions concerning the topology of the objective function, a method which can make this topology more abrupt is a solution to perform a more effective inversion. This kind of information can be reached using the L1-norm rather than the L2-norm, and with the comparison of the two norms for both reflection events (PP and PS) of the model and both approximations, it is possible to understand which kind of improvement it brings concerning the complexity and accuracy analysis.

Keywords: objective function, nonhyperbolicity, probability distribution.

RESUMO. Várias aproximações não-hiperbólicas multiparamétricas de tempos de trânsito foram desenvolvidas nas últimas décadas. Com a inversão sísmica se tornando cada vez mais popular, houve estudos relacionados à função objetivo desse tipo de equação. Muitas dessas aproximações apresentam um comportamento unimodal, onde há apenas uma região de mínimo global, enquanto outras apresentam uma distribuição estatística multimodal, com a região de mínimo global e uma ou mais regiões de mínimos locais. Entretanto, duas aproximações mostraram ambos os comportamentos, unimodal e multimodal, variando a depender do modelo. Como a variação do modelo gera apenas distorções sutis com relação à topologia da função objetivo, um método no qual é capaz de tornar a topologia mais abrupta é uma forma de realizar a inversão com maior efetividade. Este tipo de informação pode ser obtido usando a norma L1 ao invés da norma L2, e com a comparação das duas normas para ambos os eventos de reflexão (PP e PS) do modelo e para ambas as aproximações, é possível entender qual tipo de melhoria é alcançada com relação à análise de complexidade e de precisão.

Palavras-chave: função objetivo, não-hiperbolicidade, distribuição probabilística.

[1]Universidade de São Paulo, Instituto de Astronomia, Geofísica e Ciências Atmosféricas (IAG-USP), Departamento de Geofísica, Rua do Matão, 1226 - Butantã, 05508-090, São Paulo, SP, Brazil – E-mails: nelson.zuniga@iag.usp.br, fernando.brenha@iag.usp.br

[2]Universidade Estadual do Norte Fluminense Darcy Ribeiro, Laboratório de Engenharia e Exploração de Petróleo (LENEP-UENF), Av. Brennand, s/n, Rod. Amaral Peixoto, km 163, Imboassica, Macaé, 27925-535 Rio de Janeiro, RJ, Brazil – E-mail: slava@lenep.uenf.br

INTRODUCTION

Concerning the large offsets with layered media, the converted PS waves and OBN (Ocean Bottom Nodes) data, there is a significant challenge during the velocity analysis step, once these three characteristics increase the nonhyperbolicity. For this reason, there were developed many nonhyperbolic approximations to deal with many causes of the nonhyperbolicity (*e.g.* Malovichko, 1978; Muir & Dellinger, 1985; Alkhalifah & Tsvankin, 1995; Li & Yuan, 2001; Ursin & Stovas, 2006; Blias, 2009).

In recent works (Zuniga et al, 2015, 2016a, 2016b, 2017; Zuniga, 2017), the objective function analysis was used to understand the complexity of these approximations, and helps to understand their behavior during the inversion procedure. Some approximations presented a unimodal statistical distribution (*e.g.* Malovichko, 1978; Alkhalifah & Tsvankin, 1995) due to their simplicity, while other approximations showed a multimodal behavior (*e.g.* Muir & Dellinger, 1985; Li & Yuan, 2001; Ursin & Stovas, 2006; Blias, 2009). However, the approximations proposed by Ursin & Stovas (2006) and Blias (2009) presented both unimodal and multimodal behaviors, varying according the model, as observed by Zuniga et al. (2018). More tests were performed for deep-water models and showed very well results concerning a better accuracy and lower processing time (Zuniga et al, 2019).

Since there is a substantial range of models in the thresholds of the statistical distribution behaviors, it is difficult to define in which kind of model these approximations must be considered unimodal or multimodal. Thus, to consider these two approximations always unimodal, it is necessary to find a way in which it is possible to make a topology of the objective function less complex. Therefore, it must be simpler enough to suppress the local minimum regions and the more subtle features.

To perform this kind of enhance, it shall be used the L1-nom rather than the L2-norm. The L2-norm, also known as the least squares, makes a more delineated objective function topology due to it minimizing the sum of the square of the difference between the targeted value and the calculated value. Otherwise, the least absolute deviation (L1-norm) minimizes the error between the observed and the calculated value (Khaleelulla, 1982; Bourbaki, 1987).

So, with the Model defined and its travel-time curves generated as a direct problem, it is possible to perform the minimization between the calculated curves with the two approximations and the observed curves. The objective function can be analyzed by a residual function map where it is possible

to study its topological structure. Therefore, for the Ursin & Stovas (2006) and Blias (2009) approximations and for both conventional and converted wave events, it is possible to test the L2-norm and the L1-norm, and find out the differences between them, and define if it is more suitable to work with L1-norm for this kind of travel-time approximation.

MODEL

The Model studied here (Table 1), is an offshore layered model, based on a Campos Basin reservoir with a sandstone reservoir (V_P = 2952 m/s and V_S = 1593 m/s) beneath the 5th layer (the shale sealing layer).

The soft increase of the P-wave and S-wave velocities can be easier observed with the velocities profile (Fig. 1). With the parameters of the Model it is possible to produce the ray tracing and extract the travel-time curves of the events PP and PS (Margrave, 2000 and 2003; Thorbecke & Draganov, 2012), as it can be observed in Figure 2.

Table 1 – The parameters of the Model: Layer thickness (Δz), P-wave velocity (V_P), S-wave velocity (V_S) and V_P/V_S ratio.

| Layer	Δz(m)	V_P (m/s)	V_S (m/s)	V_P/V_S
Water	1052	1500	0	-
1	298	1930	643	3.00
2	559	2127	1134	1.88
3	311	2357	1202	1.96
4	161	2554	1390	1.84
5	77	2733	1403	1.95

The nonhyperbolic multiparametric travel-time approximations with multimodal and unimodal behavior

The approximation developed by Ursin & Stovas (2006) uses the heterogeneity parameter S also used by Malovichko (1978) for the shifted hyperbola which were adapted from the hyperbola equation proposed by Dix (1955). However, for this approximation (Eq. 1), the authors proposed that the S parameter is expressed in a quasi-acoustic case, as a function of the Thomsen anisotropic parameters (Thomsen, 1986).

$$t = \sqrt{t_0^2 + \frac{x^2}{v^2} - \frac{(S-1)x^4}{4v^4\left(t_0^2 + \frac{(S-1)}{2}\frac{x^2}{v^2}\right)}} \tag{1}$$
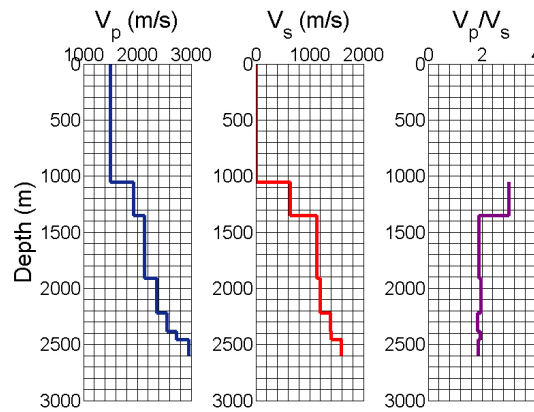
Figure 1 – P-wave velocity (V_P), S-wave velocity (V_S) and V_P/V_S ratio profiles of the Model.
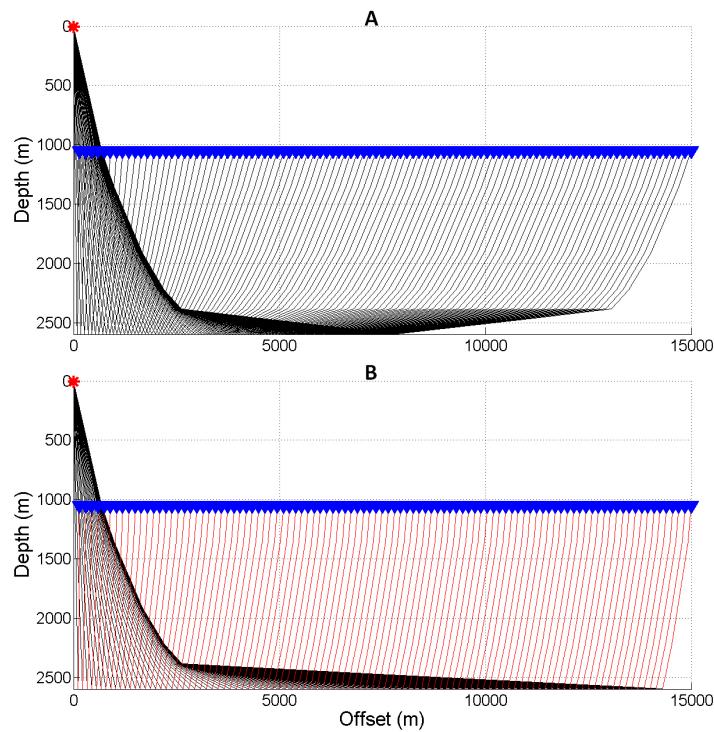
Figure 2 – Ray tracing of the (A) PP wave reflection event and (B) PS wave reflection event of the Model.

The S parameter depends on the μ_4 and μ_2 by the relation $S = \mu_4/\mu_2^2$, where $\mu_j(j = 2, 4)$ is the j-th velocity momentum (Eq. 2).

$$\mu_j = \sum_{k=1}^{n} t_k v_k^j / \sum_{k=1}^{n} t_k \qquad (2)$$

and v_k is the interval velocity of the k-th layer and t_k is the travel-time of the k-th layer.

Blias (2009) proposed an approximation (Eq. 3) which also uses the heterogeneity parameter S, proposed by Malovichko (1978). Different than the Equation 1, this approximation was developed performing several numerical tests related to the walkway vertical seismic profile (VSP).

$$t = \frac{1}{2}\sqrt{t_0^2 + \frac{1-\sqrt{S-1}}{v^2}x^2} + \frac{1}{2}\sqrt{t_0^2 + \frac{1+\sqrt{S-1}}{v^2}x^2} \qquad (3)$$

Once both approximations showed both statistical distributions in previous works, they must be tested concerning the L1-norm to observe if they behave sufficiently better than the L2-norm aiming to suppress the local minimum region.

Complexity analysis of the objective function for L2- and L1-norm

The complexity analysis by the observation of residual function maps (RFM) is necessary to understand the complexity of the topology of the objective function (Larsen, 1999; Kurt, 2007). The RFM shows the relation between the additional parameter (the S parameter in this case) with the velocity of the event, while the third dimension of the hyperplane represents the values of minimum. As the t_0 is the less sensible variable, it was fixed as constant after the recovering of the parameters during the inversion.

A norm is the total length of a set of vectors in a vector space or the total size of a set of matrices in a matrix space. The norm is a function which assigns a strictly positive length to each vector in a vector space, or a positive size to each matrix in a matrix space, being not valid to zero vector or zero matrix (Khaleelulla, 1982; Bourbaki, 1987). The L2-norm also known as least squares method sums the square of the difference between the observed value and the estimated one (Eq. 3).

$$R^2 = \sum_{j=1}^{n} \left(t_{jobs} - t_{jest} \right)^2 \qquad (4)$$

On the other hand, the L1-norm, known as least absolute deviation aims to minimize the sum of the absolute difference between the observed value and the estimated one (Eq. 4).

$$R = \sum_{j=1}^{n} \left| t_{jobs} - t_{jest} \right| \qquad (5)$$

Where R is the error between the observed and estimated value, t_{jobs} and t_{jest} are, respectively, the observed and the estimated travel-time for a value j-th.

In this work, the focus is to observe the variation of behavior between L2- and L1-norm for each reflection travel-time event (PP and PS) with the selected approximation.

It is possible to observe for each approximation and each event whether the use of L1-norm affects the statistical distribution concerning the objective function by analyzing the variation of behavior between L2- and L1-norm for each reflection event and for each approximation.

The RFM applied to both norms provides information to have a deeper understanding concerning the optimization algorithm (global or local search) that should be used for this kind of problem.

It can be observed in Figure 3A, that for the PP wave reflection event the topology of the objective function has some features that cannot be observed in Figure 3B, with the approximation proposed by Ursin & Stovas (2006). As these subtle features are suppressed by the use of the L1-norm, the Figure 3B showed a unimodal behavior, and a narrower global minimum region, with a more abrupt behavior of the topology of the objective function.

For the converted wave event, also for the Ursin & Stovas (2006) approximation, it is possible to observe the same kind of variation when the L1-norm is applied. Before (Fig. 4A), it is clearly observed a global and a local minimum region, while in the Figure 4B, it is shown a unimodal behavior with the local minimum region completely suppressed, a narrower global minimum region and a little more abrupt topological structure.

For the approximation proposed by Blias (2009), it is possible to observe a more complex topology than the one proposed by Ursin & Stovas (2006). However, the same behaviors were observed. In the conventional reflection event, the Figure 5B showed a narrower global minimum region than the Figure 5A, with no local minimum region and with a little more abrupt structure.

As a similar behavior of the Figure 5, the Figure 6B showed a full suppression of the local minimum region and a narrower global minimum region. However, the variation of the abruptness is more intense in this case.

## Residual travel-time comparison and accuracy analysis

The comparison of nonhyperbolic approximations are being performed since the beginning of the decade (Aleixo & Schleicher, 2010; Golikov & Stovas, 2012). However, there is no works comparing the accuracy of nonhyperbolic travel-time approximations between the L2- and L1-norm.

The accuracy analysis is performed by comparing the calculated curve to the observed curve. After the calculated curve fits to the observed one, it is analyzed the error between them.

After perform the inversion, with the parameters recovered, it is possible to observe the relative travel-time errors. In Figure 7A, it is possible to observe for the conventional PP reflection event, that both approximations showed more accurate results with the L1-norm than with the L2-norm. The same observation can be done in Figure 7B; the L1-norm presents more accurate results than the L2-norm. However, in Figure 7B,
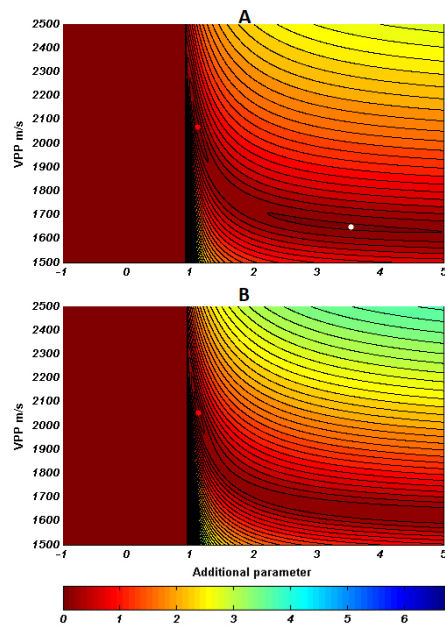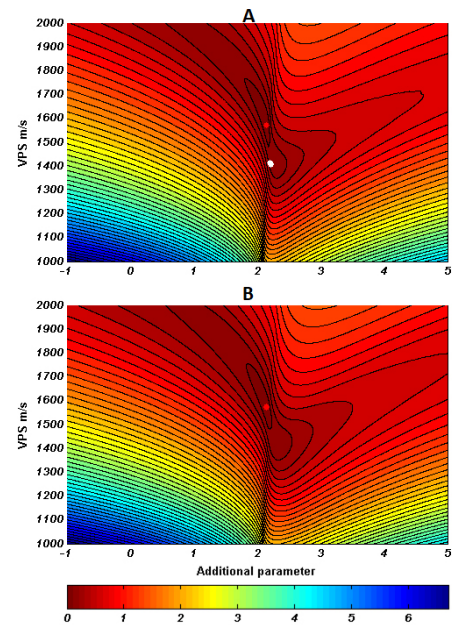
Figure 3 – Residual function maps to demonstrate the complexity of the approximation proposed by Ursin & Stovas (2006) for the PP wave reflection event with (A) L2-norm and (B) L1-norm. Red dispersions represent the global minimum region and the white dispersions represent the local minimum region.
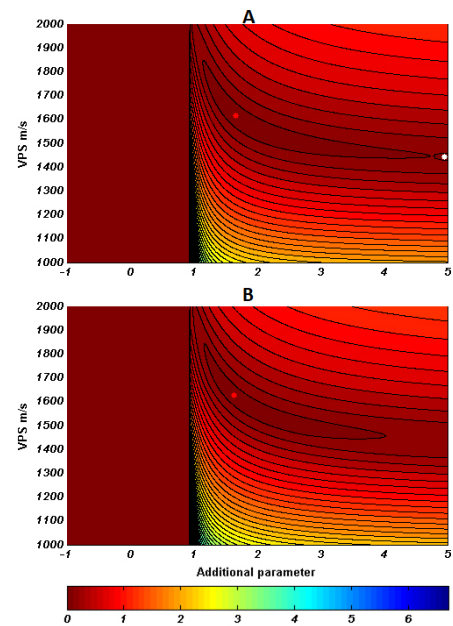

Figure 4 – Residual function maps to demonstrate the complexity of the approximation proposed by Ursin & Stovas (2006) for the PS wave reflection event with (A) L2-norm and (B) L1-norm. Red dispersions represent the global minimum region and the white dispersions represent the local minimum region.
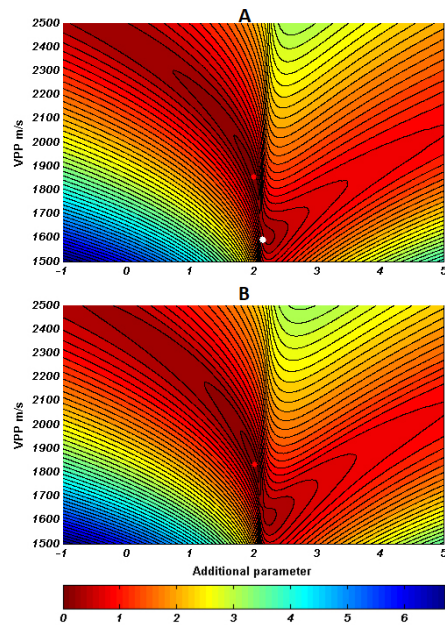
Figure 5 – Residual function maps to demonstrate the complexity of the approximation proposed by Blias (2009) for the PP wave reflection event with (A) L2-norm and (B) L1-norm. Red dispersions represent the global minimum region and the white dispersions represent the local minimum region.

Figure 6 – Residual function maps to demonstrate the complexity of the approximation proposed by Blias (2009) for the PS wave reflection event with (A) L2-norm and (B) L1-norm. Red dispersions represent the global minimum region and the white dispersions represent the local minimum region.
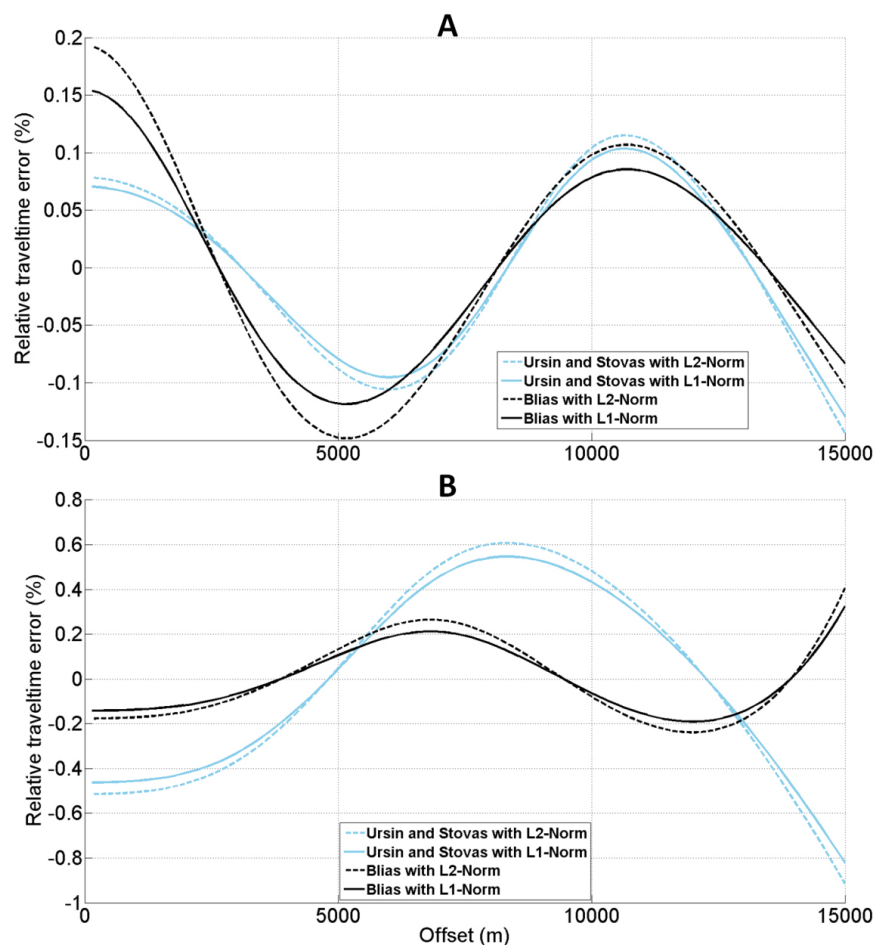
Figure 7 – Relative errors in travel-time between the observed curve and the calculated curve with each approximation and each norm for (A) PP wave reflection event and (B) PS wave reflection event. Data for Ursin & Stovas (2006) and Blias (2009).

the approximation proposed by Blias (2009) presented a much more accurate with both norms than the results shown by Ursin & Stovas (2006) approximation.

CONCLUSIONS

In all conditions tested in this work, there was an improvement in using the L1-norm rather than the L2-norm. For both reflection events and both approximations, the L1-norm showed a narrower global minimum region and a more abrupt structure of the objective function with no local minimum region.

The accuracy also increased for both nonhyperbolic approximations and for both reflection events when the L1-norm is used, what shows that even if there was no suppression of the local minimum region it would still bring a enhance in the results,

once a narrower global minimum region results in a lower relative travel-time error.

Due to these results, the use of L1-norm clearly is a reliable method to simplify the topology of the objective function of this kind of travel-time approximations and also reach a more accurate global minimum value.

ACKNOWLEDGEMENTS

REFERENCES

ALEIXO R & SCHLEICHER J. 2010. Traveltime approximations for q-P waves in vertical transversely isotropy media. Geophysical Prospecting, 58: 191-201.

ALKHALIFAH T & TSVANKIN I.1995. Velocity analysis for transversely isotropic Media. Geophysics, 60: 1550-1566.

BLIAS E. 2009. Long-offset NMO approximations for a layered VTI model: Model study. In: 79th Annual International Meeting. Houston, Texas. Society of Exploration Geophysics, Expanded Abstract, p. 3745-3749.

BOURBAKI N. 1987. Topological vector spaces. Berlin, Springer-Verlag Berlin and Heidelberg, 362 pp.

DIX CH. 1955. Seismic velocities from surface measurements. Geophysics, 20: 68-86.

GOLIKOV P & STOVAS A. 2012. Accuracy comparison of nonhyperbolic moveout approximations for qP-waves in VTI media. Journal of Geophysics and Engineering, 9: 428–432.

KHALEELULLA SM. 1982. Counterexamples in topological vector spaces. 2nd ed, Berlin, Springer-Verlag Berlin and Heidelberg, 184 pp.

KURT H. 2007. Joint inversion of AVA data for elastic parameters by bootstrapping. Computers & Geosciences, 33(3): 367-382.

LARSEN JA. 1999. AVO Inversion by Simultaneous P-P and P-S Inversion. M.Sc. Thesis, University of Calgary, Department of Geology and Geophysics, Calgary, Canada. 124 pp.

LI XY & YUAN J. 2001. Converted wave imaging in inhomogeneous, anisotropic media: Part I. Parameter estimation. In: 63rd EAGE Conference. Expanded Abstract, Amsterdam, the Netherlands. v. 1, p. 109.

MALOVICHKO AA. 1978. A new representation of the traveltime curve of reflected waves in horizontally layered media. Applied Geophysics (in Russian), 91(1): 47-53.

MARGRAVE GF. 2000. New seismic modelling facilities in Matlab. CREWES Research Report, 12: 45pp.

MARGRAVE GF. 2003. Numerical methods of exploration seismology with algorithms in MATLAB. CREWES Research Report, 219pp.

MUIR F & DELLINGER J. 1985. A practical anisotropic system. In: SEP-44. Stanford Exploration Project, p. 55-58.

THOMSEN L. 1986. Weak elastic anisotropy. Geophysics, 51: 1954-1966.

THORBECKE JW & DRAGANOV D. 2012. Finite-difference modeling experiment for seismic interferometry. Geophysics, 76: H1-H18.

URSIN B & STOVAS A. 2006. Traveltime approximations for a layered transversely isotropic medium. Geophysics, 71: 23-33.

ZUNIGA NRCF. 2017. Análise comparativa de aproximações não-hiperbólicas dos tempos de trânsito de dados sísmicos multicomponente utilizando tecnologia OBN. Master Dissertation, Universidade de São Paulo, SP, Brazil. 86 pp.

ZUNIGA NRCF, BOKHONOK O & DIOGO LA. 2015. Comparison of nonhyperbolic travel-time approximations for multicomponent seismic data. In: 14th SBGf Congress. Expanded Abstract, Rio de Janeiro, RJ, Brazil. p. 1176-1181.

ZUNIGA NRCF, MOLINA EC & PRADO RL. 2016a. Inversion of multicomponent seismic data for VTI medium using the globalized Nelder-Mead optimization algorithm. In: 3rd EAGE/SBGf Workshop. Expanded Abstract. Rio de Janeiro, RJ, Brazil.

ZUNIGA NRCF, MOLINA EC & PRADO RL. 2016b. Inversion of multicomponent seismic data of the Santos Basin. In: Far East Hydrocarbons. Russia, EAGE. Expanded Abstract.

ZUNIGA NRCF, MOLINA EC & PRADO RL. 2017. Comparison of travel-time approximations for unconventional reservoirs from Santos Basin, Brazil. Brazilian Journal of Geophysics, 35(4): 273-286.

ZUNIGA NRCF, RIBEIRO FB & PRIIMENKO VI. 2018. Relation between the model and the topography of the objective function in a velocity analysis using a nonhyperbolic multicomponent travel-time approximation. Brazilian Journal of Geophysics, 36(4): 375-384.

ZUNIGA NRCF, RIBEIRO FB & PRIIMENKO VI. 2019. L2- and L1-norm applied to inversion of nonhyperbolic travel-time. Brazilian Journal of Geophysics, 37(2): 155-161.

Revista Brasileira de Geofísica

RBGf

Brazilian Journal of Geophysics

HYDROGEOPHYSICS IN FRACTURED CRYSTALLINE AQUIFERS IN ENGLISH GUYANA

Gerlane Cavalcante Messias[1], Jose Agnelo Soares[2], Felipe Kipper[1], Igor Fernandes Gomes[3],
Vandir Pereira Soares Júnior[1] and Jefferson Fidélis Alves da Silva[1]

ABSTRACT. This work is a case study in English Guyana with the goal of finding groundwater in rock layers with fracture-controlled porosity using electrical resistivity imaging. This work was carried out in two phases by the Brazilian Army, in eight communities in the region of Alto Tacutu – Alto Essequibo in southeast Guyana. All work was done in accordance with a technical agreement between Brazil and Guyana. In the first phase, the surveys were completed by the team which collected resistivity data using a SuperSting R8 electrical resistivity meter with dipole-dipole and dipole-gradient arrays. Then the software EarthImager was used to analyze the data and create two-dimensional (2D) pseudo-sections with depths up to 70 m. In the second phase, eight wells were drilled in areas of low resistivity. The geology of this region consists of Precambrian granite rock layers with varying levels of fracturing. In this way, the effectiveness of the multielectrode resistivity imaging technique was demonstrated as a way to explore the availability of groundwater in crystalline rock formations with fracture-controlled porosity.

Keywords: electrical resistivity imaging, well siting, groundwater.

RESUMO. Este trabalho se constitui em um estudo de caso na Guiana Inglesa, com o objetivo de encontrar água subterrânea por meio de levantamentos de resistividade elétrica, nas áreas de porosidade controladas pelas zonas de fraturas. O trabalho foi realizado em duas fases pelo Exército Brasileiro em oito comunidades da região do Alto Tacutu – Alto Essequibo no sudeste da Guiana Inglesa, através de um acordo de cooperação técnica entre o Brasil e a Guiana. Na primeira fase, os levantamentos foram feitos por uma equipe que coletou dados de resistividade usando um eletrorresistivímetro SuperSting R8 com arranjos dos tipos dipolo-dipolo e dipolo gradiente. Em seguida foi utilizado o *software* EarthImager para analisar os dados e criar pseudoseções de duas dimensões (2D) até 70 m de profundidade. Na segunda fase, oito poços foram perfurados em pontos de baixa resistividade. A geologia da região é constituída de rochas graníticas Pré-cambrianas com níveis variados de fraturamento. Desse modo, demonstrou-se a efetividade do método de resistividade elétrica multieletrodo para explorar a disponibilidade de água subterrânea em aquíferos fraturados em terrenos cristalinos.

Palavras-chave: imageamento de resistividade elétrica, locação de poços, água subterrânea.

[1]Exército Brasileiro, Brasília, DF, Brazil – E-mails: gerlanec@hotmail.com, felipekippergeo@gmail.com, vandir.junior@eb.mil.br, fidelisilva1976@gmail.com
[2]Universidade Federal de Campina Grande - UFCG, Campina Grande, PB, Brazil – E-mail: agnelo.soares@ufcg.edu.br
[3]Universidade Federal de Pernambuco - UFPE, Recife, PE, Brazil – E-mail: gomes@ufpe.br

INTRODUCTION

The electrical methods of underground research (Telford et al., 1976; Kearey et al., 2009) have been successfully employed in the investigation of aquifers (Hazell et al., 1992; Wright, 1992; Coriolano, 2002; Braga, 2016), in geoenvironmental diagnostics and in geotechnical studies (Dobecki & Romig, 1985; LaBrecque et al., 1996; Steeples, 2001; Power et al., 2013). Among the geophysical methods used in the study of fractured aquifers present in the crystalline basement, the most important are the electric methods, especially the multielectrode DC resistivity method, also called electrical resistivity tomography (Braga, 2016). This method in its simplest configuration uses four electrodes in the field, two for current injection and two for the measurement of potential difference. The multielectrode configuration, which makes the acquisition more agile, consists in the use of an automatic switching mechanism that allows the simultaneous use of a much larger number of electrodes, and at every instant of the data acquisition only four electrodes (or eight in the dual mode) remain active (AGI, 2018). For the application of this method it is necessary to adopt a certain type of electrode array, which consists of the way the electrodes of current injection and electric potential measurement are arranged in the field.

Sasaki (1992) developed an algorithm for the inversion of electroresistivity data, based on the damped least squares and the finite element methods, whose resolution is relatively little affected by noise, provided that the configuration adopted for the electrode arrangement is adequate. Loke & Barker (1996), using the basis of the Sasaki algorithm (1992), developed an algorithm for the rapid inversion of electrical tomography data that presents a performance about eight to twelve times faster than the conventional inversion algorithm by minimum squares method. This algorithm is the basis of the inversion program used in this work.

Steeples (2001) presents a general framework of applications of geophysical methods in the evaluation of targets near the surface of the terrain, indicating the DC resistivity method as suitable for the exploitation of groundwater resources and for the monitoring of electrically conductive underground contaminants. Gallas (2003) applied the electroresistivity method in an area of crystalline rocks in the municipality of São José do Rio Pardo, São Paulo, suggesting techniques for acquiring, processing and interpreting the results. The main objective of the surveys was to detect fractures or faults that could act as potential aquifers. These features were identified as zones of low electrical resistivity that presented continuity in depth. Madrucci

et al. (2005) present a detailed study on the fractured aquifer in the Lindóia region, State of São Paulo, which consists in the mapping of fractures from aerial photographs and from geophysical electroresistivity survey. The integrated analysis of fracture mapping, inverted geophysical data and field geological data allowed the identification of fractures filled by water, represented by low resistivity responses in the vicinity of fractures.

Pedersen et al. (2005) applied electromagnetic methods with the objective of exploring groundwater reservoirs. The authors have shown that geoelectric sections help to substantially improve the interpretation of seismic reflection data in order to more accurately identify lithological contacts between layers of clay and sand and between sand and partially fractured crystalline basement.

Dahlin & Zhou (2004) conducted numerical simulations to compare the resolution and efficiency of electroresistivity surveys using ten different types of electrode arrays for five different geological scenarios. They concluded that the dipole-dipole and gradient arrays present high resolution, are suitable for use in automatic multielectrode acquisition configurations, and present logistic advantages in relation to the other electrode arrays. Aizebeokhai & Oyeyemi (2014) evaluated the efficiency of the multielectrode gradient array for rapid data collection. They concluded that such electrode array presents better acquisition logistics and results in a higher resolution image when compared to the Wenner electrode array. Martorana et al. (2017) generated synthetic data of electroresistivity surveys for four different electrode arrays (dipole-dipole, pole-dipole, Schlumberger and gradient). The comparison between the obtained results showed that, in order to obtain a geoelectric section with an acceptable resolution and at the same time a high speed of data acquisition, it is recommended to use dipole-dipole or gradient arrays.

STUDY AREA

This paper presents the results of a geophysical and hydrogeological evaluation of crystalline terrains located in the south of the Cooperative Republic of Guyana (English Guyana), near the border with the state of Roraima, Brazil. This geophysical data survey campaign aimed to indicate the best locations for drilling wells for the production of groundwater in fractures of the crystalline basement. The geophysical method applied was the multielectrode electroresistivity method, also known as electrical tomography. The research lines were carried out in eight communities inhabited by Amerindians, whose locations are indicated in Figure 1.
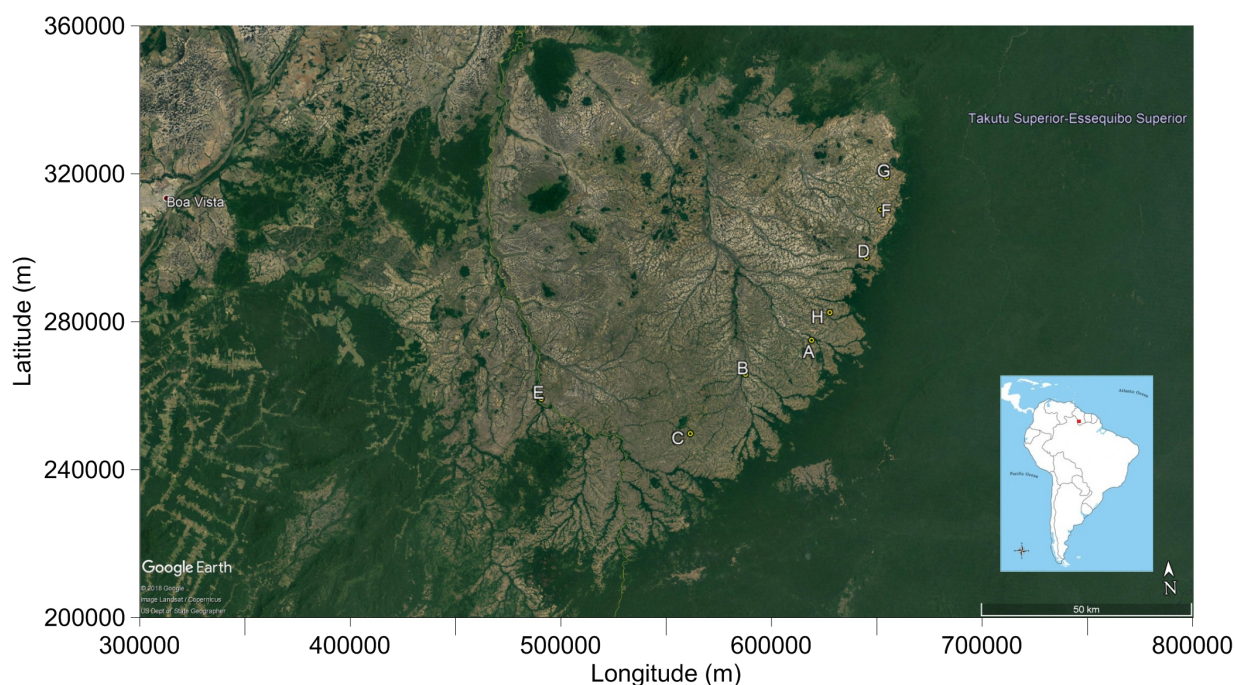
Figure 1 – Location map of communities investigated by the electroresistivity method (red box): A – Aishalton; B – Karaudarnau; C – Achawib; D – Awaruwanau; E – Bashaidrum; F – Maruranau; G – Shea; H – Churikidnau.

The geology of the region is composed of Precambrian granite rocks. The layers that constitute this type of terrain (Fig. 2), from top to bottom, are: 1st - reddish soil; 2nd - regolith - material rich in clay, derived from the decomposition of the basement, presents little thickness, locally is capped by lateritic crust, which may be absent due to erosion; 3rd - fractured igneous rock - characterized by a dense horizontal fracturing in the first meters, decreasing fracture density with depth increase (subhorizontal to subvertical fractures, much of the groundwater resources come from this zone); 4th - hard crystalline basement - permeable only locally, due to the effect of fractures.

Table 1 – Typical electrical resistivity values for the investigated lithological units.

Lithological unit	Resistivity (ohm.m)
Saturated clayey soil	4
Dry sandy regolith	1000
Laminated saprolite	30 to 120
Fractured rock	120 to 500
Hard rock	>500

METHODOLOGY

The indicator used for the location of the wells was the electrical resistivity value together with geometric parameters of the potential fractured aquifers, such as thickness and slope towards the contact with the basement, in order to reach deeper zones of water percolation. Table 1 presents the typical values of electrical resistivity for the lithological units investigated. The geophysical survey was performed using a resistivity meter SuperSting R8 with 84 electrodes and automatic data acquisition. The parameters adopted in the acquisition are listed in Table 2.

The data were processed in the EarthImager 2D software. The initial configurations considered the previous data removal with: 1) negative values of resistivity; 2) electric potential values below 0.2 mV; 3) apparent resistivity values below 1 ohm.m and above 10,000 ohm.m; 4) reciprocal error above 5%. Additionally, a maximum difference of 3% between successive iterations and an error between reciprocal positions of up to 5% were allowed. The method adopted in the inversion of the data was the smoothed inversion method (Oldenburg & Li, 1999).
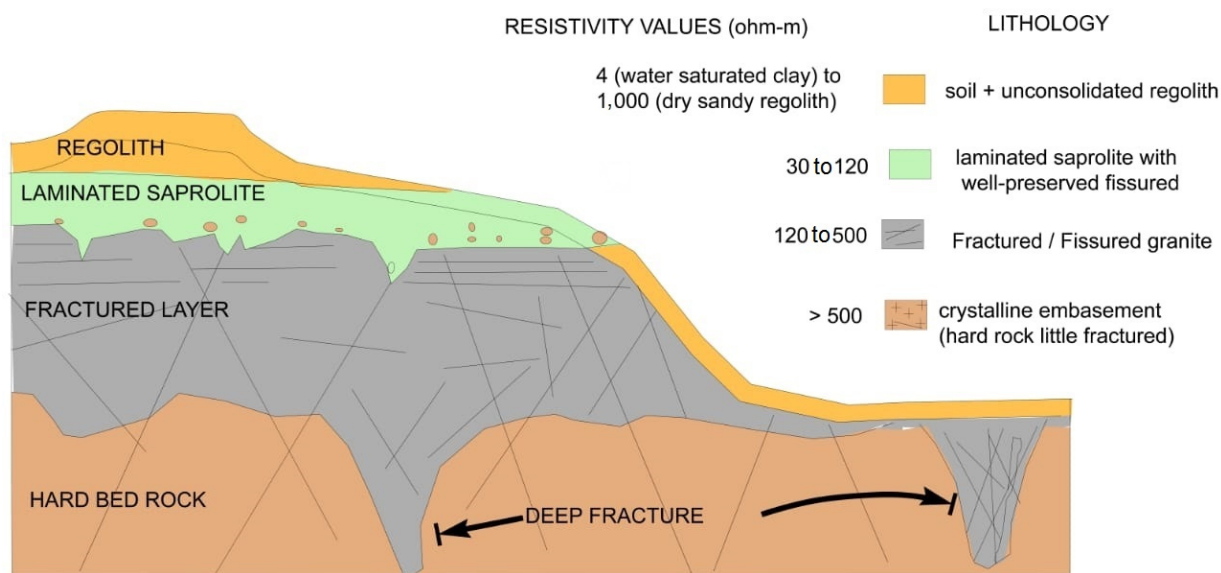
RESISTIVITY VALUES (ohm-m)   LITHOLOGY

4 (water saturated clay) to 1,000 (dry sandy regolith)   soil + unconsolidated regolith

30 to 120   laminated saprolite with well-preserved fissured

120 to 500   Fractured / Fissured granite

> 500   crystalline embasement (hard rock little fractured)

Figure 2 – Typical profile of rock alteration in crystalline terrains (Dewandel et al., 2006).

Table 2 – Field parameters adopted in the electroresistivity data survey.

Section	Community	Electrode spacing (m)	Electrode array
A	Aishalton	3	Dipole-dipole
B	Karaudarnau	3	Dipole-dipole
C	Achawib	4	Dipole-dipole
D	Awaruwanau	4	Dipole-gradient
E	Bashaidrum	4	Dipole-dipole
F	Maruranau	4	Dipole-gradient
G	Shea	4	Dipole-dipole
H	Churikidnau	4	Dipole-dipole

Drilling of the wells was performed using a Prominas model R-1S drill, with capacity for drilling wells up to 250 meters deep. In the drilling, 10.1/2" or 9.7/8" diameter bits were used in the initial phase of the well. In the intermediate phase, 8" drill bit was used and, in the final stage, 6" diameter bit.

RESULTS

Figure 3 shows the localization maps of the electroresistivity sections performed in the eight communities, as well as the sites indicated for drilling the wells. Figures 4 and 5 show the eight geoelectric sections obtained by the inversion of the recorded geophysical data, with the positions indicated for drilling the wells, as indicated by the red arrows. Figures 6 to 9 show the lithological and constructive profiles of the wells drilled at the positions indicated in Figure 3.

In the geoelectric section of the Aishalton locality (Fig. 4-A) one can identify the water level around 150 meters deep. Above this, with a thickness of 7 meters and a resistivity (ρ) of approximately 300 Ω.m, the occurrence of dry sandy-clayey regolith is indicated. Between the 137 and 150 meters there is a conductive zone ($\rho \approx 50$ Ω.m) that supposedly corresponds to the saturated saprolite. Below the dimension 137 and to the base of the geoelectric section there is a resistive region ($\rho \approx 500$ Ω.m) that should correspond to the fractured granite. The lithological profile of the well drilled in Aishalton (Fig. 6) records the presence of a clay-sandy saprolite up to 9 meters deep followed by a range of densely fractured granite to the bottom of the well (80 meters deep). It should be noted that the geoelectric sections do not present sufficient resolution to indicate individually the fractures recorded in the lithological profile, however, the average resistivity of the interval is consistent with that expected for a fractured zone, as indicated in Table 1.

In the locality Karaudarnau, the geoelectric section (Fig. 4-B) suggests that from the surface of the terrain to the depth of 4 meters a dry regolith occurs with $\rho \approx 700$ Ω.m and from

A - Aishalton

B - Karaudarnau

C - Achawib

D – Awaruwanau

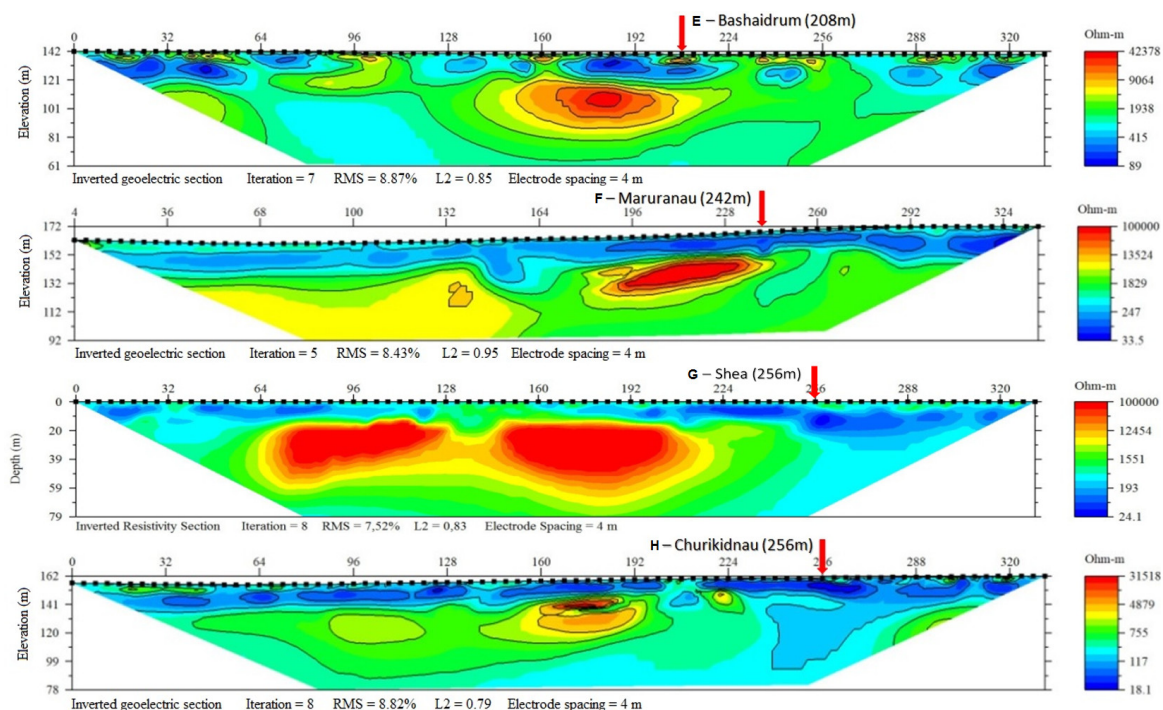E - Bashaidrum

F - Maruranau

G - Shea

H - Churikidnau
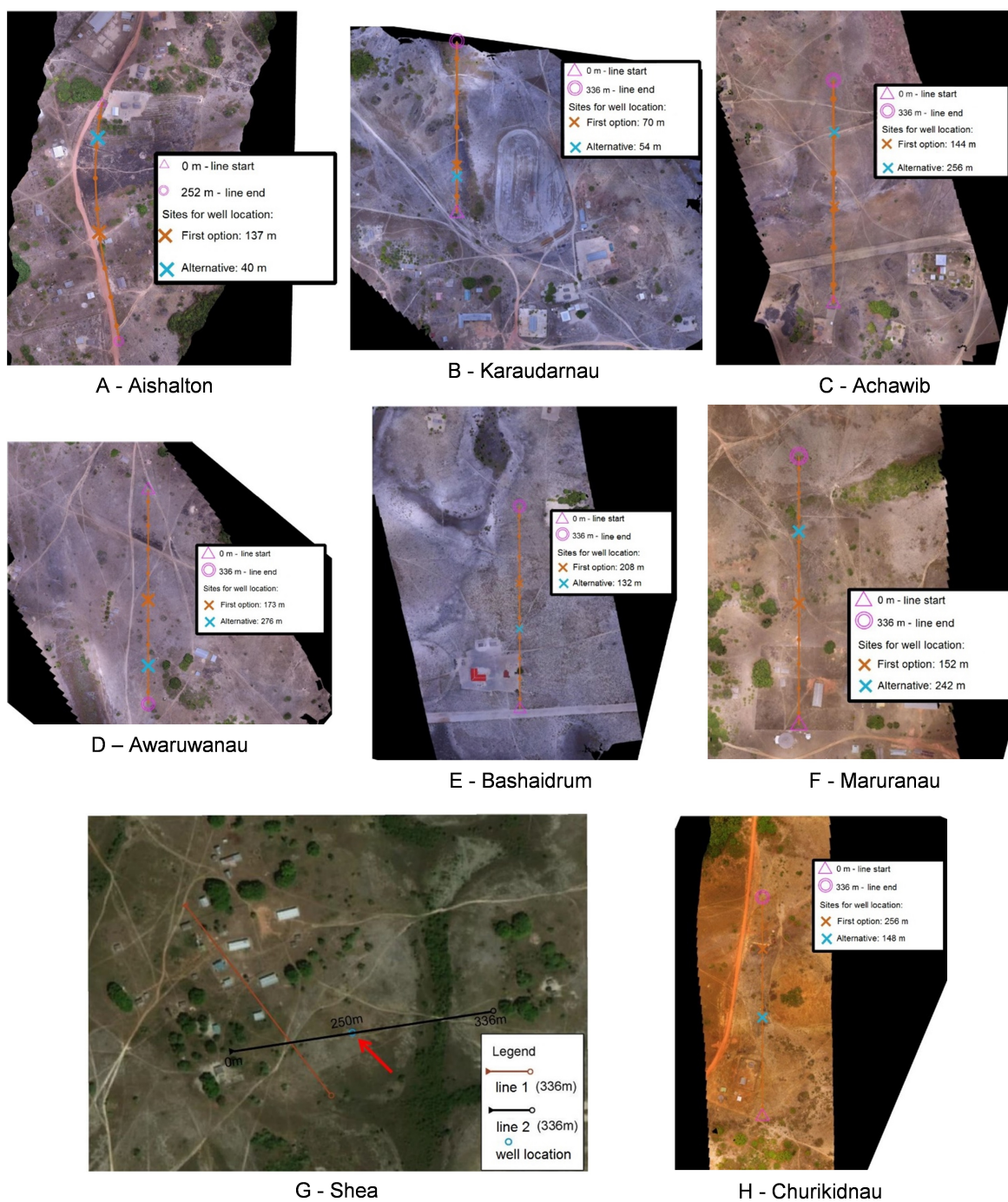
Figure 3 – Mosaic with the location of the electroresistivity data collection lines registered in the eight communities with the indication of the preferred positions for well drilling.
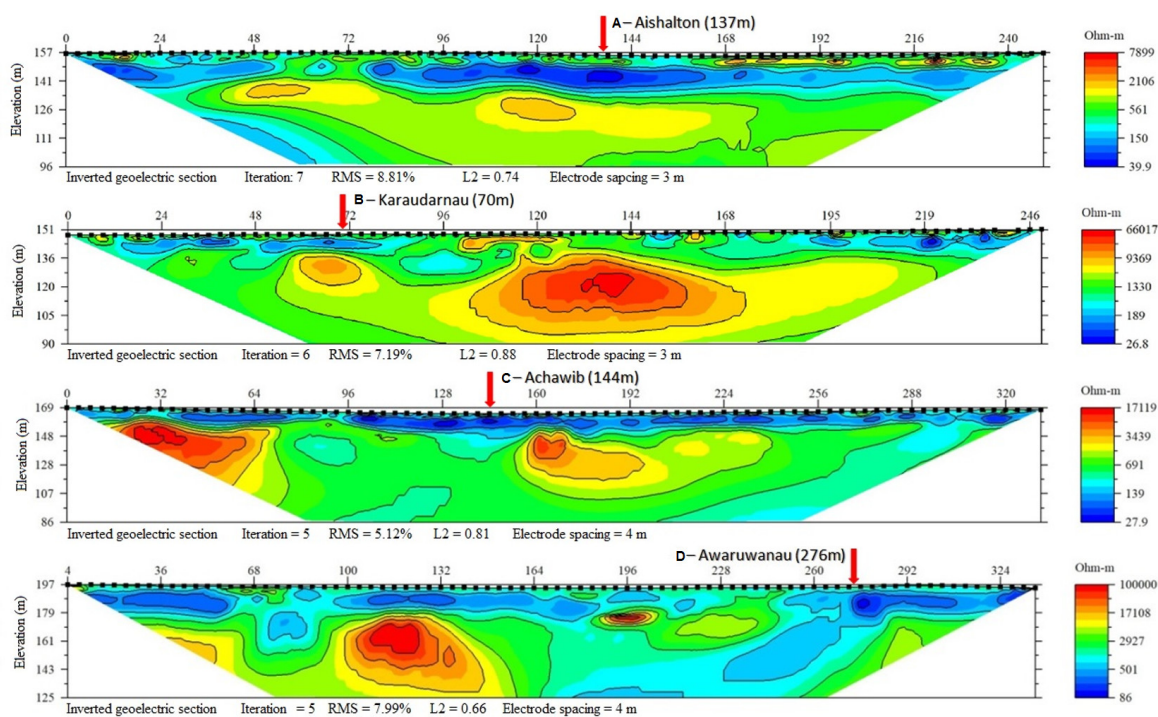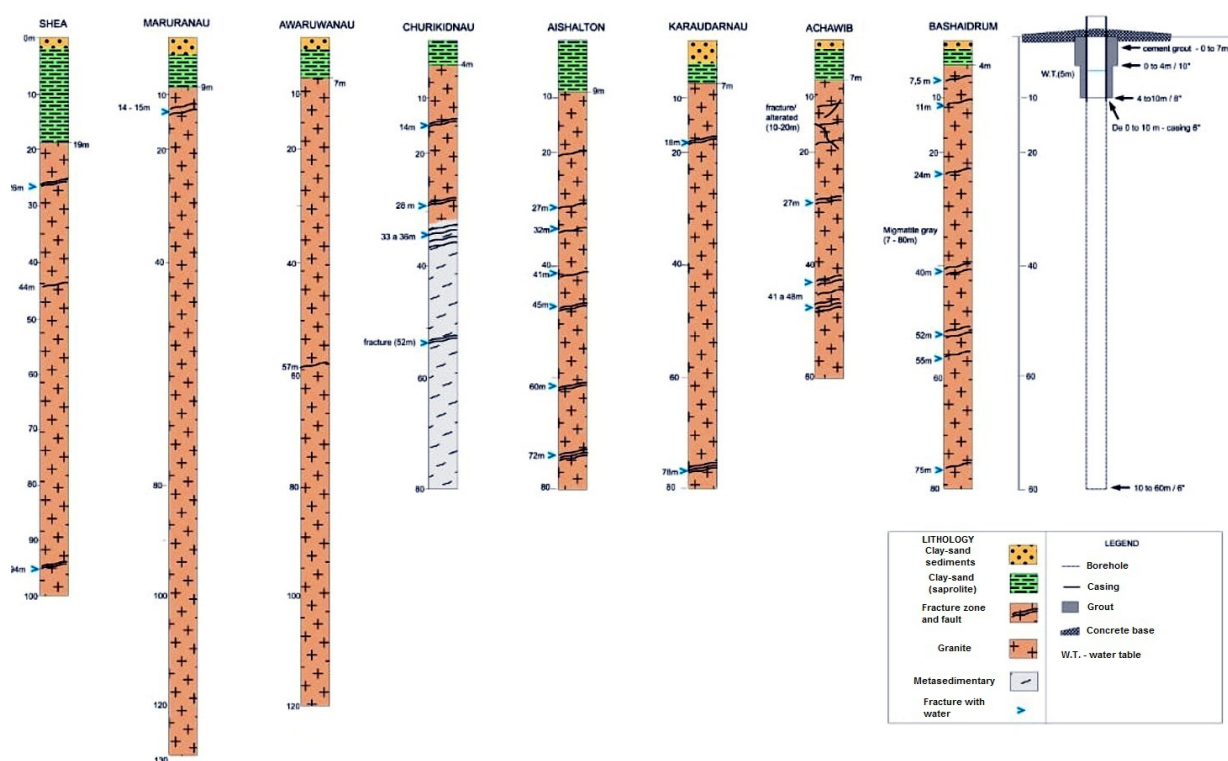
Figure 4 – Inversion models of resistivity for A – Aishalton; B – Karaudarnau; C – Achawib; D – Awaruwanau. The red arrows indicate the sites indicated for the drilling of the wells.

Figure 5 – Inversion models of resistivity for E – Bashaidrum; F – Maruranau; G – Shea; H – Churikidnau. The red arrows indicate the sites indicated for the drilling of the wells.

Figure 6 – Lithological and constructive profiles of wells drilled in the eight communities.

4 to 10 meters deep there is a range of saturated saprolite with $\rho \approx 150\ \Omega$.m followed by a granite section with low fracturing density ($\rho \approx 1300\ \Omega$.m) to the bottom of the section. In general, the lithological profile (Fig. 6) confirms the profile suggested by the geoelectric section.

In Achawib, the geoelectric section (Fig. 4-C) indicates that in the position of the well, from the surface up to about 25 meters deep occurs a saturated saprolite with $\rho \approx 100\ \Omega$.m followed by medium fractured granite ($\rho \approx 600\ \Omega$.m) to the bottom of the section. The lithological profile (Fig. 6) shows the occurrence of a zone of saprolite and altered rock up to about 20 meters deep followed by a fractured granitic interval until the end of the drilling (60 meters depth).

The geoelectric section of Awaruwanau (Fig. 4-D) suggests a dry regolith ($\rho \approx 1000\ \Omega$.m) to 4 meters deep, followed by a saturated saprolite ($\rho \approx 120\ \Omega$.m) between 4 and 18 meters deep and finally a low-fracturing rock ($\rho \approx 1500\ \Omega$.m) to the bottom of the section. Two wellbores were drilled at this site, but the first one resulted dry, then the alternative location was drilled. The lithological profile of this second location (Fig. 6) broadly

confirms the profile suggested by the geoelectric section, except that the saprolite is limited to a depth of 8 meters.

In Bashaidrum, the geoelectric section (Fig. 5-E) indicates, in the well position, the occurrence of dry regolith or rock ($\rho \approx 2000\ \Omega$.m) down to 10 meters deep, followed by a conductive interval ($\rho \approx 150\ \Omega$.m) between 10 and 20 meters deep that should correspond to a saturated saprolite. From 20 meters deep to the bottom of the section there is indication of hard or weakly fractured rock ($\rho \approx 1000\ \Omega$.m). The lithological profile (Fig. 6) in turn registers two thin layers of regolith and saprolite, each 2 meters thick, followed by densely fractured granite to the bottom of the well (80 meters deep).

The geoelectric section of Maruranau (Fig. 5-F) indicates the occurrence of saturated saprolite ($\rho \approx 100\ \Omega$.m) up to 20 meters deep, followed by hard rock ($\rho \approx 2000\ \Omega$.m) to the bottom of the section. The lithological profile (Fig. 6) shows a superficial layer of regolith, with a thickness of 3 meters, followed by a saprolite down to 9 meters deep and granite with little fracture to the final depth of the well (129 meters).

In Shea locality, the geoelectric section (Fig. 5-G) indicates that in the well position a saturated saprolite occurs

Table 3 – Maximum drilled depth, fracture degree, characteristic resistivity and instantaneous water flow.

Site	Maximum drilled depth (m)	Degree of fracturing	Characteristic resistivity (ohm.m)	Instantaneous water flow (L/h)
A - Aishalton	80	Medium	500	5000
B - Karaudarnau	80	Low	1300	4500
C - Achawib	60	Medium	600	6000
D - Awaruwanau	100	Low	1500	4000
E - Bashaidrum	80	High	1000	6000
F - Maruranau	129	Low	3000	3500
G - Shea	100	Low	300	4000
H - Churikidnau	80	High	200	6000

($\rho \approx 100$ Ω.m) down to 20 meters deep followed by a fractured granite ($\rho \approx 300$ Ω.m) down to the base of the section. The lithological profile of the well (Fig. 6) basically confirms the profile indicated by the geoelectric section. In Churikidnau, the geoelectric section (Fig. 5-H) suggests saturated saprolite ($\rho \approx 60$ Ω.m) down to 10 meters deep, followed by densely fractured rock ($\rho \approx 200$ Ω.m) to the bottom of the section. Figure 6 shows the occurrence of saprolite up to 4 meters deep followed by fractured granite to the depth of 32 meters and fractured phyllite to the final depth of the well (80 meters).

Table 3 presents the maximum drilled depths, the degree of fracture observed in the lithological profile, the characteristic values of resistivity observed in the granite occurrence intervals in the wells and the instantaneous water flows measured after the installation of the pump in each of the drilled wells. No long term flow tests were performed. The degree of fracture is a qualitative index based on the description of the lithological profiles of the wells, as can be observed in Figure 6.

In order to characterize the relationships between the quantities listed in Table 3, Figures 7, 8 and 9 show, respectively, dispersion plots between flow and fracture degree, between characteristic resistivity and fracture degree, and between flow and characteristic resistivity. In these figures the degree of low fracturing is represented by the number 1, medium degree by 2 and the high one by 3.

In general, it can be affirmed that there is a good correlation between the characteristic values of electrical resistivity observed

in the intervals corresponding to the granite, the degree of fracture observed in the lithological profiles and the instantaneous flows recorded after the installation of the pump in each well.

Figure 7 shows that there is a continuous increase in the wells flow with the increase of the fracture degree, demonstrating that the fracture of the basement strong controls the water production capacity. In Figure 8, with the exception of wells 5 and 7 (Bashaidrum and Shea), the characteristic resistivity decreases consistently with the increase in the degree of fracture of the crystalline rock. Finally, Figure 9 shows the relationship between well flow and characteristic resistivity. Again, with the exception of wells 5 and 7, the wells flow rate decreases continuously with increasing fracture degree of the crystalline bed. Since wells flow depends on the degree of crystalline fracture, resistivity can be used to map most of the fractured zones of the basement, although other factors as water salinity and interconnectivity degree of fractures may complicate this relationship, as observed in wells 5 and 7. These results are in concordance with those found by Moreira et al. (2013).

CONCLUSIONS

In this paper, eight successful cases were presented in the application of the DC resistivity method as a diagnostic tool for the location of water wells in fractured aquifers of the English Guyana crystalline basement. The water flow shown shortly after the drilling of the wells is strongly controlled by the degree of fracturing of the igneous rocks that make up the crystalline
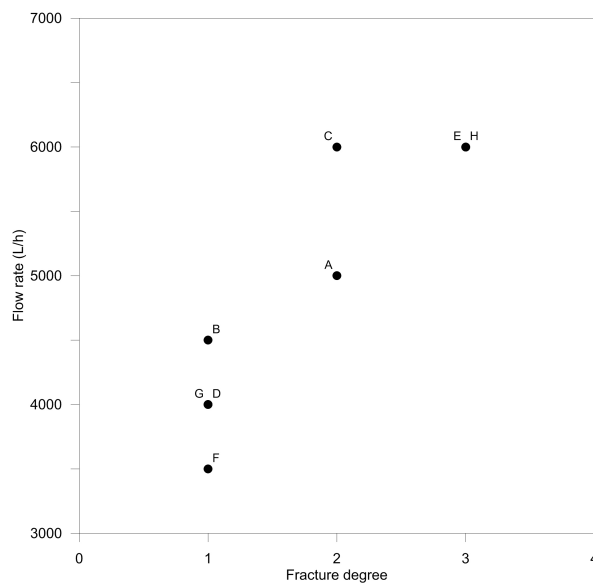
Figure 7 – Relation between instantaneous flow of wells and fracture degree of the crystalline basement.
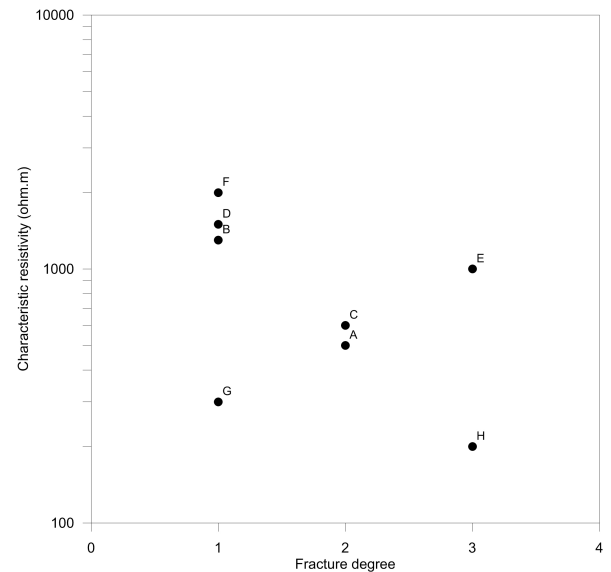
Figure 8 – Relation between characteristic resistivity and degree of fracture of the crystalline basement.
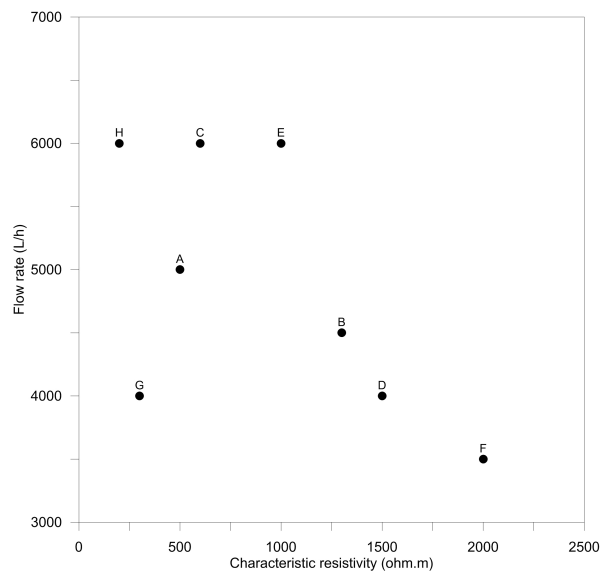
Figure 9 – Relation between instantaneous flow of wells and resistivity characteristic of the basement.

basement of the region. Of the eight wells drilled, in six of them a strong decrease of the characteristic electrical resistivity was observed with the increase of the basement fracture degree index. In addition, a consistent decrease in the wells flow was observed with the increase in the characteristic resistivity. For these reasons deep regions with low values of electrical

resistivity in the geoelectric sections are potential indicators of the presence of interconnected fracture zones in the crystalline basement, constituting in preferential zones for the drilling of wells for the production of groundwater. The same approach may be applied successfully to explore groundwater resources in fractured crystalline basement of different parts of the world.

REFERENCES

AGI. 2018. SuperSting Earth Resistivity, IP & SP System with Wi-Fi. Instruction Manual V. 20180515. Advanced Geosciences Inc.

AIZEBEOKHAI AP & OYEYEMI KD. 2014. The use of the multiple-gradient array for geoelectrical resistivity and induced polarization imaging. Journal of Applied Geophysics, 111: 364–376.

BRAGA ACO. 2016. Geofísica aplicada: métodos geoelétricos em Hidrogeologia. Oficina de Textos. São Paulo, Brazil. 160 pp.

CORIOLANO ACF. 2002. Reavaliação de critérios estruturais na hidrogeologia de terrenos cristalinos, com ênfase na neotectônica e sensoriamento remoto. PhD Thesis – Centro de Ciências Exatas e da Terra. Universidade Federal do Rio Grande do Norte, Natal, Brazil, 199 pp.

DAHLIN T & ZHOU B. 2004. A numerical comparison of 2D resistivity imaging with 10 electrode arrays. Geophysical Prospecting, 52(5): 379–398.

DEWANDEL B, LACHASSAGNE P, WYNS R, MARÉCHAL J & KRISHNAMURTHY N. 2006. A generalized 3-D geological and hydrogeological conceptual model of granite aquifers controlled by single or multiphase weathering. Journal of Hydrology, 330(1-2): 260–284.

DOBECKI T & ROMIG P. 1985. Geotechnical and groundwater geophysics. Geophysics, 50(12): 2621–2636.

GALLAS JDF. 2003. Prospecção de água subterrânea em aqüíferos cristalinos com o emprego de métodos indiretos. Revista do Instituto Geológico, 24(1-2): 43–51.

HAZELL J, CRATCHLEY C & JONES C. 1992. The hydrogeology of crystalline aquifers in northern Nigeria and geophysical techniques used in their exploration. Geological Society, London, Special Publications, 66(1): 155–182.

KEAREY P, BROOKS M & HILL I. 2009. Geofísica de exploração. Oficina de textos. São Paulo, Brazil. 438 pp.

LABRECQUE D, RAMIREZ A, DAILY W, BINLEY AM & SCHIMA S. 1996. ERT monitoring of environmental remediation processes. Measurement Science and Technology, 7(3): 375–383.

LOKE MH & BARKER RD. 1996. Rapid least-squares inversion of apparent resistivity pseudosections by a quasi-Newton method 1. Geophysical Prospecting, 44(1): 131–152.

MADRUCCI V, TAIOLI F & ARAÚJO CCD. 2005. Análise integrada de dados de Sensoriamento Remoto, Geologia e Geofísica no estudo de aqüífero fraturado, Lindóia-SP. Revista Brasileira de Geofísica, 23(4): 437–451.

MARTORANA R, CAPIZZI P, D'ALESSANDRO A & LUZIO D. 2017. Comparison of different sets of array configurations for multichannel 2D ERT acquisition. Journal of Applied Geophysics, 137: 34–48.

MOREIRA CA, CAVALHEIRO MLD, PEREIRA AM & SARDINHA DS. 2013. Análise das relações entre parâmetros geoelétricos e vazões para o aquífero livre de Caçapava do Sul(RS). Águas Subterrâneas, 27(3): 45–59.

OLDENBURG DW & LI Y. 1999. Estimating depth of investigation in DC resistivity and IP surveys. Geophysics, 64(2): 403–416.

PEDERSEN LB, BASTANI M & DYNESIUS L. 2005. Groundwater exploration using combined controlled-source and radiomagnetotelluric techniques. Geophysics, 70(1): G8–G15.

POWER C, GERHARD JI, TSOURLOS P & GIANNOPOULOS A. 2013. A new coupled model for simulating the mapping of dense nonaqueous phase liquids using electrical resistivity tomography. Geophysics, 78(4): EN1–EN15.

SASAKI Y. 1992. Resolution of resistivity tomography inferred from numerical simulation. Geophysical Prospecting, 40(4): 453–463.

STEEPLES DW. 2001. Engineering and environmental geophysics at the millennium. Geophysics, 66(1): 31–35.

TELFORD W, GELDART L, SHERIFF R & KEYS D. 1976. Applied Geophysics. Cambridge University Press. Cambridge, 860 pp.

WRIGHT EP. 1992. The hydrogeology of crystalline basement aquifers in Africa. Geological Society, London, Special Publications, 66(1): 1–27.

INTERPRETATION OF RADIOMETRIC RATIOS AND MAGNETIC ANOMALIES FROM MORRO FEIO ULTRAMAFIC COMPLEX, CENTRAL-WESTERN BRAZIL

Adolfo Barbosa Silva[1], Tiago Rocha Faria Duque[2] and Felipe da Mota Alves[3]

ABSTRACT. This study was performed to identify magnetic structures in depth and radiometric responses within and around Morro Feio Ultramafic Complex (MFUC) from the airborne geophysical (gamma-ray spectrometry and magnetic) data. Using processing techniques and profiles analysis, we have found eight gamma-ray spectrometry signatures and twenty-seven magnetic anomalies. The radiometric signatures are basically characterized by a K and eU relative enrichment in detriment eTh, with two of these signatures also characterized by K relative enrichment in detriment eU. Based on published works, we have interpreted the radiometric responses may be from serpentinite and possible areas with hydrothermal alterations. Regarding the magnetic anomalies, we concluded that the shallowest may be the magnetic responses of dikes, contact zones and other structures, while the deepest have sources with more complex geometries and are concentrated in central-western of MFUC, where the participation of Pt is larger. In this aspect, the results presented reinforce the arguments favorable to existence of Pt, Cr and Ni primary sources in depth.

Keywords: mineral research, airborne geophysical, serpentinites, hydrothermal alteration.

RESUMO. Este estudo foi realizado com o objetivo de identificar estruturas magnéticas em profundidade e respostas radiométricas dentro e no entorno do Complexo Ultramáfico de Morro Feio (CUMF) a partir de dados aerogeofísicos (gamaespectrometria e magnetometria aérea). Utilizando técnicas de processamento e análise de perfis, encontramos oito assinaturas gamaespectrométrica e vinte e sete anomalias magnéticas. As assinaturas radiométricas caracterizam-se basicamente por um enriquecimento relativo de K e eU em detrimento eTh, com duas dessas assinaturas também sendo caracterizadas pelo enriquecimento relativo de K em detrimento eU. Com base em trabalhos publicados, interpretamos que as respostas radiométricas podem ser em virtude do serpentinito e possíveis áreas com alterações hidrotermais. Com relação às anomalias magnéticas, concluímos que as mais rasas podem ser as respostas magnéticas de diques, zonas de contato e outras estruturas, enquanto as mais profundas possuem fontes com geometrias mais complexas e se concentram no centro-oeste do CUMF, onde a participação de Pt é maior. Neste aspecto, os resultados apresentados reforçam os argumentos favoráveis a existência de fontes primárias de Pt, Cr e Ni em profundidade.

Palavras-chave: pesquisa mineral, aerogeofísica, serpentinitos, alteração hidrotermal.

[1]Serviço Geológico do Brasil - CPRM, R. 148, 485 GEREMI Sala 34, 74170110, Goiânia, GO, Brazil – E-mail: adolfo.barbosa@cprm.gov.br

[2]TDMaps, Goiânia, GO, Brazil – E-mail: tiagorfduque@me.com

[3]Serviço Geológico do Brasil - CPRM, Goiânia, GO, Brazil – E-mails: felipe.alves@cprm.gov.br

INTRODUCTION

Ultramafic complexes are composed of varying proportions of harzburgite, lherzolite and dunite, usually with metamorphic textures (more or less serpentinized) and may contain important sources of *Zn*, *Cu*, *Co*, *Ni*, *Cr*, *Au*, and PGE's (Coleman, 1977; Castroviejo et al., 2004 *apud* Queiroga et al., 2012). In Brazil, considerable portions of the ultramafic complexes occur mainly in Tocantins Province, where about 180 ultramafic massifs have been discovered in the Goiás State since the 1970s. Some of these massifs, as the Morro Feio, were classified by Berbert (1977) as serpentinized dunite/peridotites of alpine type.

The Morro Feio is an elevation with around 940 m height, 4 km of length in northern direction, 2 – 2.5 km wide, located at northern of Hidrolândia city (30 km south of the Goiás Capital) near to BR–153 highway that connects Goiânia to São Paulo cities (Berbert & Mello, 1969). Previous works had identified important mineral occurrence (mainly chromite, garnierite and platinum) associated to surface deposits generated by laterization and concretion process from serpentinites (Berbert & Mello, 1969; Milliotti, 1978). However, due to the irregular character of these occurrences and the ease of exploration, the ore extractions, mainly of chromite, have been in the process of exhaustion (Valente, 1986).

Although previous works have made a detail mapping of the Morro Feio Ultramafic Complex (MFUC), such works were based on surface information, so that up today, it has not been published any research about source rocks in depth within MFUC. Such researches are import, as have already been pointed out by Berbert & Mello (1969) when they proposed drilling holes to verify the existence of *Pt*, *Cr* and *Ni* primary sources (sulfides?) in depth. Furthermore, the serpentinites may contain expressive amount of *U* without significant enrichment in *Th*, so high *U/Th* ratio may be expected (Deschamps et al., 2013). If these ratio values are high enough to be detected by airborne gamma-ray spectrometry data then *U/Th* ratio may be used as an aid tool at serpentinites mapping in other research areas. This context has motivated the development of the present study.

In this study we have analyzed the airborne geophysical data (gamma-ray spectrometry and magnetic data) with the goal to identify structures and rocks in depth and their gamma-ray spectrometry signatures, mainly high *U/Th* ratio, within and around MFUC. Our intention is to provide additional information that can complement the geological knowledge from previous studies.

GEOLOGICAL SETTING

The studied area (Fig. 1) is located in the south–center portion of the Tocantins Province. This province is a Neoproterozoic geotectonic entity developed as a result of the convergence and collision between the Amazonian, São Francisco–Congo Cratons (Dardenne, 2000; Angelim et al., 2003) and a third crustal block known as Paranapanema (Mantovani & Brito Neves, 2009). Among the several tectonic units that compose the Tocantins Province, it is of interest the tectonic unit known as Brasília Belt. This unit is a fold-and-thrust belt characterized by associations of supracrustal deformed rocks along the western flank of the São Francisco Craton. In the internal portion of the Brasília Belt (or meridional portion) (Dardenne, 2000; Angelim et al., 2003) outcrops the Araxá Group metasedimentary rocks. In the study area, the Araxá Group metasediments are basically formed by garnet-mica schist, quartz-mica schists and micaceous quartzite. The MFUC is hosted in these units.

Milliotti (1978) divided MFUC into five units: Antigorite Serpentinite (A1) – formed by antigorite, chrysotile and xenomorphic magnetite and leucoxene. The presence of olivine grain is doubtful; Silicified Serpentinite (A2) – corresponds to the silicified portions from serpentinites of the previous unit; Talcified Serpentinite (B1) – formed by antigorite, talc and magnetite; Talc schist (B2) – formed by talc, magnetite in euhedral porphyroblasts, antigorite, chlorite and actinolite in centimetric crystals, fibroradiated, and magnesite in porphyries; Chlorite Schist (C) – formed by chlorite, magnetite in euhedral porphyroblasts of up to 2 cm, epidote, talc, tremolite, in fibroradiated porphyroblasts, and black tourmaline in fibroradiated porphyroblasts and euhedral.

Besides the units mentioned above, surface deposits also occur within MFUC. These deposits, basically formed by alluvium and eluvium, are important from the economic point of view, because they contain significant amounts of chromite and platinum (Milliotti, 1978). In his studies, Milliotti (1978) identified some anomalous platinum zones with values up to 1210 ppb. Based on chemical analysis of total rock, Milliotti (1978) concluded that the geological distribution of platinum and chromite is more pronounced in serpentinites (Unit A1), with the zones of contact between serpentinites and talc schist being the most concentrations of platinum and chromite. For Ni present in garnierite, Berbert & Mello (1969) have suggested drilling holes near to the garnierite occurrence to investigate the possibility of primary sulfides in depth.
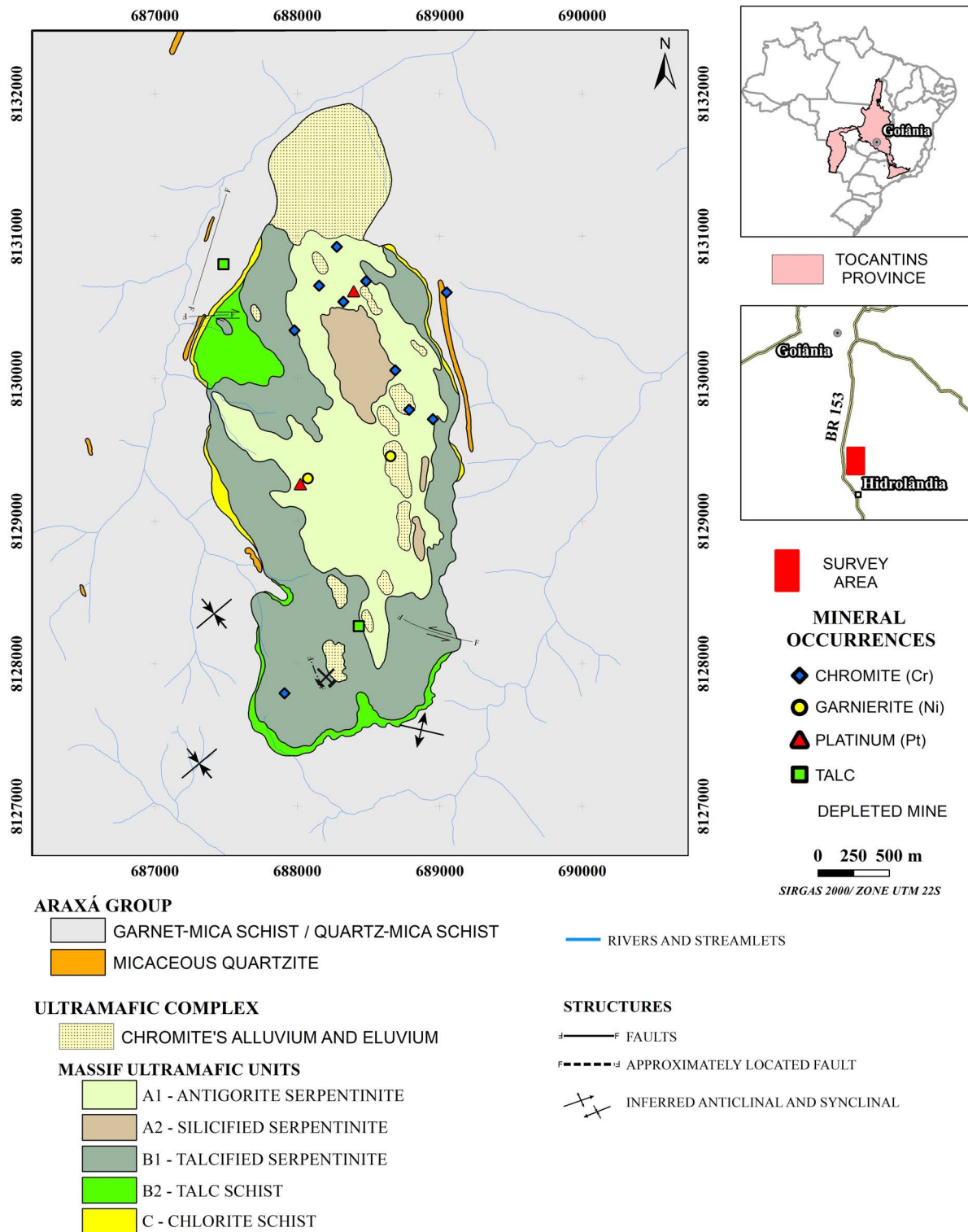
Figure 1 – MFUC Geological map and its surroundings (from Milliotti's (1978) map) presenting the mineral occurrences. The mineral occurrences were from previous maps (Berbert & Mello, 1969; Milliotti, 1978) and obtained by GEOSGB (2018) and MRDS (2018) databases.

Out of MFUC, Berbert & Mello (1969) also identified a dike with direction of N30W, 3 km long and 100 m width cutting the Araxá Group rocks. The dike is composed of calcium plagioclase, pyroxenes and magnetite and ilmenite as accessory minerals.

The MFUC rocks have been interpreted by Strieder & Nilson (1992a, 1992b) as an exotic block isolated from ophiolitic mélange in the Araxá Group garnet-mica schist. According to Deschamps et al. (2013) serpentinites from ophiolitic mélange are enriched in trace elements (LREE). These enrichments may indicate that the protoliths of the subduction-related serpentinites were enriched in a supra-subduction environment by fluids during hydration. Deschamps et al. (2013) speculated that this fluid hydration may constrain the *U* content and led its concentration without significant enrichment in *Th*, so high *U/Th* ratios may be observed in some cases.

METHODOLOGY

The airborne geophysical data used this work were part of the CPRM's Brasília South Aerogeophysics Project, acquired and pre-processed in 2005 by the company Prospecting & Engineering Lasa (LASA, 2005). The pre-processing steps consisted in the following corrections: parallax, removing diurnal variation, removing the International Geomagnetic Reference Field (IGRF), leveling and micro-levelling for airborne magnetic data and dead time, background (aircraft, cosmic and radon), height and Compton Effect and conversion to elemental concentrations for the airborne gamma-ray spectrometry data. The flight and tie lines spacings were 500 m in the N–S direction and 5 km in the E–W direction, respectively. The nominal terrain clearance height was 100 m. Geosoft® Oasis Montaj™ 9.0.2 and Esri® ArcMap 10.6 softwares were used for post-processing and interpretation of airborne geophysical data, respectively. The data were projected for UTM Zone 22S coordinate system and SIRGAS 2000 datum, magnetometric and gamma-ray spectrometry data were post-processing as following below.

Gamma-ray spectrometry data processing

A statistical analysis was performed on gamma-ray spectrometry data and we identified negative values corresponding to 5.6%, 5.0% and 24.4% for the potassium (*K*), thorium equivalent (*eTh*) and uranium equivalent (*eU*) concentrations. Following the Grant's (1998) suggestion the negative data was kept in the database and we added a constant of 2.5 in the mentioned channels.

This procedure was intended to make all values positives in order to enable qualitative analysis based on the radioelement ratios. The addition of a constant in the mentioned channels did not affect the shape of the profiles (Fig. 2). In order to investigate which interpolation method would be the most representative of gamma-ray spectrometric data, two interpolation methods, minimum curvature (Briggs, 1974) and bi-directional (Reeves, 2005), were compared. The bi-directional method, with cell size of 100 m, produced better results (Fig. 2). Using this method, we produced *K*, *eTh* and *eU* concentration maps and *eU/eTh*, *K/eU*, *K/eTh* ratio maps (Fig. 3). The airborne gamma-ray spectrometry data was also analyzed along the flight and tie lines. These lines were numbered from P – 01 to P – 10, with profiles from P – 01 to P – 09 corresponding to flight lines and profile P – 10 corresponding to tie line. The sample spacing was about 80 m. The even profiles were oriented S–N and odd profiles were oriented N–S, excepted to P – 10 that is oriented E–W.

In the profiles, besides *K*, *eTh* and *eU* concentrations and radioelements ratios data, we also calculated and analyzed hydrothermal alteration indicators profiles like parameter F (FP) (Efimov, 1978 *apud* Gnojek & Prichystal, 1985) and *K* (KD) and *eU* (UD) excesses (Galbraith & Saunders, 1983; Saunders et al., 1987; Pires, 1995). Finally, using the Seeker tool integrated to Oasis Montaj software, a 30 m resolution digital terrain model (DEM) grid acquired by Shuttle Radar Topography Mission (SRTM) was used to aim interpretations of gamma-ray spectrometry data. The DEM grid was sampled for gamma-ray spectrometry database with the same sample spacing (80 m).

Magnetometric data processing

The magnetometric data was interpolated by bi-directional method with 100 m cell size (Billings & Richards, 2001; Reeves, 2005) to obtain the Anomalous Magnetic Field (AMF) grid. To facilitate the interpretation process of the magnetic anomalies, we applied the analytical signal amplitude (ASA) (Nabighian, 1972; Roest et al., 1992) on the AMF grid to highlight the magnetization contrast zones. From the ASA grid, we produced the First order Vertical Derivative (FVD), Tilt angle (TDR) (Miller & Singh, 1994) and Total Horizontal Derivative of the Tilt angle (THDR–TDR) (Verduzco et al., 2004) grids (Fig. 4). Finally, the grids from magnetometric data were sampled for the gamma-ray spectrometry databases with the same sample spacing (80 m). The grids from magnetic data were also used to estimate the magnetic source depth. In this work, we used three different methods: The Standard Euler Deconvolution (SED) (Reid et al.,
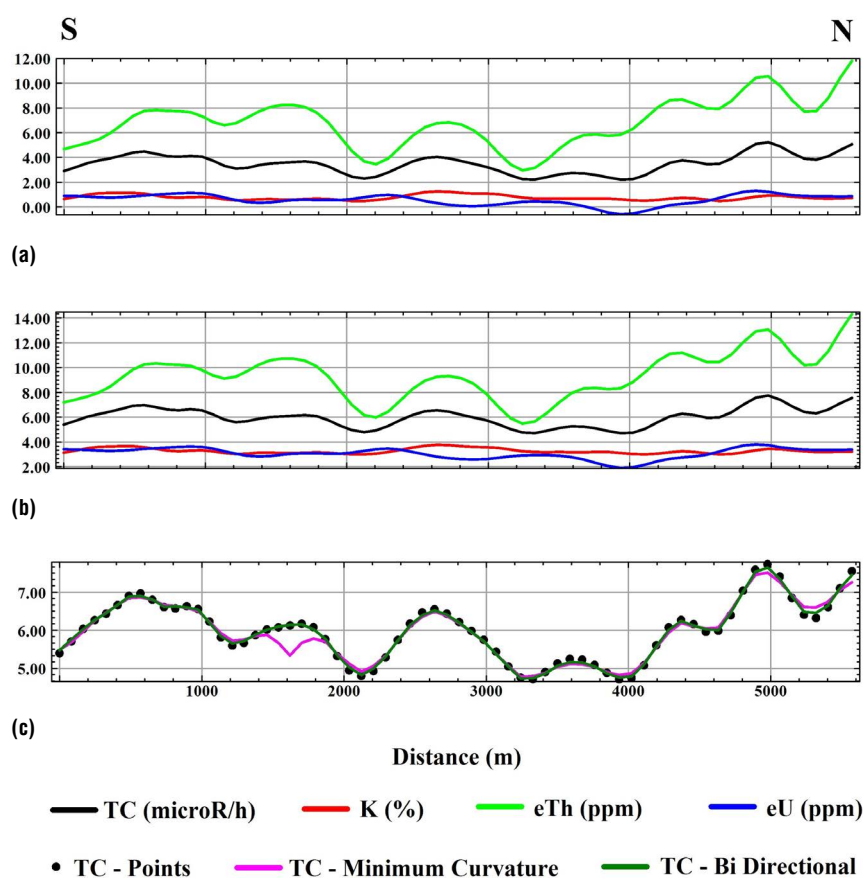
Figure 2 – Profiles of the radioelement concentrations before (a) and after (b) the addition of a constant. (c) Comparison among interpolation methods applied to the total counting channel.

1990); Source Parameter Image (SPI) (Thurston & Smith, 1997); and ASA–Euler (AN–EUL) (Salem & Ravat, 2003).

The SED method was applied on AMF grid. We considered Structural Index (SI) values of 0, 1, 2 and 3. For each SI values we considered error of 5% on estimative at depth, terrain clearance height of 100 m and window size of 20 times the grid cell size. The SED's solutions were computed by E3DECON.GX algorithm from Oasis Montaj software. For SPI method the directional derivatives (x, y and z) were computed by gridDxDy.GX and gridDz.DX algorithms integrated to the presented software. Next, using these derivatives, the local wavenumber peak was selected by the algorithm developed by Blakely & Simpson (1986). In this work, we used the highest restrictive selection level, which is, a peak was only selected if its value in the grid cell was greater than the values of the grid cells in the four adjacent directions. The solutions SPI were calculated by algorithm SPI.GX of the SPI package also integrated to the mentioned software. Finally, for AN–EUL method, the position of the center of the anomalous

source was founded based on the maximum of the ASA which was selected through the algorithm Get a Grid Location of the Euler3D package also integrated to Oasis Montaj software. The selection level was the same as selected in the SPI method with an addition of a cutoff value of 0.01 nT/m. Selected peaks below this threshold were rejected. After the selection of ASA maxima, the Located AN–EUL algorithm was used to compute the structural index and depth estimates based on Salem & Ravat's (2003) equations.

For the depth estimate obtained by SPI and AN–EUL method, only solutions located 100 meters distant from identified magnetics anomalies were selected, while for SED method all solutions were considered.

RESULTS

The maps produced from airborne geophysical data show that MFUC has some distinctive radiometric and magnetic responses regarding to the rocks surrounding (Figs. 3 and 4). The MFUC rocks show low *K*, *eTh* and *eU* concentration (Figs. 3a – 3c),
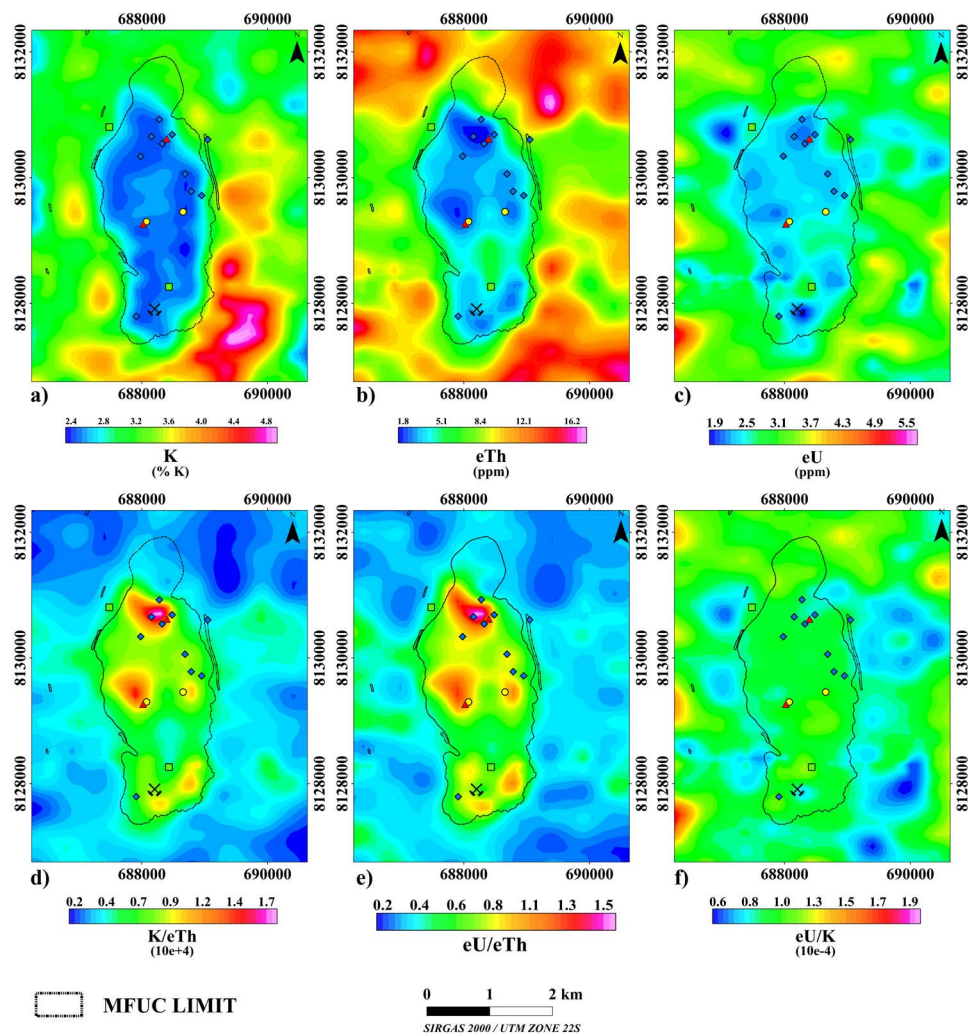
Figure 3 – MFUC Radiometric maps. a) Percentage of ^{40}K; b) Thorium equivalent concentration (measures of ^{207}Tl); c) Uranium equivalent concentration (^{214}Bi measurements); d), e) and f) *K/eTh*, *eU/eTh* and *K/eU* ratios, respectively. The mineral occurrences symbols are the same of Figure 1.

but the radioelement ratio maps outlined a few zones inside the MFUC with an evident enrichment of *K* and/or *eU* close to mineral occurrences (Figs. 3d – 3f). In the maps of Figure 4a, the MFUC shows a complex magnetic anomaly, with two positive poles around a central negative. This complex anomaly is due to the magnetic sources of MFUC are near the magnetic equator (the inclination was about –22.71° in the year 2005). In Figure 4, we identified zones within MFUC with magnetization contrasts. As well as radiometric ratio maps, we observed these zones are also close to mineral occurrences. To study these zones in more detail, we have analyzed the airborne geophysical

data in profile (P01 – P10) (Figs. 6, 7, 8, 9b and 10) and it was possible to identify eight (G1 – G8) and twenty seven (M1 – M27) regions with different gamma-ray spectrometry and magnetic responses, respectively. The Figure 5 shows an example of our procedure in the identification of the airborne geophysical responses previously mentioned. The profile locations were plotted in the map of Figure 11. Airborne geophysical responses have not been identified based our proceeding only for P - 07 (Fig. 9a).

In all cases, the gamma-ray spectrometry responses are characterized mainly by decrease in *eTh* concentration curve in
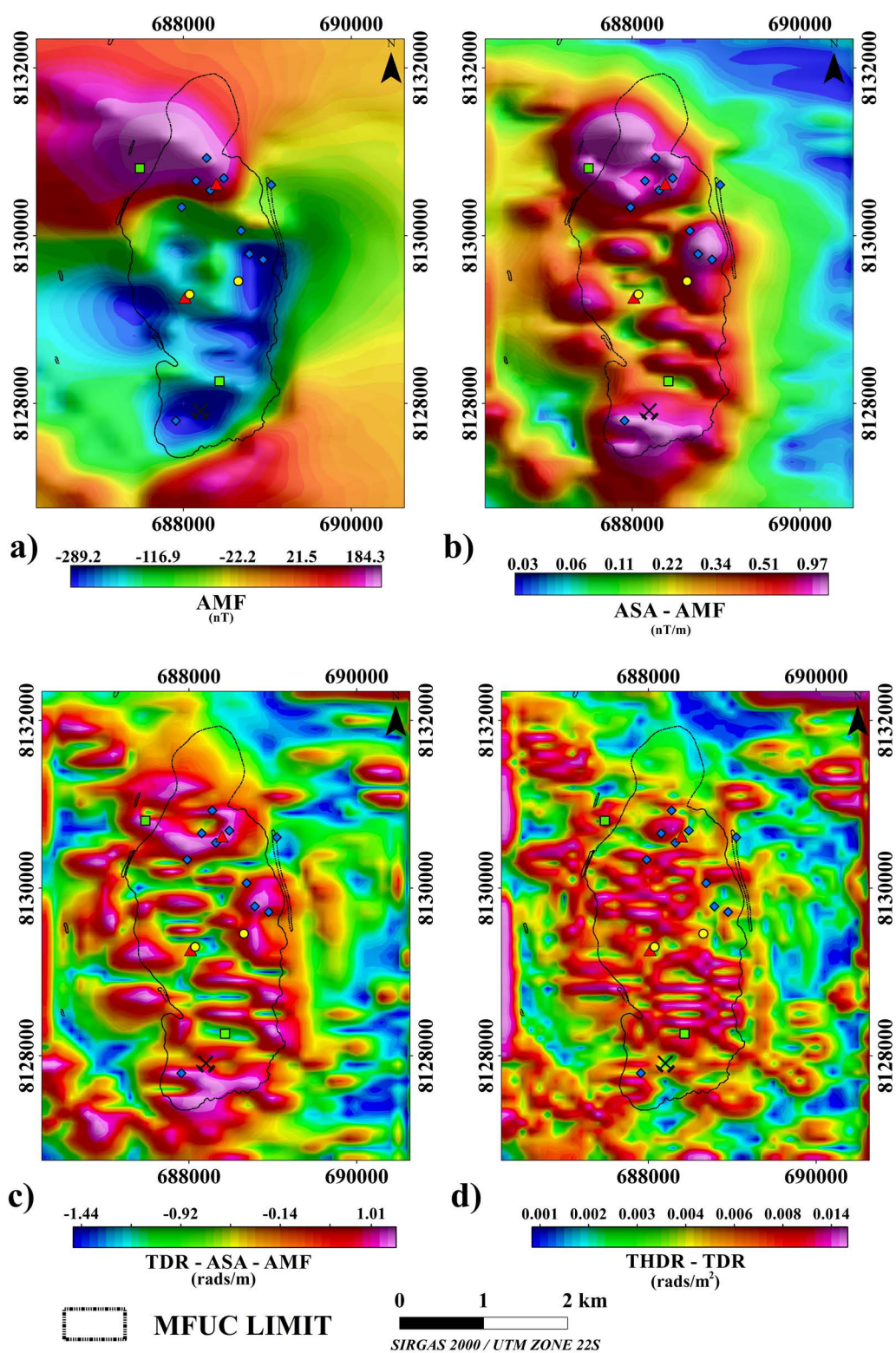
Figure 4 – Magnetometric maps. a) AMF; b) ASA from AMF; c) Tilt Angle of ASA–AMF; d) THDR of Tilt Angle from ASA–AMF. The mineral occurrences symbols are the same of Figure 1.
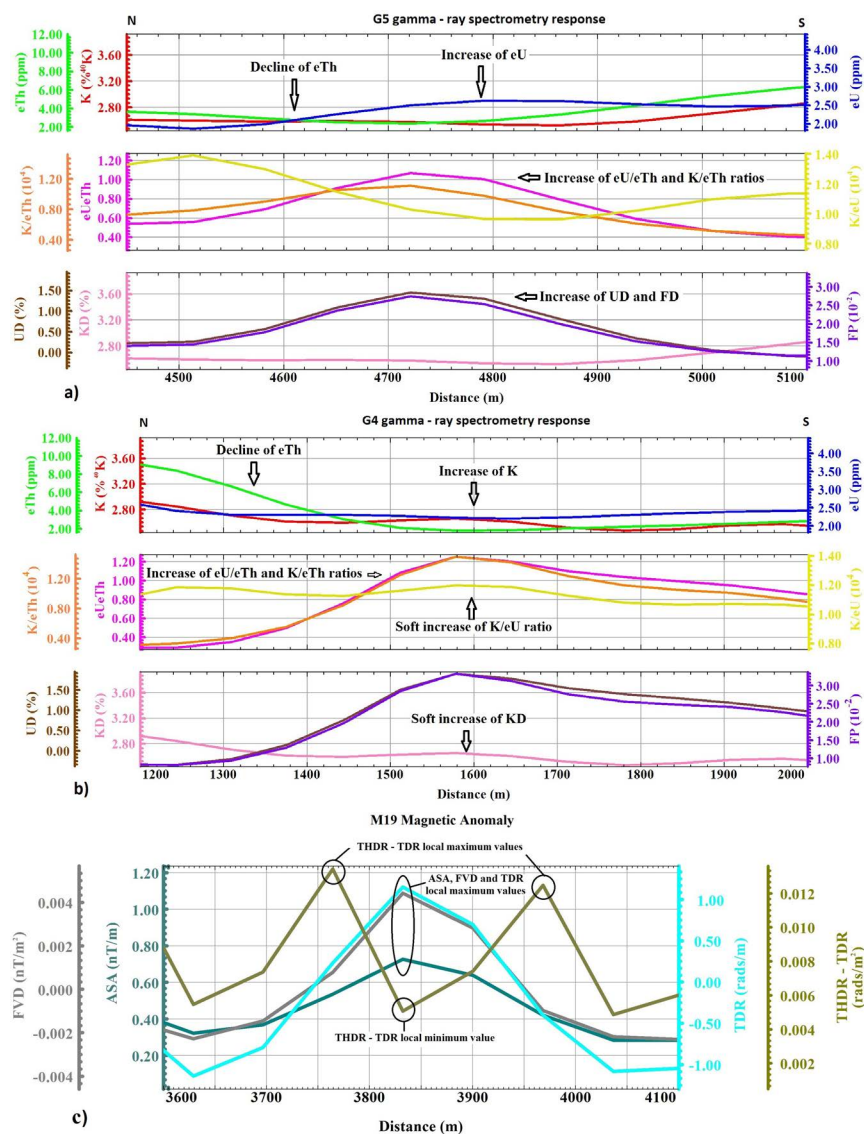
Figure 5 – Procedure used to identify the gamma-ray spectrometry responses and magnetic anomalies. a) Detail of G5 gamma-ray spectrometry response. The G1, G3, G6, G7 and G8 have shown the same gamma-ray spectrometry response of G5. b) Detail of G4 gamma-ray spectrometry response. Only G2 has shown the same gamma-ray spectrometry response of G4. c) Detail of M19 magnetic anomaly showing the procedure used to identify the magnetic anomalies. The G5, G4 and M19 airborne geophysical responses are presented in profile of Figure 8a.

according to an increase in *K* and/or *eU* concentrations curves. This behavior of the radiometric elements is highlighted on *eU/eTh* and *K/eTh* ratios curves, where is also possible to observe a correlation among positive peaks from *eU/eTh* and *K/eTh* ratios and FP and UD (Figs. 5a and 5b and Figs. 7, 8 and 10). The KD curves showed a soft increase only in G2 (Fig. 7b) and G4 (Fig. 8a). For these regions, the *K* concentration and *K/eU* curves also showed a soft increase, following *eU/eTh*, FD and UD curves. Based on *eU/eTh*, *K/eTh* and FD peaks, we plotted all radiometric

regions (G1 – G8) as points in the geological map of the Figure 1 (Fig. 11). In Figure 11, all the gamma-ray spectrometry responses occur within MFUC. The G1, G3, G6 and G8 areas are in B2 unit (talcified serpentinites), while remaining areas are in A1 unit (antigorite serpentinites). In addition, the majority of them occur in steep relief, except G7 area that appears to be located in relatively flat relief. Regarding the mineral occurrence locations, only G2 and G4 areas occur less than 200 m apart to platinum, chromite and garnierite occurrences.

P - 01

(a)

P - 02
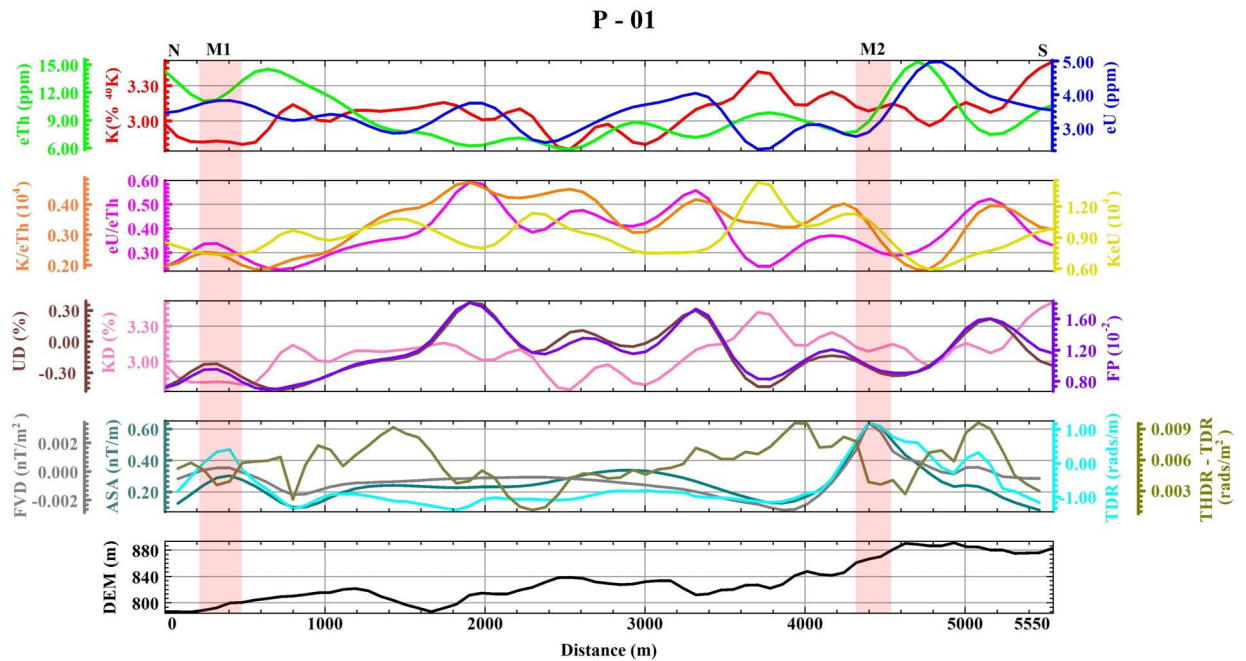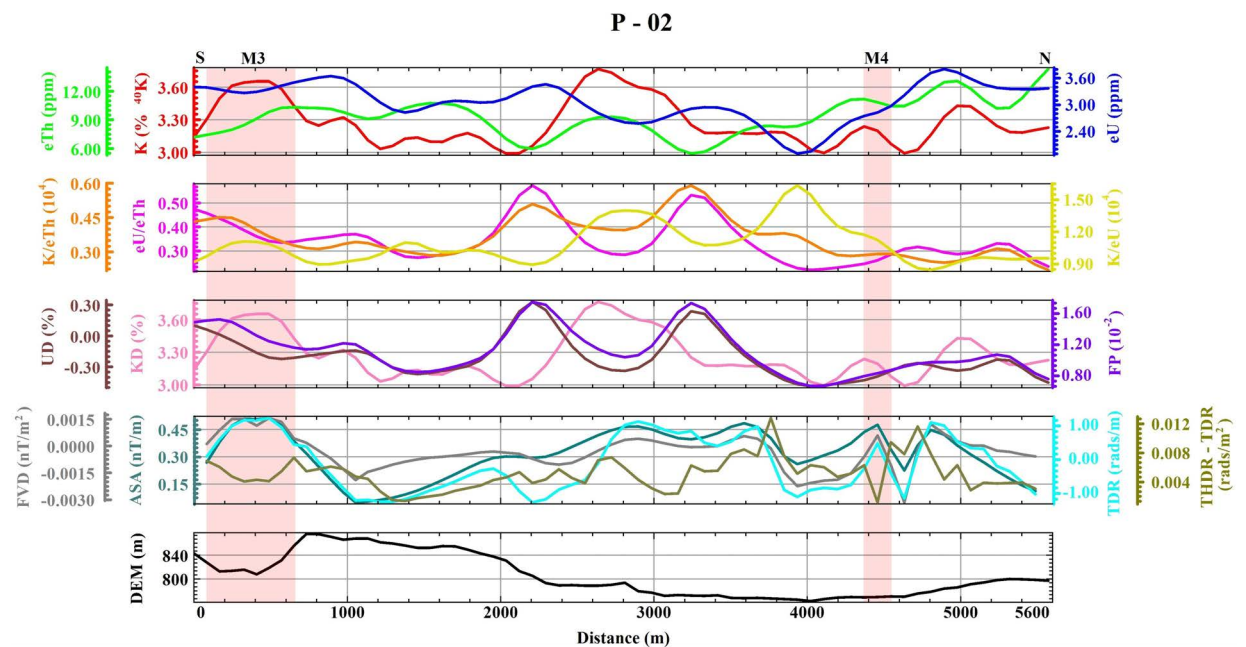
(b)

Figure 6 – Airborne geophysical responses that have been identified in: a) P - 01 profile and; b) P - 02 profile. The gamma-ray responses are highlighted in light grey and magnetic anomalies are highlighted in light pink.
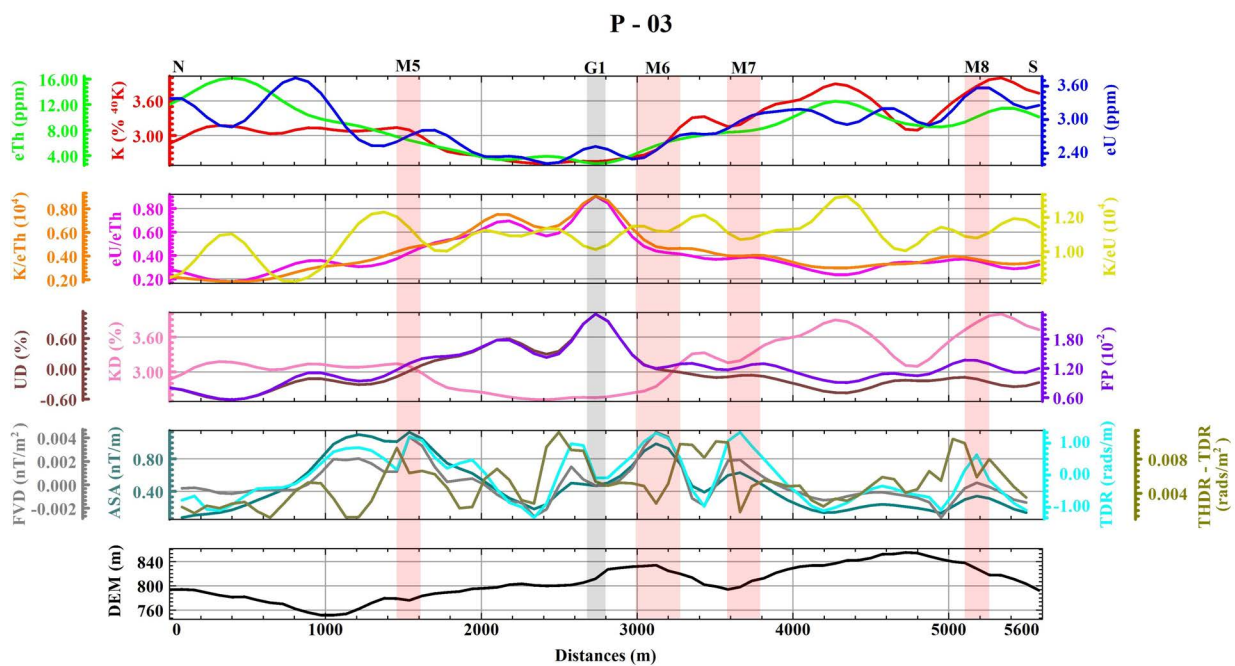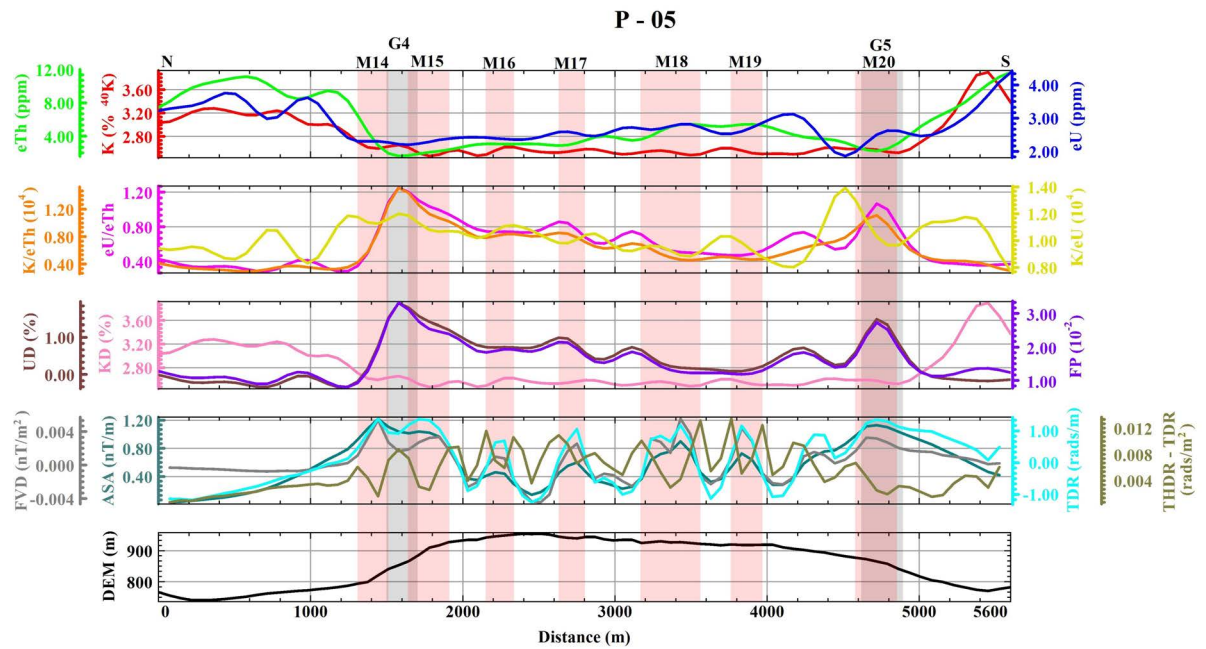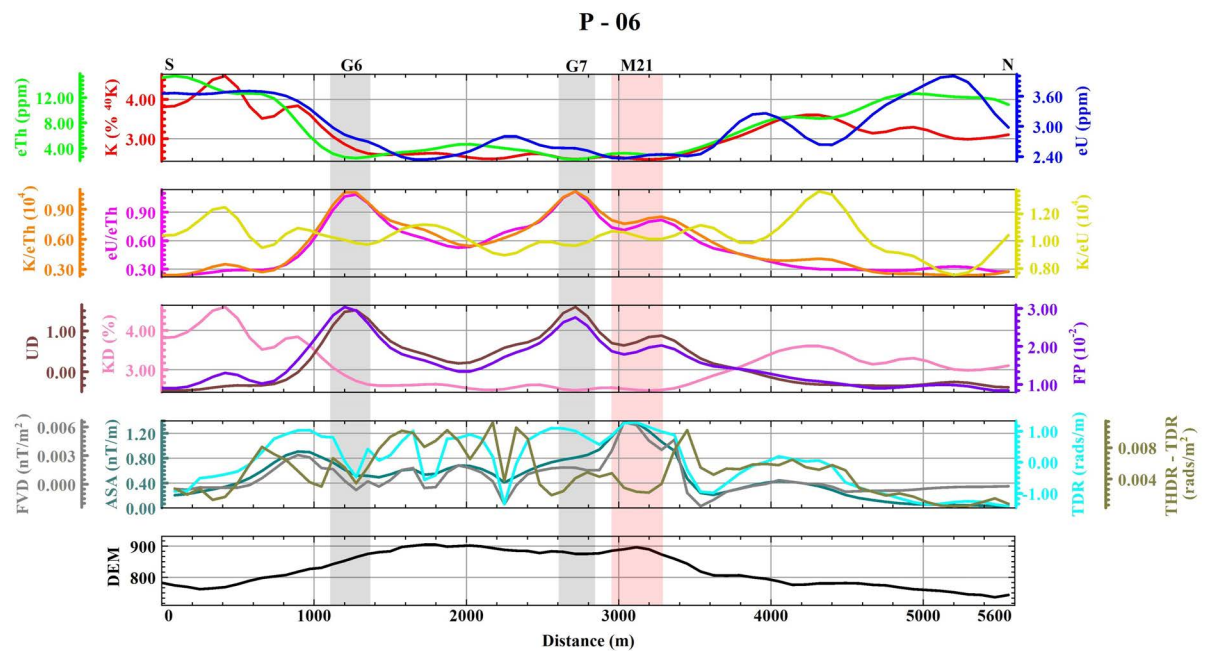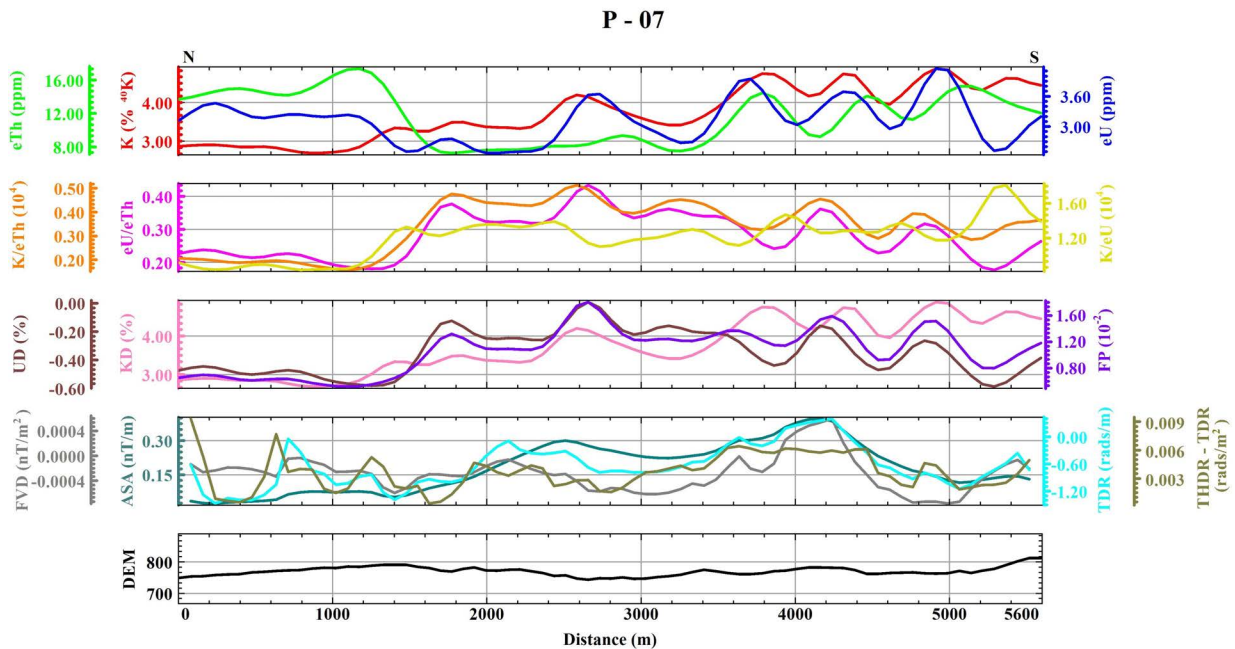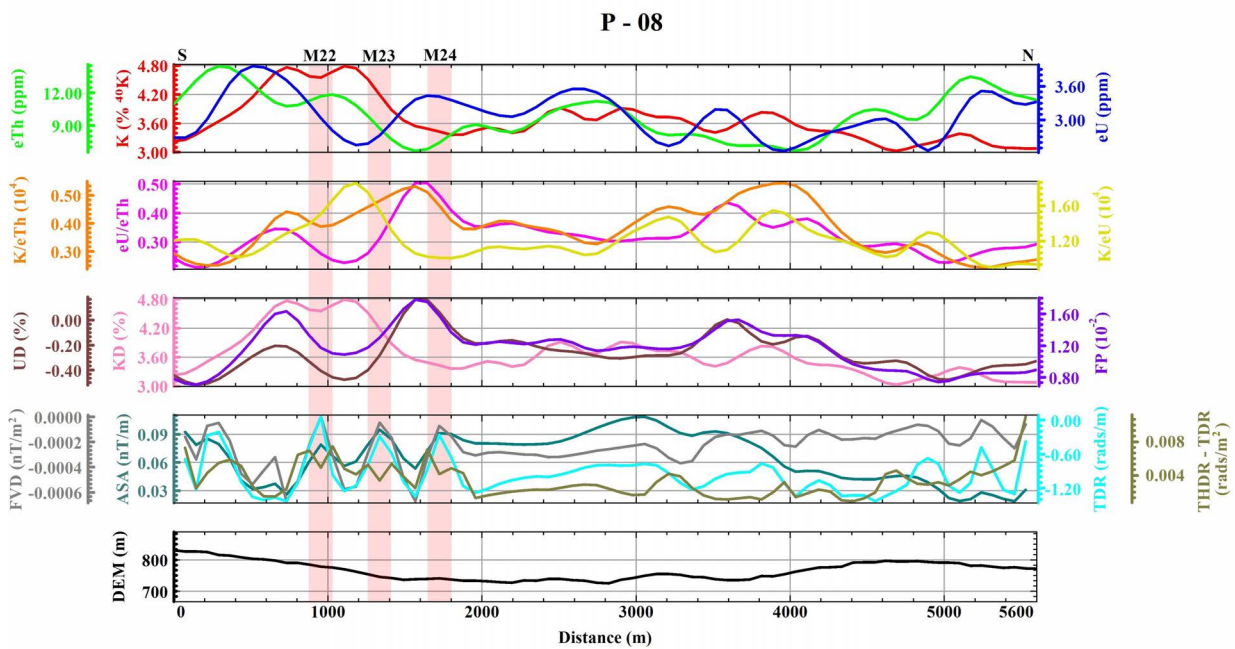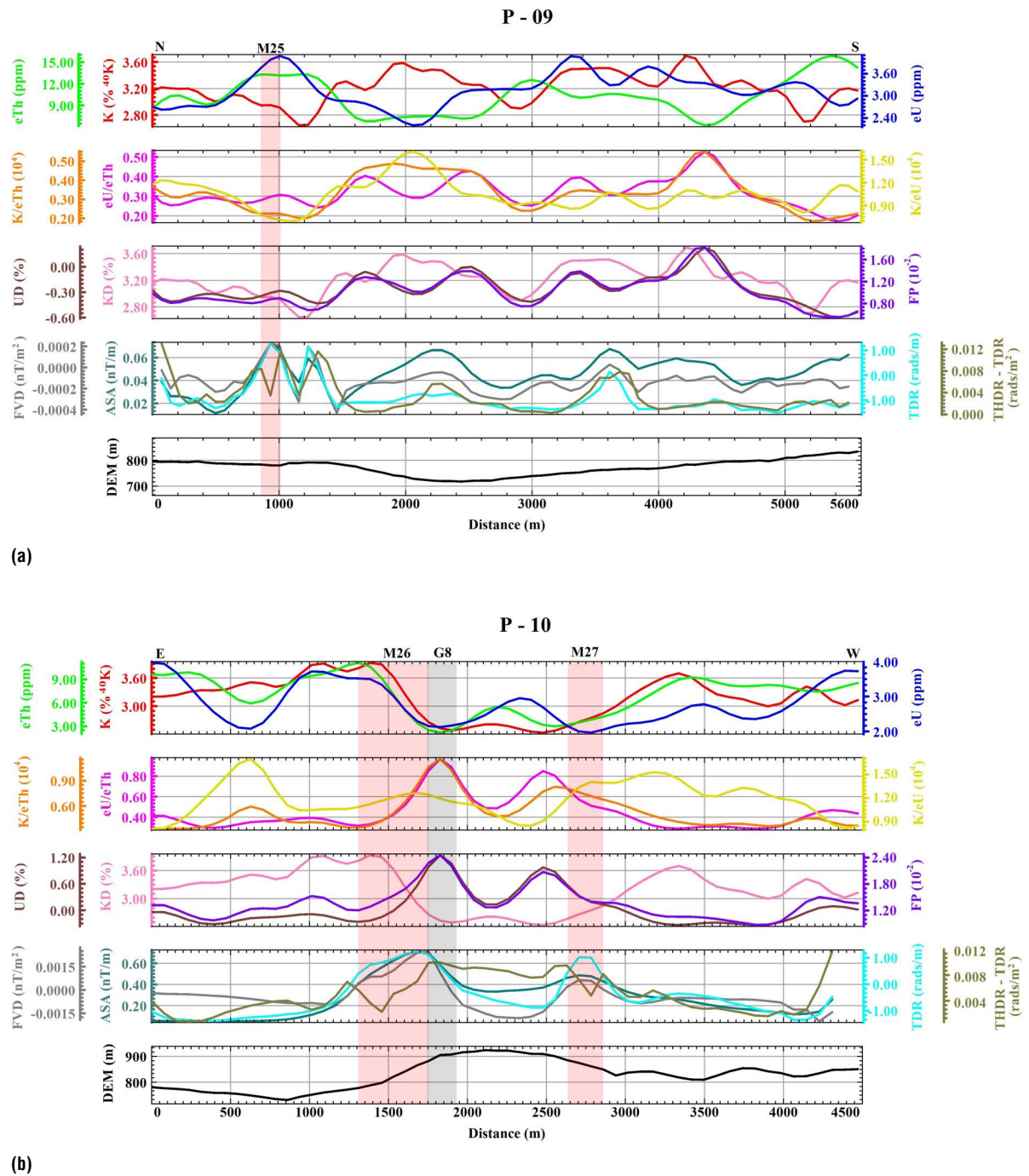
(a)
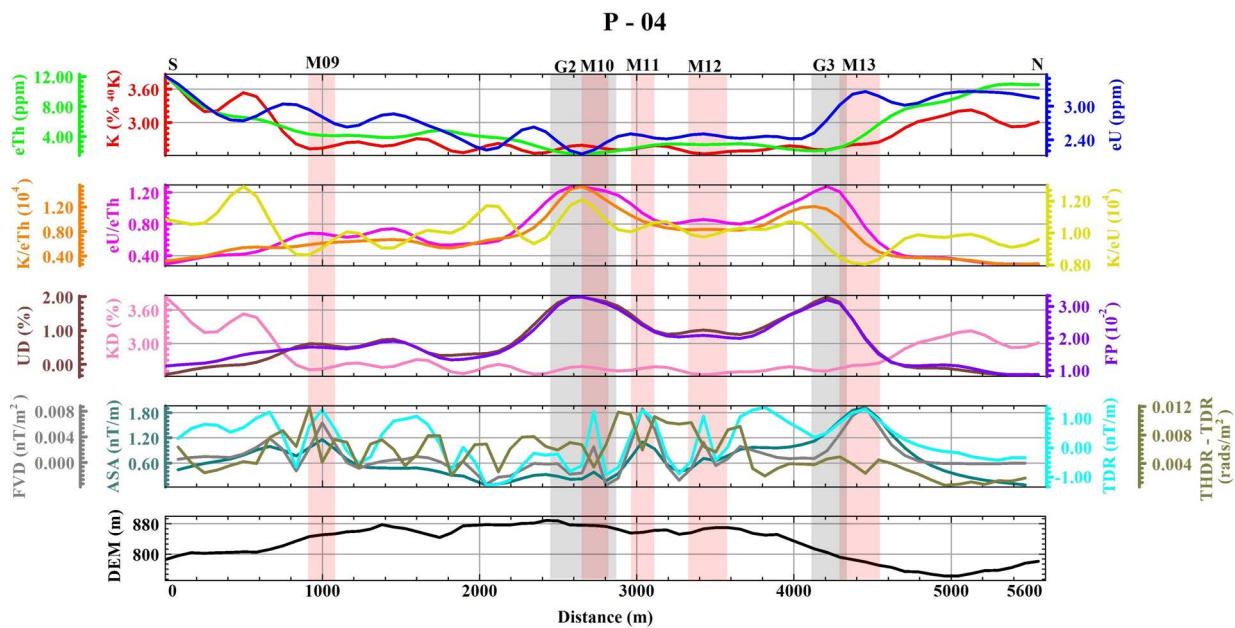
(b)

Figure 7 – Airborne geophysical responses that have been identified in: a) P - 03 profile and; b) P - 04 profile. The gamma-ray responses are highlighted in light grey and magnetic anomalies are highlighted in light pink.

(a)

(b)

Figure 8 – Airborne geophysical responses that have been identified in: a) P - 05 profile and; b) P - 06 profile. The gamma-ray responses are highlighted in light grey and magnetic anomalies are highlighted in light pink.

(a)

(b)

Figure 9 – Airborne geophysical responses that have been identified in: a) P - 07 profile and; b) P - 08 profile. The gamma-ray responses are highlighted in light grey and magnetic anomalies are highlighted in light pink.

(a)

(b)

Figure 10 – Airborne geophysical responses that have been identified in: a) P – 09 profile and; b) P - 10 profile. The gamma-ray responses are highlighted in light grey and magnetic anomalies are highlighted in light pink.
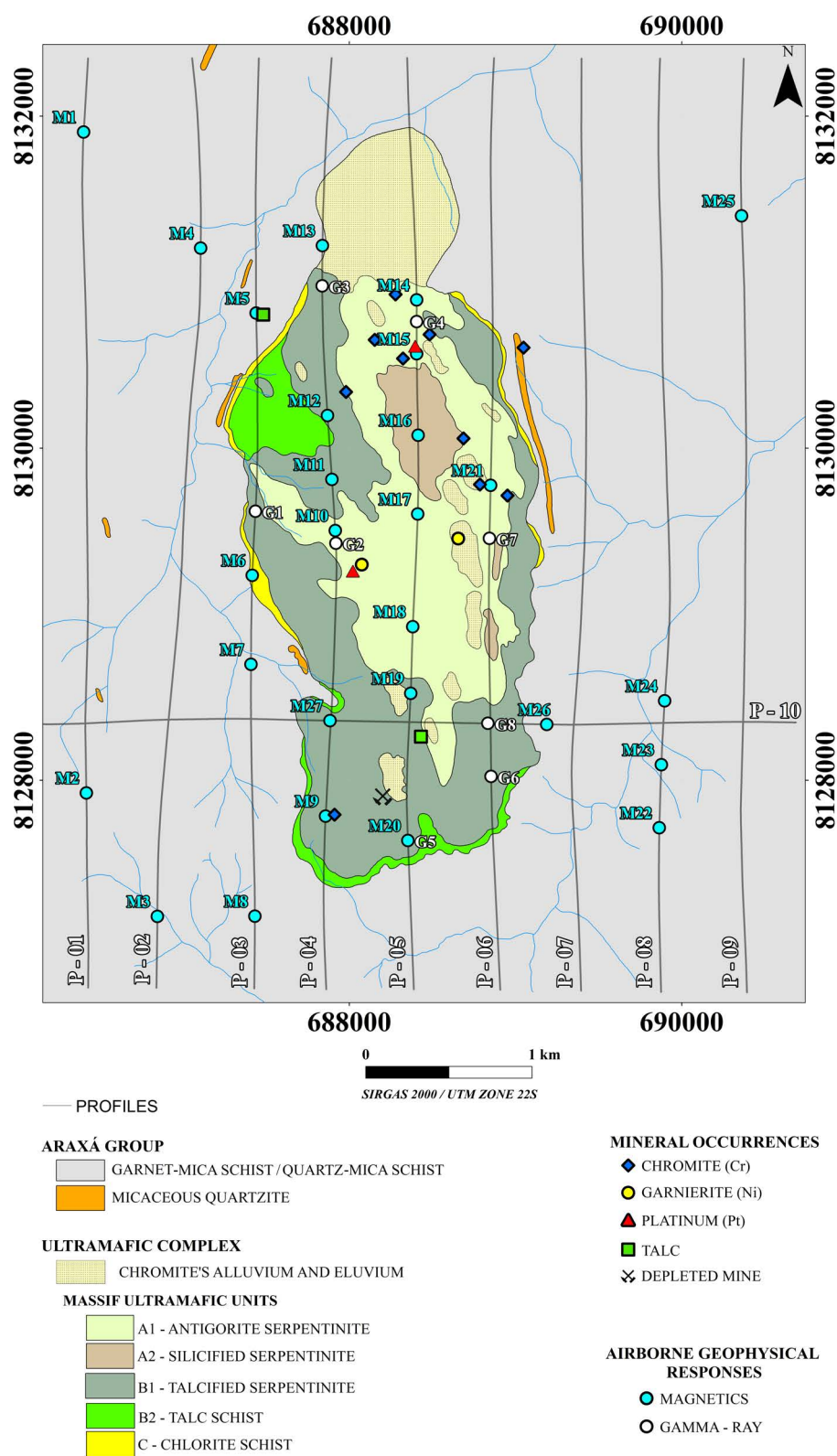
Figure 11 – MFUC geological map overlaid on DEM image with airborne geophysical responses that has been identified on the profiles plotted as point.

To identify the magnetic anomalies, we considered the Ferreira et al.'s (2010) observations, so that we have considered magnetic anomalies the regions where the local maximum values of the ASA, FVD and TDR were in agreement with one local minimum value of the THDR–TDR and all this set being limited at both ends by approximately two local maxima values of the THDR–TDR (Fig. 5c). Taking on base the ASA, FVD and TDR peak locations, we also plotted the magnetic anomaly on the map to make associations with geological information (Fig. 11). The magnetic anomalies are more spatially distributed than gamma-ray spectrometric responses, occurring in almost all geological units. Almost half of the magnetic anomalies have been located externally to MFUC. Among the magnetic anomalies within MFUC, five (M10, M14, M15 and M18) are located in antigorite serpentinites, five (M9, M11, M12, M20 and M27) are within talcified serpentinites and one (M16) is within silicified serpentinites. No magnetic anomaly was observed within talc schist and chlorite–talc schist. However, we checked that the M6 and M12 anomalies correspond to the location of the contacts between Araxá Group and chlorite schist and between talcified serpentinite and talc schist, respectively.

The M13, M19 and M21 magnetic anomalies also occur in contact zones: in the surface deposits/Araxá Group, surface deposits/talcified serpentinite and surface deposits/antigorite serpentinite contact zones, respectively. The M12 magnetic anomaly is also close to talcified serpentinite/talc schist contact zone, but it is about 40 m apart it. Regarding the mineral occurrence locations, four magnetic anomalies (M5, M9, M15 and M21) practically coincide with the mineral known occurrences and one (M14) is up to 200 m away. The M15 anomaly draws attention because it is close to three chromite occurrences and corresponds to the local where one sample rock yielded 1210 ppb of *Pt*.

Figure 12 shows the estimates results of the magnetic source depths. As it can be seen, the depths calculated by AN–EUL and SPI methods for magnetic sources identified in this study are essentially shallow (< 300 m), except for M15 anomaly which resulted in a depth > 500 m. The results obtained by AN–EUL were clustered by Structural Index to simplify the interpretation process.

The SPI method yields few solutions comparing to AN–EUL method (Fig. 12). Only one (M11) solution shows a depth value comparable with that obtained by AN–EUL method. For M13 and M14 anomalies, the SPI solutions yielded depth values larger than values obtained by AN–EUL method, while the opposite

was found for the M3, M18 and M19 anomalies. It is worthwhile outline that, apparently, the SPI method achieved better success in to estimate the magnetic source depths outside of MFUC, mainly eastern of survey area (M22, M23, M24, M25 and M26). For M1, M4, M8, M16 and M17 it was not possible to calculate the magnetic sources depths neither by SPI nor AN–EUL methods. We believe that the absence of SPI and AN–EUL solution for these anomalies may be due to high restrict level applied in the local wavenumber and ASA peaks during to processing step.

The SED method yielded solutions with a wide range of magnetic source depths. All SED solutions are concentrated within MFUC and most of them are in the eastern boundary (Fig. 13). Figure 13 displays the spatial distributions of the SED solutions for each SI. We decided not to show the SED solutions for SI = 0 in Figure 13 because they were too few and poor.

The result shows that the solution numbers with largest depth increase as SI values (Fig. 13). Visually, the well-clustered SED solutions were obtained mainly SI = 1 and SI = 2, but the solutions for SI = 3 are more scattered than the others. In general, the best solution clusters occurs close to M14, M15, M21 and M26 anomalies. For SI = 1, solutions well-clustered occur eastern M14, southeastern M21 and southwestern M26. For these clusters, the magnetic sources are mainly concentered in shallow depth (< 250 m), but largest values (250–500 m) are obtained in the southwestern M26. For SI = 2, the best solutions occur near to southwestern M14 and close to M15 and M21 anomalies. The depths estimated are around to 250–500 m for M14 and M21 anomalies and 500–750 m for M15 anomaly. Solutions within 500–750 depth range also occur to southwest M26, but these appear to be more scattered.

DISCUSSION

The results described evidences of the existence of airborne geophysical responses within and around MFUC. If we have analyzed only *K*, *eU* and *eTh* concentrations maps, we would have found difficult to interpret the G1 – G8 responses. Besides that, the interpretation of the magnetic anomalies would be harder if we have considered only AMF and/or ASA maps. Considering the airborne gamma-ray data, the option for no removing the negative values was essential because became possible to view the radiometric ratios. Moreover, for airborne magnetic data, the correlation among of the ASA, FVD, TDR and THDR–TDR made it easier to identify the magnetic anomalies.

The radiometric ratios are very useful because they suppress several effects, such as soil mixture and geometry
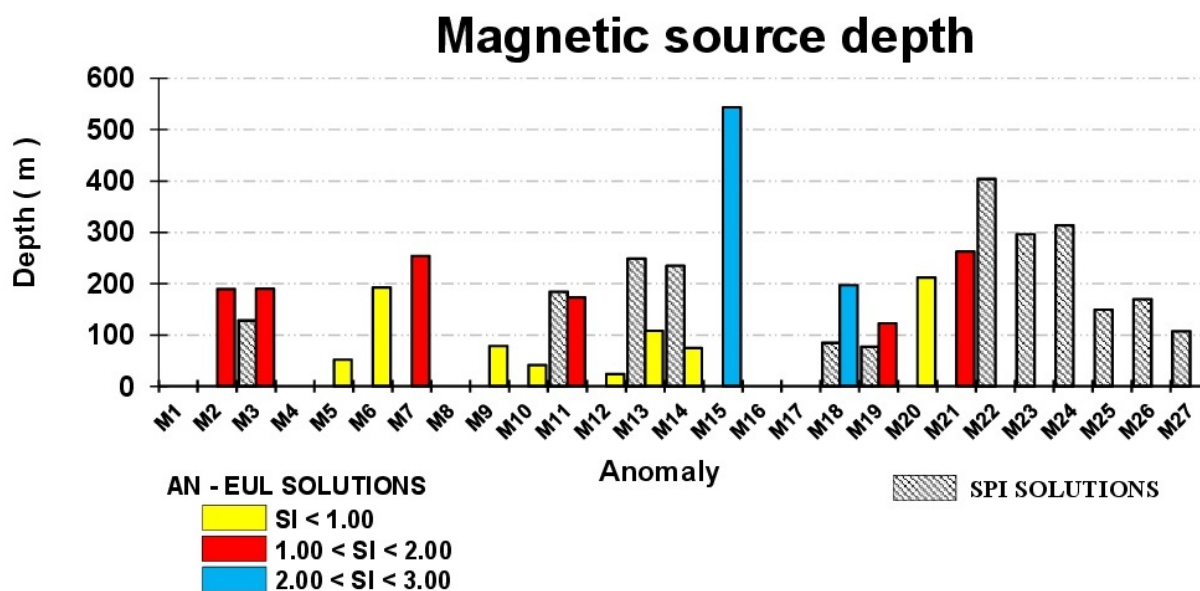
Figure 12 – Estimative of magnetic source depths obtained by AN–EUL and SPI method.

detecting, and highlight subtle variations, providing a measurement of relative enrichment between radioelements, so that this enrichment may be an indicative for mineralization or rock alterations (IAEA, 2003). Furthermore, some hydrothermal alterations indexes, like KD, UD and FP, may be useful in the mineralized zones mapping. The KD and UD express loss or gain of the K and eU, respectively, in relation to background estimated from the K and eU normalizations by eTh concentrations. This normalization takes in account that any event that affects Th abundances would also affect K and U abundances because Th is less mobile than K and U elements. So, Th concentration can be used as lithological control, therefore, the K and/or U concentrations of a lithological unit may be estimated from Th concentrations. This is possible because there is a dependency relation between K and Th and between U and Th for many rocks (Galbraith & Saunders, 1983). The K and/or eU values obtained by these relations would represent "ideal values", that is, they represent the K and/or eU distributions that are expected in the absence of remobilizations process. The difference between the observed data and this "ideal values" are interpreted as anomalous values (KD and/or UD). The areas with KD and/or UD high values are potential targets for mineral prospecting, because they may indicate hydrothermally modified rocks.

Potential areas for mineral prospecting may also be identified by FP index. Basically, FP index expresses the K and eU

product divided by eTh (Efimov, 1978 *apud* Gnojek & Prichystal, 1985). Rocks extremely altered hydrothermally show FP high values (Gnojek & Prichystal, 1985). This occurs because the hydrothermal fluids commonly contain K and, sometimes, U dissolved. When these fluids find a geochemistry barrier, K and/or U are accumulated, increasing their concentrations in the rock but without substantial rise of Th (Ostrovskiy, 1975). In this context, a peak correlation of the K/eTh, eU/eTh, FP is expected, and also KD and UD curves, because hydrothermal fluids may change the local K and/or U distributions and this change may be characterized by K and/or eU excess.

In our result, all gamma-ray spectrometry responses (G1 – G8) are characterized by an eTh decline. Furthermore, all of them occur within massive ultramafic and on steep relief. In the places where the topography is steep, the erosion process is predominant, so that the gamma-ray spectrometric response is directly related to minerals and geochemistry of fresh rock or secondary minerals from hydrothermal alteration processes (Wildfort et al., 1997). The first case seems to be the explanation for G1, G3, G5, G6, G7 and G8 responses and the last seems to be the explanation for G2 and G4 responses.

In the first case, the results show that G1, G3, G5, G6, G7 and G8 areas are characterized by an increase in the eU/eTh, FP and UD curves. As previous mentioned, subduction-related serpentinites may show high U/Th ratios due the action of fluids
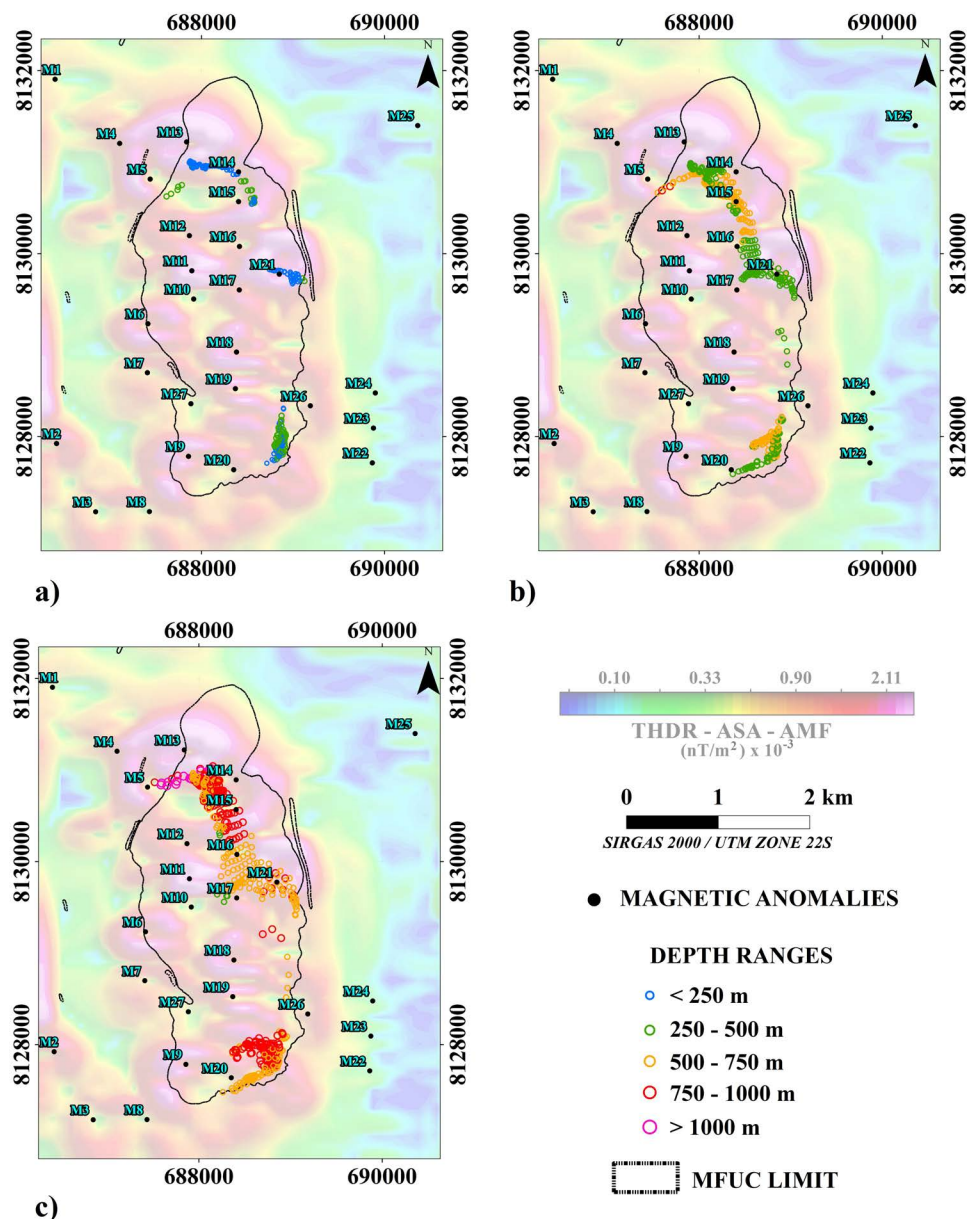
Figure 13 – Spatial distribution of SED solutions with the depth ranges obtained considering: a) SI = 1; b) SI = 2 and SI = 3.

during hydration process (Deschamps et al., 2013). We suggest that the sources of the gamma-ray spectrometry responses in questions may be related to serpentinites. This idea implies that UD peaks could also be from serpentinites. The same seems the case for FP index, that is, the FP index high values reflect the gamma-ray responses from serpentinites. Unfortunately, we have not carried out field survey to confirm if high *eU/eTh* ratios are really from serpentinites, but the results let us affirm

that airborne gamma-ray spectrometry data are able to detect such ratio in serpentinized ultramafic terrain. We suggest the accomplishment of other researches focused on verifying if this *eU/eTh* ratio is from serpentinites. A possible positive result from these researches may open a new perspective for the use for *eU/eTh* ratio applied as a tool aid in the serpentinites mapping.

For the G2 and G4, the results show that, besides these regions are characterized by increase in the *eU/eTh*, *K/eTh*, FP

and UD curve, they are also characterized by a soft increase in the *K/eU* and KD curves. This suggests that in these regions there are *K* enrichment in detriment of *eU* and *eTh*. Here, we suggest the *eU/eTh* and UD peaks may be from serpentinite but it is not the source for *K* enrichment observed. Airo (2002) observes that mafic rocks commonly have low *K* counts, even undetectable. The author points out that, in the analysis of flight lines, the increase of the *K* content in accordance with the increase of the *K/eTh* ratio may be indicative of some alteration process, thus making areas promising for prospecting. The fact that G2 and G4 are less than 200 m apart from platinum, chromite and garnierite occurrence reinforce the potentiality of these areas for mineral prospecting that would be performed by others studies.

From the airborne gamma-ray spectrometry data processing, it was identified geophysical responses possibly related to the lithology and hydrothermal alteration. However, these responses are restricted to surface. The information about sources in depth was provided by airborne magnetic data.

As seen in the previous section, the depth values were obtained from the three different methods. Due to the way each method works, we expected some differences in the depth values, but these values are in agreement with what we would expect from each method. Since SPI and AN–EUL method estimates the magnetic sources depth from the higher order derivative, we would expect shallowest depth values for both methods (Li, 2003). Our results are in agreement to this observation because they show that most of magnetic sources depths estimated by SPI and AN–EUL methods, with exception M15 and M22, are up to 300 m.

The difference in the depth values between SPI and AN–EUL may be explained due to the model that each method takes on. In the software used in this work, the SPI method takes into account a step-type source, while AN–EUL method, the magnetic source that may have other and more complex geometries depending of SI calculated. In other words, the magnetic source model is defined *a priori* in the SPI model, but in the AN–EUL it is defined *a posteriori*, which makes it possible to model a wider range of magnetic sources. However, based on geological knowledge, we believe that the SPI solutions may be more coherent externally to MFUC, while the AN–EUL solutions may be more coherent inside to MFUC.

Externally to MFUC, the M22, M23, M24 and M26 magnetic anomalies occur in places where the lithology is dominated mainly by garnet-mica schist with micaceous quartzite lenses that are essentially nonmagnetic. Based on SPI solutions, we suggest

that the magnetic sources for these anomalies may be due to structural features, like a fault or fracture, in depth up to 400 m. However, the AN–EUL solutions for M2, M3 and, possibly, M7, may be the magnetic responses from dikes in depth up to 250 m. These dikes were mapped by Berbert & Mello (1969) and correspond to a small linear segment of the mafic bodies form the Azimuth 125° lineament. The calculated SI values agree to SI values adopted by Moraes Rocha et al. (2014). The M7 anomaly may be the magnetic response of a dike in depth that has no expression on the surface.

Internally to MFUC, the AN–EUL solutions were consistent for M6, M12 and M13. Based on AN–EUL solutions, the M6 and M12 anomalies may be the magnetic response from Araxá Group/chlorite schist contact at 200 m of depth and talcified serpentinite/talc schist contact zones at less than 100 m of depth, respectively. On the map, the M13 anomaly coincides with a contact region between surface deposits and garnet-mica schist. Once the surface deposits are nonmagnetic, we believe that M13 anomaly may be due to the garnet-mica schist/ultramafic contact in 100 m of depth. On the other hand, the M19 and M21 anomalies coincide with contact zones, but the AN–EUL method yielded solutions for dike model. In this case, we understand the contact zones become structures more complex as depth increase, which may suggest the existence of magnetic sources in depth.

AN–EUL solutions for the M5, M9, M10 and M20 anomalies also provided a contact-type source model. When plotted on the map, the M5 anomaly falls within garnet-mica schist and coincides with talc occurrences, while M9 and M14 fall within MFUC and are very close to chromite occurrences. Since the garnet-mica schist is weakly magnetic, M5 may be due to garnet-mica schist/ultramafic contact zone in depth (< 100 m). The M9 and possibly M10 and M20 anomalies may be the magnetic responses of susceptibility contrast between the different MFUC units in depth.

As seen before, the M15 and M18 are the only anomalies which AN–EUL solutions yielded a more complex magnetic source model, with 2 < SI <3. However, it is noted that the depth of M18 anomaly is shallower than M15 anomaly and we have not identified any magnetic sources in depth by SED method. So, we believe that AN–EUL solutions for M15 reinforce the existence of complex magnetic sources in depth. Our results show that SED solutions have given the most support for the existence of this deepest magnetic source.

The SED solutions make use of the first derivative order and moving windows. The use of large moving windows in this work

yielded few and well-clustered solutions, which have facilitated the interpretation process (Uieda et al., 2014). Meanwhile, large moving windows may be affect the results due to anomaly superpositions effects, so that SED solutions may not coincide exactly with the positions of magnetic anomalies that we have found in this work. However, we have identified solutions clustered close to M14, M15, M21 and M26 anomalies.

Near to M14 anomaly, we have identified two magnetic sources clusters with solutions well-clustered for < 250 m and 250–500 m depth ranges, considering SI = 1 and SI = 2, respectively. AN–EUL solutions provided a different magnetic model (SI < 1) and a shallowest depth value (<100 m) for this same anomaly. In our interpretation, the shallowest depth given by AN–EUL and SED (SI = 1) solutions are relatively in agreement and may be, in fact, related to the magnetic source from M14 anomaly. However, for this same anomaly, the deepest solutions given by SI = 2 may be related to increase in the estimation of depth value due to an overestimated choice of the SI value (Uieda et al., 2014). The depth values estimated for M15 anomaly by SED solutions (SI = 2 and 500–750 m) are in agreement to AN–EUL results (2 < SI < 3 and ~540 m). The same agreement of values has been observed for M21 anomaly (AN–EUL: 0 < SI < 1 and ~260 m; SED: SI = 2 and 250–500 m). These results reinforce the evidence of deep magnetic source within MFUC. It is worthwhile outline that M15 and M21 anomalies occur in central-north portion of the ultramafic massif that Milliotti (1978) stressed as the richest in participation of *Pt*. The fact that Pt and chromite occurrences coincide with M15 and M21 anomalies location reinforce the Berbert & Mello's (1969) arguments about the existence of *Pt*, *Cr* and *Ni* primary sources in depth.

CONCLUSIONS

From the discussion above, we conclude that the present study has achieved its goal by identifying the magnetic and airborne gamma-ray spectrometry responses within and around of MFUC. From the profile analysis, we have identified twenty seven magnetic anomalies and eight gamma-ray spectrometry responses.

The magnetic anomalies can be partitioned in shallow (< 300 m) and deep (~500 m) sources. Based on works that have been published and taking in account our results, we conclude the shallowest magnetic anomalies are related dikes, contact zones and other structures, while the deepest magnetic anomalies have complex geometries and are concentrated in central-western MFUC, where the participation of Pt is large. In this aspect, we

can conclude that the existence of *Pt*, *Cr* and *Ni* primary sources in depth is possible, so that our results reinforce the Berbert & Mello's (1969) arguments.

Regarding the airborne gamma-ray spectrometry responses, we have identified not just relatively high *eU/eTh* ratio, but also *K/eTh* and *K/eU* proportions that are softly increased within ultramafic complex. Since we did not make the follow up of these gamma-ray responses, we can only conclude that airborne gamma-ray spectrometry may detect relatively high *eU/eTh* ratio in ultramafic complexes, but remains open to know if these *eU/eTh* ratios are really from serpentinites. It is also open to know the source for softly increased *K/eTh* and *K/eU* ratios. Considering that *K* low values would be expected in ultramafic rocks and that softly increased *K/eTh* and *K/eU* ratios identified in this work are near to mineral occurrences, we concluded such responses may be seen as evidence of hydrothermal alteration processes. Finally, we hope that the results of our study can complement previous studies that were performed about MFUC.

REFERENCES

AIRO ML. 2002. Aeromagnetic and Aeroradiometric Response to Hydrothermal Alteration. Surveys in Geophysics, 23: 273–302.

ANGELIM LAA, DELGADO IM, GOMES IP, GUIMARÃES JT, HEINECK CA, LACERDA FILHO JV, PERROTA MM, SANTOS RA, SILVA LC, SILVA AJP, SILVEIRA FILHO NC, SOUZA JD, VALENTE CR & VASCONCELOS AM. 2003. Província Tocantins. In: BIZZI LA, SCHOBBENHAUS C, VIDOTTI RM & GONÇALVES JH (Org.). Geologia, Tectônica e Recursos Minerais do Brasil: Texts, Maps & GIS, Companhia de Pesquisa de Recursos Minerais/Serviço Geológico do Brasil. Cap. V.

BLAKELY RJ & SIMPSON RW. 1986. Approximating edges of source bodies from magnetic or gravity anomalies. Geophysics, 51(7): 1494–1498.

BERBERT CO. 1977. Complexos máfico/ultramáficos no Brasil. In: I Simpósio de Geologia Regional, Atas. São Paulo (SP), Brazil: SBG, p. 4–28.

BERBERT CO & MELLO JCR. 1969. Investigação geológica-econômica da área de Morro Feio – Hidrolândia, Goiás, Brazil: DNPM/DFPM, Bol. Nº 132, 81 pp.

BILLINGS SD & RICHARDS D. 2001. Quality control of gridded aeromagnetic data. Exploration Geophysics, 31: 611–616.

BRIGGS IC. 1974. Machine Contouring using Minimum Curvature. Geophysics, 39(1): 39–48.

CASTROVIEJO R. 2004. El oro en ofiolitas. In: PEREIRA E, CASTROVIEJO R & ORTIZ F (Eds.). Complejos Ofiolíticos em Iberoamérica: guías de prospeccíon para metales preciosos. Madrid: Rede CYTED. Cap. 2: 25–69.

COLEMAN RG. 1977. Ophiolites: Ancient Oceanic Lithosphere? Mineral and Rocks, 12, Springer – Verlag, 229 pp.

DARDENNE MA. 2000. The Brasília Fold Belt. In: CORDANI UG, MILANI EJ, THOMAZ FILHO A, CAMPOS NETO DA (Eds.). Tectonic Evolution of South America. Rio de Janeiro, Brazil: 31st. IGC, 231–263.

DESCHAMPS F, GODARD M, GUILLOT S & HATTORI K. 2013. Geochemistry of subduction zone serpentinite. Lithos, 178: 96–127.

EFIMOV AV. 1978. Multiplikativnyj pokazatel dlja vydelenija endogennych rud aerogamma-spectrometriceskim dannym, in Metody rudnoj geofiziki: Lenigrad, Naucno-proizvodstvennoje objedinenie Geofizica Ed., p. 59–68.

FERREIRA FJ, SOUZA J, BONGIOLO ABS, CASTRO LG & ROMEIRO MAT. 2010. Realce do gradiente horizontal total de anomalias magnéticas usando a inclinação sinal analítico. Parte I – Aplicação a dados sintéticos. In: IV Simpósio Brasileiro de Geofísica. Brasília, DF, Brazil: SBGf.

GALBRAITH JH & SAUNDERS DF. 1983. Rock classification by characteristics of aerial gamma-ray measurements, Journal of Geochemical Exploration, 18: 49–73.

GEOSGB. 2018. Mineral Resources from Brazil [database], Geological Survey of Brazil. Available on: <http://geowebapp.cprm.gov.br/ViewerWEB/index_recmin.html>. Access on: January 1, 2018.

GNOJEK I & PRICHYSTAL A. 1985. A new zinc mineralization detected by airborne gamma-ray spectrometry in Northern Moravia (Czechoslovakia). Geoexploration, 28: 491–502.

GRANT JA. 1998. Ten things the textbooks don't tell you about processing and archiving airborne gamma-ray spectrometric data. Geological Survey of Canada, Current Research, 1998–D: 83–87.

IAEA. 2003. Guidelines for radioelement mapping using gamma-ray spectrometry data. IAEA, Vienna, Austria, 179 pp.

LASA ENGENHARIA E PROSPECÇÕES S.A. 2005. Projeto Levantamento Aerogeofísico do Estado de Goiás – 2ª Etapa – Faixa Brasília Sul – Relatório Final do Levantamento e Processamento dos dados magnetométricos e gamaespectrométricos. Convênio de Cooperação Técnica entre a SGM/MME/CPRM e SIC/SGM/FUNMINERAL/Estado de Goiás, Final Report, 12 vol., Texts and Maps, Rio de Janeiro, Brazil.

LI X. 2003. On the use of different methods for estimating magnetic depth. The Leading Edge, 22(11): 1090–1099.

MACLOAD IN, JONES K & DAI TF. 1993. 3D Analytical signal in the interpretation of total magnetic fields data at low magnetics latitudes. Exploration Geophysics, 24; 679–688.

MANTOVANI MSM & BRITO NEVES BB. 2009. The Paranapanema lithospheric block: its nature and role in the accretion of Gondwana. In: GAUCHER C, SIAL AN, HALVERSON GP & FRIMMEL HE (Eds.). Neoproterozoic Cambrian Tectonics, Global Change and Evolution: a focus on southwestern Gondwana. Developments in Precambrian Geology, 16: 257–272.

MILLER HG & SINGH V. 1994. Potential field tilt – A new concept for location of potential field sources. Journal of Applied Geophysics, 32(2–3): 213–217.

MILLIOTTI CA. 1978. Distribuição e controles da mineralização de platina no Morro Feio – GO. Master Dissertation, Universidade de Brasília, DF, Brazil. 149 pp.

MRDS. 2018. Mineral Resources Data System [database]. United States Geological Survey (USGS). Available on: <https://mrdata.usgs.gov/mrds/show--mrds.php?dep_id=10279692>. Access on: January 15, 2018.

MORAES ROCHA LG, PIRES ACB, CARMELO AC & ARAÚJO FILHO JO. 2014. Geophysical characterization of the Azimuth 125º lineament with aeromagnetic data: Contributions to the geology of central Brazil. Precambrian Research, 249: 273–287.

NABIGHIAN MN. 1972. The analytic signal of two-dimensional magnetic bodies with polygonal cross-section: Its properties and use for automated anomaly interpretation. Geophysics, 37(3): 507–517.

OSTROVSKIY EYA. 1975. Antagonism of radioactive elements in wallrock alterations fields and its use in aerogamma spectrometric prospecting. International Geology Review, 17(4): 461–468.

PIRES ACB. 1995. Identificação geofísica de áreas de alteração hidrotermal, Crixás – Guarinos, Goiás. Revista Brasileira de Geociências, 25(1): 61–68.

QUEIROGA GN, SUITA MTF, PEDROSA-SOARES AC, MARTINS MS & PINHEIRO MAP. 2012. Síntese sobre ofiolitos: evolução dos conceitos. Rem: Revista Escola de Minas, 65(1): 47–58.

REEVES C. 2005. Aeromagnetic Surveys: Principles, Practice & Interpretation. Earthworks, Geosoft: Cap 6, 6–18.

REID AB, ALLSOP JM, GRANSER H, MILLETT AJ & SOMERTON IW. 1990. Magnetic interpretation in three dimensions using Euler deconvolution. Geophysics, 55(1): 80–91.

ROEST WR, VERHOEF J & PILKINGTON M. 1992. Magnetic interpretation using the 3-D analytic signal. Geophysics, 57: 116–125.

SALEM A & RAVAT D. 2003. A combined analytic signal and Euler method (AN–EUL) for automatic interpretation of magnetic data. Geophysics, 68(6): 1952–1961.

SAUNDERS D, TERRY AS & THOMPSON CK. 1987. Test of National uranium Resource Evaluation gamma-ray spectral data in petroleum reconnaissance. Geophysics, 52(11): 1547–1556.

STRIEDER AJ & NILSON AA. 1992a. Melange ofiolítica nos metassedimentos Araxá de Abadiânia (GO) e implicações tectônicas regionais. Revista Brasileira de Geociências, 22(2): 204–215.

STRIEDER AJ & NILSON AA. 1992b. Estudo petrológicos de alguns fragmentos tectônicos da melange ofiolítica em Abadiânia (GO): I – O protolito dos corpos de serpentinito. Revista Brasileira de Geociências, 22(3): 338–352.

THURSTON JB & SMITH RS. 1997. Automatic conversion of magnetic data to depth, dip, and susceptibility contrast using the SPI™ method.

Geophysics, 62(3): 807–813.

UIEDA L, OLIVEIRA JUNIOR VC & BARBOSA VCF. 2014. Geophysical tutorial: Euler deconvolution of potential-field data. The Leading Edge, 33: 448–450.

VALENTE CR. 1986. Projeto mapas metalogenéticos e de previsão de recursos minerais: Goiânia, Folha SE. 22–X–B. Brasília, Brazil, Convênio DNPM/CPRM, 14 pp.

VERDUZCO B, FAIRHEAD JD, GREEN CM & MACKENZIE C. 2004. New insights into magnetic derivatives for structural mapping. The Leading Edge, 23: 116–119.

WILDFORT JR, BIERWIRTH PN & CRAIG MA. 1997. Application of airborne gamma-ray spectrometry in soil/regolith mapping and applied geomorphology. Journal of Australian Geology & Geophysics, 17(2): 201–216.

Revista Brasileira de Geofísica

RBGf

Brazilian Journal of Geophysics

UNDERWATER ACOUSTIC CHANNEL MODELING PROPOSAL
FOR SHALLOW WATER COMMUNICATION LINK OPTIMIZATION

Marcus Vinícius da Silva Simões[1], Carlos Eduardo Parente Ribeiro[2] and Luiz Gallisa Guimarães[2]

ABSTRACT. Since 80's, underwater acoustic digital communication has being one of the principal topic in underwater acoustics research. Besides, underwater waveguide modeling also has been a subject of intensive research taking benefit of the increase in available computational power and data volume provided by the new generation of ocean data measurements instruments. In shallow water specific scenario, normal-mode acoustic propagation models are still based on classic Pekeris two layers ocean model. Our paper also starts from Pekeris but uses some different approaches based on waveguide coupling and in generalized adiabatic coupled mode theory. In other words, we used the property that all waveguides could be acoustically excited by transmission resonance of consecutive modes, considering an adiabatic invariant channel. Trying to validate the model, synthetic results are compared with transmission loss measurements in field experiment.

Keywords: waveguide, adiabatic, couple modes, resonance.

RESUMO. Desde a década de 80, a comunicação digital tem sido um dos principais tópicos nos estudos de acústica subaquática. Além disso, a modelagem do guia de ondas submarino também tem sido objeto de pesquisa intensa aproveitando-se do aumento do poder computacional disponível e do volume de dados fornecido pela nova geração de instrumentos de coleta de dados oceânicos. Em um cenário específico para águas rasas, os modelos de propagação acústica de modo normal ainda têm como base o modelo clássico de oceano em duas camadas de Pekeris. Nosso artigo também começa a partir de Pekeris mas usando algumas abordagens diferentes, baseadas no acoplamento de guias de ondas e na teoria de modos adiabáticos acoplados. Em outras palavras, usamos a propriedade em que os guias de ondas podem ser acusticamente excitados por transmissão ressonante de modos consecutivos, considerando um canal adiabático invariante. Buscando a validação do modelo, os resultados sintéticos são comparados com medidas de perda de transmissão em um experimento de campo.

Palavras-chave: guia de ondas, adiabático, modos acoplados, ressonância.

[1]Marinha do Brasil, Instituto de Estudos do Mar Almirante Paulo Moreira – IEAPM – Departamento de Acústica Submarina – Rua Kioto 253, Praia do Anjos, Arraial do Cabo, Rio de Janeiro – E-mails: mvssimoes@gmail.com, marcus.simoes@marinha.mil.br

[2]Universidade Federal do Rio de Janeiro – UFRJ, Programa de Pós-graduação em Engenharia Oceânica – PENO, LIOc - Laboratório de Instrumentação Oceanográfica – E-mails: parente@peno.coppe.ufrj.br, lula@if.ufrj.br

INTRODUCTION

In deep water it is well known that vertical temperature variation behavior is a major single factor determining the transmission of sound of a given frequency. Sea surface roughness constitutes a second factor, and other oceanographic variables are poorly quantified on sound transmission (Urick, 1983).

In shallow water, the number of factors affecting sound transmission increases conceivably. Considering that in shallow water not only the vertical temperature of the ocean is the preponderant parameter as in deep water, Bergmann et al. (1969) on Part 1 Chapter 6 states that *"...it would be impractical to make a large number of sound transmission runs and then obtain rules of sound propagation empirically merely by subjecting the data amassed to and unprejudiced statistical analysis. Rather, it was found necessary to assess beforehand the possible effects of bottom character, roughness of the sea surface, and refraction conditions, and then to analyze the transmission run data purposefully"*. Nowadays, not only computational analysis, data assimilation and modeling but also new oceanographic and geological instruments for *in situ* measurements keep the same approach valid with the obvious advantage of speed processing and data amount collected.

The main goal of this paper is to model part of the problem, studying the waveguide energy transmission behavior using modal propagation under certain boundary conditions to analyze qualitatively energy flux along of the water column at certain range from the source. This approach could be useful to suggest a methodology for 3D topology fix node network implementation (latitude and longitude node position and optimized depth for the transducers) on a underwater acoustic communication network (UAN) in shallow waters.

The synthetic results were confronted with the RASCOMM'14 sea trial transmission loss computation results obtained among pre-chosen network node spots, proposed for the UAN 2D topology with fixed depth hydrophone position.

METHODOLOGY

Theoretical Approach for proposed propagation model development

In this work we assume the following premises: harmonic field propagation ($e^{-i\omega t}$, with $\omega = 2\pi f$), azimuthal symmetry, a temporal frequency f and adopted the cylindrical coordinated system (r, z).

Under these assumptions, for a punctual source located at depth $z = z_s$ the Helmholtz equation related to the sound pressure behavior p in range r as well as in depth z could be written as proposed in Jensen et al. (2011)

$$\frac{1}{r}\frac{\partial}{\partial r}\left(r\frac{\partial p}{\partial r}\right) +$$
$$+ \rho(z)\frac{\partial}{\partial z}\left(\frac{1}{\rho(z)}\frac{\partial p}{\partial z}\right) + \tag{1}$$
$$+ \frac{\omega^2}{c^2(z)}p = \frac{-\delta(z-z_s)\delta(r)}{2\pi r}.$$

Considering the wave propagation point of view, it is suitable to describe the present waveguide as the superposition of two distinct layers and an infinite seabed set up as in Figure 1. More specifically, mixture and thermocline layers are characterized by density and sound velocity profile ρ_0, c_0 and ρ_1, c_1 respectively, while in the seabed we have ρ_2, c_2. Besides, we define the local depth as H and the effective thermocline waveguide depth as $h = H - z_M$ respectively and z_M as the final depth of the mixture layer.

Applying the separable variable method such that $p(r, z) = \Psi(z)H_0^1(r)$, where H_0^1 is the zero order outgoing Hankel function as in Jensen et al.(2011) assuming that depth pressure behavior wave function $\Psi(z)$ should satisfies:

$$\Psi(z) = \begin{cases} f_0 = A_0\sinh(q_0 z);\ z > 0\ and\ z \leq z_M \\ f_1 = A1\sin(k_1(z - \frac{(z_M+H)}{2})) + \\ + B1\cos(k_1(z - \frac{(z_M+H)}{2})); \\ z > z_M\ and\ z \leq H \\ f_2 = A_2 e^{-q_2(z-H)}; z > H. \end{cases}$$
$$(2)$$

Where the constants A_0, A_1, B_1 and A_2 are determined by problem boundary conditions as well as by the wave function Ψ orthogonality criteria as in Jensen et al. (2011).

In addition, we assume that the stratified fluid density $\rho(z)$ behaves in depth as:

$$\rho(z) = \begin{cases} \rho_0\ ;\ z > 0\ and\ z \leq z_M \\ \rho_1\ ;\ z > z_M\ and\ z \leq H \\ \rho_2\ ;\ z > H. \end{cases} \tag{3}$$

Besides, here we adopted $c_2 > c_0 > c_1$ and for a given radial wavenumber k_r, we define for the *j–th* layer the depth wave propagation k_j and penetration q_j numbers respectively as:

$$k_j(k_r) = \sqrt{\frac{\omega^2}{c_j^2} - k_r^2}, \tag{4}$$

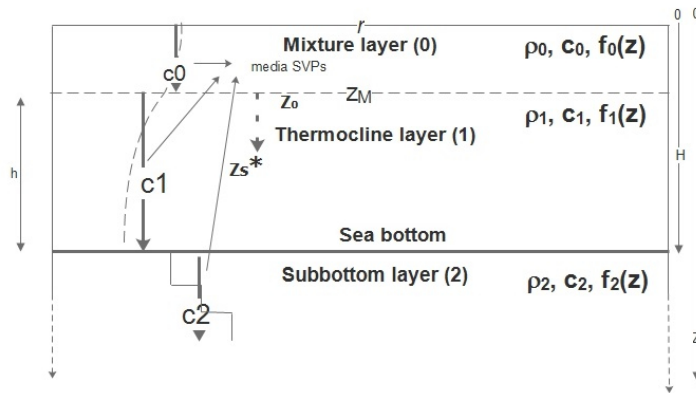$$q_j(k_r) = \sqrt{k_r^2 - \frac{\omega^2}{c_r^2}} \tag{5}$$

Figure 1 – The Double Layer Pekeris Waveguide (DLPW).

Figure 2 – Possible modes in three distinct DLPW.

In order to satisfy the acoustic problem boundary conditions, it is necessary to impose the conservation of pressure as well as the continuity of normal component to surface of particle velocity at each interface between layers as in Frisk (1994)and Jensen et al. (2011). Under these assumptions, an approximated far field problem modal solution is given by the following residue series (Jensen et al., 2011),

$$p(r,z) \approx \frac{i\, p_0}{\rho(z_s)\sqrt{8\pi r}} e^{\frac{-i\pi}{4}} \sum_{n=1}^{\infty} Z_n(z_s) Z_n(z) \frac{e^{ik_n r}}{\sqrt{k_n}} \quad (6)$$

Where p_0 is the value of the reference pressure close to the source located at the depth z_s and the integers $n = 1, 2, \ldots$ are the normal mode number related to discrete $k_r \mapsto k_{r;n}$ radial wavenumber $k_{r;n}$ and wavelength $\lambda_{r;n}$ such that $k_{r;n} = 2\pi/\lambda_{r;n}$, which are the n–th solution of the transcendental equation Δ given by the following determinant Eq.(7). For frequencies and local depths around few kHz and some meters respectively Figure 2 sketches for three distinct DLPW the typical behavior of allowed propagating modes for three different local depths $H_1 < H_3 < H_2$ respectively.

$$\Delta = \begin{vmatrix} \rho_0 \sinh(q_0 z_M) & -\rho_1 \sin(1/2 k_1 (z_M - H)) & -\rho_1 \cos(1/2 k_1 (z_M - H)) & 0 \\ \cosh(q_0 z_M) q_0 & -\cos(1/2 k_1 (z_M - H)) k_1 & \sin(1/2 k_1 (z_M - H)) k_1 & 0 \\ 0 & -\rho_1 \sin(1/2 k_1 (z_M - H)) & \rho_1 \cos(1/2 k_1 (z_M - H)) & -\rho_2 \\ 0 & \cos(1/2 k_1 (z_M - H)) k_1 & \sin(1/2 k_1 (z_M - H)) k_1 & q_2 \end{vmatrix} \quad (7)$$

In general, in underwater acoustic problems, it is common to measure sound scales in dB (Fig. 3). Considering that the *Transmission Loss* (TL) in the waveguide is given by:

$$TL(r,z) = -20 log \left| \frac{p(r,z)}{p_0} \right|. \quad (8)$$

Furthermore, it is possible to relate some $\lambda_{r;n}$ to a distinct modal number value n_j, in other words, *the phases of distinct modal waves can radially constructively interfere each other if the related wavelengths are similar* (Fig. 4). Moreover,

this constructive interference process can be improved if the separation between consecutive nodes of distinct vertical modal wave functions Ψ_{n_j} are similar too (Fig. 5). When these radial and vertical modal phases simultaneously match, the conditions to excitation of *Adiabatic Transmission Resonance* - ATR wave propagation is fulfilled. We show along this paper that ATR has a fundamental role in the physical mechanism related to acoustic energy propagation in real underwater waveguides. In the following sections, we will detail our numerical and experiment results.
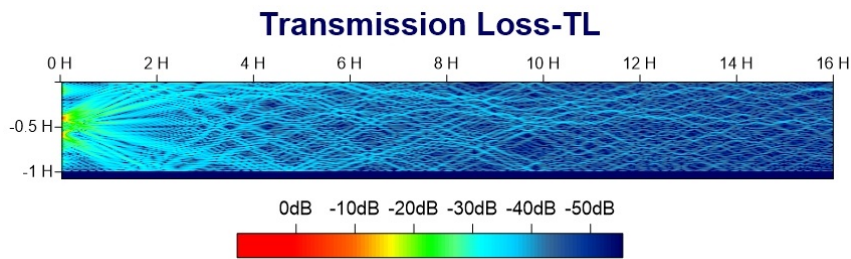
Transmission Loss-TL

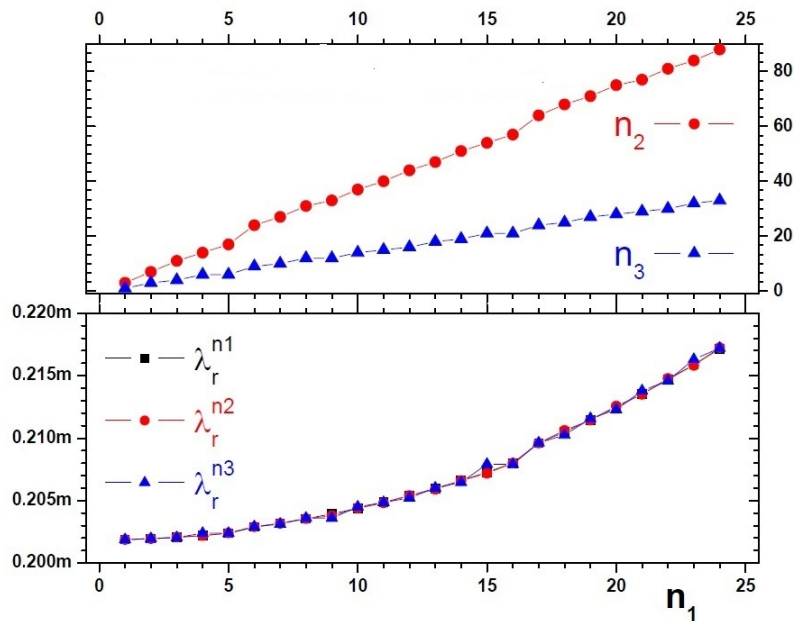**Figure 3** – Transmission Loss with source on half-way position on depth (H).

Figure 4 – Radial Phase Matching.

Collecting data: The RASComm'14 experiment

The experiment objective was to collect data for transmission loss (TL) computation in a specific topology with a preset hydrophone and source geometry. All major parameters that influence on the waveguide (ocean) variability were measured. Some parameters like currents and subbottom composition even taking part on attenuation of the signal, and consequently on TL computation, were released due to its secondary role on qualitative results for proposed model validation.

Source, Receiver and Signals

The experiment uses a 10 min (5 min LFM (CHIRP) and 5 min CW (Tone)) transmission period with one second LFM signals from 5 kHz to 10 kHz with same silence interval and a 1 second tone at frequencies 5, 5.5, 6.0...10 kHz with one second interval starting

and ending with same silence period. Only the LFM signals were used for TL computation. Unfortunately, due to operational problems during ship positioning not only both vessels (AvPq Aspirante Moura (U14) and AvPq Diadorim (IEAPM-01) but also receiving (RX at P5) and transmission stations (TX at P1, P2, P3 and P4) (Fig. 9) were set in non-ideal depths. The source was lowered at 10 m from midship (middle) with double anchorage scheme (bow (front) and stern (rear)), to provide alignment with local wind to avoid rotation and keeping midship and source front direct pointed to P5. The source deployment was made using bow and stern fixed point onboard (inside) IEAPM01 to guarantee midship position and 10 m depth for transmission. All this configuration was necessary to minimize positions and movement errors due to the absent of attitude sensor for TX and RX configuration. At the receiver site U14 anchored at 25 m bottom (expected hydrophone position at
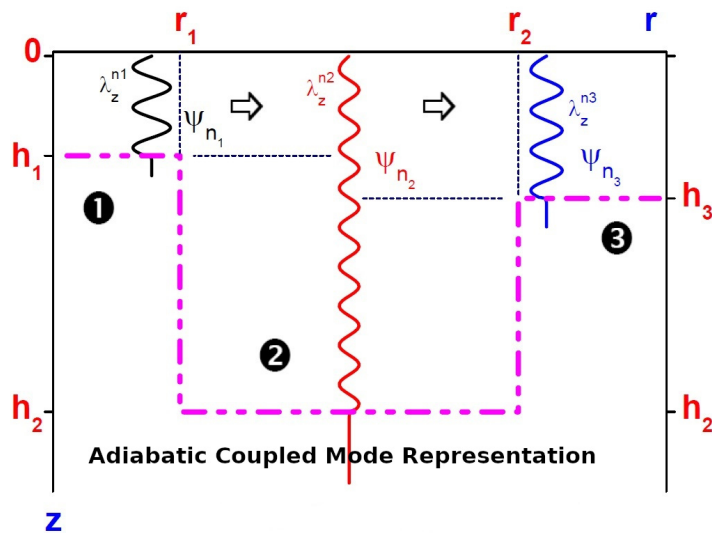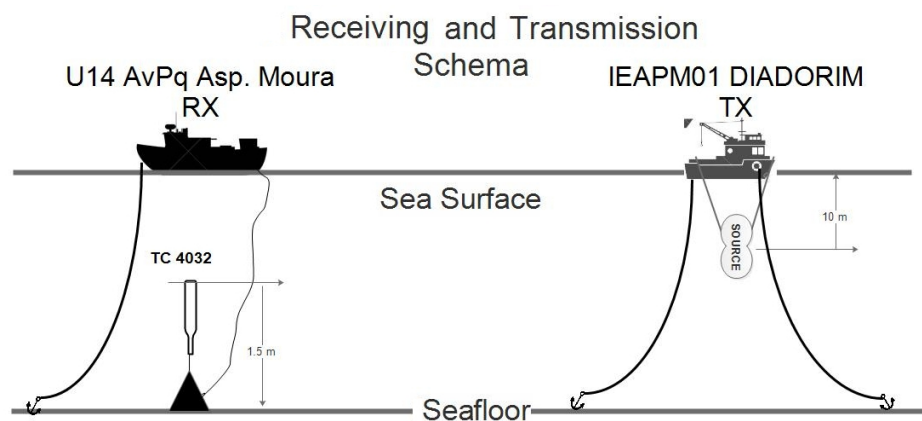
Figure 5 – Adiabatic Nodes Coupling.

Figure 6 – Receiving and Transmission Scheme of RASComm'14 experiment.

-23 m) abeam positioned to IEAPM01 to allow a direct bearing to all transmission points. This ship alignment also allowed the smallest variation on position due to swell, wind direction change and ship wave movements (Fig. 6).

The transmission was made with a linear array of three sources tonpilz type model EDO 610E with a transmission voltage response (TVR) measured in lab as shown in Figure 7. The applied voltage was 960v to obtain around 280 dB of sound pressure level (SPL - re 1v per μPa) positioned at a 10 m depth facing toward the receiving station.

At receiving point (P5) we set up two hydrophones, one RESON TC4032 with 10 dB preamplifier differential connection and 5 Hz do 120 kHz receiving band (Fig. 8) and a PI hydrophone without preamplifier and unknown specifications[1] in same receiving position (2.0 m above seafloor), see Figure 6. The used transmission set up (stationary source around 10 m) did not avoid influence of ship movement and currents (tidal inflow and outflow were observed but not measured at the experiment site), which insert some Doppler spread on the signal but with minimum influence on TL computation. Unfortunately, the

---

[1]This equipment worked fine on lab tests, but were not calibrated for the experiment. It was used to double check if the transmitting signal has enough sound pressure level (SPL) to sensitize a non-amplified hydrophone.
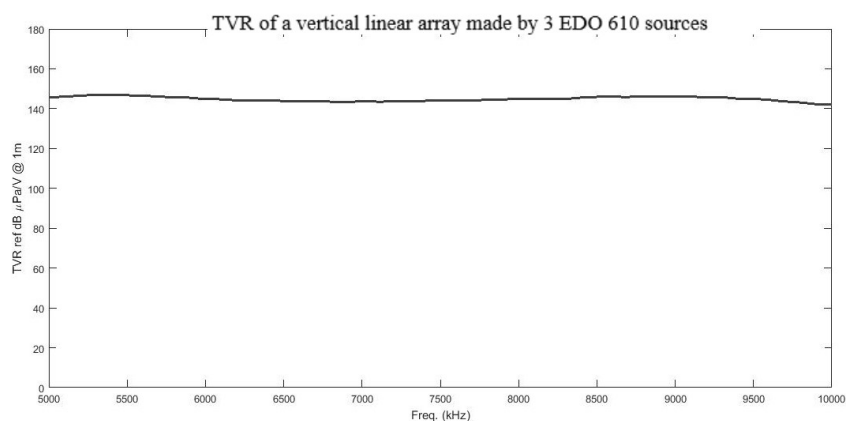
Figure 7 – TVR of vertical linear array with 3 sources type EDO 610.
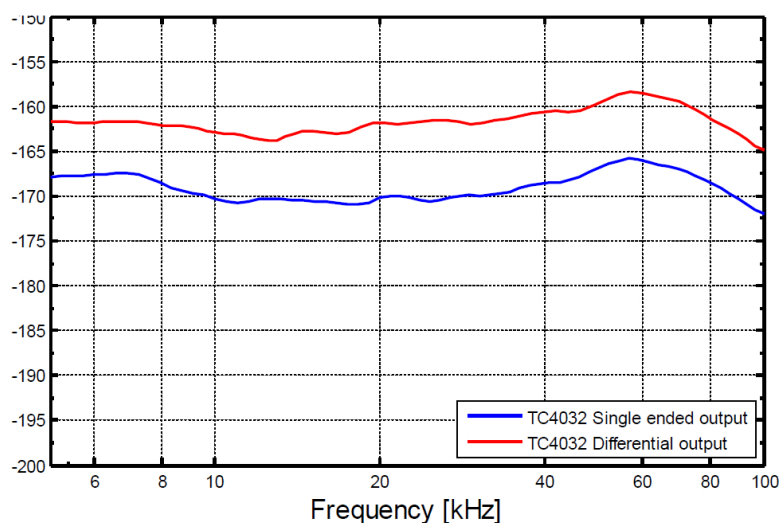
Figure 8 – OCRR (sensibility) of RESON TC4032.

accurate active array hydrophone positioning was not possible due to a lack of sensors as mentioned above.

Network topology, waveguide geometry and parameters

Topology

The nodes network positions were chosen with three main future objectives: first to capture all vessels traffic (anthropogenic noise) of Arraial do Cabo port; second to capture biological noise of secondary coves in the region (Anjos, Forno and Carneiro) and Porcos Island and North part of Cabo Frio Island (CFI); and third, node in shallow water with easy access in a depth that could be

easily reached by divers (for maintenance purposes). This choice of set up for topology of the future communication and sensing network demands that the peer to peer links among node must be on all time allowing the best rate of transmission as long as possible (Fig. 9).

Waveguide

To measure the waveguide (or the channel) robustness to sustain communication we choose to measure the transmission loss (TL) parameter at different frequencies using the largest band that our equipment allowed. To do it we set four transmission points (TX) aiming a three sources linear array to a receiving position (RX)
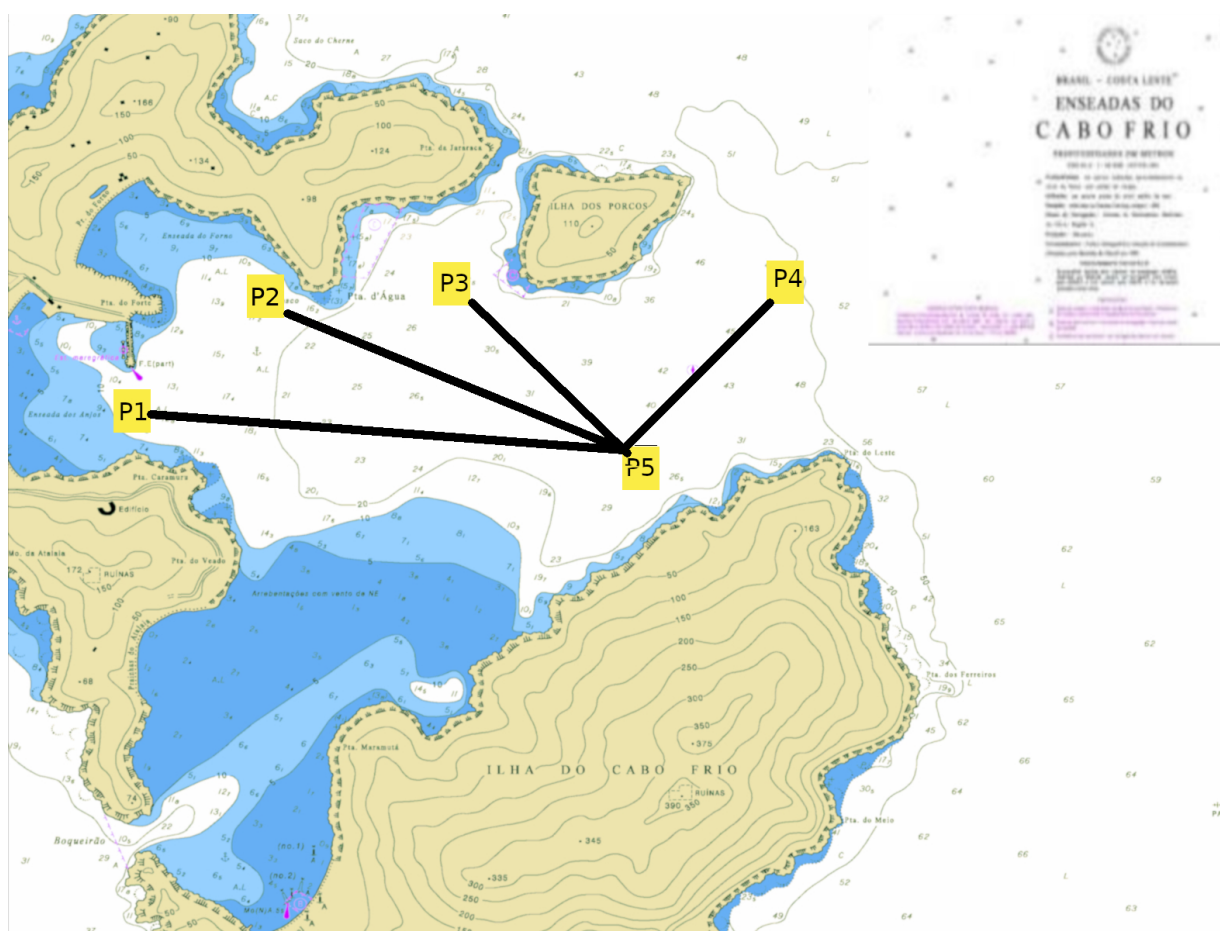
Figure 9 – UAN proposed topology for Arraial do Cabo's coves (subset of DHN 1503 Nautical Chart).

in four different bathymetric bearings among transmission points (P1, P2, P3 and P4) and a fixed receiving point (P5) Figure 9. Figures 10 and 11 show P1-P5 and P4-P5 profiles, respectively.

Winds and upwelling condition

Waveguide conditions were typical of fall upwelling period (Torres Junior, 1995; Elias, 2009) with winds blowing from E and NE direction with peaks of 11 m/s and at least three days persistence as show in Figure 12. This condition allowed upwelling development which get in Arraial's Coves from two main entrances: first from *Boqueirão* (mouth between continent and SW part of CFI) increased by tidal influx and secondly from the cove region main entrance between East point of CFI and *Porcos' Island* (small island between point P4 and P3 on Fig. 9) with a secondary influx from small mouth between *Jararaca's point* and *Porcos' Island*. Most measurements were made during tidal influx which facilitated subsurface upwelling

insertion confirmed by CTD (Conductivity, Temperature and Depth) profilers, with Sound Velocity Profile (SVP) computed (Wilson, 1960) and direct SVP profilers on RX position P5 (Fig. 13).

Bathymetry

Bathymetry was obtained from a series of multibeam and singlebeam hydrographic surveys (Fig. 14) which allowed a quite precise bathymetric profile between TX and RX points as show in Figures 10 and 11 used to compute mean depth for waveguide model use on TL computation.

Seafloor, currents, subbottom and sea surface

Seafloor is characterized by fine mobile sand (Silva, 2009) that changes place from time to time due to wind regime, tidal generated bottom currents and extreme wave events, mainly on the shallow sand bank between CFI and the continent (dark blue
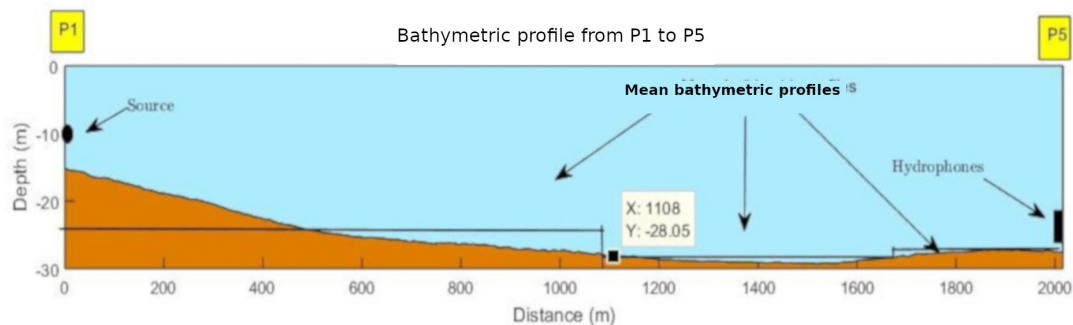
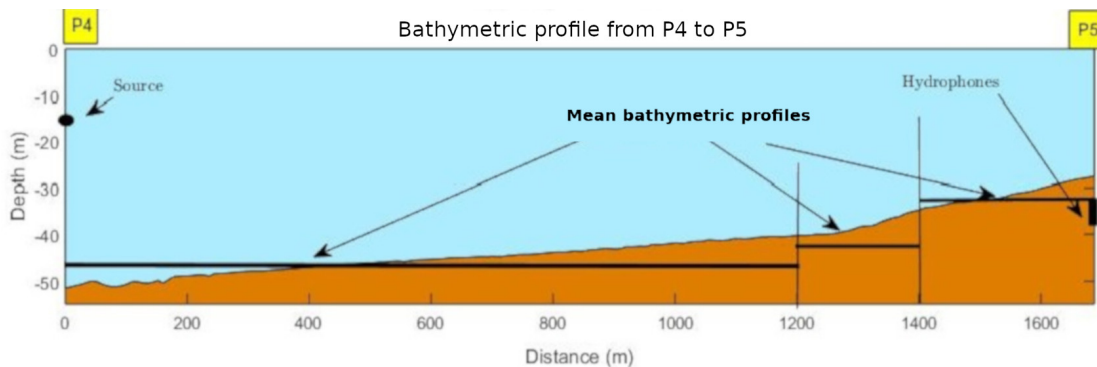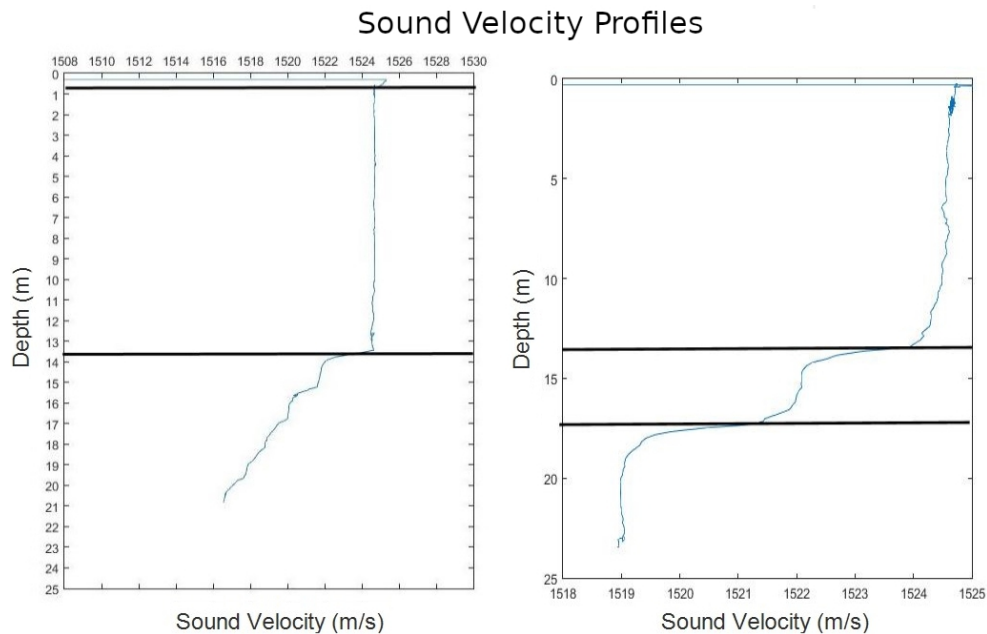**Figure 10** – Bathymetric profile heading from P1 and P4 (TX) to P5 (RX).

Figure 11 – Bathymetric profile heading from P4 (TX) to P5 (RX).

Figure 12 – Wind regime (direction and velocity) on site during the trail RASCOMM'14.

Sound Velocity Profiles

Figure 13 – SVP on P5 during P25 and P45 transmission.

on the nautical chart 1503 - Fig. 9) with minor changes in grain diameter inside the inner region (Silva, 2009).

The absence of current measurements did not affect the results since the Doppler effect has a minimum influence in TL computation due to the position of the nodes are fixed. The influence of the source and receiver movements are also considered negligible.

Taking into account that the proposed model was designed to compute mode propagation that have almost non-interference with seabed and sea surface, the measurements of seabed properties and sea surface, movement were considered outside the scope of this paper.

MODEL VALIDATION: SYNTHETIC VERSUS REAL DATA

Computing real data transmission loss

Signal Processing

All receiver signals collected were processed to obtain the TL values for all LFM signals received. Total signal has 320 seconds (16Mi samples) using a sample rate of 50K samples/s of 1s LFM from 5 to 10 kHz and 1s silence that were cut in 20s signal bundles. The 5 to 10 kHz signal band was extracted from the frequency domain and brought back to time domain to be autocorrelated with the transmitted LFM to identify and mark the

beginning of the received LFMs to allow individual extraction of TL (Fig. 15).

After LFM separation, we used Hilbert transform envelope to obtain the correct voltages amplitude on the LFM signal for each desire frequency (Fig. 16). From all 5 do 10 kHz band we chose round frequencies of 5, 5.5, 6.0 ...9.5 and 10 kHz to compare field results with synthetic ones to provide a measurement model's fitness to real measurements.

To compute Transmission Loss, we used the well-known relation stated in Eq.(9) (Souza, 1997):

$$TL = 20log(\tfrac{V_{TX}}{V_{RX}}) + TVR_{Source} +$$
$$+ \ OCRR_{Hydrophone} \quad dB \ re \ \mu Pa \ @ \ 1m \tag{9}$$

where V_{TX} is the transmission source applied voltage in Volts (V), V_{RX} is the receiving hydrophone delivered voltage in Volts (V), TVR is the Transmission Voltage Response in $dB \, ref \, \mu Pa/V \ @ \ 1m$ and $OCRR$ is the Open Circuit Receiving Response in $dB \ re \ 1V/\mu \ Pa \ @ \ 1m$. Figure 17 presents all receiving LFMs in frequencies from 5 to 10 kHz in 100 Hz interval computed from all CHIRPS received during 320s of receiving data. Red line indicates the mean from all values from all LFM transmitted. All these values are the base for model results comparisons.
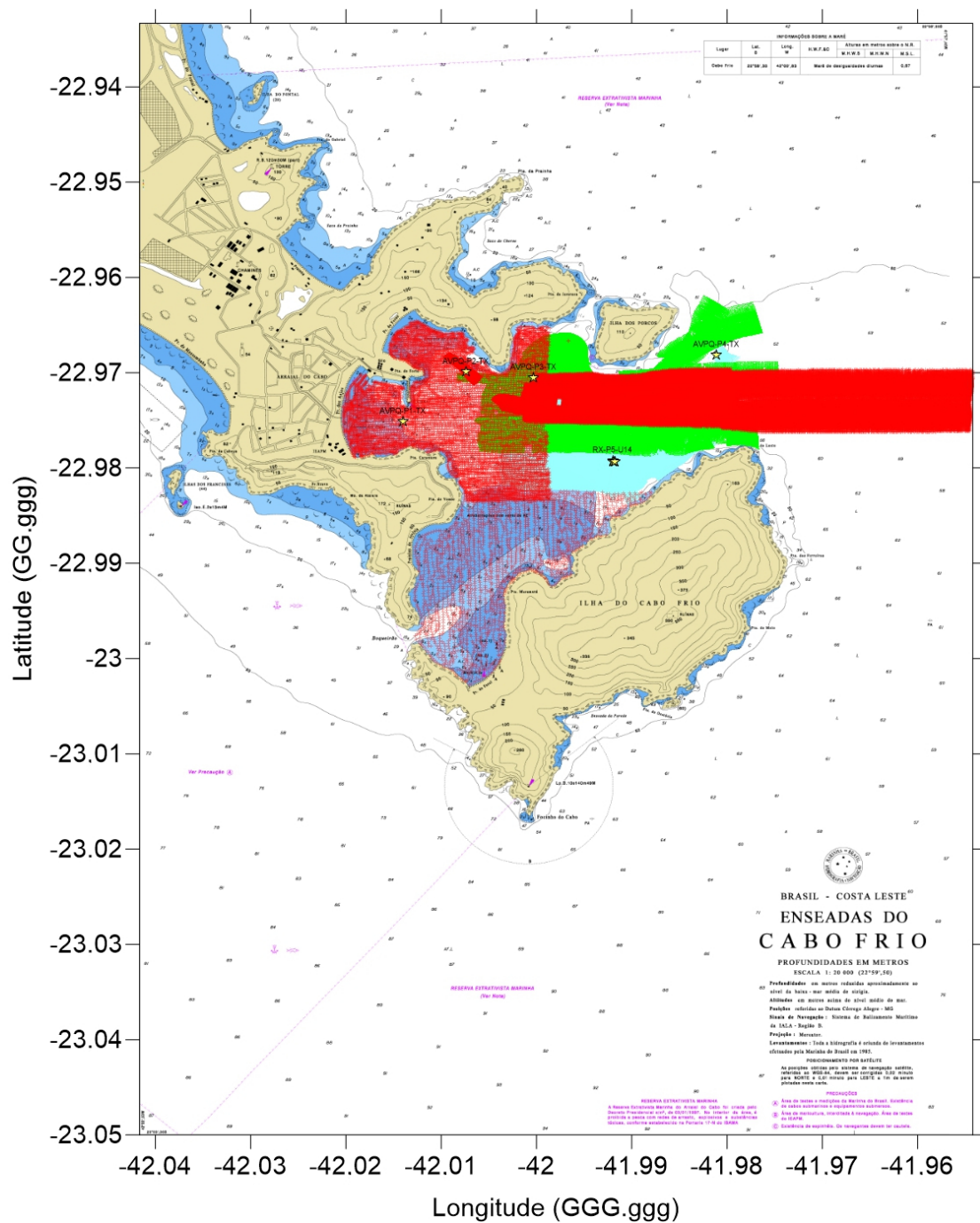
Figure 14 – All hydrographic surveys used to generate bathymetric profiles between TX and RX nodes.
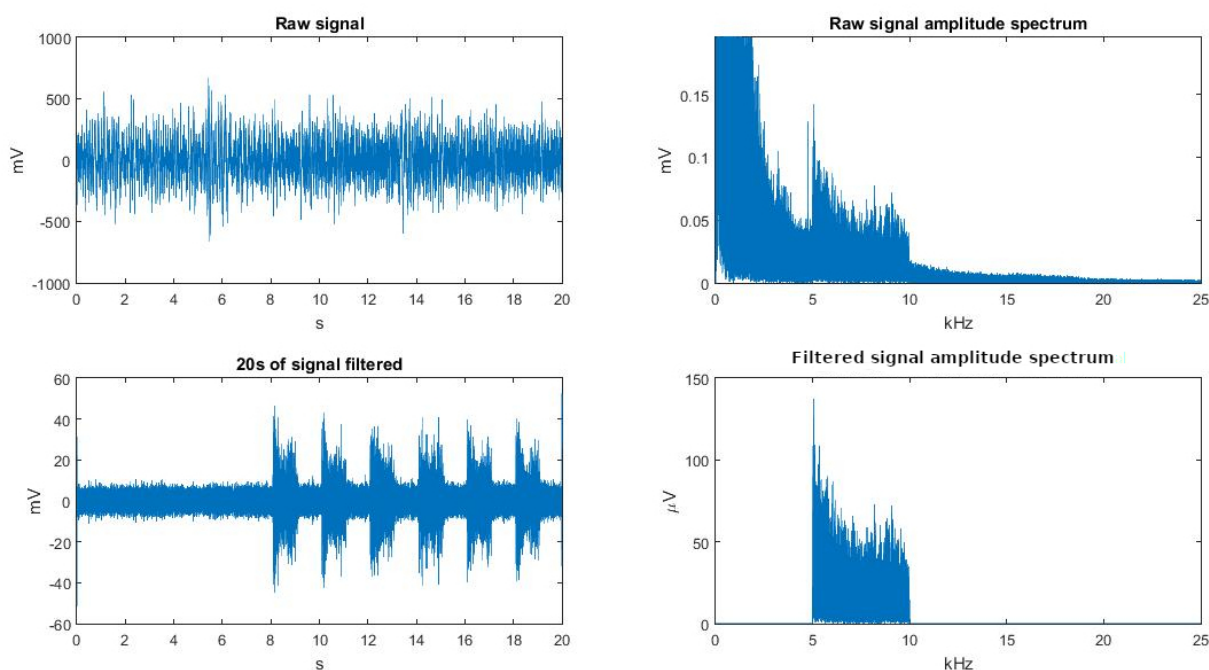
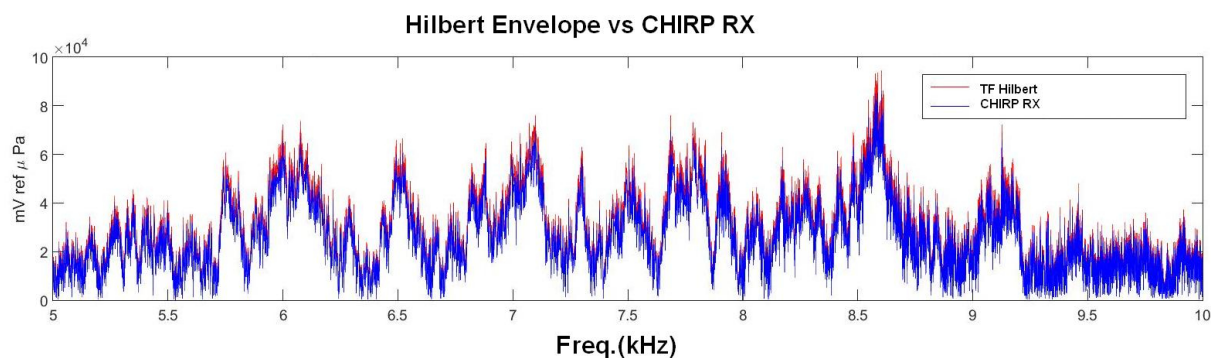**Figure 15** – CHIRP Signal Extracted from RESON TC4032.

Figure 16 – TF Hilbert applied on a CHRIP Signal Extracted from RESON TC4032.

Computing Synthetic Data

Results of transmission loss were generated by Eq.(8) for three distinct bearings (P1-P5, P2-P5 and P4-P5) in different frequencies (5, 7.5 and 10 kHz) using the final depth of the mixture layer at 12 m (collected *in situ*) and with source placed in two different positions: at 10 m depth (inside the mixture layer duct) and at half-way of thermocline waveguide (ideal position). Figures 18 to 21 are showing the model results.

RESULTS

Synthetic results on Figure 22 are inside the range of spherical and cylindrical ideal spreading values as in Frisk (1994); Medwin & Clay (1998); Brekhovskikh & Lysanov (2003); Jensen et al. (2011); and with numerical results at 23 m with 10 dB different from the measured mean and values closed spherical TL. This difference should be attributed due to the leaking energy backward and sideways from the source added to the non-absorption computation in range. Likewise, Figure 17 shows some important features like: energy duct formation, shadow and bright convergent zones as well increasing dispersion as frequency increases in different headings and frequencies. This result testify
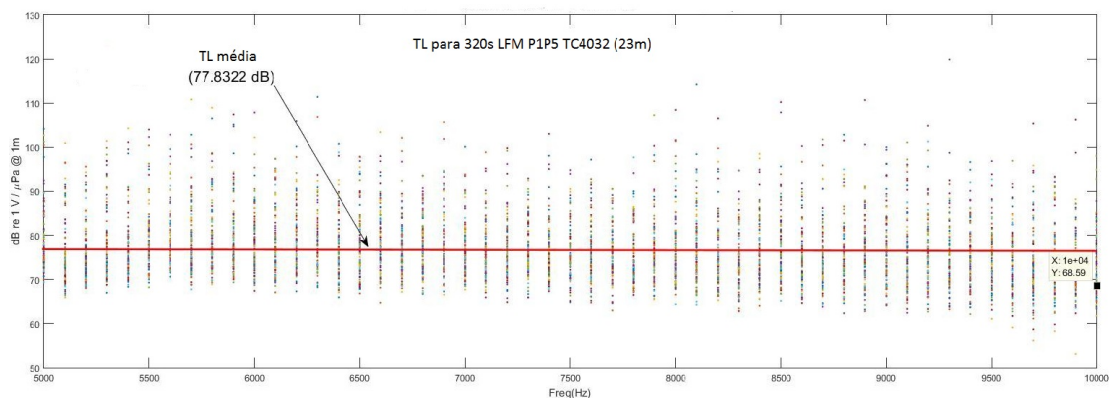
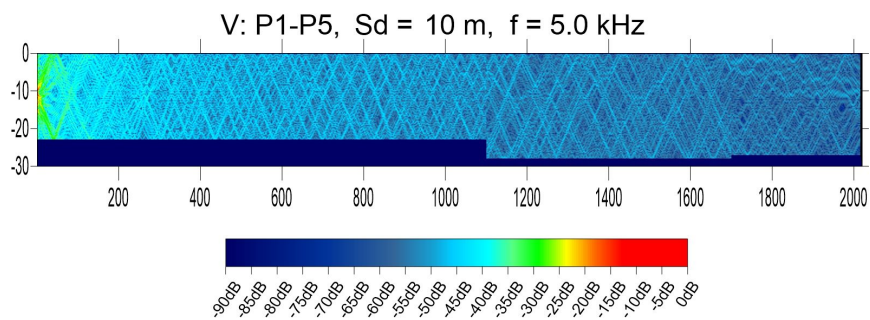**Figure 17** – TL computed at 23 m on RESON TC4032.

Figure 18 – TL field from P1 to P5 at 5.0 kHz, source at 10 m with mixture layer depth 12 m.
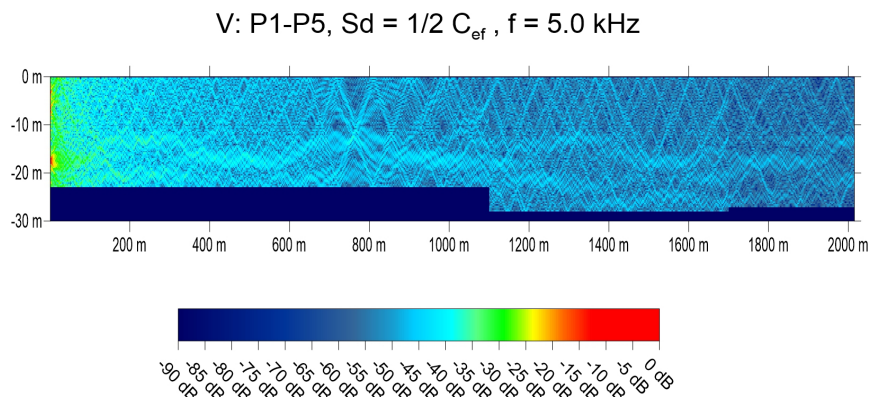

Figure 19 – TL field from P1 to P5 at 5.0 kHz, source in the middle of thermocline layer with mixture layer depth at 12 m.
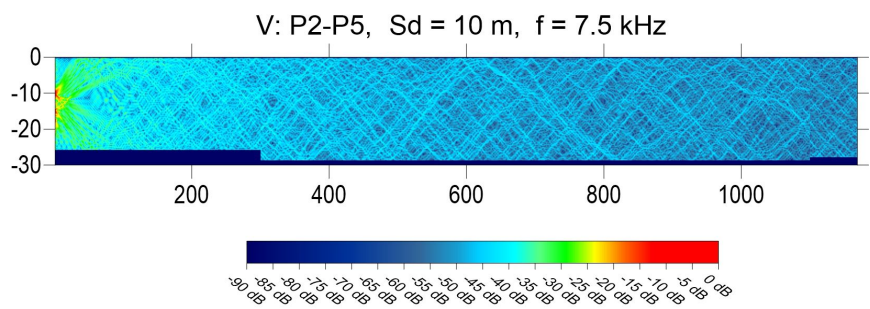

Figure 20 – TL field from P2 to P5 at 7.5 kHz, source at 10 m with mixture layer depth at 12 m.
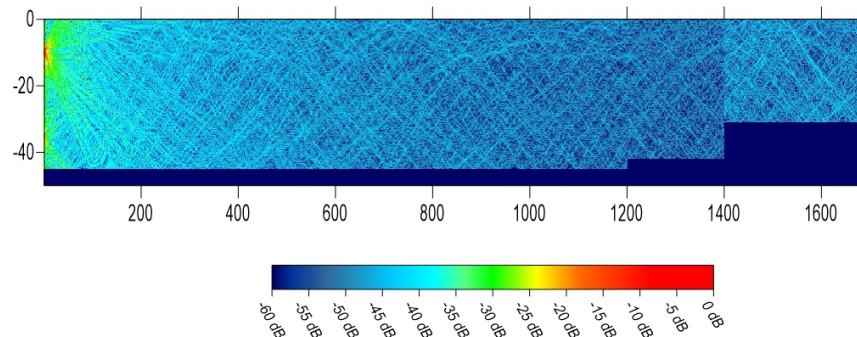
V: P4-P5, Sd = 10 m, f = 10.0 kHz

Figure 21 – TL field from P4 to P5 at 10.0 kHz, source at 10 m with mixture layer depth at 12 m.
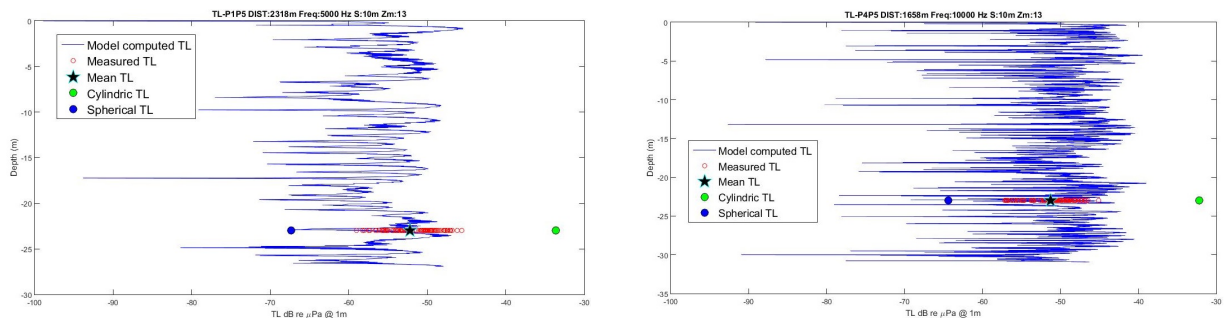

Figure 22 – TL computed at 23 m depth versus model results for 5 and 10 kHz frequencies, at 2318 m and 1658 m distance from P1, with source at 10 m depth.

the qualitative agreement with real underwater acoustic field behavior but also impose further *in situ* measurements to improve results quantitatively and qualitatively in different scenarios.

Experiment results are not showing good agreement with model results and should be repeated in the same site but in different positions to confirm not only values and signal behavior but mainly to identify the reason for a non-expected difference greater than 30 dB between measured and synthetic transmission loss values.

CONCLUSIONS

About the model

The presented theoretical model is to explains qualitatively the mechanism of acoustic energy transport, considering bathymetric and meteo-oceanographic variable parameters, to allow real time improvements on link performance for underwater acoustic network in shallow waters. Using the physical fundamental concepts of adiabatic resonance transmission phenomena it was possible to develop a peer to peer underwater acoustic theoretical propagation model based on modal propagation which describes

satisfactorily the main flux of energy between source and receiver as showed in Figures 17 and 22. Nevertheless, the model did not respond satisfactorily not only to lateral and retroactive energy losses but also to absorption in all possible directions of propagation. Furthermore, numerical algorithms used are the most usual and tested ones allowing further researches and development on more effective and efficient numerical approaches.

About the experiment

A large amount of improvements can be done on sea experiment for *in situ* data collection to support model's improvements. For example, the use of divers to positioning devices (source and hydrophone arrays) in a controlled set up, include underwater attitude control instruments on hydrophone cables, install underwater current meters at all waveguide depth, set up hydrophone arrays in all waveguide depth and floating and subfloating devices to mitigate ship movement influence on hydrophone and source position.

Future work

Theoretical approach should include lateral and backward energy leaking to mitigate the non-expected large difference between effective channel transmission loss measured from signal values and synthetic results. *In situ* measurements in different scenarios to stress qualitative validation and to confirm quantitatively models' results; and development of hardware and software for a real network node to install on Arraial do Cabo coves sites.

ACKNOWLEDGMENTS

REFERENCES

BERGMANN PG. 1969. Shallow water transmission. In: Physics of Sound in the Sea, originally issued in 1948 as Division 6 Summary Technical Report of National Research Defense Committee - NDRC, Department of the Navy, Headquarters of Naval Material Command, vol. 8, 1969 reprint, 2nd ed., CRC Press, Boca Baton, Part I, chapter 6, pages 137-157.

BREKHOVSKIKH LM. 1968. Waves in Layered Media. In: FRENKIEL FN & TEMPLE G (Eds.). Applied Mathematics and Mechanics: An International Series of Monographs. 2nd ed., vol. 6, Academic Press Elsevier, 503 pp.

BREKHOVSKIKH LM & LYSANOV YP. 2003. Fundamentals of Ocean Acoustics. In: FELSEN LB (Ed.). Springer Series on Wave Phenomena. 2nd ed., vol. 8, Springer-Verlag New York, Inc., 267 pp.

ELIAS LMC. 2009. Variabilidade interanual da ressurgência de Cabo Frio - RJ. Master Science Dissertation on Ocean Engineering, Postgraduate Program in Oceanic Engineering, COPPE, Universidade Federal do Rio de Janeiro, Brazil, 104 pp.

FRISK GV. 1994. Ocean and Seabed Acoustics, a theory of Wave Propagation. PTR Prentice Hall, NJ, USA, ISBN 0-13-630112-6, 291 pp.

JENSEN FB, KUPERMAN WA, PORTER MB & SCHMIDT H. 2011. Computational Ocean Acoustics. In: AIP Series in Modern Acoustics and Signal Processing, Springer Science+Business Media, 2nd ed., LLC, New York, NY, USA, 783 pp.

MEDWIN H & CLAY CS. 1998. Fundamentals of Acoustical Oceanography. In: STERN R & LEVY M (Eds.). Applications of Modern Acoustics Series. Academic Press, San Diego, CA, USA, 708 pp.

PEKERIS CL, WORZEL JL & EWING M. 1948. Propagation of Sound in the Ocean. Geological Society of America Memoir, vol. 27, Chapter: Theory of Propagation of Explosive Sound in Shallow Water, 1-116.

SILVA AC da. 2009. Dinâmica Batimétrica e Sedimentólogica da Região do Cabo Frio - Rio de Janeiro. PhD Thesis on Geology, Postgraduate program in Geology, Geoscience Institute of Universidade Federal do Rio de Janeiro, Brazil, 178 pp.

SOUZA LA de. 1997. Princípios de SONAR. Instituto de Pesquisas da Marinha - IPqM, Ilha do Governador, Rio de Janeiro, Brazil, IPqM-013-0177-ET/97, 248 pp.

TORRES JUNIOR AR. 1995. Resposta da Ressurgência Costeira de Cabo Frio a Forçantes Locais. Master Dissertation on Ocean Engineering, Programa de Pós-graduação em Engenharia Oceânica, COPPE, Universidade Federal do Rio de Janeiro, Brazil. 132 pp.

URICK RJ. 1983. Principles of Underwater Sound. 3rd ed., McGraw-Hill Book Company, USA, 423 pp.

WILSON WD. 1960. Equation for the Speed of Sound in Sea Water. The Journal of the Acoustical Society of America, 32(10): 1357.